eman ta zabal zazu

Universidad del País Vasco
Euskal Herriko Unibertsitatea

HYBRID PHOTOCATALYTIC MATERIALS FOR CONTAMINANTS OF EMERGING CONCERN DEGRADATION

FANGYUAN ZHENG

2023

Supervisors: Dr. José Luis Vilas Vilela

Dr. Javier Reguera Gómez

(c)2023 FANGYUAN ZHENG

eman ta zabal zazu
Universidad del País Vasco
Euskal Herriko Unibertsitatea

ZIENTZIA
ETA TEKNOLOGIA
FAKULTATEA
FACULTAD
DE CIENCIA
Y TECNOLOGÍA

BCMATERIALS
BASQUE CENTER FOR MATERIALS, APPLICATIONS & NANOSTRUCTURES
ehugroup

HYBRID PHOTOCATALYTIC MATERIALS FOR CONTAMINANTS OF EMERGING CONCERN DEGRADATION

Doctoral Thesis presented by:

FANGYUAN ZHENG

Supervisors: Dr. José Luis Vilas Vilela
Dr. Javier Reguera Gómez

Leioa, 2023

(c)2023 FANGYUAN ZHENG

Acknowledgements

When I was 17 years old, I emigrated, together with my parents, from China to Basque Country. Since then, I have come to love this land and the many surprises it contains. I have also met many people who taught me, helped me, understood me and respected me and my dream, which motivates me never to give up studying in spite of facing the culture clash, the language and the different education system. Finally, I have pursued my PhD. Now, I am handing in my thesis to you.

This document presents the results of almost three years intense work and the final step of a long, hard but unique journey. I would like to acknowledge many people who have helped me in different ways during this adventure.

Firstly, to both Basque Center for Materials, Applications and Nanostructures (BCMaterials) and University of Basque Country (UPV/EHU) for the predoctoral grant (PIFI20/08) of this project. Also, thanks to SGIker group of UPV/EHU for the technical support.

I have to express my deepest appreciation to Prof. Senentxu Lanceros-Méndez for accepting my application and giving me the opportunity to carry out this thesis in BCMaterials. I could not have undertaken this challenging journey without his constant support, valuable advice and dedication. Thank you for always opening the door for me to not only share the scientific expertise, but also to help me stop worrying under any "circumstances". Thank you for believing me, encouraging me and providing me with the opportunity to carry out the scientific stays in Portugal.

I have to thank my supervisors, Prof. José Luis Vilas Vilela and Dr. Javier Reguera Gómez, for trusting me and giving me the research freedom. To Vilas, for welcoming me to his lab and for his kind words, constant concern, positive attitude and warm encouragement. To Javier, for introducing me to the world of nanoscience and teaching me the synthesis of nanoparticles.

Many thanks to all my colleagues at BCMaterials for the coffee-breaks, lunches, laughs, and especially to Nagore Barroso and Bosco Rodríguez who started this journey together with me, for the good moments we shared and the “issues” that we got. I will never forget the sunrise we enjoyed every morning when we started this adventure. I would like to extend my sincere thanks to the former members Adriana Gallardo and Dr. David Payno, for their availability, encouragement and patience during these years. Additionally, I should address

a particular thank to Dr. Sheila Maíz, not only for her constant companionship and precious advice during my first scientific stay but also for her moral support. I am also grateful to Leire Celaya and Sara Martín, for their constant encouragement and understanding and I will remember the trip that we enjoyed during my second scientific stay forever. A word to Dr. Bruno Hermenegildo, for his positive words from time to time. My gratitude also to Dr. Roberto Fernandez and Dr. Arkaitz Fidalgo, for their advice and help during characterization, especially to Roberto for his patience and constant positive encouragement over these years. Eskerrik asko!

The two scientific stays in University of Minho, Portugal, were the most important stages of my PhD. I not only obtained the crucial results to let my thesis go ahead but also gained a lot of experience for personal and professional development. I am thankful to all the people I met for their warm welcome and help that let me feel at home, especially to Joana M. Queirós for her companionship and collaboration. Words cannot express my gratitude to Dr. Pedro M. Martins since this endeavour would not have been possible without his advice and assistance. Many thanks Pedro, for your empathy, patience, respect and motivation. I was lucky to meet you and have collaboration with you. Thank you for introducing me to the interesting world of photocatalysis and water remediation, providing me with all the necessary equipment to facilitate the work, and most importantly guiding me when I got “lost”. Thank you for giving me the opportunity to become a part of your group when I was in Portugal, teaching me a different way of thinking and working, and believing in my capabilities and potential in research. Muito obrigada!

I would like to thanks all my friends for always believing in me, encouraging me and listening to me whenever I need. Finally, I am deeply indebted to my parents, for their crucial support, constant concern, and unconditional love. Thank you for always believing in me and never giving up on me. Without your invaluable companionship, I could not finish this difficult journey. 最后，我深深地感谢我的父母，感谢他们的重要支持、一直以来的关心和无条件的爱。谢谢你们一直相信我，从不放弃我。如果没有你们的陪伴，我无法完成这段艰难的旅程。

Thanks to everyone! Eskerrik asko denoi! Obrigada a todos! 谢谢大家!

-Fangyuan Zheng
-郑方圆

“疏杂念，身如水之虚，体似水之流。入杯，即杯；至瓶，成瓶；进壶，为壶。亦舒亦急，可湍可缓。可谓人水合一也。

Empty your minds, be formless, shapeless, like water. Now you put water into a cup, it becomes the cup. You put it into a bottle, it becomes the bottle. You put it in a teapot, it becomes the teapot. Water can flow, or it can crash. Be water, my friend.”

— 李小龙

— Bruce Lee

“The way of water has no beginning and no end. Our hearts beat in the womb of the world. Water connects all things, life to death, darkness to light. The sea gives and the sea takes.”

—Avatar 2: The way of water

“We never know the worth of water till the well is dry.”

—Thomas Fuller

Acknowledgements

Abstract

Water is a natural resource, critical for human life, and is an essential part of any ecosystem. However, the uneven distribution of water resources, the constant increase in the demand for clean and safe water, and the ever-increasing water pollution due to anthropogenic activity growth lead to significant water stress. Thus, clean water and sanitation are identified as the sixth goal of the Sustainable Development Goals (SDGs) adopted by the United Nations Member States. In this context, one of the main concerns is the presence of contaminants of emerging concerns (CECs) such as pharmaceuticals and personal care products in the aquatic environment. Among them, pharmaceuticals, which are used to treat a wide variety of diseases, are gained great interest since they can be found in different water matrices including groundwater and drinking water, entering the environment through different pathways such as livestock waste, urban, industry and hospital wastewater.

Antibiotics, non-steroidal anti-inflammatory drugs (NSAIDs), analgesics and β-blockers are the most commonly detected pharmaceuticals in water. Although these pharmaceuticals appear at very low concentrations, in the order of ng/L to µg/L, their prolonged exposure in water can cause an adverse impact on aquatic organisms like fishes, crustaceans, and algae. In addition, the configuration and design of conventional wastewater treatment plants (WWTPs) cannot remove them completely because of the highly persistent nature and difference in the physicochemical properties of the present pharmaceuticals. Hence, it is highly crucial to develop advanced materials and efficient technologies in wastewater treatment.

Among several approaches, photocatalysis has received considerable attention in water remediation applications to degrade contaminants of emerging concern. This technology consists of using photocatalysts to generate highly oxidising species under light radiation (UV or sunlight), which will destroy contaminants into innocuous compounds. TiO_2 and ZnO semiconductors are the most used photocatalysts for water pollutants degradation due to their remarkable properties like low cost and high photocatalytic efficiency. However, these semiconductors present some drawbacks such as only being excited under UV radiation due to the wide bandgap, leading to a poor photocatalytic efficiency under solar radiation since only less than 4% of this radiation corresponds to UV. Additionally, the fast recombination of photogenerated electron-hole pairs also reduces the photocatalytic efficiency. Apart from these limitations, another hindrance is the recovery/reusability of the photocatalyst after water treatment. Photocatalysts in suspension show limitations in their recovery and reuse, requiring time-consuming and expensive processes. Furthermore, the possible secondary pollution from nanoparticles released into water bodies may cause long-term harmful effects on aquatic organisms. The proposed work will address these relevant issues, the modification of photocatalyst towards a broader wavelength absorbance under sunlight, as well as the immobilisation of photocatalysts to improve the reusability, eco-friendliness, and cost-effectiveness of the photocatalytic process for water remediation.

Taking into account these main objectives, the work are structured into five main chapters, starting with a brief introduction to the current problem and the solutions proposed in this research trying to make more practical the application of photocatalysis in pharmaceuticals degradation (Chapter 1).

In the second chapter, the research lies on the systematic studies which correlate the interaction between pharmaceuticals pollutants and photocatalysts, the generation of reactive oxygen species (ROS), and the photocatalytic performance. All of it added to the development of Au-functionalised plasmonic photocatalysts, enhancing the photocatalytic performance under sunlight. To understand how the high diversity of pharmaceuticals determines the selection of an adequate photocatalyst for efficient and broadband pollutants removal, two photocatalysts TiO_2 and ZnO were synthesised by the co-precipitation method, and then were systematically compared in the photocatalytic degradation of four representative pharmaceuticals: chloroquine phosphate (CLQ), paracetamol (PAR), diclofenac sodium (DCF), and ciprofloxacin (CIP). The results showed that key physicochemical properties of photocatalysts and pharmaceuticals play a significant role in the adsorption behaviour of pollutants on the surface of the photocatalyst and the generation of ROS, which have a crucial influence on the photocatalytic degradation performance. Under UV and at neutral pH, zwitterionic molecules such as CIP were highly degraded by all photocatalysts, with a degradation efficiency of 83% and 94% for TiO_2 and ZnO. Cationic molecules such as CLQ were superiorly degraded by negatively charged TiO_2 showing a degradation efficiency of 54%. At the same time, anionic molecules such as DCF were more efficiently degraded by positively charged ZnO, with a degradation efficiency of 28%, but lowly or negligibly degraded by TiO_2. In the case of the neutral molecules such as PAR, ZnO presented higher degradation, attributed in this case to the higher amount of generated ROS. After spherical Au nanoparticles functionalisation, the correlation between the affinity of pollutants and nanoparticles' surface and the photocatalytic performance under UV radiation was maintained. Most importantly, this sensitisation of semiconductors with Au made the photocatalysis possible under visible light; the nanoparticles could absorb a higher amount of light (reflectance decreased from 94% to 74% for TiO_2:Au, and from 88% to 68% for ZnO:Au).

In the third chapter, novel hybrid nanoparticles TiO_2:Au-NSs were synthesised through a seed-mediated-growth process in order to further improve the efficiency of TiO_2:Au-based photocatalysts and overcome the limitation of the narrow plasmonic band (~520 nm) given by spherical Au nanoparticles. The synthesis was focused on the modification of the shape of Au nanoparticles, from spherical morphology to branched morphology (nanostar). A multistep approach was developed, where Au spherical nanoparticles were initially generated onto commercial TiO_2 nanoparticles (TiO_2-P25) through a deposition–precipitation method, and then further modified (growth) to induce a change in shape by a surfactant-free nanostars synthesis, generating a branched morphology. Once the synthesis process was optimised, TiO_2:Au-NSs with different sizes of Au nanostar were produced by changing the synthesis conditions (seeds to growth Au ratio). The characterisation results showed that the change of the shape of Au nanoparticles on the TiO_2 surface, from spherical morphology to branched morphology (nanostar), can enhance the visible light absorption decreasing the reflectance from 75% to 51% in the visible region and reduce bandgap from 3.14 eV to 3.10 eV. When increasing the size of the Au nanostar, the reflectance of the hybrid nanoparticles decreased from 51% to 14% in the visible region. Additionally, the increase in the size of the Au nanostar extended the light absorption to the whole visible and part of the NIR region and reduced the bandgap from 3.10 eV to 2.86 eV.

The different versions of hybrid nanoparticles TiO_2:Au-NSs with different Au nanostar sizes were evaluated and compared for their photocatalytic activity under UV and visible light radiation to degrade the antibiotic ciprofloxacin (CIP). TiO_2:Au-NSs nanoparticles with smaller Au nanostar morphology and the lowest amount of added Au showed a better photocatalytic performance degrading 83% and 89% ciprofloxacin under 30 min of UV radiation and 150 min of visible radiation, respectively. On the other hand, the photocatalytic assay under different wavelengths from the visible to NIR region was also carried out to understand the effect of the increase of size of Au branched nanoparticles. The TiO_2:Au-NSs nanoparticles with smaller Au nanostar could be activated under blue, green, and red light radiation showing a CIP degradation efficiency of 57%, 34% and 39%, respectively. The bigger size of Au-branched nanoparticles limited the light-harvesting of TiO_2, and reduced the photocatalytic activity, although they showed a broader light absorption in the whole visible and part of the NIR region of sunlight radiation. Afterwards, the TiO_2:Au-NSs nanoparticles with the best performance were successfully incorporated into poly(vinylidene fluoride-co-hexafluoropropylene) (PVDF-HFP) polymer matrix through Non-solvent-Induced Phase Separation (NIPS) technique to degrade ciprofloxacin, opening the door to future application in a cost-effective way to degrade a high number of contaminants of emerging concern.

Once PVDF-HFP polymer matrix was experimentally validated as support for novel nanoparticles TiO_2:Au-NSs incorporation, further research shifted to study the immobilisation technique of photocatalysts. Hence, in Chapter 4, the influence of immobilisation processing techniques was evaluated. For that, different microstructures/morphologies of PVDF-HFP-based polymeric membranes with varying amounts of incorporated nanoparticles were correlated with the final photocatalytic performance. Different amounts of synthesised TiO_2:Au-NSs hybrid nanoparticles (0, 3, 8, and 10 wt.%) were incorporated into PVDF-HFP polymer matrix, through two different methods, doctor blade and salt leaching, in combination with Temperature-Induced Phase Separation (TIPS), giving rise to two types of photocatalytic membranes with different porous microstructures. Both types of membranes presented high porosity (80-90%) with well-distributed and interconnected pores regardless of the nanoparticle content, nevertheless, they showed marked differences. Doctor blade membranes showed a narrower pore (0.5-7 µm) and hydrophobic character regardless of UV radiation and nanoparticles load. On the contrary, salt leaching membranes presented a broader pore size distribution with a larger pore size (5-200 µm) and a more hydrophilic character when increasing nanoparticle content (contact angle from 96 to 80°) or under UV radiation (contact angle down to 71°). Later, the influence of the microstructure of the membrane on photocatalytic performance was studied through the degradation of ciprofloxacin (CIP) as a model antibiotic, under UV and visible radiation. Although an increase in nanoparticle load improved photocatalytic efficiency, the salt leaching membranes presented higher photocatalytic activity attributed to the higher porosity and access of the contaminant to the nanoparticle surface under the same conditions. Salt leaching membranes containing 10 wt.% nanoparticles presented the highest degradation efficiencies, 45% with a rate constant of 16×10^{-3} min^{-1} under 300 min of UV radiation and 35% with a rate constant of 8.0×10^{-3} min^{-1} under 480 min of visible radiation. In contrast, doctor blade membranes showed a more limited degradation efficiency of 36% with a rate constant of 12×10^{-3} min^{-1} under UV radiation and 32% with a rate constant of 8.0×10^{-4} min^{-1} under visible radiation.

For all membranes, the photocatalytic efficiency of nanoparticles immobilised is reduced compared with those in suspension (in Chapter 3) due to the loss of available active sites which are blocked in the attachment area. However, this efficiency loss can be gained in the reusability. Hence, reusability assays were carried out for the both most efficient membranes. The membrane robustness was demonstrated, with an average efficiency loss of only around 2% for the worst case after three consecutive uses, and even improved efficiencies for salt leaching membranes. After showing the potential reusability of the prepared membranes, the suitability of these membranes for ciprofloxacin degradation in the real treated effluent water matrix was finally assessed. It was demonstrated that the membranes were fully functional, reaching degradation efficiency of 50 and 48% under UV and visible radiation, respectively, after three consecutive photocatalytic uses.

Thus, the present work shows a set of different approaches that tackle the main issues related to the application of photocatalysis degrading pharmaceuticals for water remediation: poor efficiency of photocatalysts under sunlight and time-consuming and expensive processes for photocatalyst recovery/reuse. Finally, in chapter 5, the main conclusion and outlook are collected. Different plasmonic photocatalysts were prepared with enhanced photocatalytic efficiency under sunlight when compared to pristine semiconductors. The produced immobilized systems displayed an efficient functional performance and suitable reusability, degrading contaminants of emerging concern in a cost-effective way and avoiding harmful secondary pollution in the aquatic environment caused by the release of nanoparticles.

Abstract

Resumen

El agua es un recurso natural y crítico para la vida humana, y forma parte esencial de cualquier ecosistema. Sin embargo, la distribución desigual de los recursos hídricos, el constante aumento de la demanda de agua limpia y segura y el incremento de la contaminación del agua debido a la actividad antropogénica han conducido a un significativo estrés hídrico. Tal es la importancia que tiene abordar su escasez y calidad que ha llevado a su inclusión como sexto objetivo entre los Objetivos de Desarrollo Sostenible (SDGs) adoptados por los Estados Miembros de las Naciones Unidas. En este contexto, una de las principales preocupaciones es la presencia de contaminantes de emergentes (CECs) en el medio acuático, como pueden ser los productos farmacéuticos, los productos de cuidado personal, los disruptores endocrinos, etc. Entre ellos, requieren de especial atención los productos farmacéuticos, que se utilizan para tratar una amplia variedad de enfermedades, y cuya presencia ha aumentado en diferentes matrices de agua, incluidas las aguas subterráneas y el agua potable. Los productos farmacéuticos pueden entrar al medio ambiente a través de diferentes vías, habitualmente desechos ganaderos, aguas residuales urbanas, industriales y hospitalarias.

Los antibióticos, los medicamentos antiinflamatorios no esteroideos (NSAIDs), los analgésicos y los β-bloqueadores son los fármacos detectados con mayor frecuencia en el agua. Aunque estos productos farmacéuticos aparecen en concentraciones muy bajas, del orden de ng/L a µg/L, su exposición prolongada en el agua puede causar un impacto adverso en organismos acuáticos como peces, crustáceos y algas. Sin embargo, la configuración y el diseño de las plantas de tratamiento de aguas residuales (WWTPs) convencionales no pueden eliminarlos completamente debido a su naturaleza altamente persistente y la diferencia en las propiedades fisicoquímicas es, por lo tanto, muy importante desarrollar materiales avanzados y tecnologías eficientes en el tratamiento de las aguas residuales.

Entre las nuevas soluciones para la remediación ambiental del agua, la fotocatálisis aplicada a la degradación de contaminantes emergentes está recibiendo un considerable interés. Esta tecnología consiste en el uso de fotocatalizadores para generar especies altamente oxidantes bajo la radiación de la luz (UV o luz solar), que destruyen los contaminantes convirtiéndolos en compuestos inocuos. Los semiconductores TiO_2 y ZnO son los fotocatalizadores más utilizados en este ámbito gracias a algunas de sus propiedades, como son su bajo coste y alta eficiencia fotocatalítica. Sin embargo, estos semiconductores presentan algunos

inconvenientes, como es el hecho de que solo se activan bajo radiación UV, debido al amplio bandgap, lo que conduce a una baja eficiencia fotocatalítica bajo radiación solar, ya que menos del 4% de esta radiación corresponde a UV. Además, la rápida recombinación de pares electrón-hueco fotogenerados también reduce la eficiencia fotocatalítica. Aparte de estas limitaciones, otro obstáculo es la recuperación/reutilización del fotocatalizador después del tratamiento del agua. Los fotocatalizadores en suspensión presentan limitaciones en su recuperación y reutilización, lo que implica procesos lentos y costosos. Además, la posible contaminación secundaria de las nanopartículas liberadas en agua puede causar a largo plazo efectos nocivos en los organismos acuáticos. El trabajo presentado aquí abordará estos problemas relevantes, la modificación del fotocatalizador para una absorción de luz de mayor longitud de onda bajo radiación solar, así como la inmovilización de fotocatalizadores para un proceso fotocatalítico más reutilizable, amigable ambientalmente y económico para la remediación ambiental en agua.

En función de estos objetivos principales, el trabajo se ha estructurado en cinco capítulos, comenzando por una breve introducción a la problemática actual y a las soluciones propuestas en esta investigación para realizar una aplicación más práctica de la fotocatálisis en la degradación de fármacos (Capítulo 1).

En el segundo capítulo, se presentan los estudios sistemáticos que correlacionan la interacción entre los fármacos y los fotocatalizadores, la generación de especies de oxígeno reactiva (ROS) y la eficiencia fotocatalítica. El estudio también incluye la preparación de fotocatalizadores plasmónicos que incorporan Au a los semiconductores para mejorar la eficiencia fotocatalítica bajo luz solar. Para comprender cómo la alta diversidad de productos farmacéuticos determina la selección de un fotocatalizador adecuado para eliminar eficientemente a un amplio grupo de contaminantes, se sintetizaron dos fotocatalizadores, TiO_2 y ZnO, por el método de co-precipitación, y luego se compararon sistemáticamente en la degradación fotocatalítica de cuatro fármacos representativos: fosfato de cloroquina (CLQ), paracetamol (PAR), diclofenaco sódico (DCF) y ciprofloxacina (CIP). Los resultados mostraron que las propiedades fisicoquímicas de los fotocatalizadores y los productos farmacéuticos juegan un papel crucial en la adsorción de contaminantes en la superficie del fotocatalizador y la generación de ROS, lo cual significativamente influye en el rendimiento de la degradación fotocatalítica. Bajo UV y a pH neutro, las moléculas zwitteriónicas como CIP fueron altamente degradadas por todos los fotocatalizadores, con una eficiencia de degradación del 83% y del 94% para TiO_2 y ZnO. Las moléculas catiónicas

como CLQ se degradaron mejor con TiO_2 cargado negativamente, mostrando una eficiencia de degradación del 54%. Al mismo tiempo, las moléculas aniónicas como DCF se degradaron de manera más eficiente con ZnO cargado positivamente, con una eficiencia de degradación del 28%, pero se degradaron de forma baja o insignificante con TiO_2. En el caso de las moléculas neutras como PAR, el ZnO presentó una mayor eficiencia de degradación debido a la mayor cantidad de ROS generada. Después de incorporar la nanopartículas esféricas de Au, se mantuvo la correlación entre la afinidad de los contaminantes y la superficie de los fotocatalizadores y la eficiencia fotocatalítica bajo radiación UV. Esta modificación de los semiconductores hizo posible la fotocatálisis bajo luz visible ya que los fotocatalizadores pudieron absorber una mayor cantidad de luz en la zona visible (la reflectancia disminuyó del 94% al 74% para TiO_2:Au, y del 88% al 68% para ZnO:Au).

En el tercer capítulo, se sintetizaron nuevas nanopartículas híbridas TiO_2:Au-NS a través de un método de crecimiento mediado por semillas para mejorar aún más la eficiencia de los fotocatalizadores basados en TiO_2:Au y superar la limitación de la banda plasmónica (~520 nm) típica de nanopartículas esféricas de Au. La síntesis se centró en la modificación de la forma de las nanopartículas de Au, pasando de una morfología esférica a una morfología ramificada (nanoestrella). Se desarrolló un proceso de varios pasos, donde las nanopartículas esféricas de Au se generaron inicialmente en nanopartículas comerciales de TiO_2 (TiO_2-P25) a través de un método de deposición-precipitación, y luego se modificaron (crecimiento) para inducir un cambio en la forma mediante una síntesis de nanoestrellas sin surfactante, generando una morfología ramificada. Una vez que se optimizó el proceso de síntesis, se produjeron TiO_2:Au-NS con diferentes tamaños de nanoestrellas de Au cambiando la condición de síntesis (proporción de solución de semillas a Au añadida). Los resultados de caracterización mostraron que el cambio de forma de las nanopartículas de Au en la superficie de TiO_2, de morfología esférica a morfología nanoestrella, puede mejorar la absorción de luz visible disminuyendo la reflectancia de 75% a 51% en la región visible y reducir el bandgap de 3,14 eV a 3,10 eV. Al aumentar el tamaño de la nanoestrella de Au, la reflectancia de las nanopartículas híbridas disminuyó del 51% al 14% en la región visible. Además, el aumento en el tamaño de la nanoestrella Au extendió la absorción de luz a todo el visible y parte de la región de infrarrojo cercano (NIR) y redujo el bandgap de 3,10 eV a 2,86 eV, respectivamente.

Las nanopartículas híbridas TiO_2:Au-NSs, con diferentes tamaños de nanoestrellas de Au, se evaluaron y compararon sus actividades fotocatalíticas bajo radiación de luz visible y UV

para degradar el antibiótico ciprofloxacina (CIP). Las nanopartículas de TiO_2:Au-NSs con una morfología de nanoestrella de Au más pequeña y la cantidad más baja de Au añadida mostraron un mejor rendimiento fotocatalítico al degradar el 83% y 89% de CIP bajo 30 min de radiación UV y 150 min de radiación visible, respectivamente. Por otro lado, también se llevó a cabo el ensayo fotocatalítico bajo diferentes longitudes de onda, desde la región visible hasta la NIR, para comprender el efecto del aumento de tamaño de las nanoestrella de Au. Las nanopartículas de TiO_2:Au-NSs con nanoestrellas de Au más pequeñas pudieron activarse bajo radiación de luz azul, verde y roja mostrando una eficiencia de degradación de CIP del 57%, 34% y 39%, respectivamente. El mayor tamaño de nanoestrella de Au limitó la captación de luz de TiO_2 y redujo la actividad fotocatalítica, aunque mostraron una absorción de luz más amplia en toda la región visible y parte de la región NIR de la radiación solar. Posteriormente, las nanopartículas de TiO_2:Au-NSs con la mejor eficiencia fotocatalítica se incorporaron con éxito a la matriz polimérica de poli(fluoruro de vinilideno-co-hexafluoropropileno) (PVDF-HFP) mediante la técnica de separación de fases no inducida por disolventes (NIPS) para degradar la ciprofloxacina, abriendo la puerta a futuras aplicaciones de una manera rentable para degradar una gran cantidad de contaminantes emergentes.

Una vez que la matriz polimérica de PVDF-HFP se validó experimentalmente como soporte para la incorporación de nuevas nanopartículas de TiO_2:Au-NSs, la investigación se desplazó hacia el estudio de la técnica de inmovilización de fotocatalizadores. Por lo tanto, en el Capítulo 4, se evaluó la influencia de las técnicas de procesamiento de inmovilización. Para ello, se correlacionaron diferentes microestructuras/morfologías de membranas poliméricas basadas en PVDF-HFP con cantidades variables de nanopartículas incorporadas con la eficiencia fotocatalítica final. Se incorporaron diferentes cantidades de nanopartículas híbridas de TiO_2:Au-NSs sintetizadas (0, 3, 8 y 10 % en peso) en la matriz polimérica de PVDF-HFP, a través de dos métodos diferentes, “Doctor Blade” y “*salt leaching*”, en combinación con la separación de fases inducida térmicamente (TIPS), dando lugar a dos tipos de membranas fotocatalíticas con diferentes microestructuras porosas. Ambos tipos de membranas presentaron alta porosidad (80-90%) con poros bien distribuidos e interconectados independientemente del contenido de nanopartículas, sin embargo, mostraron grandes diferencias. Las membranas obtenidas por Doctor Blade mostraron una estrecha distribución de tamaños de poro (0,5-7 µm) y un carácter hidrófobo independientemente de la radiación UV y la cantidad de nanopartículas. Por el contrario, las membranas obtenidas por *salt leaching* presentaron una amplia distribución de tamaños de poros (5-200 µm) y un carácter más hidrófilo al aumentar el contenido de nanopartículas (ángulo de contacto de 96 a 80°) o bajo radiación UV (ángulo de contacto bajó hasta 71°). Posteriormente, se estudió la influencia de la microestructura de la membrana sobre el rendimiento fotocatalítico mediante la degradación de antibiótico ciprofloxacina (CIP), bajo radiación UV y visible. Aunque un aumento en la cantidad de nanopartículas mejoró la eficiencia fotocatalítica, las membranas obtenidas por *salt leaching* presentaron una mejor actividad fotocatalítica atribuido a la mayor porosidad y acceso del contaminante a la superficie de las nanopartículas bajo las mismas condiciones. Las membranas obtenidas por *salt leaching* que contenían 10% en peso de nanopartículas presentaron la eficiencia de degradación más alta, de 45%, con una constante cinética de degradación de 16×10^{-3} min^{-1} bajo 300 min de radiación UV y una eficiencia de degradación de 35% con una constante cinética de $8{,}0 \times 10^{-3}$ min^{-1} bajo 480 min de radiación visible. Por el contrario, las membranas obtenidas por Doctor Blade mostraron una eficiencia de degradación más limitada, del 36 % con una constante cinética de 12×10^{-3} min^{-1} bajo radiación UV y del 32 % con una constante cinética de $8{,}0 \times 10^{-4}$ min^{-1} bajo radiación visible.

Para todas las membranas, la eficiencia fotocatalítica de las nanopartículas inmovilizadas se reduce en comparación con aquellas en suspensión (en el Capítulo 3) debido a la pérdida de centros activos al estar en contacto con la matriz polimérica. Sin embargo, esta pérdida de eficiencia se compensa con la capacidad de reutilización y prolongada vida útil. Por lo tanto, se llevaron a cabo ensayos de reutilización para las dos membranas más eficientes. Se demostró la robustez de la membrana, con una pérdida de eficiencia promedio de alrededor del 2% en el peor caso después de tres usos consecutivos, e incluso eficiencias mejoradas para las membranas obtenidas por *salt leaching*. Finalmente se evaluó el uso de estas membranas para la degradación de ciprofloxacina en agua residual tratada. Se demostró que las membranas eran completamente funcionales, alcanzando una eficiencia de degradación del 50 y 48% bajo radiación UV y visible, respectivamente, después de tres usos fotocatalíticos consecutivos.

Por lo tanto, el presente trabajo muestra un conjunto de diferentes métodos que abordan los principales problemas relacionados con la aplicación de fotocatálisis en la degradación de fármacos: baja eficiencia de los fotocatalizadores bajo luz solar y procesos costosos y lentos para la recuperación/reutilización del fotocatalizador. Se prepararon diferentes fotocatalizadores plasmónicos con una eficiencia mejorada bajo radiación solar en

comparación con los semiconductores puros. Los sistemas inmovilizados producidos mostraron un eficiente funcionamiento y una apropiada reutilización para degradar de una manera rentable los contaminantes emergentes y evitar la contaminación secundaria causada por la liberación de nanopartículas. En el capítulo 5, se recogen las principales conclusiones, así como las perspectivas para su implementación y mejora, de este trabajo.

Laburpena

Kezka sortzen ari diren kutsatzaileek, hala nola, produktu farmazeutikoek, arazo global berri bat dakarte uraren kalitaterako; konposatu horiek oso erresistenteak dira ohiko hondakin-uren tratamenduetan, eta ingurumena kutsa dezakete. Hori dela eta, kalte larriak eragiten dizkiete uretako organismoei eta ondorioz, gizakien osasunari. Azken hamarkadetan, fotokatalisi erdieroalea etorkizun handiko teknologia bihurtu da kutsatzaile horiek degradatzeko. Hala ere, eguzki-argipean dauden fotokatalizatzaileen eraginkortasuna eskasa da. Gainera, uraren erremedizazioan aplikatzeko bi arazo nagusienak dira denbora asko kontsumitzea eta fotokatalizatzaileak berreskuratzeko/berrerabiltzeko prozesu garestiak izatea. Doktore-tesi honek oztopo horiek gainditzea du helburu. Lehenik eta behin, kontuan hartu da kutsatzaileen eta fotokatalizatzaileen arteko elkarrekintzaren garrantzia, errendimendu fotokatalitikorako oxigeno espezie erreaktiboak (ROS) sortuz. Gero, fotokatalizatzaile plasmoniko funtzionalak garatu dira. Ondoren, TiO_2 funtzionalizatzen duen urrezko nanoizarrek erabiltzen duten fotokatalizatzaile berriak eta eraginkorragoak garatu eta probatu dira aplikazio fotokatalitikorako. Azkenik, fotokatalizatzaile berriak polimeroen matrizean erantsi dira teknika ezberdinen bidez aplikazio fotokatalitikoetan berrerabili eta berreskuratzeko. Lortutako emaitzei esker, ondoriozta daiteke garatutako material hibrido fotokatalizatzaileek atea irekitzen dutela CEC kutsatzaileen mota asko modu eraginkorrean degradatzeko eguzkiaren argia erabiliz, uraren purifikazio prozesuan.

Laburpena

总结

药物等新兴污染物 (CECs) 的出现已成为全球性的问题。由于传统污水处理方法不能有效地去除这些污染物，使其进入大自然对水生生物和人类健康造成严重威胁。近来，半导体光催化技术在新兴污染物降解方面的应用得到了广泛的关注。然而，光触媒在阳光下的低利用效率，耗时、昂贵的回收和再利用等过程限制了光催化在水修复中的应用。这篇博士论文的重点是克服这些障碍。首先，考虑了污染物与光催化剂之间相互作用和活性氧物种 (ROS) 的产生对光催化性能的影响。然后，进行了等离子体光催化剂的开发。使用金纳米星改良过的二氧化钛来制备新型高效的光催化剂。最后，通过不同的技术将新型光催化剂固定在聚合物中，以实现其在光催化应用中的可重复使用和回收。实验结果表明，所制备的光催化材料能高效利用太阳能降解多种新兴污染物，为光催化在污水处理方面的应用打开了大门。

Table of Contents

List of Figures V

List of Tables XI

List of abbreviations, symbols and acronyms XIII

1. Introduction 1

1.1. Motivation 3

1.2. Contaminants of emerging concern and pharmaceuticals 4

1.3. Advanced oxidation processes 6

1.4. Heterogeneous photocatalysis in water remediation 8

1.4.1. Mechanism and reaction pathways 8

1.4.2. Kinetics of reaction 10

1.4.3. Operational parameters of photocatalysis 12

1.4.3.1. Photocatalyst concentration 12

1.4.3.2. Illumination conditions 12

1.4.3.3. pH of solution 13

1.4.3.4. Reaction temperature 14

1.4.3.5. Dissolved oxygen 14

1.4.3.6. Initial concentration of the pollutant 14

1.4.3.7. Morphology of the photocatalysts 15

1.4.3.8. Presence of chemical species 15

1.4.4. Photocatalytic materials 16

1.5. Strategies to improve the photocatalytic process 17

1.5.1. Modification of photocatalysts 17

1.5.1.1. Plasmonic photocatalysis 19

1.5.2. Immobilisation of photocatalysts 22

1.5.2.1. Poly(vinylidene fluoride) and its copolymers 24

1.6. General objectives and outline of the thesis 27

1.7. References 29

2. Au-sensitised TiO_2 and ZnO photocatalysts for broadband pharmaceuticals degradation 47

2.1. Introduction 49

2.2. Experimental 52

2.2.1. Materials 52

2.2.2. Sample preparation 52

2.2.2.1. TiO_2 and ZnO nanoparticles synthesis 52

2.2.2.2. TiO_2:Au and ZnO:Au nanoparticles synthesis 53

2.2.3. Sample characterisation 53

2.2.4. Photogenerated ROS ($^{\bullet}OH$ and $^1O_2$) measurements 55

2.2.4.1. Detection of hydroxyl radicals ($^{\bullet}OH$) 55

2.2.4.2. Detection of singlet oxygen ($^1O_2$) 56

2.2.5. Photocatalytic degradation under UV and visible radiation 57

2.3. Results and discussion 59

2.3.1. Nanoparticles synthesis and characterisation 59

2.3.2. Photogenerated ROS ($^{\bullet}OH$ and $^1O_2$) measurements 64

2.3.3. Photocatalytic degradation under UV radiation 67

2.3.4. Photocatalytic degradation under visible radiation 74

2.4. Conclusions 77

2.5. References 79

3. Size effect in hybrid TiO_2:Au nanostar for photocatalysis 91

3.1. Introduction 93

3.2. Experimental 94

3.2.1. Materials 94

3.2.2. Sample preparation ____ 95

3.2.2.1. TiO_2:Au-NSs nanoparticles synthesis ____ 95

3.2.2.2. Membranes production ____ 96

3.2.3. Sample characterisation ____ 97

3.2.4. Photogenerated ROS ($^\bullet OH$ and $^1O_2$) measurements ____ 98

3.2.4.1. Detection of hydroxyl radicals ($^\bullet OH$) ____ 98

3.2.4.2. Detection of singlet oxygen ($^1O_2$) ____ 99

3.2.5. Photocatalytic degradation under UV and visible radiation ____ 100

3.2.6. Photocatalytic degradation under different wavelengths ____ 102

3.3. Results and discussion ____ 102

3.3.1. Nanoparticle synthesis and characterisation ____ 102

3.3.2. Photocatalytic degradation under UV and visible radiation ____ 109

3.3.3. Photocatalytic degradation under different wavelengths ____ 113

3.3.4. Membranes production and characterisation ____ 116

3.4. Conclusions ____ 118

3.5. References ____ 120

4. Hybrid TiO_2:Au nanostars based polymeric membranes for photocatalysis _ 129

4.1. Introduction ____ 131

4.2. Experimental ____ 132

4.2.1. Materials ____ 132

4.2.2. Sample preparation ____ 132

4.2.2.1. TiO_2:Au-NSs nanoparticles synthesis ____ 132

4.2.2.2. Doctor blade membranes production ____ 133

4.2.2.3. Salt leaching membranes production ____ 133

4.2.3. Sample characterisation ____ 134

4.2.4. Photocatalytic degradation under UV and visible radiation ____ 135

4.3. Results and discussion ______ 137

4.3.1. Nanoparticles and membranes characterisation ______ 137

4.3.2. Photocatalytic degradation under UV and visible radiation ______ 143

4.3.3. Reusability of the membranes ______ 148

4.3.4. Photocatalytic degradation in a real treated effluent ______ 153

4.4. Conclusions ______ 156

4.5. References ______ 158

5. Conclusions and Future Work ______ 163

5.1. Conclusions ______ 165

5.2. Future work ______ 166

Curriculum Vitae & Contributions ______ 171

Copyright and Licencing information ______ 181

List of Figures

Figure 1.1. Proportion of the population using at least basic drinking water services in 2020 according to the assessment of UNICEF and WHO. Adapted from [2]. 3

Figure 1.2. Sources and pathways of the pharmaceuticals in the environment [3,14,16,17]. 4

Figure 1.3. Schematic representation of the photocatalytic mechanism on a semiconductor nanoparticle in the presence of a water pollutant and with light irradiation (hυ). 9

Figure 1.4. The number of scientific papers with the keywords "photocatalysis" and "sunlight". Source: Web of Science in November of 2022. 17

Figure 1.5. Principle of the plasnomic photocatalytic mechanism. Here Au used as an example of metal nanoparticles dispersed on the semiconductor surface [91]. 19

Figure 1.6. Illustration of the excitation of localised surface plasmon resonance in spherical metal particle. Adapted from [92]. 20

Figure 1.7. Transmission electron microscopy images of Au seed particles and those obtained after different growth steps. The particle size increases from 13.5 ± 2.1 to 19.2 ± 2.6, 24.8 ± 3.4, and 30.5 ± 3.9 nm after 3, 6, and 13 growth steps, respectively (a). Absorption spectra of spherical gold nanoparticles with different size obtained after different growth steps, normalized at 400 nm to facilitate comparison (b). Adapted from [94]. 20

Figure 1.8. Illustration of the excitation of localised surface plasmon resonance in nanorod metal particle at longitudinal and transverse plasmon bands (a). Absorption spectra of nanorod (b). Adapted from [92]. 21

Figure 1.9. Structure of Au nanostar (a) and illustration of plasmon hybridization in the nanostar (b). Adapted from [97]. Absorption spectra of nanostar (c) with transmission electron microscopy image of Au nanostar with core diameters of 49.72 ± 0.10 nm and tip length of 19.44 ± 0.35 nm (inset). Adapted from [99]. 22

Figure 1.10. The number of scientific papers with the keywords "suspended photocatalysis" vs. "immobilised photocatalysis". Source: Web of Science in November of 2022. 23

Figure 1.11. A schematic representation of the chain conformation of α, β, and γ-phases of PVDF. Adapted from [119]. 25

Figure 1.12. Polymerization of PVDF-HFP. Adapted from [122]. 26

Figure 2.1. Molecular structure of Chloroquine phosphate (CLQ) (a), Paracetamol (PAR) (b), Diclofenac (DCF) (c) and Ciprofloxacin (CIP) (d). 51

Figure 2.2. Scheme of hydroxylation reaction of terephthalic acid (TA). 55

Figure 2.3. Mechanism of histidine test. 57

Figure 2.4. Xenon Lamp arc (with UV filter) and sunlight spectra. 58

Figure 2.5. TEM images of pristine TiO_2 (a) with different magnification (inset) and ZnO (b) nanoparticles. 59

Figure 2.6. STEM-HAADF images of TiO_2:Au (a) and ZnO:Au (b) hybrid nanoparticles with different magnification. 60

Figure 2.7. X-ray diffraction spectra (a, b) and UV-Vis reflectance spectra (c, d) with the estimation of the bandgap (inset) at $[F(R)h\upsilon]^{1/2} \rightarrow 0$ for pristine TiO_2 and TiO_2:Au nanoparticles (a, c) and ZnO and ZnO:Au nanoparticles (b, d). 61

Figure 2.8. N_2 adsorption-desorption isotherms (a, b) and the intensity size distribution and respective Z-average hydrodynamic size (c, d) with zeta potential measurements (inset) performed at different pHs (3, 5, 7, 9, and 11) for pristine TiO_2 and TiO_2:Au nanoparticles (a, c) and ZnO and ZnO:Au nanoparticles (b, d). 63

Figure 2.9. Quantification of photogenerated hydroxyl radical ($^{\bullet}OH$) (a) and singlet oxygen ($^1O_2$) (b) by TiO_2 and ZnO under 60 min of UV radiation. 66

Figure 2.10. Photocatalytic degradation with TiO_2 (a) and ZnO (b) and comparison of degradation efficiency (%) between TiO_2 and ZnO (c) for CLQ (30 mg/L), PAR (15 mg/L), DCF (30 mg/L) and CIP (5 mg/L) removal under 60 min of UV radiation. 68

Figure 2.11. Photolysis assay of CLQ (30 mg/L) (a), PAR (15 mg/L) (b), DCF (30 mg/L) (c) and CIP (5 mg/L) (d) under 60 min of UV radiation. 69

Figure 2.12. Comparison of degradation efficiency (%) between TiO_2 and TiO_2:Au (a), ZnO and ZnO:Au (b) for CLQ (30 mg/L), PAR (15 mg/L), DCF (30 mg/L) and CIP (5 mg/L) removal under 60 min of UV radiation. 71

Figure 2.13. Photocatalytic degradation with TiO_2:Au (a) and ZnO:Au (b) and comparison of degradation efficiency (%) between TiO_2:Au and ZnO:Au (c) for CLQ (30 mg/L), PAR (15 mg/L), DCF (30 mg/L) and CIP (5 mg/L) removal under 240 min of visible radiation. 75

Figure 2.14. Photolysis assay of CLQ (30 mg/L) (a), PAR (15 mg/L) (b), DCF (30 mg/L) (c) and CIP (5 mg/L) (d) under 240 min of visible radiation. ______ 76

Figure 3.1. Scheme of hydroxylation reaction of terephthalic acid (TA).______ 99

Figure 3.2. Mechanism of histidine test. ______ 100

Figure 3.3. Xenon Lamp arc (with UV filter) and sunlight spectra. ______ 101

Figure 3.4. STEM-HAADF micrographs of TiO_2:Au-NSph with different magnifications (a, b). Au nanoparticles appear as whiter, smaller, and quite circular shapes, scattered through the sample. The zoom-in, with the green arrow, shows one of these Au nanoparticles bound to a TiO_2 nanoparticle surface. EDX mapping of TiO_2:Au-NSph: Au (red) and Ti (blue) (c). ______ 103

Figure 3.5. STEM-HAADF micrographs with the different magnifications (a, b, d, e, g, h) and EDX mapping (c, f, i) of TiO_2:Au-NSs, Sample A (a–c), Sample B (d–f), and Sample C (g–i). ______ 104

Figure 3.6. X-ray diffraction spectra of pristine TiO_2, TiO_2:Au-NSph, TiO_2:Au-NSs-A, B, and C nanocomposites and identification of the representative diffraction peaks for anatase (A) and rutile (R) phases (a). XRF spectrum of TiO_2:Au-NSs-A (b), TiO_2:Au-NSs-B (c), and TiO_2:Au-NSs-C (d). ______ 105

Figure 3.7. The intensity size distribution of the TiO_2:Au-NSs-A, B, and C nanocomposite and respective Z-average hydrodynamic size (a). Zeta potential measurements performed at different pHs (3, 5, 7, 9, and 11) for TiO_2:Au-NSs-A, B, and C nanocomposite (b). ______ 107

Figure 3.8. UV-Vis reflectance spectra (a, b) and UV-Vis absorption spectra (c, d) of the nanoparticles in the different synthesis steps (a, c) and nanoparticles with different Au NS sizes (b, d). Estimation of the bandgap for nanoparticles at different steps of the synthesis (e) and nanoparticles with different Au-NS sizes (f). (The bandgap is taken as the extrapolation of the linear part at $[F(R)h\upsilon]^{1/2} = 0$).______ 108

Figure 3.9. Photocatalytic degradation of CIP (5 mg/L) with TiO_2:Au-NSph, TiO_2:Au-NSs-A, B, and C nanoparticles under 30 min of UV radiation (a) and 150 min of visible radiation (b). ______ 110

Figure 3.10. Photolysis assay of CIP (5 mg/L) under 30 min of UV radiation (a) and 150 min of visible radiation (b). ______ 110

Figure 3.11. X-ray diffraction spectra of TiO_2:Au-NSs-A, B, and C nanocomposites after photocatalytic application (a). Quantification of photogenerated hydroxyl radical ($^{\bullet}OH$) and singlet oxygen ($^1O_2$) by TiO_2:Au-NSs-A under 30 min of UV radiation (b). 112

Figure 3.12. Photocatalytic degradation of CIP (5 mg/L) with TiO_2:Au-NSs-A, B and C nanoparticles under 180 min of different wavelengths of light (inset): blue (a), green (b), red (c) and NIR light (d) radiation. 114

Figure 3.13. Photolysis assay of CIP (5 mg/L) under 180 minutes of blue (a), green (b), red (c) and NIR light (d) radiation. 115

Figure 3.14. Cross-section SEM images of 0 wt.% (a) and 10 wt.% TiO_2:Au-NSs/PVDF-HFP membranes (b) with EDS spectrum (inset). Photocatalytic degradation of CIP (5 mg/L) with 10 wt.% TiO_2:Au-NSs/PVDF-HFP membrane under 600 min of visible radiation (c). 117

Figure 4.1. Xenon Lamp arc (with UV filter) and sunlight spectra. 136

Figure 4.2. STEM-HAADF micrographs of TiO_2:Au-NSs. 137

Figure 4.3. SEM micrographs with porous diameter histogram distribution (inset) of the doctor blade (a, b) and salt leaching membranes (c, d) with 0 wt.% (a, c) and 10 wt.% (b, d) incorporated TiO_2:Au-NSs nanoparticles. Porosity obtained by mercury intrusion porosimetry (MIP) for the doctor blade and salt leaching membranes (e). 138

Figure 4.4. EDX chemical mapping of Ti along the membrane cross-section (a, b) and surface (inset) of the 10% TiO_2:Au-NSs_PVDF-HFP doctor blade (a) and salt leaching membrane (b). 139

Figure 4.5. FTIR spectrum of doctor blade (a) and salt leaching membranes (b). 140

Figure 4.6. DSC thermograms of doctor blade (a) and salt leaching membranes (b). 141

Figure 4.7. Average water contact angle of three measurements at room temperature of doctor blade and salt leaching membranes before (a) and after (b) UV radiation 30 min. 143

Figure 4.8. Photocatalytic degradation of CIP (5 mg/L) with doctor blade (a, b) and salt leaching membranes (c, d) under 300 min of UV radiation (a, c) and 480 min of visible radiation (b, d). 144

Figure 4.9. Photolysis assay of CIP (5 mg/L) under 300 min of UV radiation (a) and 480 min of visible radiation (b). Adsorption of CIP (5 mg/L) in the dark, using pristine PVDF-HFP doctor blade (c) and salt leaching membrane (d). 145

Figure 4.10. Chromatograms of CIP degradation using 10% TiO_2:Au-NSs_PVDF-HFP salt leaching membrane under 300 min of UV radiation. 147

Figure 4.11. Degradation efficiency for CIP (5 mg/L) removal in three consecutive uses in ultrapure water with 10% TiO_2:Au-NSs_PVDF-HFP doctor blade and salt leaching membranes under 300 min of UV radiation (a) and 480 min of visible radiation (b). 148

Figure 4.12. Cross-section SEM images of 10% TiO_2:Au-NSs_PVDF-HFP doctor blade (a, b) and salt leaching membranes (d, e) before (a, d) and after (b, e) the reusability assays with the corresponding pore diameter histograms distribution (inset). EDX mapping of the cross-section (c, f) and surface (inset) of 10% TiO_2:Au-NSs_PVDF-HFP doctor blade (c) and salt leaching membranes (f) after the reusability assays. 150

Figure 4.13. Elemental percentage of C, O, F, Ti in surface (a, b) and cross-section (c, d) of 10% TiO_2:Au-NSs_PVDF-HFP doctor blade (a, c) and salt leaching membranes (b, d) before and after the reusability assays. 151

Figure 4.14. FTIR spectrum (a, c) and DSC thermograms (b, d) of 10% TiO_2:Au-NSs_PVDF-HFP doctor blade (a, b) and salt leaching membranes (c, d) before and after the reusability assays. 152

Figure 4.15. Degradation efficiency (a, c) and rate constant (b, d) for CIP (5 mg/L) removal in three consecutive uses in real treated effluent with 10% TiO_2:Au-NSs_PVDF-HFP salt leaching membranes under 300 min of UV radiation (a, b) and 480 min of visible radiation (c, d). 155

List of Figures

List of Tables

Table 1.1. Common detected pharmaceuticals in environmental waters. ______ 6

Table 2.1. Physicochemical properties of CLQ, PAR, DCF, and CIP. ______ 52

Table 2.2. Summary of the characteristics of TiO_2, TiO_2:Au, ZnO, and ZnO:Au nanoparticles. ______ 62

Table 2.3. Surface area (S_{BET}), analysis pressure range ($\Delta P/P_0$), goodness of fit (R^2), microporous surface (S_{micro}), external surface (S_{ext}), microporous volume (V_{micro}) and total volume (V_T) for TiO_2, TiO_2:Au, ZnO, and ZnO:Au nanoparticles. ______ 63

Table 2.4. CLQ, PAR, DCF, and CIP degradation efficiencies (DE) and corresponding apparent reaction rate constants (*k*) under 60 min of UV radiation for TiO_2 and ZnO. ______ 69

Table 2.5. CLQ, PAR, DCF, and CIP degradation efficiencies (DE) and corresponding apparent reaction rate constants (*k*) under 60 min of UV radiation for TiO_2:Au, and ZnO:Au. ______ 71

Table 2.6. Comparison of degradation efficiency (DE) between the present work and previous works that used TiO_2 on CLQ, PAR, DCF and CIP degradation. ______ 72

Table 2.7. Comparison of degradation efficiency (DE) between the present work and previous works that used ZnO on the degradation of CLQ, PAR, DCF and CIP. ______ 73

Table 2.8. CLQ, PAR, DCF, and CIP degradation efficiencies (DE) and corresponding apparent reaction rate constants (*k*) under 240 min of visible radiation for TiO_2:Au and ZnO:Au. ______ 74

Table 3.1. Amount of Au with respect to TiO_2 (wt. %) in the samples, theoretical value (considering the added reagents in the synthesis reaction) vs. XRF measurement. ______ 106

Table 3.2. CIP degradation efficiencies (DE) and corresponding apparent reaction rate constants (*k*) under 30 min of UV radiation and 150 min of visible radiation for TiO_2:Au-NSs-A, B, and C nanoparticles. ______ 109

Table 3.3. Comparison of degradation efficiency (DE) between the present work and previous work that used plasmonic nanoparticles to functionalise TiO_2 for ciprofloxacin (CIP) degradation under visible light. ______ 113

Table 3.4. CIP degradation efficiencies (DE, %) and corresponding apparent reaction rate constants (*k*) under 150 min of blue, green, red and NIR radiation for TiO_2:Au-NSs-A, B, and C nanoparticles. ____ 114

Table 4.1. β phase content (%) of doctor blade and salt leaching membranes. ____ 141

Table 4.2. Degree of crystallinity (%) of doctor blade and salt leaching membranes.____ 142

Table 4.3. CIP degradation efficiencies (DE) and corresponding apparent reaction rate constants (*k*) under 300 min of UV radiation and 480 min of visible radiation for doctor blade and salt leaching membranes. ____ 146

Table 4.4. Detected degradation products of CIP. ____ 147

Table 4.5. CIP degradation efficiencies (DE) and corresponding apparent reaction rate constants (*k*) in three consecutive uses with 10% TiO_2:Au-NSs_PVDF-HFP doctor blade and salt leaching membranes in ultrapure water under 300 min of UV radiation and 480 min of visible radiation. ____ 149

Table 4.6. β phase content (%) and degree of crystallinity (%) of 10% TiO_2:Au-NSs_PVDF-HFP doctor blade and salt leaching membranes before and after the reusability assays. 152

Table 4.7. Comparison of the efficiency losses after reusability assays in the present work with previous studies using immobilised photocatalysts for pollutants degradation.____ 153

Table 4.8. Chemical and physical properties of the real treated effluents.____ 154

Table 4.9. CIP degradation efficiencies (DE) and corresponding apparent reaction rate constants (*k*) in three consecutive uses with 10% TiO_2:Au-NSs_PVDF-HFP salt leaching membranes in real treated effluent under 300 min of UV radiation and 480 min of visible radiation. ____ 155

Table 4.10. Comparison of efficiency losses between using real treated effluent water matrix and ultrapure water for pollutants degradation in the present work with previous works. In our case, we presented the maximum efficiency loss after 3 cycles (worst case). ____ 156

List of abbreviations, symbols and acronyms

List of acronyms

A	Anatase
AA	L-ascorbic acid
AOPs	Advanced Oxidation Processes
ARB	Antibiotic resistant bacteria
B	Brookite
BDD	Boron-doped diamond
BET	Brunauer-Emmett-Teller
C	Graphite
CB	Conduction band
CECs	Contaminants of emerging concern
CIP	Ciprofloxacin
CLQ	Chloroquine phosphate
CVD	Chemical vapour deposition
DCF	Diclofenac sodium
DE	Degradation efficiencies
$DE_{db,vis}$	Degradation efficiency of pollutants using doctor blade membranes under visible radiation
$DE_{sl,vis}$	Degradation efficiency of pollutants using salt leaching membranes under visible radiation
DE_{vis}	Degradation efficiency of pollutants under visible radiation
$DE_{db,uv}$	Degradation efficiency of pollutants using doctor blade membranes under UV radiation
$DE_{sl,uv}$	Degradation efficiency of pollutants using salt leaching membranes under UV radiation
DE_{uv}	Degradation efficiency of pollutants under UV radiation
DLS	Dynamic light scattering
DMF	*N*, *N*-dimethylformamide
DO	Dissolved oxygen
DP	Deposition-Precipitation
DRS	Diffuse reflectance spectroscopy
DSC	Differential scanning calorimetry
EDCs	Endocrine-disrupting chemicals
EDX	Energy Dispersive X-ray spectroscopy

EP	European Pharmacopoeia
ESI+	Electrospray ionisation source in positive mode
FEG-SEM	Field emission gun scanning electron microscope
FTIR	Fourier-transform infrared spectroscopy
HFP	Hexafluoropropylene
HTA	Hydroxyterephthalic acid
IMP	Impregnation
IR	Infrared
K-M	Kubelka-Munk
L-H	Langmuir-Hinshelwood
LSPR	Localised surface plasmon resonance
MB	Methylene blue
MIP	Mercury intrusion porosimetry
NHE	Normal hydrogen electrode
NIPS	Non-solvent-Induced Phase Separation
NIR	Near infrared
NOR	Norfloxacin
NPs	Nanoparticles
NSph	Spherical particles
NS	Star-shaped
NSs	Nanostars
NSAIDs	Non-steroidal anti-inflammatory drugs
PAR	Paracetamol
PDI	Polydispersity index
PDINH	34,910-pyre- netetracarboxydiimine
PDS	Synergistic effects of peroxydisulfate
PMMA	Poly(methyl methacrylate)
PR	Photoreduction
PVDF	Poly(vinylidene fluoride)
PVDF-CTFE	Poly(vinylidene fluoride-*co*-chlorotrifluoroethylene
PVDF-HFP	Poly(vinylidene fluoride-co-hexafluoropropene
PVDF-TrFE	Poly(vinylidene fluoride-trifluoroethylene)
PZC	Point of zero charge
R	Rutile
RO	Reverse osmosis

ROS	Reactive oxygen species
SDD	Silicon drift detector
STEM-HAADF	High-angle annular dark-field scanning transmission electron microscopy
TA	Terephthalic acid
TEM	Transmission electron microscopy
TGTG′	Trans-gauche-trans-gauche
TIPS	Temperature-Induced Phase Separation
TOF-HRMS	Time-of-flight high-resolution mass spectrometry
TTT	All trans planar zigzag
UHPLC	Ultrahigh-performance liquid chromatography
UNICEF	United Nations Children’s Fund
UV	Ultraviolet
UV-Vis	Ultraviolet-Visible
VB	Valence band
VDF	Vinylidene fluoride
WHO	World Health Organization
WWTPs	Wastewater treatment plants
XRD	X-ray diffraction
XRF	X-ray fluorescence

List of abbreviations and symbols

A_α	Absorbance of α-phase at 766 cm^{-1}
A_β	Absorbance of β-phase at 840 cm^{-1}
C_0	Concentration of the pollutant at time 0
C	Concentration of the pollutant at time t
e^-	Electron
e_{CB}^{-}	Electron excited from the valence band of photocatalyst into the conduction band
E_g	Bandgap
E_e	Energy of free electrons on the hydrogen scale
E_g	Bandgap energy of the semiconductor
E^0	Standard redox potential
E_{CB}	Conduction band edge potential
E_{VB}	Valence band edge potential
F(R)	Sample's absorbance
F(β)	Relative fraction of the β-phase
h	Planck's constant
h_υ	Energy
h^+	Hole
h_{VB}^{+}	Hole in the valence band
I_A	Integral areas of anatase peaks in the XRD spectra
I_B	Integral areas of brookite peaks in the XRD spectra
I_R	Integral areas of rutile peaks in the XRD spectra
k	Apparent reaction rate constant
$k_{db,uv}$	Apparent reaction rate constant of pollutants degradation using doctor blade membranes under UV radiation
$k_{sl,uv}$	Apparent reaction rate constant of pollutants degradation using salt leaching membranes under UV radiation
k_{uv}	Apparent reaction rate constant of pollutants degradation under UV radiation
k_{vis}	Apparent reaction rate constant of pollutants degradation under visible radiation
$k_{\mathrm{db,vis}}$	Apparent reaction rate constant of pollutants degradation using doctor blade membranes under visible radiation
$k_{\mathrm{sl,vis}}$	Apparent reaction rate constant of pollutants degradation using salt leaching membranes under visible radiation

k_r	Reaction rate constant
K_A	Correction coefficient for anatase
K_B	Correction coefficient for brookite
K_L	Langmuir adsorption constant
K_α	Absorption coefficient of α-phase at 766 cm^{-1}
K_β	Absorption coefficient of β-phase at 840 cm^{-1}
m/z	Mass-to-charge
n	Sample transition parameter
r	Reaction rate
R_∞	Sample's reflectance
R^2	Goodness of fit
S_{micro}	Microporous surface
S_{ext}	External surface
S_{BET}	Surface area
t	Time
V_{micro}	Microporous volume
V_T	Total volume
W_A	Weight fractions of anatase
W_B	Weight fractions of brookite
W_R	Weight fractions of rutile
wt.%	Phase composition
x	α-phase contents calculated from the FTIR spectrum
X	Electronegativity of the semiconductor
y	β-phase contents calculated from the FTIR spectrum
λ_{max}	Main absorption peak
Φ_{SB}	Electron-transfer efficiency
Φ_M	Work function of the metal, Au
χ_c	Degree of crystallinity
χ_{SM}	Electron affinity of the semiconductor, TiO_2
υ	Frequency
ΔH_α	Melting enthalpies of pure crystalline α-PVDF
ΔH_β	Melting enthalpies of pure crystalline β-PVDF
ΔH_f	Melting enthalpy of the polymer obtained from the DSC
$\Delta P/P_0$	Analysis pressure range

Chapter 1

1. Introduction

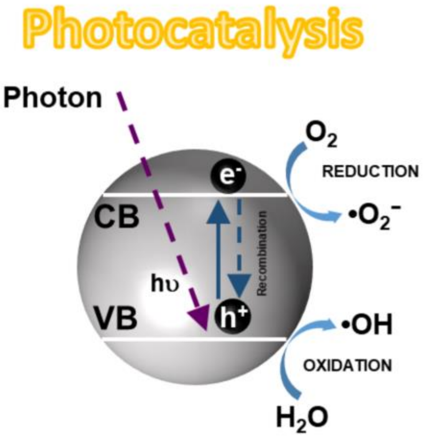

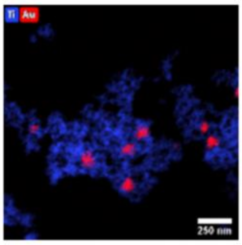

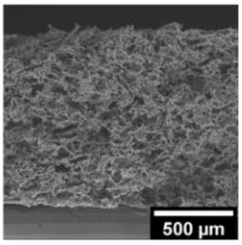

The presence of pharmaceuticals in the environment has gained increasing attention and many efforts have been made to tackle it. Among many solutions, photocatalysis arises as a promising technology for degrading pharmaceuticals in water. This chapter presents a state-of-the-art of the central concepts of photocatalysis and photocatalytic materials used in the current work. The primary objectives and structure of the thesis are also indicated.

1.1. Motivation

Nowadays, water scarcity affects a significant part of the worldwide population [1]. According to United Nations Children's Fund (UNICEF) and World Health Organization (WHO), nearly 785 million people in the world - almost 10% of the global population, in particular in underdeveloped countries, have no access to safe drinking water (**Figure 1.1**) [2]. Thus, addressing clean water scarcity has been selected as the sixth goal of the Sustainable Development Goals (SDGs) adopted by the United Nations Member States in 2015 [1].

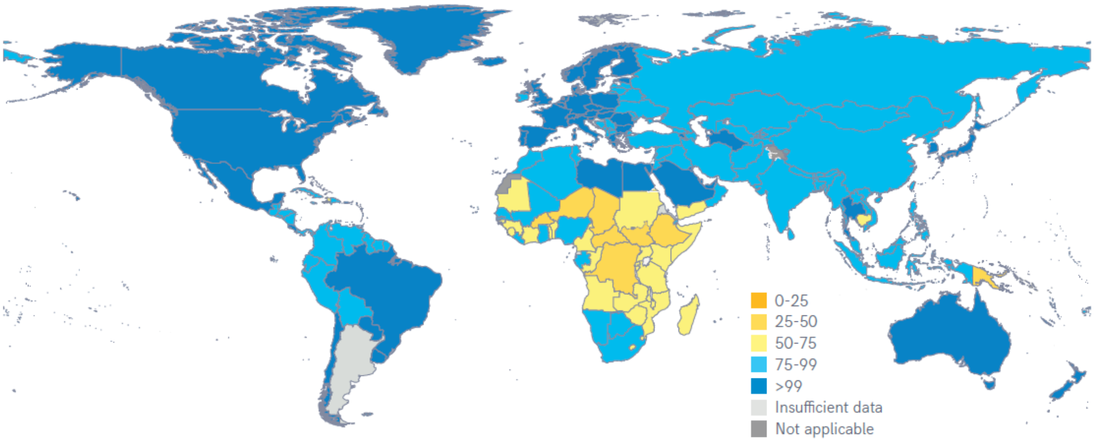

Figure 1.1. Proportion of the population using at least basic drinking water services in 2020 according to the assessment of UNICEF and WHO. Adapted from [2].

The increasing water pollution due to world population and humankind activity growth is aggravating the water stress [3–5] which is estimated to affect over half of the global population by 2050 [4]. Additionally, more than 1.5 million deaths per year are estimated due to the consumption of unsafe/contaminated water [6]. The pollutants such as pathogens, fertilizers, pesticides, dyes and heavy metals mainly coming from agriculture and industry effluents [5,7], have traditionally been considered the main cause of water pollution [7]. People are aware of these conventional pollutants because of their known permissible standard limit and well-described harmful effects on ecosystems and human health [7,8].

In recent decades, one of the biggest concerns in the environmental field is the contaminants of emerging concern (CECs) [3,9]. Although their risk of health hazardous is uncertain due to a lack of studies and there are no established regulations [7,9,10], the elimination of CECs from the water bodies has raised attention to prevent their potentially toxic consequences and possible adverse effects on the health of living aquatic organisms and humans [9,11].

On the other hand, a watch list for nearly 30 priority pollutants has been established by European Commission to monitor these concerned substances in water for human consumption [8,12].

1.2. Contaminants of emerging concern and pharmaceuticals

Contaminants of emerging concern (CECs) are a group of natural and synthetic chemicals such as pharmaceuticals, personal care products, endocrine-disrupting chemicals (EDCs), disinfection byproducts and nanomaterials [3,11,13]. Among them, pharmaceuticals, which are used to treat a wide variety of diseases, have gained great interest since they can be found in different water matrices such as wastewater [3], hospital sewers [11], surface waters [11,14], groundwater [14] and drinking water [14], entering the environment through different pathway [3,14–16], as shown in **Figure 1.2**.

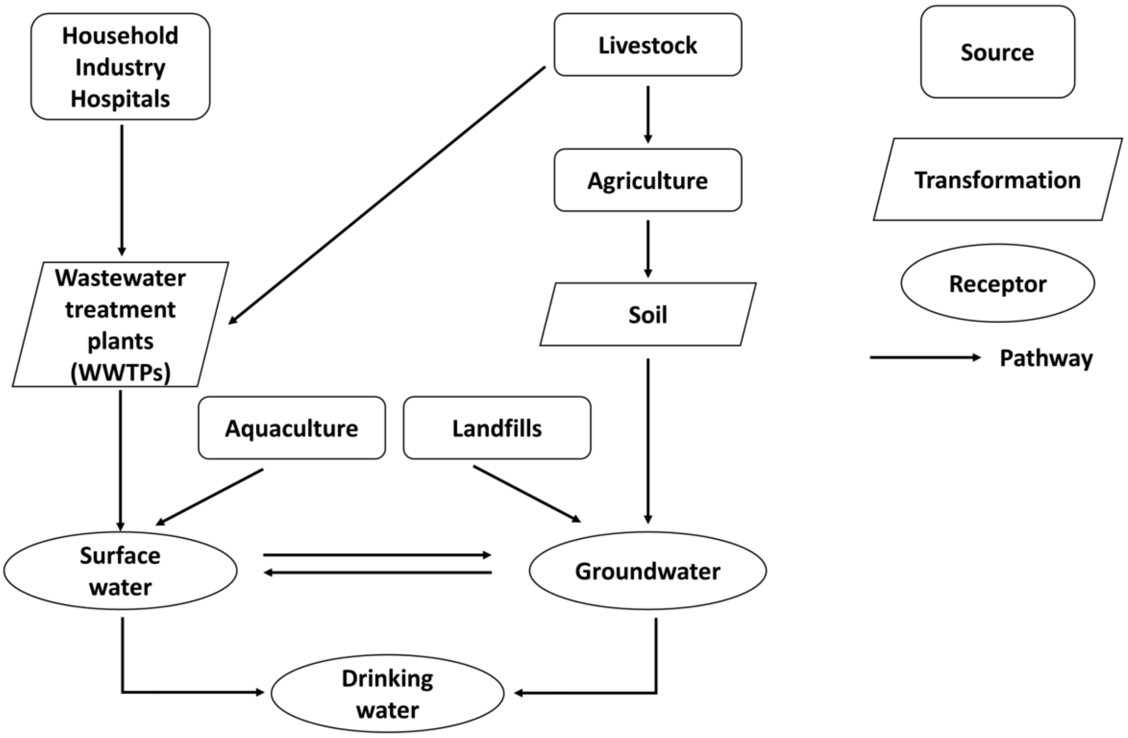

Figure 1.2. Sources and pathways of the pharmaceuticals in the environment [3,14,16,17].

The urban wastewater and livestock waste are the main sources, which contains a high load of pharmaceuticals from human and animal excrement [14,16] because certain pharmaceuticals cannot be completely metabolized in their body [3,14]. Furthermore, the inadequate disposal of unused drugs can also be one of the pathways of pharmaceuticals into the environment [14,16]. The pharmaceutical industry and hospital wastewater are other direct sources, with high concentrations of pharmaceuticals [16,17]. These types of wastewater enter into wastewater treatment plants (WWTPs) before discharging into the environment [16,17]. However, these resilient pharmaceutical compounds cannot be removed efficiently by the conventional treatment processes and may end up in effluents [3,14], contaminating the aquatic environment [16,18]. On the other hand, chemicals used in aquaculture and animal excreta used in agriculture as fertilizers are other sources for pharmaceuticals entering surface water and groundwater [3,16].

Among pharmaceuticals, antibiotics, non-steroidal anti-inflammatory drugs (NSAIDs), analgesics and β-blockers are the most commonly detected classes in water [3,13,16,19]. **Table 1.1** shows the most frequently detected pharmaceuticals according to their type [3,16,19]. Usually, these pharmaceuticals appear at a very low concentration, in the order of ng/L to µg/L [3,20,21]. However, their prolonged exposure in water can cause an adverse impact on aquatic organisms [3,11] like fishes [17], crustaceans [22], and algae [23]. Furthermore, many of them can even be bioaccumulated and, ultimately, end up in human bodies through the food chain and drinking water [3,11,15]. For example, antibiotics are of special concern due to their high consumption, persistent nature, partial metabolism and easy movement through ecosystems [11,16,24]. Moreover, their presence in nature water can develop antimicrobial resistance in microorganisms leading to antibiotic resistant bacteria (ARB) [3,16,21], which reduces the efficiency of current antibiotics to treat infections and diseases [11,16]. NSAIDs and analgesics, having a high production and consumption, are often combined with antibiotics in veterinary medicine [16]. Their release into the environment has biological effects on living organisms and plant growth [16]. β-blockers is another highly consumed pharmaceutical group for hypertension treatment [25]. Their dissemination in nature can cause neurotoxic and reproductive disorders in living organisms [16]. On the other hand, there is a suddenly increased use of many pharmaceuticals including analgesics, mucolytics and anti-biotic/viral/inflammatory drugs to control and treat COVID-19 [26] ignoring their potential environmental impact [27].

Table 1.1. Common detected pharmaceuticals in environmental waters.

Type	Pharmaceuticals
Antibiotics	Ciprofloxacin, Norfloxacin, Sulfamethoxazole, Trimethoprim
Non-steroidal anti-inflammatory drugs (NSAIDs)	Diclofenac, Ibuprofen, Naproxen, Ketoprofen
Analgesics	Paracetamol, Acetylsalicylic acid
β-blockers	Propranolol, Atenolol, Metoprolol, Bisoprolol

Due to the highly persistent nature and difference in the physicochemical properties of the present pharmaceuticals [3,28], the configuration and design of conventional technologies such as coagulation/flocculation, filtration and biological processes in WWTPs facilities cannot remove them completely [28,29]. For instance, the small size of many pharmaceuticals makes them difficult to be removed completely by filtration [11] and bio-recalcitrant nature of pharmaceuticals render the biological treatment ineffective [28,29]. Hence, it is crucial to develop advanced materials and efficient technologies in wastewater treatment. Several approaches have been studied and tested to tackle this problem, such as activated carbon adsorption [3], membrane technology [20] and Advanced Oxidation Processes (AOPs) [13,29].

Although activated carbon adsorption is extensively used in wastewater treatment with high removal efficiency of NSAIDs type pharmaceuticals [3], the pollutants are not eliminated and only pass from a liquid to a solid phase requiring further treatments [30]. In membrane filtration like nanofiltration and reverse osmosis (RO), pollutants are retained in the pressurised side of the membrane while the clean water passes to the other side. This technology shows the same disadvantage as adsorption that cannot remove the pollutants completely and generates new waste. Furthermore, membrane technologies require an enormous energy demand [11]. To overcome these challenges, AOPs as an innovative water treatment technology has attracted attention [29].

1.3. Advanced oxidation processes

Advanced Oxidation Processes (AOPs) are efficient environmentally friendly processes based on the generation of highly reactive species such as hydroxyl radical ($^{\bullet}HO$), which can degrade the pollutants in wastewater [9,28,31]. The most common AOPs include techniques such as ozonation, photolysis, Fenton oxidation, electrochemical oxidation, ultrasound irradiation and photocatalysis, among others [9,21,28].

Ozonation has proven to be capable of efficiently oxidise a wide range of pollutants [9,11]. In this process, ozone is decomposed in water to form hydroxyl radicals, which is a stronger oxidising agent than ozone [32]. This technique has the advantage of allowing the application even at unstable flow rates [9,32]. Additionally, the ozonation treatment can be enhanced by coupling with hydrogen peroxide and/or light radiation [9]. However, there are many disadvantages to this process, mainly high cost, mass transfer limitations of O_3, and high temperature and pH dependence [9,13].

Photolysis is the decomposition of pollutants dissolved in water through chemical reactions induced by light radiation (artificial or natural) [21,32]. However, the process efficiency depends on the absorption spectrum of the target pollutant, radiation intensity and frequency, and water matrix, among others [9,32]. Direct photolysis is relatively ineffective in the removal of recalcitrant contaminants effluents towards other treatments [9]. It is typically applied with photo-sensitive compounds like oxygen, hydroxyl or peroxyl radicals [9,21,32].

Fenton oxidation is another widely applied AOP [21], which takes place under mild acidic conditions with a mixture of hydrogen peroxide solution and an iron salt catalyst (ferrous or ferric ions) [21,28]. The mechanism is based on the decomposition of ferric ions by the hydrogen peroxide in the aqueous phase, yielding hydroxyl radicals [9,32]. Moreover, this process can be significantly increased through combination with UV light (photo-Fenton), with an electrochemical process (electro-Fenton) or even with both (photo-electro-Fenton) [21,28]. However, the process is highly dependent on the pH, temperature and hydrogen peroxide, among others [9,32], and requires a time-consuming process to recover the precipitates [21].

During the electrochemical processes, oxidation occurs on the surface of the anodes in the presence of an electrolyte [32]. Typically, graphite (C), titanium dioxide (TiO_2), Ti-based alloys, iridium oxide (IrO_2) and, more recently, boron-doped diamond (BDD) are used for anodes [28]. In this way, pollutants are firstly adsorbed onto the anode surface and then destroyed through a direct anodic oxidation-anodic electron exchange [32]. Although there is no need any additional chemicals, this process requires high energy and its efficiency depends on the selection and maintenance of the electrode materials [28,29,33].

Another AOP which has gained popularity is ultrasound irradiation, which is based on the production of hydroxyl radical ($^{\bullet}OH$) from water pyrolysis due to the high intensity of cavity bubbles produced by acoustic radiation [28]. Despite not requiring additional chemicals, this technique is rather energy-demanding, limiting its application in the industry [28,29].

It is in this context that semiconductor photocatalysis becomes a promising technology. Mainly because when compared with other AOPs, it is eco-friendly and only requires a source of radiation (UV or sunlight) and a photocatalyst without the addition of any chemicals or current, making it a straightforward and a cost-effective process [9,21,34]. Furthermore, photocatalysis can be carried out at ambient conditions and could allow the use of solar energy as a light source [21]. A more detailed explication of it is given in the following section.

1.4. Heterogeneous photocatalysis in water remediation

Catalysis is a term introduced by Baron J. J. Berzelius in 1835 to describe the property of substances, the so-called catalysts, that facilitate chemical reactions without being consumed in them [35]. Homogeneous catalysts are present in the same phase as reactants and products, while heterogeneous catalysts are present in a different phase which can be easily separated from the product stream [35]. The term "photocatalysis" was mentioned for the first time in 1911 by Eibner when referring to catalytic processes induced by radiation absorption (ultraviolet, visible, or infrared), using a photocatalyst [36]. In 1960's, Fujishima and Honda published a work related to water splitting under visible radiation with a titanium dioxide (TiO_2) electrode and without an application of external voltage [36,37]. Later, in 1977, Frank and Bard reported the degradation of cyanide and sulfite from water with different photocatalysts [36,38]. This work proved that photocatalysis was an effective wastewater treatment method because it allowed the degradation of organic contaminants into innocuous compounds such as CO_2 and H_2O [39,40]. Our work will focus on heterogeneous photocatalysis.

1.4.1. Mechanism and reaction pathways

The photocatalysis, as shown in **Figure 1.3**, takes place when a photocatalyst absorbs a photon with energy ($h\upsilon$) equal or higher than its bandgap (E_g) under light radiation [41,42].

This makes an electron (e_{CB}^{-}) excited from the valence band (VB) of photocatalyst into the conduction band (CB), leaving a hole (h_{VB}^{+}) in the valence band (VB) [42,43]. This photogenerated electron-hole (e^{-}-h^{+}) pair can recombine again producing heat [21,42] or migrate to the photocatalyst surface being involved in the redox reactions to produce highly reactive oxygen species (ROS) [21,41]. Holes react with water to produce hydroxyl radicals ($^{\bullet}OH$) and electrons react with dissolved O_2 in water to form superoxide radicals ($^{\bullet}O_2^{-}$), which degrade pollutants into harmless compounds [41,43,44].

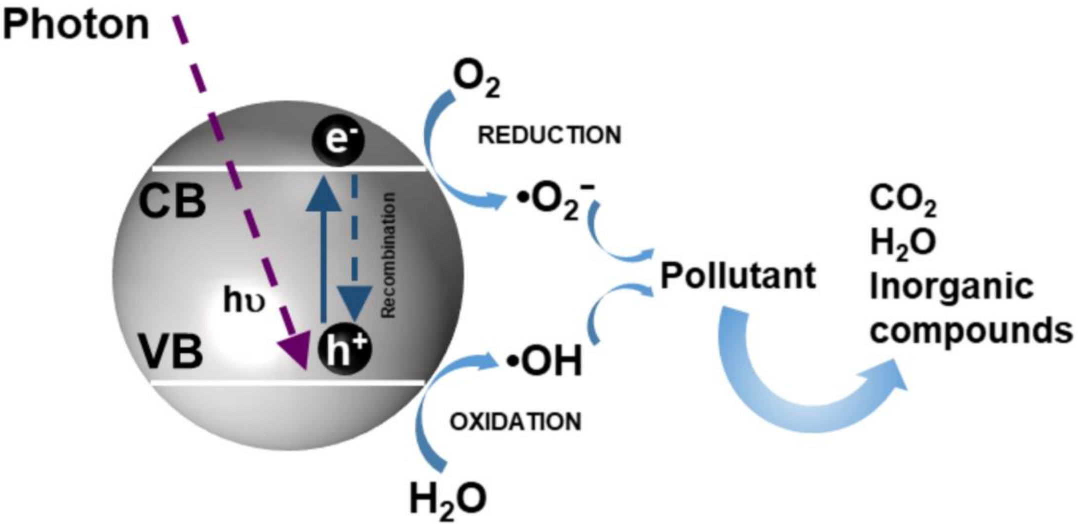

Figure 1.3. Schematic representation of the photocatalytic mechanism on a semiconductor nanoparticle in the presence of a water pollutant and with light irradiation (hυ).

In brief, the mechanism of photocatalysis and formation of ROS can be presented in the following equations (**Equation 1.1-1.8**) [21,44,45]. As mentioned, the principle of photocatalysis lies on the activation of the photocatalyst by an energy source (light radiation), represented in **Equation 1.1**.

$$Photocatalyst \xrightarrow{h\upsilon} h_{VB}^{+} + e_{CB}^{-} \qquad \textbf{(1.1)}$$

The photogenerated holes (h_{VB}^{+}) have a high oxidation potential yielding hydroxyl radicals ($^{\bullet}OH$) by oxidising water molecules (**Equation 1.2**). The electrons (e_{CB}^{-}) reduce the dissolved oxygen, originating superoxide radicals ($^{\bullet}O_2^{-}$) (**Equation 1.3**). These can subsequently react with hydrogen ions (H^{+}) to form hydroperoxyl radicals ($^{\bullet}HO_2$) (**Equation 1.4**), which afterwards are converted into hydrogen peroxide (H_2O_2) (**Equation 1.5**).

$$h_{VB}^{+} + H_2O \rightarrow {}^{\bullet}OH + H^{+} \qquad \textbf{(1.2)}$$

$$e_{CB}^{-} + O_2 \rightarrow {}^{\bullet}O_2^{-} \quad (1.3)$$

$$^{\bullet}O_2^{-} + H^{+} \rightarrow {}^{\bullet}OOH \quad (1.4)$$

$$^{\bullet}OOH + {}^{\bullet}OOH \rightarrow H_2O_2 + O_2 \quad (1.5)$$

The produced H_2O_2 may act as an electron receptor generating other hydroxyl radicals (**Equation 1.6**) or may react with the $^{\bullet}O_2^{-}$ (**Equation 1.7**):

$$e_{CB}^{-} + H_2O_2 \rightarrow OH^{-} + {}^{\bullet}OH \quad (1.6)$$

$$^{\bullet}O_2^{-} + H_2O_2 \rightarrow OH^{-} + {}^{\bullet}OH \quad (1.7)$$

Finally, the generated ROS degrade pollutants through several cascade reactions to finally give rise to smaller molecules such as water or carbon dioxide (**Equation 1.8**):

$$^{\bullet}OH / {}^{\bullet}O_2^{-} / {}^{\bullet}OOH + Pollutant \rightarrow H_2O + CO_2 \quad (1.8)$$

1.4.2. Kinetics of reaction

Kinetic is another widely studied issue related to photocatalytic degradation of water pollutants since it is useful for the understanding of the mechanisms involved in the reaction as well as process scale-up [46,47]. The overall heterogeneous photocatalysis process can be decomposed into the following steps [42,48,49]:

1) Mass transfer of the pollutants from the liquid phase to the photocatalyst surface
2) Adsorption of the pollutant on the photocatalyst surface
3) Redox reactions in the adsorbed phase for pollutants
4) Desorption of products
5) Mass transfer of the products into the liquid phase

The kinetic model is developed considering the step 2, 3 and 4 [21,48]. Several studies have stated that these photocatalytic reactions usually follow the classical Langmuir-Hinshelwood (L-H) model which is simplified to pseudo-first order kinetics or zero-order kinetics, depending on the experimental conditions [46,50,51]. The initial concentration of the pollutant is an important factor since it directly affects the coverage of the surface of the catalyst [21]. Under a high concentration, the pollutant completely covers and saturates the photocatalyst surface and the Langmuir-type kinetic rate is the zero-order type, which implies that the overall rate does not depend on external mass transfer. When the initial concentration of the pollutant is low, the kinetic rate is pseudo-first order type. In this case, the kinetic depends on mass transfer regardless of the initial concentration [46,47,52].

This L-H model (**Equation 1.9**) is commonly used to estimate the kinetics of heterogeneous photocatalytic materials, on the assumption of the adsorption/desorption equilibrium of the reactants to the catalyst [47]:

$$r = -\frac{dC}{dt} = \frac{k_r K_L C}{1+K_L C} \tag{1.9}$$

where, r is the reaction rate, t is time, C is pollutant concentration, k_r is the reaction rate constant and K_L is the Langmuir adsorption constant.

If the reactant concentration is low (< 1 mM), ($K_L C < 1$), it is possible to simplify to an "apparent" pseudo-first-order kinetic law (**Equation 1.10**) [49,51]:

$$r = -\frac{dC}{dt} = kC \tag{1.10}$$

where $k = k_r K_L$ is the apparent reaction rate constant. After the integration of **Equation 1.10** [51]:

$$C = C_0 e^{-kt} \tag{1.11}$$

where C_0 and C represent the concentration of the pollutant at time 0 min and at time t, respectively. *k* is the apparent reaction rate constant.

However, the L-H model is not able to define the relationship between the reaction rate (r) and the intensity of the photon flux [47,48]. Although the L-H model is used in the general situation of heterogeneous photocatalytic reactions, it disregards several steps of the process such as [47,48]:

1) Generation of free holes in the valence band and free electrons in the conduction band
2) Reduction of the dissolved oxygen by the photogenerated electrons
3) Trapping of the photogenerated holes in surface states
4) Charge carriers recombination

In spite of the cited restrictions, a significant number of works continue to use the L-H model, mainly because the majority of these studies deal with low contaminants concentration avoiding photocatalyst saturation, following the L-H kinetics [47,53]. In addition, it offers a simple tool that can be used to empirically compare variations in the catalyst to evaluate its performance.

1.4.3. Operational parameters of photocatalysis

Apart from the photocatalytic mechanism, it is important to understand the main operating conditions to achieve an efficient photocatalytic degradation for pollutant removal [54–56]. Several works have studied some crucial operational parameters that influence photocatalytic efficiencies, such as the photocatalyst concentration, the contaminant concentration (presence of other chemicals, or water matrix effect), the dissolved oxygen concentrations, pH, temperature, and the illumination conditions [21,42,44]. For easy readability and comprehension, the different parameters are discussed separately.

1.4.3.1. Photocatalyst concentration

The photocatalyst concentration is one of the most important factors affecting the photocatalytic process [56]. Many works have studied its influence on photocatalytic efficiency. In general, a higher concentration of photocatalyst led to a higher reaction rate [57–60] due to a larger surface area of photocatalysts improving light harvesting, which indicated that there are more available active sites and higher rates of reactive oxygen species generation [21,44,56]. However, above a threshold concentration the photocatalytic efficiency decreased with increasing the photocatalyst concentration [61–64]. Since the sedimentation and aggregation of photocatalysts increased the turbidity of the reaction solution reducing the penetration of light radiation [44,56,64]. Furthermore, the agglomeration of the particles decreased the active surface area of photocatalysts [21,55,62]. It is also important to indicate that the optimum concentration of photocatalysts depends on the types of photocatalysts and contaminants and the experimental conditions [55,56].

1.4.3.2. Illumination conditions

The light source is considered an essential factor to initiate the photocatalysis [56]. The light wavelength and intensity should be adequate to excite the electron-hole pair in the photocatalyst to start the photodegradation of pollutants [44].

The photocatalytic degradation rate depends on the light intensity and three regimes can be identified [21]. Under low intensity (< 20 mW/cm^2), the reaction rate increases linearly with light intensity indicating that the reaction rate can be enhanced by light intensity [45,51]. At medium intensity (≈ 25 mW/ cm^2) [56], the reaction rate becomes square root dependent on the light intensity since the electron-hole pair formation competes with electron-hole pair recombination causing a reduction of photocatalytic efficiency [45,51,56,65]. However, at very high intensities the reaction rate is independent of the light intensity because there is a predominance of electron-hole recombination [51,65].

1.4.3.3. pH of solution

The solution pH plays an essential role in photocatalytic reaction because it affects the amount of hydroxyl radicals ($^{\bullet}OH$), which takes part in the photodegradation of pollutants [21,56]. Under basic condition, the high concentration of OH^{-} can improve the production of $^{\bullet}OH$ radicals, enhancing the photocatalytic degradation of pollutants [59,62].

Additionally, pH also influences the surface charge on the photocatalysts and deprotonation process of pollutants molecule affecting the adsorption behaviours between pollutants and photocatalysts – the first step of the photodegradation of pollutants [21,42,55]. The point of zero charge (PZC) is the point at which the surface of the photocatalyst is zero charged, i.e., there is a low coulombic interaction between the photocatalyst particles and charged pollutants due to the absence of any electrostatic forces [21,42,46]. In addition, when the pH of the solution is equal to the PZC of the photocatalyst and this is in a colloidal suspension, the uncharged photocatalysts surface leads to agglomeration and sedimentation of photocatalysts and limits the penetration of light [42,46]. When pH is above the PZC value, the photocatalyst surface becomes negatively charged, while pH below this value, photocatalyst surface becomes positively charged [21,46]. Cationic pollutants can adsorb on the negatively charged surface of photocatalyst, while it is repelled from the positively charged surface and vice versa [45,56]. In this way, the electrostatic attraction or repulsion between the photocatalyst surface and the pollutant may enhance or inhibit the photocatalytic efficiency, respectively [45,55]. An optimum pH of solution for improving photocatalytic reaction rate should take into account the characteristics of photocatalysts and pollutants under different pH values [56,59]. In addition, some works reported on the influence of the pH of the solution on the position of conduction and valence bands of photocatalysts also affecting the generation of electron-hole pairs and therefore the photocatalyst performance [42,45].

1.4.3.4. Reaction temperature

The photocatalytic systems can be operated at room temperature being a promising method for water remediation [42]. The optimum temperature for photocatalysis is between 20 °C and 80 °C [42,51], and a slight increase in temperature in this range leads to an increase in reaction rate probably due to the increasing fraction of collisions in the Arrhenius equation [46,66]. At high temperature (> 80 °C), the adsorption of pollutants on the photocatalyst surface is disfavoured and the electron-hole pair recombination is favoured, which decreases the efficiency of photocatalytic process [42,46]. At very low temperature (< 0 °C), the apparent activation energy is increased, which limits the desorption of the final product and reduces the photocatalytic activity [42,51,65]. On the other hand, it should be noted that the increase in temperature results in a decrease of the dissolved oxygen, which affects the photocatalytic process [65].

1.4.3.5. Dissolved oxygen

The presence of dissolved oxygen (DO) is an important parameter affecting the photocatalytic efficiency, but does not affect the adsorption on the photocatalyst surface [21,44]. Oxygen acts as a trap for photogenerated electrons avoiding them from recombination with the photogenerated hole [42,44]. Moreover, it involves the formation of reactive oxygen species such as the superoxide radical ($^{\bullet}O_2^{-}$) improving the photocatalytic degradation of pollutants [44,46].

1.4.3.6. Initial concentration of the pollutant

The photocatalytic efficiency depends on the initial concentration of pollutants in the solution [21,46,56]. It is observed that higher pollutants concentration decreases the photocatalytic degradation rate [57,59,67,68]. This is attributed to the fact that higher amount of pollutant molecules were adsorbed on the active sites of the photocatalyst reducing the formation of reactive oxygen species (ROS) [21,46,62]. Furthermore, high concentrations of pollutants produced more byproducts and intermediates during the photocatalysis, which competed with pollutants molecules for the limited number of active sites on the photocatalyst surface decreasing the degradation rate of pollutants [21,45,61]. In addition, the pollutants absorbed the photon of light radiation and attenuated the absorption of photon on the photocatalyst surface reducing the generation of ROS and photocatalytic efficiency [21,45,63].

1.4.3.7. Morphology of the photocatalysts

The photocatalytic behaviour of photocatalyst significantly depends on its size and morphology [42,69]. To date, different synthesis methods are used to obtain photocatalysts with controlled structure such as nanofibers, nanoplates, nanosphere and nanorods [70–73]. The morphology can affect the surface area increasing or decreasing the contact area between the pollutants and photocatalyst, improving or reducing the photocatalytic activity [42,69,72]. Additionally, photocatalyst with small particles´ size possess larger surface area increasing the number of active sites and photocatalytic activity [42,72]. Furthermore, the small photocatalyst size can shorten the pathway for electron-hole pair to migrate to the surface of photocatalysts, reducing the possible recombination and enhancing the photocatalytic efficiency [72,74].

1.4.3.8. Presence of chemical species

The photocatalytic efficiency also depends on the presence of chemical species in the water [42]. Adding chemical oxidants, such as hydrogen peroxide, into photocatalytic system can improve the reaction rate by preventing the electron-hole pair recombination and generating more reactive oxygen species, mainly $^{\bullet}OH$ [21,43,44].

The presence of inorganic anions in water body has a significant influence on the photocatalytic degradation of pollutants [21,45]. These inorganic species, such as Cl^-, SO_4^{2-}, HCO_3^-, NO_3^-, NO_2^- and HCO_3^-, can be absorbed on the photocatalyst surface and react with holes and hydroxyl radicals reducing the number of active sites and inhibiting the photocatalytic efficiency [21,45,75]. On the other hand, they can affect solution pH leading to agglomeration of photocatalysts and decreasing the photocatalytic degradation [21].

Organic matter is widely present in natural water body, which reduces the photocatalytic efficiency for pollutant removal [21,76,77], since it competes with pollutants for the same generated reactive oxygen species [21,77]. The presence of organic matter has an influence on the adsorption process reducing the contact between pollutants and the photocatalyst surface [76,78]. Furthermore, the organic matter can also absorb the light creating an inner filter effect and reducing the amount of hole-pairs generation and the photocatalytic activity [21].

1.4.4. Photocatalytic materials

Semiconductors such as TiO_2 [21], ZnO [79], CeO_2 [80], Fe_2O_3 [54] and CdS [44] have been widely used as photocatalysts for water pollutants degradation [21,34,56]. Among these materials, TiO_2 and ZnO are highly used photocatalysts [81,82]. TiO_2, which has a bandgap between 3.0 and 3.2 eV, presents remarkable properties: low cost, high stability, and high photocatalytic efficiency to degrade multiple organic contaminants [21,34,61]. Anatase, rutile and brookite are the three main crystalline phases of TiO_2 [34,56]. The photocatalytic efficiency of each phase is different, with the anatase presenting the best photocatalytic activity [34,56]. The Evonik TiO_2-P25 with a mixed phase of anatase and rutile is the most widely used photocatalyst because it presents the better photocatalytic performance [56]. ZnO, with a similar bandgap than TiO_2 (≈3.2 eV), is another promising photocatalyst, it has low cost, and good piezoelectric and photochemical properties [54,56,79]. Moreover, the oxygen vacancies on the ZnO surface tend to produce more hydroxyl ions, improving the formation of hydroxyl radical ($^{\bullet}OH$) and having a faster response rate, enhancing the photocatalytic efficiency [79,83]. However, ZnO is less photo-stable and presents photo corrosion in aqueous solution under UV radiation [44,81]. Likewise, ZnO is also soluble in strong acids and alkalis, which limits the working pH in the solution [44].

In spite of the mentioned photocatalytic properties, these semiconductors present some drawbacks such as only being excited under UV radiation due to the wide bandgap [21,79]. Thus, it leads to a poor photocatalytic efficiency under solar radiation, since only less than 4% of this radiation corresponds to UV [34]. Additionally, the fast recombination of photogenerated electron-hole pairs reduces the photocatalytic efficiency [21,79]. Apart from these limitations, another hindrance is the recovery of the photocatalyst particles after water treatment [42,45,84]. Photocatalysts in suspension show limitations in their recovery and reuse, being time-consuming and expensive processes [42,45,84]. Furthermore, the possible secondary pollution from nanoparticles released into water bodies may cause long-term harmful effects on aquatic organisms [45,46,85].

The following section will address both setbacks, the modification of photocatalyst towards a broader wavelength absorbance under sunlight, as well as the immobilisation of photocatalysts to improve reusability, eco-friendliness, and cost-effectiveness of photocatalytic processes for water remediation.

1.5. Strategies to improve the photocatalytic process

1.5.1. Modification of photocatalysts

The enhancement of the light absorption of semiconductors under sunlight has been studied to improve photocatalytic efficiency, leading to an increasing number of publications in the last two decades (**Figure 1.4**). Many approaches have been reported to enhance their photocatalytic efficiency such as doping, semiconductor combination, surface dye sensitisation and noble metal deposition [44,54,79,84].

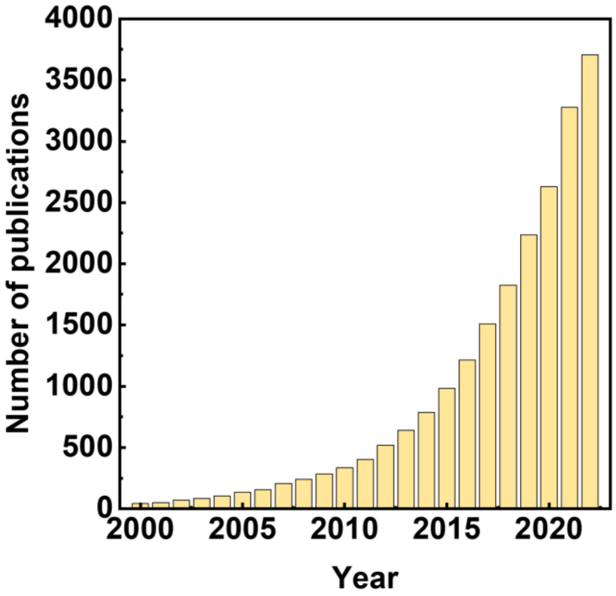

Figure 1.4. The number of scientific papers with the keywords "photocatalysis" and "sunlight". Source: Web of Science in November of 2022.

Doping is one of the most common and effective methods for improving semiconductor performance under visible light [44,54]. According to the type of dopants, doping can be divided into doping with metals (including rare earth elements) or non-metals [44,54]. Metal ion doping on the photocatalyst can narrow the band gap to improve the light absorption region from UV to visible light, which enhances the photocatalytic efficiency under sunlight [54,65]. Moreover, doping with metals can delay the recombination of photogenerated electron-hole pairs to enhance the formation of ROS, as well as the photocatalytic efficiency. [44,79]. Different metals such as silver, platinum, iron and copper have been used [54,56].

Doping with rare earth metal ions can cause semiconductor lattice distortion and impurity defects, which favours the electron-hole pair separation enhancing the photocatalytic activity [44,54]. The non-metallic dopants, namely N, C, S and F [54,84], may alter both the electronic and structural properties of semiconductors by creating oxygen-defect sites to narrow the bandgap of photocatalysts improving the photocatalytic efficiency [44,79]. Although doping can enhance the overall efficiency of photocatalyst, there are many crucial factors that should be considered, namely dopant concentration, type and number of dopants, and preparation method [44,45,65].

Combination between different semiconductors is an interesting strategy for improving the photocatalytic activity of semiconductors [44,54]. The essence of semiconductor blending to improve the photocatalytic performance is that photogenerated electrons or holes generated by a semiconductor move to the conduction or valence band of another semiconductor to separate photogenerated electrons and holes suppressing effectively the recombination of photogenerated electron-hole [44,54]. Nonetheless, the stable interfacial structures of semiconductor combinations depend on their content, the structural stability of the heterojunction and the surface properties [44].

Surface dye sensitisation is another approach, which uses photosensitizing dyes to broaden the wavelength response range of semiconductors [54]. The dye is adsorbed onto the semiconductor surface having a high surface area and forms a dye-sensitized semiconductor film [55]. The most reported photosensitizers include various organic dyes and transition metal complexes such as Ru and Pt chloride [44,54]. However, dyes can fall off from the semiconductor surface, resulting in secondary contamination of water [44,65]. Moreover, the dye may suffer from photolysis under radiation changing its structure [44,54]. On the other hand, the synthesis process of dyes could be expensive [44,54].

Noble metal deposition on the semiconductor surface is an effective way to enhance photocatalytic efficiency under sunlight radiation [44,86], which takes place the plasmonic photocatalysis [87,88]. Several plasmonic nanoparticles have been used and studied for this purpose, such as Au [89] and Ag [90]. The plasmonic resonance of such nanomaterials depends on the size, shape and type of metal [86,88], which will be discased in detail in the following section. During this thesis, this method for photocatalysts modification will be further studied and Au nanoparticles with different shapes will be used to functionalise the semiconductor surface.

1.5.1.1. Plasmonic photocatalysis

Plasmonic photocatalysis is an emerging growing field in heterogeneous catalysis to improve the photocatalytic efficiency by harvesting the visible light spectrum of sunlight for environmental and energy applications [86,91]. Compared to photocatalysis using pristine semiconductors, plasmonic photocatalysis present two important features — localised surface plasmon resonance (LSPR) and, in many cases, a Schottky junction [44,86]. As presented in **Figure 1.5**, when the noble metal and the semiconductor are in contact, the equilibration of Fermi levels of metal and semiconductor causes the bending of the conduction band of semiconductor at the interface to form the Schottoky barrier [87,88], which improves the separation of photogenerated electrons and holes therefore favouring the photocatalytic activity [44,86]. The most prominent feature of noble metals is their LSPR, which contributes to the strong absorption of visible light and the excitation of active charge carriers (hot electrons), as shown in **Figure 1.5** [84,86].

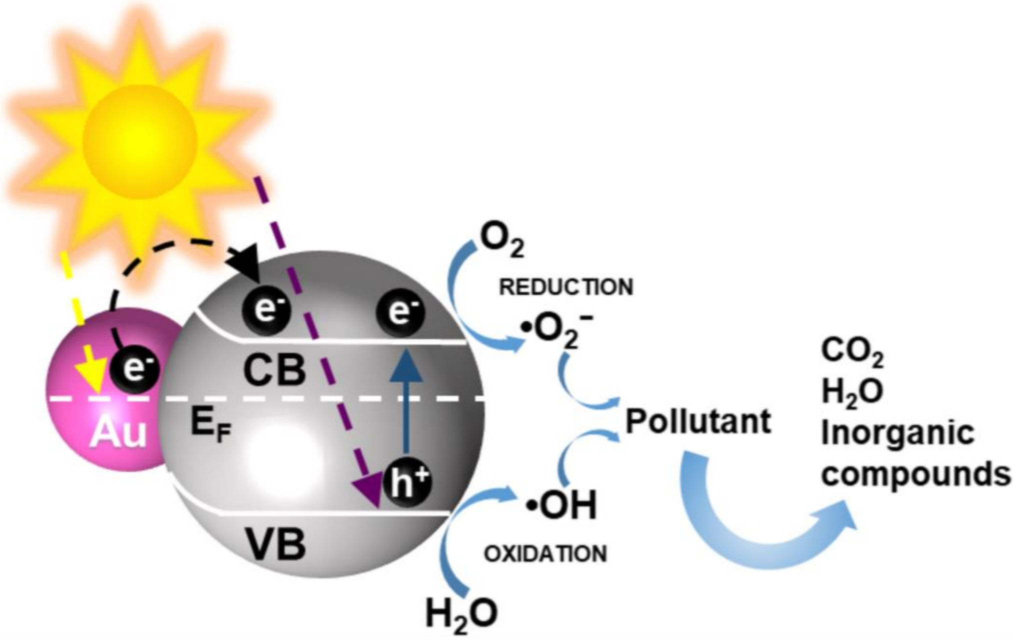

Figure 1.5. Principle of the plasnomic photocatalytic mechanism. Here Au used as an example of metal nanoparticles dispersed on the semiconductor surface [91].

The term "plasmonic" in plasmonic photocatalysis refers to the LSPR that takes places in the confined space of a nanoparticle and the induced effects [86,88]. The plasmon is considered a mechanical oscillation of the electron gas of a metal resulting from an external oscillating electric field [92]. Under this circumstance, surface plasmons can be described as coherent oscillations of delocalised electrons in a metal particle which are excited by the electromagnetic field of incident light at a metal-dielectric interface [88,92]. LSPR is created when surface plasmon is excited at the surface of a metallic nanoparticle with a size comparable to the wavelength of the incident light, the free electrons are confined, creating oscillating dipoles [88,92], as presented in **Figure 1.6**.

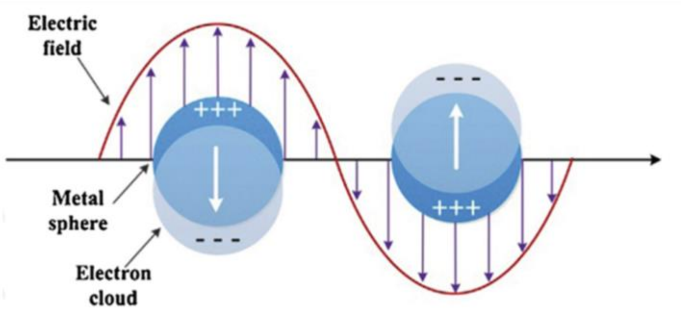

Figure 1.6. Illustration of the excitation of localised surface plasmon resonance in spherical metal particle. Adapted from [92].

Furthermore, the resonance frequency of the plasmon oscillation depends on the nanoparticle material, the dielectric constant of the external media, size, and shape of the nanoparticle. An increase in the size of metal particles, for instance, can produce a redshift of the dipolar plasmonic peak in the absorption spectrum [88,93], as shown in **Figure 1.7**.

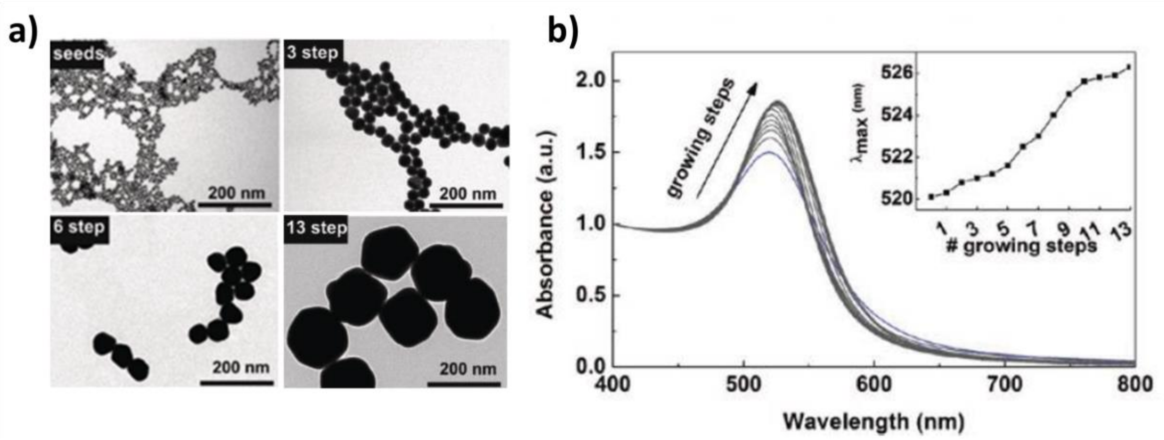

Figure 1.7. Transmission electron microscopy images of Au seed particles and those obtained after different growth steps. The particle size increases from 13.5 ± 2.1 to 19.2 ± 2.6, 24.8 ± 3.4, and 30.5 ± 3.9 nm after 3, 6, and 13 growth steps, respectively (a). Absorption spectra of spherical gold nanoparticles with different size obtained after different growth steps, normalized at 400 nm to facilitate comparison (b). Adapted from [94].

Apart from the size, the shape of the metal nanoparticles is an important factor that highly influences the LSPR resonance frequencies [87,93]. The change in shape can affect the frequency, and appearance of different dipolar and higher polar order plasmon modes, absorption to scattering relative ratios, and magnitude of the generated local electric fields close to the surface [93]. Moreover, charges tend to concentrate in corners and tips in anisotropic nanoparticles, also known as lightning rod effect, generating an enhanced local electromagnetic field [88,93,95]. For example, particles with nanorod morphology have two peaks, one corresponding to the transverse plasmon dipolar mode and the other corresponding to the longitudinal plasmon dipolar mode, as a consequence of the change in polarizability (**Figure 1.8**) [92,96]. Nanostar is another interesting morphology of anisotropic nanoparticles. Its plasmon resonances result from the hybridization of plasmons associated with the core and the individual tips of the particle [97,98], as shown in **Figure 1.9**.

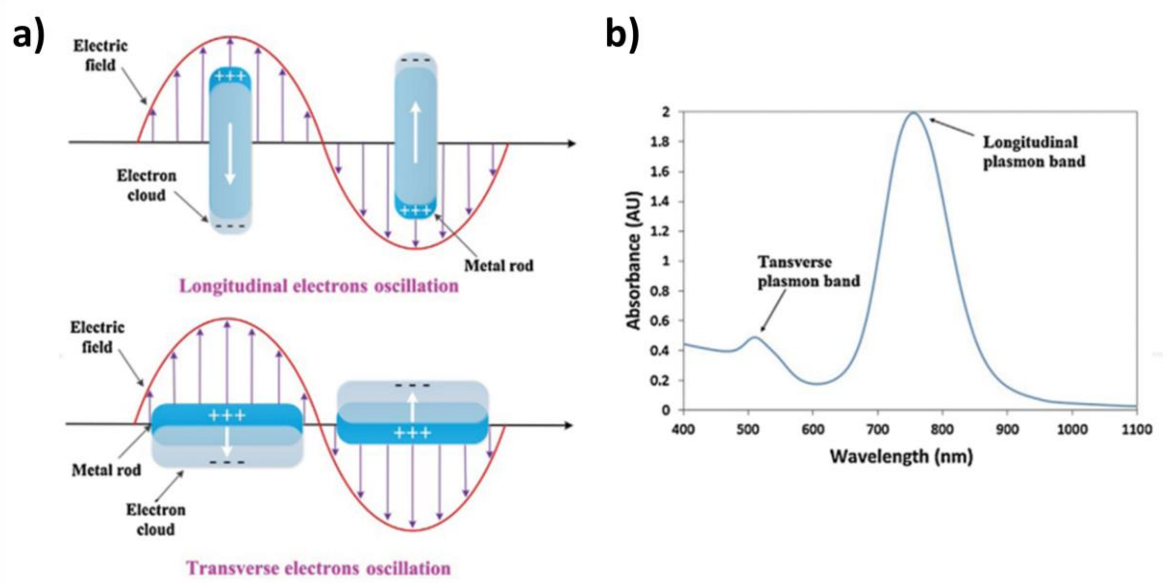

Figure 1.8. Illustration of the excitation of localised surface plasmon resonance in nanorod metal particle at longitudinal and transverse plasmon bands (a). Absorption spectra of nanorod (b). Adapted from [92].

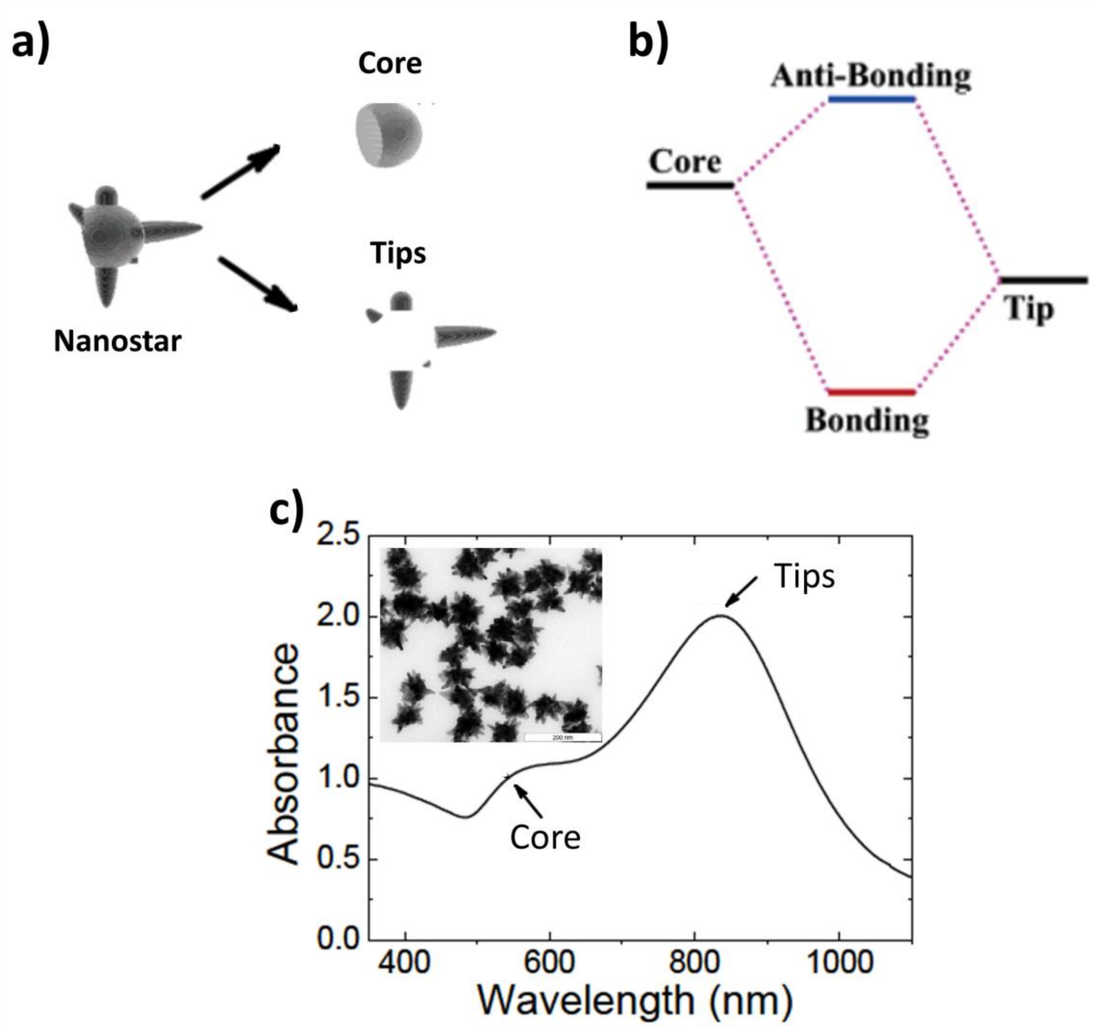

Figure 1.9. Structure of Au nanostar (a) and illustration of plasmon hybridization in the nanostar (b). Adapted from [97]. Absorption spectra of nanostar (c) with transmission electron microscopy image of Au nanostar with core diameters of 49.72 ± 0.10 nm and tip length of 19.44 ± 0.35 nm (inset). Adapted from [99].

1.5.2. Immobilisation of photocatalysts

As previously mentioned, another drawback of photocatalytic suspended systems lies on the recovery of the suspended nanoparticles from the treated water [42,45,84], which is also a critical obstacle towards applications in industrial scale [45]. Additionally, this difficulty is associated with secondary pollution from the nanoparticles [85,100], the loss of photocatalyst [45,84], increasing the overall cost of the treatment [45,84]. Thus, the immobilisation of photocatalysts is the right path to endow a photocatalytic system with reusability and to prevent the discharge of suspended photocatalyst in the treated effluents.

A literature review for “suspended photocatalysis” and “immobilised photocatalysis” (**Figure 1.10**) presents that the immobilised photocatalytic system has gained increasing attention during the recent two decades, being continuously increased from 2000 to 2022. In contrast, the number of publications on “suspended photocatalysis” increases slowly and tends to be stable.

An efficient immobilisation of photocatalysts requires many critical conditions [45]. For instance, the support should allow a durable adherence to the photocatalyst, high specific surface area, high adsorption and affinity to the pollutants, and the catalytic properties of the catalyst should not be negatively affected by the immobilisation process [45,84,101]. Moreover, there are limitations in immobilisation, such as the mass transfer limitation, reduction of light-harvesting, loss of surface area and available active sites and photocatalyst agglomeration in the support materials, resulting in a lower photocatalytic efficiency compared with photocatalysis in suspension [84,101].

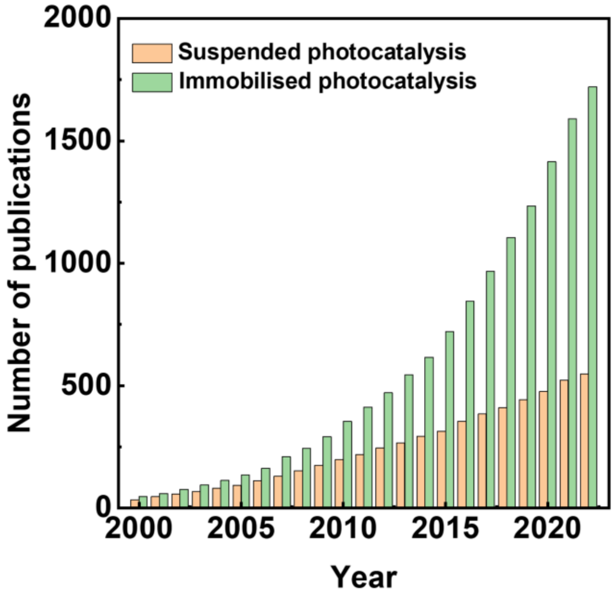

Figure 1.10. The number of scientific papers with the keywords "suspended photocatalysis" vs. "immobilised photocatalysis". Source: Web of Science in November of 2022.

Over the last few decades, significant advances were made in the scope of immobilised photocatalysts at lab scale, while the application of this technology for real water/waste water treatment still need be more studies [45,55,56]. Many efforts have been made to select appropriate supports for photocatalysts immobilisation [45,84]. Various types of opaque and transparent support materials have been studied, such as glass [102,103], activated carbon [104,105], stainless steel [106,107] and polymers [79,108]. Furthermore, many immobilisation techniques, namely chemical vapour deposition (CVD), dip coating, sol-gel, and electrospinning were developed to achieve photocatalyst immobilisation [55,109]. For instance, gas-phase methods (e.g., CVD) are typically used for the catalyst deposition on glass and metals substrates, while liquid phase methods (e.g., dip coating) are usually used for deposition onto polymeric and heat sensitive substrates [110]. The liquid phase methods require simple equipment and mild conditions [110]. Additionally, electrospinning seems to be an effective and suitable immobilisation method since it is a simple and low-cost approach used to produce fibres with thinner diameter (from nanometre to micrometre) and a larger surface area [55,111,112].

Despite the many materials and techniques tested, the optimal immobilisation of photocatalytic nanoparticles remains a challenge. Many of the mentioned supports lack the conditions required for photocatalytic applications, such as adequate adhesion of the nanoparticles to the substrate and catalyst reactivity after its attachment [101,113]. Among all the materials, the attention seems to be growing towards polymers [79,101]. Many synthetic polymers have been tested as photocatalyst support [79,101], for example, polyester [114], poly(methyl methacrylate) (PMMA) [115] and poly(vinylidene fluoride) (PVDF) [116]. Their growing interest lies on their properties as chemically inert, inexpensive, flexible, mechanically stable and durable materials, which matches the conditions of an ideal support material [79,101].

1.5.2.1. Poly(vinylidene fluoride) and its copolymers

In particular, poly(vinylidene fluoride) (PVDF) and its copolymers have attracted interest due to their chemical resistance and good mechanical properties. Moreover, their good UV radiation resistance, because of the C-F bonds of the polymer chain, makes them suitable for photocatalytic applications [108,117].

PVDF is a semi-crystalline fluoropolymer with the repeating unit ($-CH_2CF_2-$) [117,118]. Many of the interesting properties of PVDF are related to the strong electrical dipole moment of the PVDF monomer unit ($5\text{-}8 \times 10^{-30}$ Cm), due to the electronegativity of fluorine atoms [119]. PVDF shows a complex structure and possesses five crystalline phases, corresponding to different chain conformations [119,120]. Among them the three most investigated PVDF phases, as shown in **Figure 1.11**, are TTT (all trans planar zigzag) for the β phase, TGTG′ (trans-gauche-trans-gauche) for the α phases and T_3GT_3G' for the γ phase [119,120]. The β phase presents the highest dipolar moment per unit cell (8×10^{-30} C m) [119]. Several co-polymers of PVDF such as Poly(vinylidene fluoride-Trifluoroethylene) (PVDF-TrFE), Poly(vinylidene fluoride-*co*-chlorotrifluoroethylene) (PVDF-CTFE) and Poly(vinylidene fluoride-co-hexafluoropropene) (PVDF-HFP) have been developed to enhance certain properties and adjust them to the increasing technological demands [119,121].

PVDF-HFP is one of the most common PVDF copolymers, which can be synthesised by polymerization of VDF (vinylidene fluoride) and amorphous phase of HFP (hexafluoropropylene) [119,122], as presented in **Figure 1.12.** Compared to pure PVDF, PVDF-HFP presents a lower crystallinity degree because of the bulky CF_3 groups having a negative effect on obtaining high piezoelectricity [122]. However, its flexibility is increased greatly compared to pure PVDF [122,123]. Moreover, the increase in fluorine content from HFP group makes it more hydrophobic than pure PVDF [122,124]. This copolymer has been mainly studied as an electrolyte material for lithium batteries [119,123]. Furthermore, PVDF-HFP can be produced in various structure/morphology through different processing technologies [85,120,125]. The simple and well-studied processability of PVDF-HFP opens the perspective to shape it as a membrane with controlled porous structures [24,125]. Thus, PVDF-HFP has been widely used in water remediation as a support material for the removal of heavy metals [100,125–127], organic matter [128,129] and contaminants of emerging concern [24,85,100] among others. During this thesis, PVDF-HFP will be used as substrate to immobilise the photocatalysts.

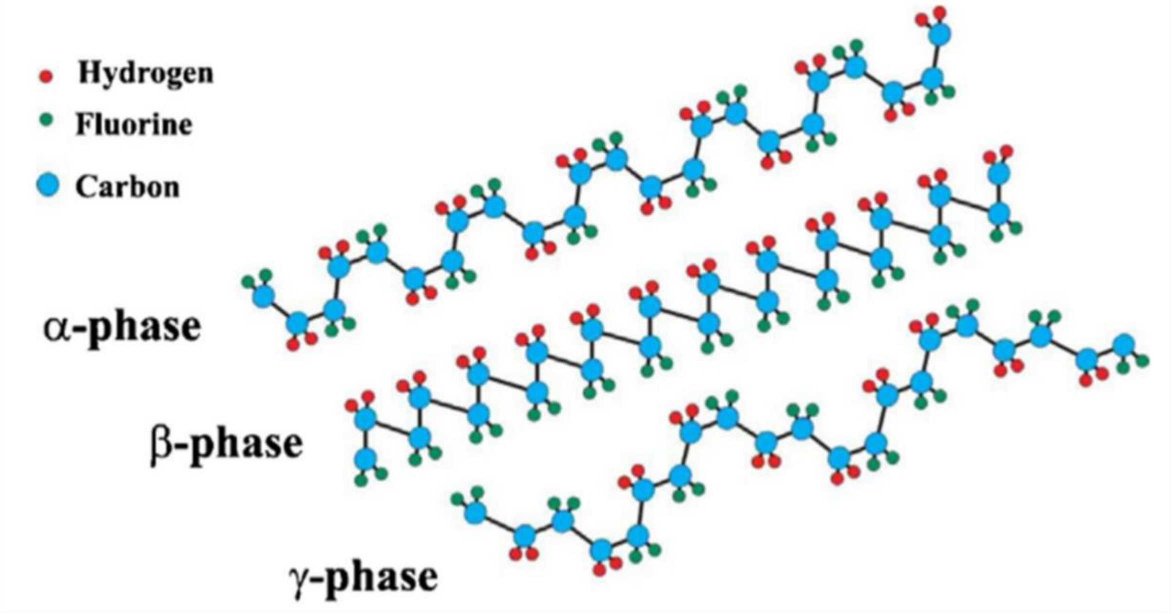

Figure 1.11. A schematic representation of the chain conformation of α, β, and γ-phases of PVDF. Adapted from [119].

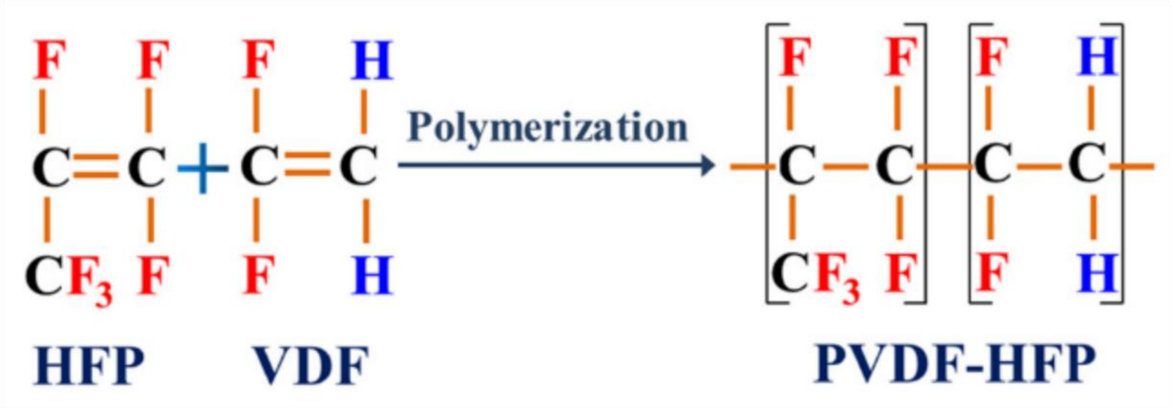

Figure 1.12. Polymerization of PVDF-HFP. Adapted from [122].

On the other hand, it is important to emphasise that when using polymeric membranes, the photocatalytic reaction can take place, not only at the surface of the membrane but also in the inside pores [18,46,85,130]. There is, however, always the risk of problems such as the deterioration of the membrane structure, low photocatalytic activity and the loss of the attached photocatalysts over time/use [46,130].

Numerous processing techniques have been proposed and employed for production of PVDF-HFP membranes with porous structures. This thesis will focus on Non-solvent-Induced Phase Separation (NIPS), Temperature-Induced Phase Separation (TIPS) methods, and salt leaching methods [120]. NIPS is one of the most commonly used to prepare asymmetric porous membranes because of its simplicity [120,131]. In this approach, the polymer solution is cast on a suitable support and then immersed in a coagulation bath containing a non-solvent. The exchange of the solvent in the polymer solution with the non-solvent in the coagulation bath results in the phase separation and formation of pores [117,120]. It should be noted that the processing conditions such as polymer concentration, solvent and non-solvent type can affect the morphology of the film leading to different degrees of porosity and pore sizes of films [117,120].

Apart from NIPS, porous membrane can be produced through TIPS method [120]. A homogeneous polymer solution is cast into the desired shapes on a suitable support and dried to eliminate the solvent [120]. The temperature during the solvent dry process affects the rate of evaporation and phase separation, which determines the degree of porosity and pore size of the membrane [117]. For instance, rapid evaporation of the solvent may cause a less porous structure and slow evaporation leads to a small pore size distribution in the membranes [120]. Furthermore, TIPS can produce membranes with high mechanical strength and narrow pore size distribution [120].

On the other hand, the addition of sacrificial material such as NaCl particles in the polymer solution can affect the final morphology of the membrane [120]. After the elimination of solvent in the membrane [117], the NaCl can be washed and eliminated easily by water to form additional pores in the membrane [120,132]. The size and amount of these additional pores depend on the size and content of NaCl particles [120].

1.6. General objectives and outline of the thesis

Considering the previously mentioned limitation of applying photocatalysis for pharmaceuticals degradation in water remediation, the main objective of this thesis is to produce, characterise and test photocatalytic nanoparticles and nanocomposites to enhance photocatalytic efficiency under sunlight radiation and enable reuse/recycling the photocatalysts by immobilisation technique.

Thus, several specific objectives of this work are detailed as follows:

- Systematic studies correlate the interaction between pollutants and photocatalysts and the generation of ROS with photocatalytic performance
- Development of Au functionalised plasmonic photocatalysts enhancing the photocatalytic performance
- Optimisation and study of the influence of synthesis conditions of novel TiO_2:Au-NSs hybrid nanoparticles improving the photocatalytic performance
- Study of the possibility to incorporate the synthesised nanoparticles into PVDF-HFP polymer matrix for photocatalytic applications
- Study of the influence of the different morphologies of the PVDF-HFP polymer matrix and the incorporated photocatalysts´ load on photocatalytic performance
- Study of the reusability of the photocatalytic membranes and their suitability in a real treated effluent water matrix for pollutant degradation

As the core subject of this thesis is to develop and study the photocatalytic materials for water treatment to degrade pharmaceuticals, the thesis has been divided into five chapters taking into account the previously mentioned objectives.

Chapter 1 concerns the presence and impact of pharmaceuticals on the environment and the importance of their removal from water bodies. Then, a general overview of photocatalysis as a promising technology for pollutant degradation, in particular, its mechanism, kinetics, operational parameters, limitations and strategies for enhanced efficiency are presented. It is to notice that the specific state of the art on the different issues related to the present work are provided in all the chapters. The main objectives and the structure of the thesis are described in this chapter.

Chapter 2 comprises the synthesis and characterisation of two common photocatalysts, TiO_2 and ZnO, for the degradation of different pharmaceuticals in a suspended photocatalytic system under UV radiation. The obtained results by both photocatalysts are compared and analysed considering the physicochemical properties of pollutants and photocatalysts. This chapter also introduces the production of plasmonic photocatalysts (TiO_2:Au and ZnO:Au) by functionalising TiO_2 and ZnO with spherical Au nanoparticles to enhance photocatalytic efficiency under visible light.

Chapter 3 is focused on the improvement of photocatalytic efficiency of TiO_2:Au-based plasmonic photocatalyst by means of expanding the absorption wavelength under sunlight. This chapter is dedicated to the synthesis and characterisation of novel nanoparticles, TiO_2:Au-NSs, modifying the shape of Au nanoparticles on the TiO_2 surface, from spherical to branched morphology (nanostar). The increase of Au nanostar size influence on the photocatalytic degradation of ciprofloxacin, under UV, visible and different wavelength radiation is assessed. Finally, the possibility to incorporate these hybrid nanoparticles into PVDF-HFP polymer matrix for photocatalytic application is also studied.

Chapter 4 shows the immobilisation of the hybrid nanoparticles, TiO_2:Au-NSs, in PVDF-HFP polymer matrix by two different technologies, doctor blade and salt leaching, to obtain porous membranes with two different morphologies. The influence of the membrane morphology on photocatalytic performance is assessed by ciprofloxacin degradation in an immobilised photocatalytic system under UV and visible radiation. Furthermore, the reusability of the membranes is also tested. The suitability of these membranes for ciprofloxacin degradation in the real treated effluent water matrix was finally assessed.

Finally, **Chapter 5** presents the main results, conclusions and suggestions for future work.

1.7. References

1. Nations, U. Sustainable Development Goals. Available online: https://www.undp.org/content/undp/en/home/sustainable-development-goals.html (accessed on 24 October 2022).
2. *Progress on Household Drinking Water, Sanitation and Hygiene 2000-2020: Five Years into the SDGs. Geneva: World Health Organization (WHO) and the United Nations Children's Fund (UNICEF)*; 2021; ISBN 9789240030848. Available online: https://data.unicef.org/resources/progress-on-household-drinking-water-sanitation-and-hygiene-2000-2020/ (accessed on 24 October 2022).
3. Dey, S.; Bano, F.; Malik, A. Pharmaceuticals and Personal Care Product (PPCP) Contamination—a Global Discharge Inventory. In *Pharmaceuticals and Personal Care Products: Waste Management and Treatment Technology*; Elsevier Inc., 2019; pp. 1–26 ISBN 9780128161890, doi:10.1016/B978-0-12-816189-0.00001-9.
4. Wang, D.; Hubacek, K.; Shan, Y.; Gerbens-leenes, W.; Liu, J. A Review of Water Stress and Water Footprint Accounting. *Water* **2021**, *13*, 201, doi:10.3390/w13020201.
5. Panchamoorthy, K.; Vikas, N.; Krishnan, A.; Malolan, R.; Rangarajan, G. Present Applications of Titanium Dioxide for the Photocatalytic Removal of Pollutants from Water: A Review. *J. Environ. Manage.* **2020**, *270*, 110906, doi:10.1016/j.jenvman.2020.110906.
6. *WHO, UNICEF, World Bank. State of the World ' s Drinking Water. Geneva: World Health Organization.*; 2022; ISBN 9789240060807. Available online: https://cdn.who.int/media/docs/default-source/wash-documents/water-safety-and-quality/state-of-drinking-water-report-web.2_v-lowres.pdf?sfvrsn=e2479151_3 (accessed on 24 October 2022).
7. Pooja, D.; Kumar, P.; Singh, P.; Patil, S. *Sensors in Water Pollutants Monitoring: Role of Material*; Springer Singapore, 2020; ISBN 9789811506703, doi: 10.1007/978-981-15-0671-0.
8. *DIRECTIVE (EU) 2020/2184 OF THE EUROPEAN PARLIAMENT AND OF THE COUNCIL of 16 December 2020 on the Quality of Water Intended for Human Consumption (Recast)*; 2020. Available online: https://eur-lex.europa.eu/legal-

content/EN/TXT/PDF/?uri=CELEX:32020L2184&from=EN (accessed on 24 October 2022).

9. Cuerda-correa, E.M.; Alexandre-franco, M.F.; Fern, C. Antibiotics from Water. An Overview. *Water* **2020**, *12*, 102, doi:10.3390/w12010102.

10. Tang, Y.; Yin, M.; Yang, W.; Li, H.; Zhong, Y.; Mo, L.; Liang, Y.; Ma, X.; Sun, X. Emerging Pollutants in Water Environment: Occurrence, Monitoring, Fate, and Risk Assessment. *Water Environ. Res.* **2019**, *91*, 984–991, doi:10.1002/wer.1163.

11. Vasilachi, I.C.; Asiminicesei, D.M.; Fertu, D.I.; Gavrilescu, M. Occurrence and Fate of Emerging Pollutants in Water Environment and Options for Their Removal. *Water* **2021**, *13*, 181, doi:10.3390/w13020181.

12. Gomez Cortes, L.; Marinov, D.; Sanseverino, I.; Navarro Cuenca, A., Niegowska, M.; Porcel Rodriguez, E., Stefanelli, F.; Lettieri, T. *Selection of Substances for the 4 Th Watch List under the Water Framework Directive*; 2022; ISBN 9789276550211, doi:10.2760/01939.

13. Bracamontes-Ruelas, A.R.; Ordaz-Díaz, L.A.; Bailón-Salas, A.M.; Ríos-Saucedo, J.C.; Reyes-Vidal, Y.; Reynoso-Cuevas, L. Emerging Pollutants in Wastewater, Advanced Oxidation Processes as an Alternative Treatment and Perspectives. *Process* **2022**, *10*, 1041, doi:10.3390/pr10051041.

14. Reyes, N.J.D.G.; Geronimo, F.K.F.; Yano, K.A. V.; Guerra, H.B.; Kim, L.-H. Pharmaceutical and Personal Care Products in Different Matrices: Occurrence, Pathways, and Treatment Processes. *Water* **2021**, *13*, 1159, doi:10.3390/ w13091159.

15. Bavumiragira, J.P.; Ge, J.; Yin, H. Fate and Transport of Pharmaceuticals in Water Systems: A Processes Review. *Sci. Total Environ.* **2022**, *823*, 153635, doi:10.1016/j.scitotenv.2022.153635.

16. Ortúzar, M.; Esterhuizen, M.; Olicón-hernández, D.R. Pharmaceutical Pollution in Aquatic Environments: A Concise Review of Environmental Impacts and Bioremediation Systems. *Front. Microbiol.* **2022**, *13,* 869332, doi:10.3389/fmicb.2022.869332.

17. Li, W.C. Occurrence, Sources, and Fate of Pharmaceuticals in Aquatic Environment and Soil. *Environ. Pollut. J.* **2014**, *187*, 193–201, doi:10.1016/j.envpol.2014.01.015.

18. Martins, P.M.; Ribeiro, J.M.; Teixeira, S.; Petrovykh, D.Y.; Cuniberti, G.; Pereira, L.; Lanceros-Méndez, S. Photocatalytic Microporous Membrane against the Increasing Problem of Water Emerging Pollutants. *Materials (Basel).* **2019**, *12*, 1649, doi:10.3390/ma12101649.

19. Kaya, S.I.; Gumus, E.; Cetinkaya, A.; Zor, E.; Ozkan, S.A. Trends in On-Site Removal, Treatment, and Sensitive Assay of Common Pharmaceuticals in Surface Waters. *Trends Anal. Chem.* **2022**, *149*, 116556, doi:10.1016/j.trac.2022.116556.

20. Eniola, J.O.; Kumar, R.; Barakat, M.A.; Rashid, J. A Review on Conventional and Advanced Hybrid Technologies for Pharmaceutical Wastewater Treatment. *J. Clean. Prod.* **2022**, *356*, 131826, doi:10.1016/j.jclepro.2022.131826.

21. Anastasiya Kutuzova, Tetiana Dontsova, W.K. Application of TiO_2-Based Photocatalysts to Antibiotics Degradation: Cases of Sulfamethoxazole, Trimethoprim and Ciprofloxacin. *Catalysts* **2021**, *11*, 728, doi:10.3390/catal11060728.

22. Vernouillet, G.; Eullaffroy, P.; Lajeunesse, A.; Blaise, C.; Gagné, F.; Juneau, P. Toxic Effects and Bioaccumulation of Carbamazepine Evaluated by Biomarkers Measured in Organisms of Different Trophic Levels. *Chemosphere* **2010**, *80*, 1062–1068, doi:10.1016/j.chemosphere.2010.05.010.

23. Vannini, C.; Domingo, G.; Marsoni, M.; Mattia, F. De; Labra, M.; Castiglioni, S.; Bracale, M. Effects of a Complex Mixture of Therapeutic Drugs on Unicellular Algae Pseudokirchneriella Subcapitata. *Aquat. Toxicol.* **2011**, *101*, 459–465, doi:10.1016/j.aquatox.2010.10.011.

24. Aoudjit, L.; Salazar, H.; Zioui, D.; Sebti, A.; Martins, P.M.; Lanceros-Mendez, S. Reusable Ag@TiO_2-Based Photocatalytic Nanocomposite Membranes for Solar Degradation of Contaminants of Emerging Concern. *Polymer (Guildf).* **2021**, *13*, 3718, doi:10.3390/polym13213718.

25. Maszkowska, J.; Stolte, S.; Kumirska, J.; Paulina, Ł.; Mioduszewska, K.; Puckowski, A.; Caban, M.; Wagil, M.; Stepnowski, P.; Białk-Bielińska, A. Beta-Blockers in the Environment: Part I. Mobility and Hydrolysis Study. *Sci. Total Environ.* **2014**, *493*, 1112–1121, doi:10.1016/j.scitotenv.2014.06.023.

26. Ebrahimi, M.; Akhavan, O. Nanomaterials for Photocatalytic Degradations of Analgesic, Mucolytic and Anti-Biotic/Viral/Inflammatory Drugs Widely Used in Controlling SARS-CoV-2. *Catalysts* **2022**, *12*, 667, doi:10.3390/catal12060667.

27. Domingo-Echaburu, S.; Irazola, M.; Prieto, A.; Rocano, B.; Torre-Querejazu, A.L. De; Quintana, A. Science of the Total Environment Drugs Used during the COVID-19 First Wave in Vitoria-Gasteiz (Spain) and Their Presence in the Environment. *Sci. Total Environ.* **2022**, *820*, 153122, doi:10.1016/j.scitotenv.2022.153122.

28. Kanakaraju, D.; Glass, B.D.; Oelgem, M. Advanced Oxidation Process-Mediated Removal of Pharmaceuticals from Water: A Review. *J. Environ. Manage.* **2018**, *219*, 189–207, doi:10.1016/j.jenvman.2018.04.103.

29. Priyadarshini, M.; Das, I.; Ghangrekar, M.M.; Blaney, L. Advanced Oxidation Processes: Performance, Advantages, and Scale-up of Emerging Technologies. *J. Environ. Manage.* **2022**, *316*, 115295, doi:10.1016/j.jenvman.2022.115295.

30. Rivera-Utrilla, J.; Sánchez-Polo, M.; Ferro-García, M.Á.; Prados-Joya, G.; Ocampo-Pérez, R. Pharmaceuticals as Emerging Contaminants and Their Removal from Water. A Review. *Chemosphere* **2013**, *93*, 1268–1287, doi:10.1016/j.chemosphere.2013.07.059.

31. Mansouri, F.; Chouchene, K.; Roche, N.; Ksibi, M. Removal of Pharmaceuticals from Water by Adsorption and Advanced Oxidation Processes: State of the Art and Trends. *Appl. Sci.* **2021**, *11*, 6659, doi:10.3390/app11146659.

32. Homem, V.; Santos, L. Degradation and Removal Methods of Antibiotics from Aqueous Matrices - A Review. *J. Environ. Manage.* **2011**, *92*, 2304–2347, doi:10.1016/j.jenvman.2011.05.023.

33. Zhang, Y.; Zhao, Y.; Maqbool, F.; Hu, Y. Removal of Antibiotics Pollutants in Wastewater by UV-Based Advanced Oxidation Processes: Influence of Water Matrix Components, Processes Optimization and Application : A Review. *J. Water Process Eng.* **2022**, *45*, 102496, doi:10.1016/j.jwpe.2021.102496.

34. Byrne, C.; Subramanian, G.; Pillai, S.C. Recent Advances in Photocatalysis for Environmental Applications. *J. Environ. Chem. Eng.* **2018**, *6*, 3531–3555, doi:10.1016/j.jece.2017.07.080.

35. Davis, M.E.; Davis, R.J. *Fundamentals of Chemical Reaction Engineering*; McGraw-Hill, 2003; ISBN 0-07-119260-3. Available online: https://authors.library.caltech.edu/25070/1/FundChemReaxEng.pdf (accessed on 1st November 2022).

36. Coronado, J.M.; Fresno, F.; Hernández-Alonso, M.D.; Portela, R. *Design of Advanced Photocatalytic Materials for Energy and Environmental Applications*; Springer, 2013; ISBN 9781447150602, doi:10.1007/978-1-4471-5061-9.

37. Fujishima, A.; Honda, K. Electrochemical Photolysis of Water at a Semiconductor Electrode. *Nature* **1972**, *238*, 38–40, doi:10.1038/238038a0.

38. Frank, S.N.; Bard, A.J. Heterogeneous Photocatalytic Oxidation of Cyanide and Sulfite in Aqueous Solutions at Semiconductor Powders. *J. Phys. Chem.* **1977**, *81*, 1484–1488, doi:10.1021/j100530a011.

39. Hashimoto, K.; Irie, H.; Fujishima, A. TiO_2 Photocatalysis: A Historical Overview and Future Prospects. *Jpn. J. Appl. Phys.* **2005**, *44*, 8269–8285, doi:10.1143/JJAP.44.8269.

40. Hosseini, S.N.; Borghei, S.M.; Vossoughi, M.; Taghavinia, N. Immobilization of TiO_2 on Perlite Granules for Photocatalytic Degradation of Phenol. *Appl. Catal. B Environ.* **2007**, *74*, 53–62, doi:10.1016/j.apcatb.2006.12.015.

41. Byrne, C.; Subramanian, G.; Pillai, S.C. Recent Advances in Photocatalysis for Environmental Applications. *J. Environ. Chem. Eng.* **2018**, *6*, 3531–3555, doi:10.1016/j.jece.2017.07.080.

42. Ahmed, S.N.; Haider, W. Heterogeneous Photocatalysis and Its Potential Applications in Water and Wastewater Treatment: A Review. *Nanotechnology* **2018**, *29*, 342001, doi:10.1088/1361-6528/aac6ea.

43. Akerdi, A.G.; Bahrami, S.H. Application of Heterogeneous Nano-Semiconductors for Photocatalytic Advanced Oxidation of Organic Compounds: A Review. *J. Environ. Chem. Eng.* **2019**, *7*, 103283, doi:10.1016/j.jece.2019.103283.

44. Belver, C.; Bedia, J.; Gómez-Avilés, A.; Manuel Peñas-Garzón; Rodriguez, J.J. Chapter 22. Semiconductor Photocatalysis for Water Purification. In *Nanoscale Materials in Water Purification*; 2019; pp. 581–651 ISBN 9780128139264, doi:10.1016/B978-0-12-813926-4.00028-8.

45. Ahmad, R.; Ahmad, Z.; Ullah, A.; Riaz, N.; Aslam, M.; Kim, J. Photocatalytic Systems as an Advanced Environmental Remediation: Recent Developments, Limitations and New Avenues for Applications. *J. Environ. Chem. Eng.* **2016**, *4*, 4143–4164, doi:10.1016/j.jece.2016.09.009.

46. Chong, M.N.; Jin, B.; Chow, C.W.K.; Saint, C. Recent Developments in Photocatalytic Water Treatment Technology: A Review. *Water Res.* **2010**, *44*, 2997–3027, doi:10.1016/j.watres.2010.02.039.

47. Ateia, M.; Alalm, M.G.; Awfa, D.; Johnson, M.S.; Yoshimura, C. Modeling the Degradation and Disinfection of Water Pollutants by Photocatalysts and Composites: A Critical Review. *Sci. Total Environ.* **2020**, *698*, 134197, doi:10.1016/j.scitotenv.2019.134197.

48. Valencia, S.; Cataño, F.; Rios, L.; Restrepo, G.; Marín, J. A New Kinetic Model for Heterogeneous Photocatalysis with Titanium Dioxide: Case of Non-Specific Adsorption Considering Back Reaction. *Appl. Catal. B Environ.* **2011**, *104*, 300–304, doi:10.1016/j.apcatb.2011.03.015.

49. Herrmann, J.-M. Heterogeneous Photocatalysis: Fundamentals and Applications to the Removal of Various Types of Aqueous Pollutants. *Catal. Today* **1999**, *53*, 115–129, doi:10.1016/S0920-5861(99)00107-8.

50. Li, Y.; Sun, S.; Ma, M.; Ouyang, Y.; Yan, W. Kinetic Study and Model of the Photocatalytic Degradation of Rhodamine B (RhB) by a TiO_2-Coated Activated Carbon Catalyst: Effects of Initial RhB Content, Light Intensity and TiO_2 Content in the Catalyst. *Chem. Eng. J.* **2008**, *142*, 147–155, doi:10.1016/j.cej.2008.01.009.

51. Mozia, S. Photocatalytic Membrane Reactors (PMRs) in Water and Wastewater Treatment. A Review. *Sep. Purif. Technol.* **2010**, *73*, 71–91, doi:10.1016/j.seppur.2010.03.021.

52. Lin, H.; Valsaraj, K.T. Development of an Optical Fiber Monolith Reactor for Photocatalytic Wastewater Treatment. *J. Appl. Electrochem.* **2005**, *35*, 699–708, doi:10.1007/s10800-005-1364-x.

53. Lazar, M.A.; Varghese, S.; Nair, S.S. Photocatalytic Water Treatment by Titanium Dioxide: Recent Updates. *Catalysts* **2012**, *2*, 572–601, doi:10.3390/catal2040572.

54. Zhang, F.; Wang, X.; Liu, H.; Liu, C.; Wan, Y.; Long, Y.; Cai, Z. Recent Advances and Applications of Semiconductor Photocatalytic Technology. *Appl. Sci.* **2019**, *9*, 2489, doi:10.3390/app9122489.

55. Akerdi, A.G.; Bahrami, S.H. Application of Heterogeneous Nano-Semiconductors for Photocatalytic Advanced Oxidation of Organic Compounds: A Review. *J. Environ. Chem. Eng.* **2019**, *7*, 103283, doi:10.1016/j.jece.2019.103283.

56. Koe, W.S.; Lee, J.W.; Chong, W.C.; Pang, Y.L.; Sim, L.C. An Overview of Photocatalytic Degradation: Photocatalysts, Mechanisms, and Development of Photocatalytic Membrane. *Environ. Sci. Pollut. Res.* **2020**, *27*, 2522–2565, doi:10.1007/s11356-019-07193-5.

57. Rizzo, L.; Meric, S.; Kassinos, D.; Guida, M.; Russo, F.; Belgiorno, V. Degradation of Diclofenac by TiO_2 Photocatalysis: UV Absorbance Kinetics and Process Evaluation through a Set of Toxicity Bioassays. *Water Res.* **2009**, *43*, 979–988, doi:10.1016/j.watres.2008.11.040.

58. Martins, P.M.; Miranda, R.; Marques, J.; Tavares, C.J.; Botelhob, G.; Lanceros-Mendez, S. Comparative Efficiency of TiO_2 Nanoparticles in Suspension vs. Immobilization into P(VDF–TrFE) Porous Membranes. *RSC Adv.* **2016**, *6*, 12708–12716, doi:10.1039/c5ra25385c.

59. Zyoud, A.H.; Zubi, A.; Hejjawi, S.; Zyoud, S.H.; Helal, M.H.; Zyoud, S.H.; Qamhieh, N.; Hajamohideen, A.; Hilal, H.S. Removal of Acetaminophen from Water by Simulated Solar Light Photodegradation with ZnO and TiO_2 Nanoparticles: Catalytic Efficiency Assessment for Future Prospects. *J. Environ. Chem. Eng.* **2020**, *8*, 104038, doi:10.1016/j.jece.2020.104038.

60. Tanveer, M.; Tezcanli, G.; Sadiq, M.T.; Kazmi, S.M.; Noshad, N.; Abbas, G.; Ali, A. Degradation of Diclofenac under Irradiation of UV Lamp and Solar Light Using ZnO Photo Catalyst. *Eng. Proc.* **2021**, *12*, 76, doi:10.3390/engproc2021012076.

61. Martins, P.; Kappert, S.; Le, H.N.; Sebastian, V.; Kühn, K.; Alves, M.; Pereira, L.; Cuniberti, G.; Melle-franco, M.; Lanceros-Méndez, S. Enhanced Photocatalytic Activity of Au/TiO_2 Nanoparticles against Ciprofloxacin. *Catalysts* **2020**, *10*, 234, doi:10.3390/catal10020234.

62. Dalida, M.L.P.; Amer, K.M.S.; Su, C.; Lu, M. Photocatalytic Degradation of Acetaminophen in Modified TiO_2 under Visible Irradiation. *Environ. Sci. Pollut. Res.* **2014**, *21*, 1208–2016, doi:10.1007/s11356-013-2003-4.

63. Nasr, O.; Mohamed, O.; Al-shirbini, A.; Abdel-wahab, A. Photocatalytic Degradation of Acetaminophen over Ag, Au and Pt Loaded TiO_2 Using Solar Light. *J. Photochem. Photobiol. A Chem.* **2019**, *374*, 185–193, doi:10.1016/j.jphotochem.2019.01.032.

64. Eskandari, M.; Goudarzi, N.; Moussavi, S.G. Application of Low-Voltage UVC Light and Synthetic ZnO Nanoparticles to Photocatalytic Degradation of Ciprofloxacin in Aqueous Sample Solutions. *Water Environ. J.* **2018**, *32*, 58–66, doi:10.1111/wej.12291.

65. Zangeneh, H.; Zinatizadeh, A.A.L.; Habibi, M.; Akia, M.; Isa, M.H. Photocatalytic Oxidation of Organic Dyes and Pollutants in Wastewater Using Different Modified Titanium Dioxides: A Comparative Review. *J. Ind. Eng. Chem.* **2015**, *26*, 1–36, doi:10.1016/j.jiec.2014.10.043.

66. Evgenidou, E.; Fytianos, K.; Poulios, I. Semiconductor-Sensitized Photodegradation of Dichlorvos in Water Using TiO_2 and ZnO as Catalysts. *Appl. Catal. B Environ.* **2005**, *59*, 81–89, doi:10.1016/j.apcatb.2005.01.005.

67. Al-gharibi, M.A.; Kyaw, H.H.; Al-sabahi, J.N.; Zar, T.M.M.; Al-sharji, Z.A.; Al-abri, M.Z. Silver Nanoparticles Decorated Zinc Oxide Nanorods Supported Catalyst for Photocatalytic Degradation of Paracetamol. *Mater. Sci. Semicond. Process.* **2021**, *134*, 105994, doi:10.1016/j.mssp.2021.105994.

68. Bohdziewicz, J.; Kudlek, E.; Dudziak, M. Influence of the Catalyst Type (TiO_2 and ZnO) on the Photocatalytic Oxidation of Pharmaceuticals in the Aquatic Environment. *Desalin. Water Treat.* **2016**, *57*, 1552–1563, doi:10.1080/19443994.2014.988411.

69. Hitam, C.N.C.; Jalil, A.A. A Review on Exploration of Fe_2O_3 Photocatalyst towards Degradation of Dyes and Organic Contaminants. *J. Environ. Manage.* **2020**, *258*, 110050, doi:10.1016/j.jenvman.2019.110050.

70. Lotfi, S.; Ouardi, M. El; Ahsaine, H.A.; Assani, A. Recent Progress on the Synthesis, Morphology and Photocatalytic Dye Degradation of $BiVO_4$ Photocatalysts: A Review. *Catal. Rev.* **2022**, *00*, 1–45, doi:10.1080/01614940.2022.2057044.

71. Muruganandham, M.; Zhang, Y.; Suri, R.; Lee, G.; Chen, P.; Hsieh, S.; Sillanpää, M.; Wu, J.J. Environmental Applications of ZnO Materials. *J. Nanosci. Nanotechnol.* **2015**, *15*, doi:10.1166/jnn.2015.10725.

72. Chen, T.; Liu, L.; Hu, C.; Huang, H. Recent Advances on Bi_2WO_6-based Photocatalysts for Environmental and Energy Applications. *Chinese J. Catal.* **2021**, *42*, 1413–1438, doi:10.1016/S1872-2067(20)63769-X.

73. Ray, S.K.; Hur, J. A Review on Monoclinic Metal Molybdate Photocatalyst for Environmental Remediation. *J. Ind. Eng. Chem.* **2021**, *101*, 28–50, doi:10.1016/j.jiec.2021.06.027.

74. Guo, J.; Liang, J.; Yuan, X.; Jiang, L.; Zeng, G.; Yu, H.; Zhang, J. Efficient Visible-Light Driven Photocatalyst, Silver (Meta)Vanadate: Synthesis, Morphology and Modification. *Chem. Eng. J.* **2018**, *352*, 782–802, doi:10.1016/j.cej.2018.07.071.

75. Hassani, A.; Khataee, A.; Karaca, S. Photocatalytic Degradation of Ciprofloxacin by Synthesized TiO_2 Nanoparticles on Montmorillonite: Effect of Operation Parameters and Artificial Neural Network Modeling. *J. Mol. Catal. A Chem.* **2015**, *409*, 149–161, doi:10.1016/j.molcata.2015.08.020.

76. Doorslaer, X. Van; Dewulf, J.; Maerschalk, J. De; Langenhove, H. Van; Demeestere, K. Heterogeneous Photocatalysis of Moxifloxacin in Hospital Effluent: Effect of Selected Matrix Constituents. *Chem. Eng. J.* **2015**, *261*, 9–16, doi:10.1016/j.cej.2014.06.079.

77. Malesic-Eleftheriadou, N.; Evgenidou, E.N.; Kyzas, G.Z.; Bikiaris, D.N.; Lambropoulou, D.A. Removal of Antibiotics in Aqueous Media by Using New Synthesized Bio-Based Poly(Ethylene Terephthalate)-TiO_2 Photocatalysts. *Chemosphere* **2019**, *234*, 746–755, doi:10.1016/j.chemosphere.2019.05.239.

78. Hu, Z.; Ge, M.; Guo, C. Efficient Removal of Levofloxacin from Different Water Matrices via Simultaneous Adsorption and Photocatalysis Using a Magnetic Ag_3PO_4/RGO/ $CoFe_2O_4$ Catalyst. *Chemosphere* **2021**, *268,* 128834, doi:10.1016/j.chemosphere.2020.128834.

79. Abdullah, F.H.; Bakar, N.H.H.A.; Bakar, M.A. Current Advancements on the Fabrication, Modification, and Industrial Application of Zinc Oxide as Photocatalyst

in the Removal of Organic and Inorganic Contaminants in Aquatic Systems. *J. Hazard. Mater.* **2022**, *424*, 127416, doi:10.1016/j.jhazmat.2021.127416.

80. Kusmierek, E. A CeO_2 Semiconductor as a Photocatalytic and Photoelectrocatalytic Material for the Remediation of Pollutants in Industrial Wastewater: A Review. *Catalysts* **2020**, *10*, 1435, doi:10.3390/catal10121435.

81. Reddy, C.V.; Reddy, K.R.; Shetti, N.P.; Mishra, A.; Basu, S. Chapter 30. Recent Progress in TiO_2- and ZnO-Based Nanostructured Hybrid Photocatalysts for Water Purification and Hydrogen Generation. In *Nanoscale Materials in Water Purification*; Elsevier Inc., 2019; pp. 815–843 ISBN 9780128139264, doi:10.1016/B978-0-12-813926-4.00039-2.

82. Kumar, C.S.S.G. Advancements in the Zinc Oxide Nanomaterials for Efficient Photocatalysis. *Chem. Pap.* **2017**, *71*, 2023–2042, doi:10.1007/s11696-017-0217-5.

83. Udom, I.; Ram, M.K.; Stefanakos, E.K.; Hepp, A.F.; Goswami, D.Y. One Dimensional-ZnO Nanostructures: Synthesis, Properties and Environmental Applications. *Mater. Sci. Semicond. Process.* **2013**, *16*, 2070–2083, doi:10.1016/j.mssp.2013.06.017.

84. Akerdi, A.G.; Bahrami, S.H. Application of Heterogeneous Nano-Semiconductors for Photocatalytic Advanced Oxidation of Organic Compounds: A Review. *J. Environ. Chem. Eng.* **2019**, *7*, 103283, doi:10.1016/j.jece.2019.103283.

85. Salazar, H.; Martins, P.M.; Santos, B.; Fernandes, M.M.; Reizabal, A.; Sebastian, V.; Botelho, G.; Tavares, C.J.; Vilas-Viela, J.L.; Lanceros-Mendez, S. Photocatalytic and Antimicrobial Multifunctional Nanocomposite Membranes for Emerging Pollutants Water Treatment Applications. *Chemosphere* **2020**, *250*, 126299, doi:10.1016/j.chemosphere.2020.126299.

86. Zhang, X.; Chen, Y.L.; Liu, R.-S.; Tsai, D.P. Plasmonic Photocatalysis. *Reports Prog. Phys.* **2013**, *76*, 046401, doi:10.1088/0034-4885/76/4/046401.

87. Meng, X.; Liu, L.; Ouyang, S.; Xu, H.; Wang, D.; Zhao, N.; Ye, J. Nanometals for Solar-to-Chemical Energy Conversion: From Semiconductor-Based Photocatalysis to Plasmon-Mediated Photocatalysis and Photo-Thermocatalysis. *Adv. Mater.* **2016**, *28*, 6781–6803, doi:10.1002/adma.201600305.

88. Wang, M.; Ye, M.; Iocozzia, J.; Lin, C.; Lin, Z. Plasmon-Mediated Solar Energy Conversion via Photocatalysis in Noble Metal/Semiconductor Composites. *Adv. Sci.* **2016**, *3*, 1600024, doi:10.1002/advs.201600024.

89. Wang, C.; Astruc, D. Nanogold Plasmonic Photocatalysis for Organic Synthesis and Clean Energy Conversion. *Chem. Soc. Rev.* **2014**, *43*, 7188–7216, doi:10.1039/c4cs00145a.

90. Shi, Y.; Ma, J.; Chen, Y.; Qian, Y.; Xu, B.; Chu, W.; An, D. Recent Progress of Silver-Containing Photocatalysts for Water Disinfection under Visible Light Irradiation: A Review. *Sci. Total Environ.* **2022**, *804*, 150024, doi:10.1016/j.scitotenv.2021.150024.

91. Manchala, S.; Elayappan, V.; Lee, H. Chapter 7. Plasmonic Photocatalysis: An Extraordinary Way to Harvest Visible Light. In *Photocatalytic Systems by Design*; INC, 2021; pp. 187–216 ISBN 9780128205327, doi:10.1016/B978-0-12-820532-7.00015-1.

92. Zunic, B.; Peter, S. *Applications of Molecular Spectroscopy to Current Research in the Chemical and Biological Sciences*; Intech, 2016; doi:10.5772/61896.

93. Kumar, A.; Choudhary, P.; Kumar, A.; Camargo, P.H.C.; Krishnan, V. Recent Advances in Plasmonic Photocatalysis Based on TiO_2 and Noble Metal Nanoparticles for Energy Conversion, Environmental Remediation, and Organic Synthesis. *Small* **2022**, *18*, 2101638, doi:10.1002/smll.202101638.

94. Bastús, N.G.; Comenge, J.; Puntes, V. Kinetically Controlled Seeded Growth Synthesis of Citrate-Stabilized Gold Nanoparticles of up to 200 Nm: Size Focusing versus Ostwald Ripening. *Langmuir* **2011**, *27*, 11098–11105, doi:10.1021/la201938u.

95. Reguera, J.; Langer, J.; Jime, D.; Liz-marza, L.M.; Langer, J. Chem Soc Rev Anisotropic Metal Nanoparticles for Surface Enhanced Raman Scattering. **2017**, 3866–3885, doi:10.1039/c7cs00158d.

96. Xiao, Y.; Huang, Y.; Xue, S.; Zhao, J. Light Switching of Amine Oxidation Products from Oximes to Imines: Superior Activity of Plasmonic Gold Nanorods-Loaded TiO_2(B) Nanofibers under Visible-near IR Light. *Appl. Catal. B Environ.* **2020**, *265*, 118596, doi:10.1016/j.apcatb.2020.118596.

97. Hao, F.; Nehl, C.L.; Hafner, J.H.; Nordlander, P. Plasmon Resonances of a Gold Nanostar. *Nanoletters* **2007**, *7*, 729–732, doi:10.1021/nl062969c.

98. Pazos-perez, N.; Guerrini, L.; Alvarez-puebla, R.A. Plasmon Tunability of Gold Nanostars at the Tip Apexes. *ACS Omega* **2018**, *3*, 17173–17179, doi:10.1021/acsomega.8b02686.

99. Chirea, M. Electron Transfer at Gold Nanostar Assemblies: A Study of Shape Stability and Surface Density Influence. *Catalysts* **2013**, *3*, 288–309, doi:10.3390/catal3010288.

100. Martins, P.M.; Santos, B.; Salazar, H.; Carabineiro, S.A.C.; Botelho, G.; Tavares, C.J.; Lanceros-Mendez, S. Multifunctional Hybrid Membranes for Photocatalytic and Adsorptive Removal of Water Contaminants of Emerging Concern. *Chemosphere* **2022**, *293*, 133548, doi:10.1016/J.CHEMOSPHERE.2022.133548.

101. Singh, S.; Mahalingam, H.; Singh, P.K. Polymer-Supported Titanium Dioxide Photocatalysts for Environmental Remediation: A Review. *Appl. Catal. A Gen.* **2013**, *462–463*, 178–195, doi:10.1016/j.apcata.2013.04.039.

102. Cunha, D.L.; Kuznetsov, A.; Achete, C.A.; Machado, A.E. da H.; Marques, M. Immobilized TiO_2 on Glass Spheres Applied to Heterogeneous Photocatalysis: Photoactivity, Leaching and Regeneration Process. *PeerJ* **2018**, *6*, e4464, doi:10.7717/peerj.4464.

103. Shen, C.; Wang, Y.J.; Xu, J.H.; Luo, G.S. Facile Synthesis and Photocatalytic Properties of TiO_2 Nanoparticles Supported on Porous Glass Beads. *Chem. Eng. J.* **2012**, *209*, 478–485, doi:10.1016/j.cej.2012.08.044.

104. Bo, Y.I.N.; Ji-tong, W.; Wei, X.U.; Dong-hui, L.; Wen-ming, Q. Preparation of TiO_2/ Mesoporous Carbon Composites and Their Photocatalytic Performance for Methyl Orange Degradation. *New Carbon Mater.* **2013**, *28*, 47–54, doi:10.1016/S1872-5805(13)60064-5.

105. Lee, H.U.; Lee, G.; Park, J.C.; Lee, Y.-C.; Lee, S.M.; Son, B.; Park, S.Y.; Kim, C.; Lee, S.; Lee, S.C.; et al. Efficient Visible-Light Responsive TiO_2 Nanoparticles Incorporated Magnetic Carbon Photocatalysts. *Chem. Eng. J.* **2014**, *240*, 91–98, doi:10.1016/j.cej.2013.11.054.

106. Baig, U.; Matin, A.; Gondal, M.A.; Zubair, S.M. Facile Fabrication of Superhydrophobic, Superoleophilic Photocatalytic Membrane for Efficient Oil-Water

Separation and Removal of Hazardous Organic Pollutants. *J. Clean. Prod.* **2018**, *208*, 904–915, doi:10.1016/j.jclepro.2018.10.079.

107. Byrne, J.A.; Eggins, B.R.; Brown, N.M.D.; Mckinney, B.; Rouse, M. Immobilisation of TiO_2 Powder for the Treatment of Polluted Water. *Appl. Catal. B Environ.* **1998**, *17*, 25–36, doi:10.1016/S0926-3373(97)00101-X.

108. Martins, P.M.; Santos, B.; Salazar, H.; Carabineiro, S.A.C.; Botelho, G.; Tavares, C.J.; Lanceros-Mendez, S. Multifunctional Hybrid Membranes for Photocatalytic and Adsorptive Removal of Water Contaminants of Emerging Concern. *Chemosphere* **2022**, *293*, 133548, doi:10.1016/j.chemosphere.2022.133548.

109. Alhaji, M.H.; Khan, K.S.A.; Muhammad, A.H.A. Recent Developments in Immobilizing Titanium Dioxide on Supports for Degradation of Organic Pollutants in Wastewater- A Review. *Int. J. Environ. Sci. Technol.* **2017**, *14*, 2039–2052, doi:10.1007/s13762-017-1349-4.

110. Faure, B.; Salazar-alvarez, G.; Ahniyaz, A. Dispersion and Surface Functionalization of Oxide Nanoparticles for Transparent Photocatalytic and UV-Protecting Coatings and Sunscreens. *Sci. Technol. Adv. Mater.* **2013**, *14*, 023001, doi:10.1088/1468-6996/14/2/023001.

111. Cossich, E.; Bergamasco, R.; Amorim, M.T.P. De; Martins, P.M.; Marques, J. Development of Electrospun Photocatalytic TiO_2-Polyamide-12 Nanocomposites. *Mater. Chem. Phys.* **2015**, *164*, 91–97, doi:10.1016/j.matchemphys.2015.08.029.

112. Bhardwaj, N.; Kundu, S.C. Electrospinning: A Fascinating Fiber Fabrication Technique. *Biotechnol. Adv.* **2010**, *28*, 325–347, doi:10.1016/j.biotechadv.2010.01.004.

113. Shan, A.Y.; Ghazi, T.I.M.; Rashid, S.A. Immobilisation of Titanium Dioxide onto Supporting Materials in Heterogeneous Photocatalysis: A Review. *Appl. Catal. A Gen.* **2010**, *389*, 1–8, doi:10.1016/j.apcata.2010.08.053.

114. Du, Z.; Cheng, C.; Tan, L.; Lan, J.; Jiang, S.; Zhao, L.; Guo, R. Enhanced Photocatalytic Activity of Bi_2WO_6/TiO_2 Composite Coated Polyester Fabric under Visible Light Irradiation. *Appl. Surf. Sci.* **2018**, *435*, 626–634, doi:10.1016/j.apsusc.2017.11.136.

115. Ounas, O.; Lekhlif, B.; Jamal-eddine, J. The Facile Immobilization of ZnO into a Polymer Surface for Photodegradation of Organic Contaminants. *Mater. Today Proc.* **2020**, *30*, 816–822, doi:10.1016/j.matpr.2020.04.179.

116. Vatanpour, V.; Karami, A.; Sheydaei, M. Central Composite Design Optimization of Rhodamine B Degradation Using TiO_2 Nanoparticles/UV/PVDF Process in Continuous Submerged Membrane Photoreactor. *Chem. Eng. Process. Process Intensif.* **2017**, *116*, 68–75, doi:10.1016/j.cep.2017.02.015.

117. Liu, F.; Hashim, N.A.; Liu, Y.; Abed, M.R.M.; Li, K. Progress in the Production and Modification of PVDF Membranes. *J. Memb. Sci.* **2011**, *375*, 1–27, doi:10.1016/j.memsci.2011.03.014.

118. Saxena, P.; Shukla, P. A Comprehensive Review on Fundamental Properties and Applications of Poly(Vinylidene Fluoride) (PVDF). *Adv. Compos. Hybrid Mater.* **2021**, *4*, 8–26, doi:10.1007/s42114-021-00217-0.

119. Martins, P.; Lopes, A.C.; Lanceros-Mendez, S. Electroactive Phases of Poly(Vinylidene Fluoride): Determination, Processing and Applications. *Prog. Polym. Sci.* 2014, *39*, 683–706, doi:10.1016/j.progpolymsci.2013.07.006.

120. Ribeiro, C.; Costa, C.M.; Correia, D.M.; Nunes-pereira, J.; Oliveira, J.; Martins, P.; Gonçalves, R.; Cardoso, V.F.; Lanceros-méndez, S. Electroactive Poly(Vinylidene Fluoride)-Based Structures for Advanced Applications. *Nat. Protoc.* **2018**, *13*, 681–704, doi:10.1038/nprot.2017.157.

121. Silva, M.M.; Liu, L.; Costa, C.M. Poly(Vinylidene Fluoride-Co-Chlorotrifluoroethylene) (PVDF-CTFE) Lithium-Ion Battery Separator Membranes Prepared by Phase Inversion. *RSC Adv.* **2015**, *5*, 90428–90436, doi:10.1039/c5ra19335d.

122. Wu, L.; Jin, Z.; Liu, Y.; Ning, H.; Liu, X.; Hu, N. Recent Advances in the Preparation of PVDF-Based Piezoelectric Materials. *Nanotechnol. Rev.* **2022**, *11*, 1386–1407, doi:10.1515/ntrev-2022-0082.

123. Abbrent, S.; Plestil, J.; Hlavata, D.; Lindgren, J.; Tegenfeldt, J.; Wendsjö, A. Crystallinity and Morphology of PVdF–HFP-Based Gel Electrolytes. *Polymer (Guildf).* **2001**, *42*, 1407–1416, doi:10.1016/S0032-3861(00)00517-6.

124. Ji, J.; Liu, F.; Hashim, N.A.; Abed, M.R.M.; Li, K. Poly(Vinylidene Fluoride) (PVDF) Membranes for Fluid Separation. *React. Funct. Polym.* **2015**, *86*, 134–153, doi:10.1016/j.reactfunctpolym.2014.09.023.

125. Queirós, J.M.; Salazar, H.; Valverde, A.; Botelho, G.; Luis, R.F. de; Teixeira, J.; Martins, P.M.; Lanceros-Mendez, S. Reusable Composite Membranes for Highly Efficient Chromium Removal from Real Water Matrixes. *Chemosphere* **2022**, *307*, 135922, doi:10.1016/j.chemosphere.2022.135922.

126. Salazar, H.; Nunes-pereira, J.; Correia, D.M.; Cardoso, V.. F.; Gonçalves, R.; Martins, P.M.; Ferdov, S.; Martins, M.D.; Botelho, G.; Lanceros-Méndez, S. Poly(Vinylidene Fluoride-Hexafluoropropylene)/Bayerite Composite Membranes for Efficient Arsenic Removal from Water. *Mater. Chem. Phys.* **2016**, *183*, 430–438, doi:10.1016/j.matchemphys.2016.08.049.

127. Salazar, H.; Martins, P.M.; Valverde, A.; Luis, R.F. De; Vilas-vilela, J.L.; Ferdov, S.; Botelho, G.; Lanceros-mendez, S. Reusable Nanocomposite Membranes for Highly Efficient Arsenite and Arsenate Dual Removal from Water. *Adv. Mater. Interfaces* **2022**, *9*, 2101419, doi:10.1002/admi.202101419.

128. Zioui, D.; Salazar, H.; Aoudjit, L.; Martins, P.M.; Lanceros-Méndez, S. Polymer-Based Membranes for Oily. *Polymers (Basel).* **2020**, *12*, 42, doi:10.3390/polym12010042.

129. Aljumaily, M.M.; Ali, N.S.; Mahdi, A.E.; Alayan, H.M.; Alomar, M.; Hameed, M.M.; Ismael, B.; Alsalhy, Q.F.; Alsaadi, M.A.; Majdi, H.S.; et al. Membranes with DES-Functionalized Carbon Nanospheres for Removal of Methyl Orange by Membrane Distillation. *Water* **2022**, *14*, 1396, doi:10.3390/w14091396.

130. Teixeira, S.; Martins, P.M.; Kühn, K.; Cuniberti, G. Reusability of Photocatalytic TiO_2 and ZnO Nanoparticles Immobilized in Poly(Vinylidene Difluoride)-Co-Trifluoroethylene. *Appl. Surf. Sci.* **2016**, *384*, 497–504, doi:10.1016/j.apsusc.2016.05.073.

131. Tasselli, F. Non-Solvent Induced Phase Separation Process (NIPS) for Membrane Preparation. *Encycl. Membr.* **2014**, 1–3, doi:10.1007/978-3-642-40872-4.

132. Correia, D.M.; Ribeiro, C.; Sencadas, V.; Vikingsson, L.; Gasch, M.O.; Ribelles, J.L.G.; Botelho, G.; Lanceros-méndez, S. Strategies for the Development of Three

Dimensional Scaffolds from Piezoelectric Poly (Vinylidene Fluoride). *Mater. Des.* **2016**, *92*, 674–681, doi:10.1016/j.matdes.2015.12.043.

Chapter 2

2. Au-sensitised TiO_2 and ZnO photocatalysts for broadband pharmaceuticals degradation

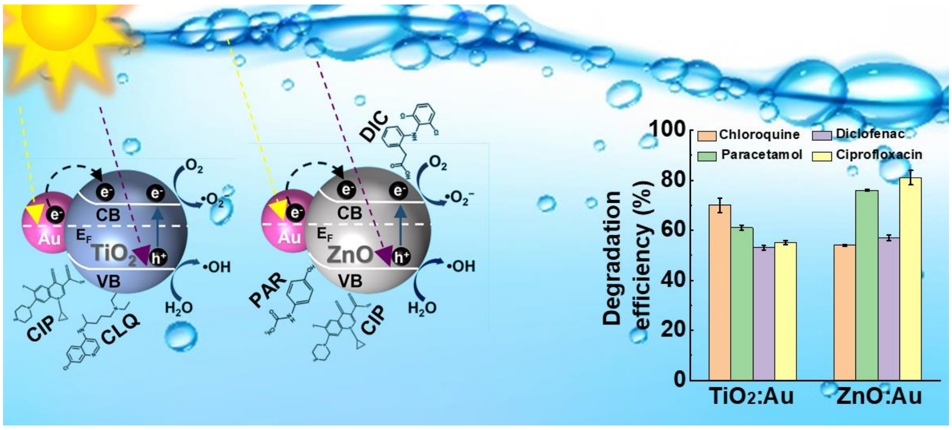

This work reports on the comparative study of photocatalytic performance of TiO_2 and ZnO in the degradation of four pharmaceuticals: chloroquine phosphate, paracetamol, diclofenac sodium, and ciprofloxacin. Additionally, TiO_2 and ZnO were functionalised with spherical Au nanoparticles to enhance the photocatalytic efficiency under visible light.

This chapter is based on the following publication: Zheng, F., et al., Au-sensitised TiO_2 and ZnO nanoparticles for broadband pharmaceuticals photocatalytic degradation in water remediation. (Under revision)

2.1. Introduction

As stated in the first chapter, a large number of contaminants of emerging concern (CECs), such as most pharmaceuticals, exhibit high persistency in water bodies due to the difficulty of their removal by conventional treatment methods, causing severe environmental issues [1,2]. Hence, developing efficient materials and technologies to degrade these resilient compounds is essential. In this context, photocatalysis has become an exciting solution to remove these pollutants through photocatalytic degradation [3,4].

Semiconductors have been widely used as photocatalysts [4–6], particularly titanium dioxide (TiO_2), which has a bandgap between 3.0 and 3.2 eV depending on the crystalline phase, which presents remarkable properties, including low cost, high stability, low toxicity, and high photocatalytic efficiency in degrading multiple organic contaminants [5–7]. Additionally, TiO_2 nanoparticles have also been used to provide photocatalytic properties to discarded materials such as recovered cellulose-based materials [8]. Zinc oxide (ZnO), with a similar bandgap (≈ 3.2 eV), is another commonly used photocatalyst due to its suitable optoelectronic, piezoelectric and photochemical properties [4,9,10]. Moreover, the oxygen vacancies on the ZnO surface produce more hydroxyl ions, improving the formation of hydroxyl radical ($^{\bullet}OH$) and showing a faster response rate, enhancing the photocatalytic efficiency [10,11]. Thus, a systematic comparison of TiO_2 and ZnO nanoparticles photocatalytic degradation under the same conditions, for diverse pharmaceutical pollutants, is important to understand how the type of semiconductor and generation of ROS affect the photocatalytic efficiency.

Despite the described advantageous properties of TiO_2 and ZnO nanoparticles, these photocatalysts also present relevant drawbacks. The main one is that they require excitation under UV radiation due to their wide bandgap [6,10], limiting their efficiency under solar radiation [5,6,10] and requiring a UV lamp to provide radiation, which makes the process less cost-effective [7,12,13]. Furthermore, the fast recombination of the photogenerated electron-hole pair, decreasing the photocatalytic efficiency, is another limitation [6,10]. Among several strategies to overcome these limitation, the use of plasmonic nanoparticles, mainly Au [14], Ag [15] and Cu [16], to sensitise semiconductor nanoparticles results in one of the most promising strategies, as it allows efficient photocatalytic activities under visible light due to the metal-semiconductor Schottky junction and the localised surface plasmon resonance (LSPR) [13,17,18]. The former benefits charge separation and transfer, reducing the recombination rate, whereas the latter contributes to the strong absorption of visible light and the excitation of active charge carriers (hot electrons) [13,17]. Au has been extensively studied because of its excellent plasmonic resonance in visible and UV ranges, ease of synthesis, low toxicity, and physical and chemical stability [7,13,14].

Different techniques have been used to synthesise Au/semiconductor hybrid nanoparticles to enhance their photocatalytic activity under visible light [7,19–21]. Among those commonly used methods, the impregnation (IMP) method is a simple method for synthesising Au-supported catalysts [20]. However, large Au nanoparticles are often produced by the IMP method [20,21], which reduces the light-harvesting of the semiconductor, reducing the photocatalytic efficiency [13]. Photoreduction (PR) method is an alternative to depositing the smaller Au nanoparticles on the semiconductor surface [19,22], resulting in a higher deposition ratio of Au [22]. Despite these advantages, the PR method requires light illumination of appropriate wavelength [19,22]. Deposition-Precipitation (DP) method is the most used and effective method to obtain small Au nanoparticles on semiconductor surface [19–21]. However, the control of the size of Au depends on pH values and Au loading during the process [19,20,22]. Herein, an optimised DP method [7] is used to prepare cost-effectively TiO_2:Au and ZnO:Au hybrid nanoparticles using the lowest Au loading to enhance the photocatalytic activity of nanocomposite under visible light.

In this chapter, TiO_2 and ZnO were synthesised under the same conditions in the laboratory instead of using the commercial nanoparticles in order to make a more fair comparative study. The co-precipitation method [23,24] was chosen because of its ease of implementation, scalability, and relatively low cost [9]. On the other side, its functionalisation with Au nanoparticles was carried out through an optimised deposition-precipitation (DP) technique [7] due to its relative simplicity and cost-effectiveness [19–21]. The quantification of the different reactive oxygen species (ROS) generated in each sample was studied to relate it with the photocatalytic degradation efficiencies. The photocatalytic activity of the semiconductors before and after functionalising with Au was tested through the degradation of several target pharmaceuticals which are highly relevant in water remediation and with different physicochemical properties (**Figure 2.1** and **Table 2.1**): Chloroquine phosphate (CLQ), Paracetamol (PAR), Diclofenac sodium (DCF), and Ciprofloxacin (CIP). CLQ has been used for decades as an anti-inflammatory in treating and preventing malaria, rheumatoid arthritis, and systemic lupus erythematosus [25,26]. Despite not being one of the most detected compounds in water bodies, CLQ has been considered a potential treatment for the disease COVID-19, which contributed to a suddenly increased use [26–28], and there is a lack of work devoted to its photocatalytic degradation evaluation, being just a few works related to its elimination though other methods [25,29]. PAR, an analgesic and antipyretic found at high concentrations in different water matrixes [3], is one of the most commonly used drugs, being considered one of the most widely used analgesics in Europe [30], one of the top three drugs prescribed in England [31,32] and among the top 200 in USA [31,33]. Its consumption has increased since paracetamol was used as an alternative treatment for fever and systemic symptoms related to COVID-19 [34,35]. DCF, used as a pain killer and non-steroidal anti-inflammatory drug [36–38], is another widespread pharmaceutical in different water matrixes [3] since it is one of the most used pharmaceuticals worldwide without requiring a medical prescription [36,37]. CIP, a second-generation fluoroquinolone antibiotic, is often detected in all types of water matrixes worldwide [3,6,7] due to its high consumption [6].

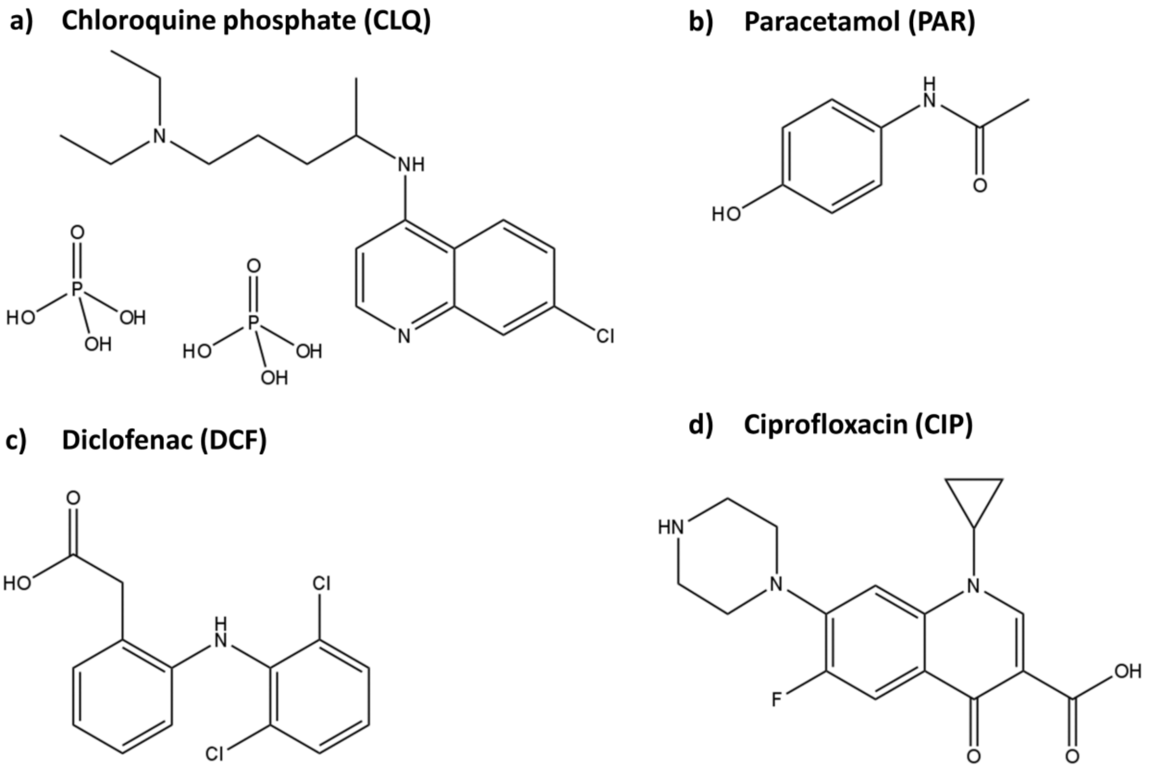

a) Chloroquine phosphate (CLQ)

b) Paracetamol (PAR)

c) Diclofenac (DCF)

d) Ciprofloxacin (CIP)

Figure 2.1. Molecular structure of Chloroquine phosphate (CLQ) (a), Paracetamol (PAR) (b), Diclofenac (DCF) (c) and Ciprofloxacin (CIP) (d).

Table 2.1. Physicochemical properties of CLQ, PAR, DCF, and CIP.

	Chloroquine phosphate (CLQ)	**Paracetamol (PAR)**	**Diclofenac (DCF)**	**Ciprofloxacin (CIP)**
Molecular formula	$C_{18}H_{26}ClN_3 \cdot 2H_3PO_4$	$C_8H_9NO_2$	$C_{14}H_{11}Cl_2NO_2$	$C_{17}H_{18}FN_3O_3$
Molecular weight (g/mol)	515.9	151.16	296.14	331.34
pK_{a1}; pK_{a2}; (pI)	8.4 [25]	9.3 [31]	4.1 [39]	6; 8.7 [39] (7.35)
Charged form at neutral pH	Cationic	Uncharged	Anionic	Zwitterionic
Solubility in water (g/L)	256 [40]	14.9 [41]	14.18 [42]	30 [6]

2.2. Experimental

2.2.1. Materials

Titanium (IV) isopropoxide ($C_{12}H_{28}O_4Ti$, 97%) and Zinc acetate dihydrate ($C_4H_6O_4Zn \cdot 2H_2O$, ≥99.0 %) were purchased from Sigma-Aldrich. Sodium hydroxide (NaOH, 98.0-100.5 %) was obtained from Panreac. Milli-Q ultrapure water (resistivity 18.2 MΩ·cm) was used in all experiments. Chloroquine phosphate (CLQ, Pharmaceutical Secondary Standard, $C_{18}H_{26}CIN_3 \cdot 2H_3PO_4$) with maximum light absorption at a wavelength of 342 nm was supplied by Sigma-Aldrich. Paracetamol (PAR, European Pharmacopoeia (EP) Reference Standard, $C_8H_9NO_2$) with maximum light absorption at a wavelength of 243 nm was supplied by Sigma-Aldrich. Diclofenac sodium (DCF, European Pharmacopoeia (EP) Reference Standard, $C_{14}H_{10}Cl_2NNaO_2$) with maximum light absorption at a wavelength of 276 nm was supplied by Sigma-Aldrich. Ciprofloxacin (CIP, ≥98 % (HPLG), $C_{17}H_{18}FN_3O_3$) with maximum light absorption at a wavelength of 277 nm was supplied by Sigma-Aldrich.

2.2.2. Sample preparation

2.2.2.1. TiO_2 and ZnO nanoparticles synthesis

TiO_2 nanoparticles were synthesised by co-precipitation method [23] with slight modification. Briefly, 200 mL of ultrapure water was added slowly into 10 g of titanium isopropoxide to generate the hydrolysis of the alkoxide and precipitation of hydrous titanium oxides. Afterwards, NaOH solution (1 M) was added dropwise to obtain a pH = 8. The mixed solution was thoroughly mixed by continuous stirring at 100 °C for 1 hour. Then, the pH was rechecked and readjusted with NaOH solution (1 M) to 8 and kept stirring at room temperature for 1 hour.

ZnO nanoparticles were synthesised using the same co-precipitation technique [24]. In this case, 10 g of zinc acetate dihydrate was initially dissolved in 300 mL of ultrapure water, and the rest of the protocol was the same as for the TiO_2 nanoparticles.

For nanoparticle purification, the white precipitate formed in the reaction was filtered and washed several times with deionised water. The last step was to dry the washed precipitate at 80 °C in an oven overnight and then anneal it at 400 °C for 3 hours. The final product was ground with a pestle and mortar to obtain a fine powder.

2.2.2.2. TiO_2:Au and ZnO:Au nanoparticles synthesis

TiO_2:Au and ZnO:Au multicomponent nanoparticles were synthesised, employing the deposition-precipitation method (DP) as previously described [7]. Briefly, 200 mg of semiconductor (TiO_2 and ZnO nanoparticles) in 40 mL of ultrapure water were dispersed in a sonication bath for 30 min. Then, this solution was stirred at room temperature, and a calculated volume of $HAuCl_4$ (1 mM) was added to achieve the Au loading of 0.05 wt.%. The solution was stirred for 10 min to disperse the gold precursor homogeneously. Afterwards, NaOH (0.1 M) was added dropwise to obtain a pH = 9 and then left to react for 10 min. Finally, the solution was centrifuged and washed two times with ultrapure water. The last step was to dry the nanoparticles at 80 °C in an oven overnight and grind it with a mortar to obtain a fine powder.

2.2.3. Sample characterisation

Transmission electron microscopy (TEM) images were acquired with a JEOL JEM 1400 Plus set up operating at 100 kV in a bright field and a Talos (Thermo Scientific) system working at 200 kV for the HAADF-STEM measurements. The analysis of the images was performed using the Image J software package. To prepare the samples, the nanoparticles powder was dispersed in ultrapure water and sonicated for 1 min, and then a drop of the suspension was placed on a 400-mesh carbon-coated copper grid and dried at room temperature.

The crystal structure of the synthesised nanoparticles was evaluated by X-ray diffraction (XRD) using a Philips X'Pert PRO automatic diffractometer operating at 40 kV and 40 mA, in theta-theta configuration, secondary monochromator with Cu-Kα radiation (λ = 1.5418 Å) and a PIXcel solid-state detector (active length in 2θ 3.347°). Data were collected from 5 to 80° 2θ, step size 0.026°, and time per step of 60 s at room temperature. 1° fixed soller slit and divergence slit giving a constant sample illumination volume were used.

The phase composition (wt.%) of TiO_2 was calculated from the integrated areas of the main peaks of anatase, brookite, and rutile by the following expressions (**Equation 2.1-2.3**) [43]:

$$W_A\% = \frac{K_A I_A}{K_A I_A + I_R + K_B I_B} \tag{2.1}$$

$$W_B\% = \frac{K_B I_B}{K_A I_A + I_R + K_B I_B} \tag{2.2}$$

$$W_R\% = \frac{I_R}{K_A I_A + I_R + K_B I_B} \tag{2.3}$$

where W_A, W_B and W_R are the weight fractions of anatase, brookite, and rutile, respectively, and I_A, I_B, and I_R are the integral areas of anatase, brookite and rutile peaks in the XRD spectra, respectively [43]. K_A=0.886 and K_B=2.721 are correction coefficients [43].

Diffuse reflectance spectroscopy (DRS) measurements were carried out in the 200-2200 nm wavelength range using a UV-Visible-NIR Jasco V-770 spectrometer equipped with a 150 mm diameter integrating sphere coated with Spectralon with 1 nm spectral resolution. A Spectralon reference was used to measure the 100 % reflectance, and internal attenuators were used to determine zero reflectance to remove background and noise. The sample was placed in a quartz cuvette, sealed, and mounted on a Teflon sample holder for the DRS measurement. The measured reflectance spectra were subsequently converted to Kubelka-Munk (K-M) absorption factors to evaluate the absorption spectra of the powders by using the K-M equation (**Equation 2.4**) [44]:

$$F(R) = (1 - R_\infty)^2/(2R_\infty) \tag{2.4}$$

where R_∞ (R_{Sample}/R_{BaSO4}) corresponds to the sample's reflectance and F(R) is the absorbance.

The sample bandgap was estimated using the Tauc plot:

$$[F(R)h\upsilon]^{1/n} \ versus \ h\upsilon$$

where *h* is Planck's constant, *υ* the frequency, and n is the sample transition parameter taken as n=2 for indirect transition [45].

N_2 adsorption-desorption isotherms were carried out at 77 K using a Quantachrome Autosorb-iQ-MP analyser. Samples were degassed in situ at 120 ºC in vacuum for 12 hours before the measurements. The specific surface area values were calculated through Brunauer-Emmett-Teller (BET) method [46,47].

Dynamic light scattering (DLS) and Zeta-potential were measured in a Zetasizer NANO ZS-ZEN3600 (Malvern Instruments Limited, United Kingdom), equipped with a He–Ne laser (wavelength 633 nm) and backscatter detection (173°). The nanoparticles were dispersed (1 mg/mL) in ultrapure water and sonicated at room temperature for 1 hour to avoid aggregation, and each sample was measured six times at pH = 11 to obtain the hydrodynamic diameter. The Zeta-potential was assessed at different pH (3, 5, 7, 9, and 11), and each sample was measured six times. HCl (0.1 M) and NaOH (0.1 M) solutions were used to adjust de pH. The result was obtained using the Smoluchowski model [48]. The manufacturer software (Zetasizer 7.13) was used to estimate the hydrodynamic diameter of the nanoparticles (Z-average), the polydispersity index (PDI), and zeta potential values.

2.2.4. Photogenerated ROS ($^•OH$ and $^1O_2$) measurements

2.2.4.1. Detection of hydroxyl radicals ($^•OH$)

The hydroxyl radicals ($^•OH$) produced after illumination were detected and quantified as previously reported [49] by fluorescence spectroscopy through the hydroxylation reaction of terephthalic acid (TA) to 2-hydroxyterephthalic acid (2-HTA) in the heterogeneous phase, as shown **Figure 2.2.**

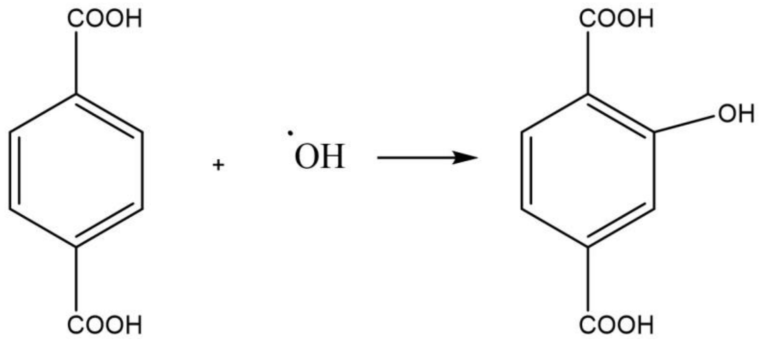

Figure 2.2. Scheme of hydroxylation reaction of terephthalic acid (TA).

Firstly, a TA solution (0.5 mM) was prepared by dissolving TA in a dilute NaOH solution (2 mM). Then, 50 mg nanoparticles as photocatalysts were dispersed in 50 mL of TA solution (0.5 mM) and stirred in the dark for 30 min. Afterwards, the suspension was stirred and irradiated for 60 min under UV illumination. An aliquot was taken out at different irradiation times and centrifuged to remove the nanoparticles. 200 µL of supernatant was collected and analysed using a microplate reader Infinite 200 Pro. This analysis was performed by evaluating the emission peak at 425 nm of the 2-HTA, which has an excitation wavelength of 315 nm [50] in the fluorescence spectrum. A standard calibration curve was constructed to quantify the relationship between the fluorescence signal and the produced hydroxyl radicals.

2.2.4.2. Detection of singlet oxygen ($^1O_2$)

Singlet oxygen ($^1O_2$) was determined as previously reported [49] by applying the histidine test (**Figure 2.3**) in a heterogeneous phase as an indirect way to quantify the generated $^\bullet O_2^-$. 50 mg of nanoparticles were added to a mixed solution of 40 mL L-histidine solution (0.2 mM) and 10 mL of N,N-p-nitrosodimethylaniline solution (0.2 mM). Afterwards, the suspension was stirred in the dark for 30 min, and then irradiated for 60 min under UV illumination. At different irradiation times, aliquots were taken out, centrifuged, and then analysed using an Agilent Cary 60 UV-Vis Spectrophotometer. This analysis evaluated the characteristic band of N,N-p-nitrosodimethylaniline at 440 nm in the UV-Vis spectrum. The reaction between histidine and $^1O_2$ produces a trans-annular peroxide, as presented in **Figure 2.3**. The latter compound was detected by bleaching the p-nitrosodimethylaniline at 440 nm. Singlet oxygen alone cannot cause bleaching of the latter compound; no bleaching occurs in the mixture of histidine and p-nitrosodimethylaniline without singlet oxygen. The produced $^1O_2$ was quantified from the calibration curve between absorbance and N,N-p-nitrosodimethylaniline solution concentration.

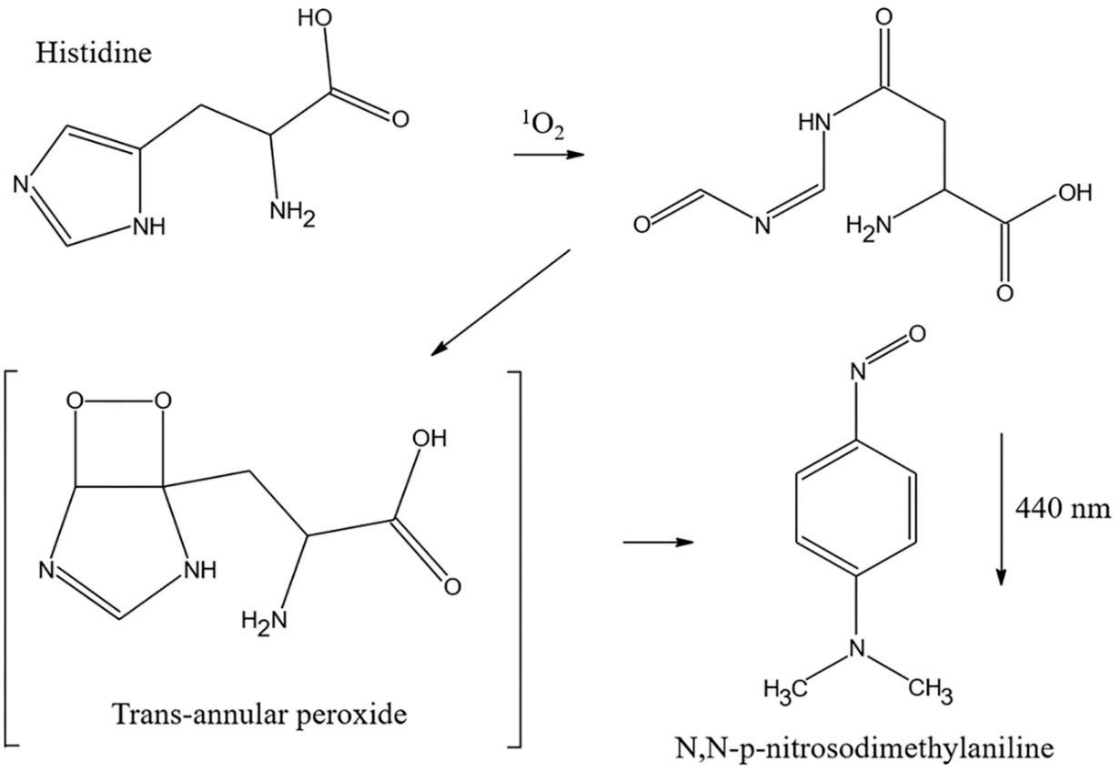

Figure 2.3. Mechanism of histidine test.

2.2.5. Photocatalytic degradation under UV and visible radiation

The nanoparticles' photocatalytic activity was tested under UV and visible radiation. Firstly, the CLQ solution of 30 mg/L, the PAR solution of 15 mg/L, the DCF solution of 30 mg/L, and the CIP solution of 5 mg/L were prepared separately as pollutants. These concentrations were selected taking into account the limitation of the pollutants detection in the UV-Vis spectrophotometer and the possibility of monitoring the degradation of pollutants. 50 mg of nanoparticles were added and stirred in 50 mL of the solutions (CLQ, PAR, DCF, or CIP) for 30 min in the dark to achieve the adsorption-desorption equilibrium before initiating the photocatalysis.

The UV degradation tests were carried out in a photoreactor with eight UV lamps of 8 W, with an emission peak at 365 nm, over 60 min. The suspensions of photocatalysts and solutions were kept stirred in a 100 mL beaker under illumination from the top. The distance between the solution and the lamp was 13.5 cm, and the irradiation at the sample was 3.3 W/m^2.

For the visible light degradation, a Xenon lamp was used with an excitation peak at 550 nm and an irradiance of 300 W/m^2 (spectra in **Figure 2.4**) over 240 min. The suspensions of photocatalysts and solutions were kept stirred in a 100 mL beaker under illumination from the lateral side. The distance between the solution and the lamp was 21 cm.

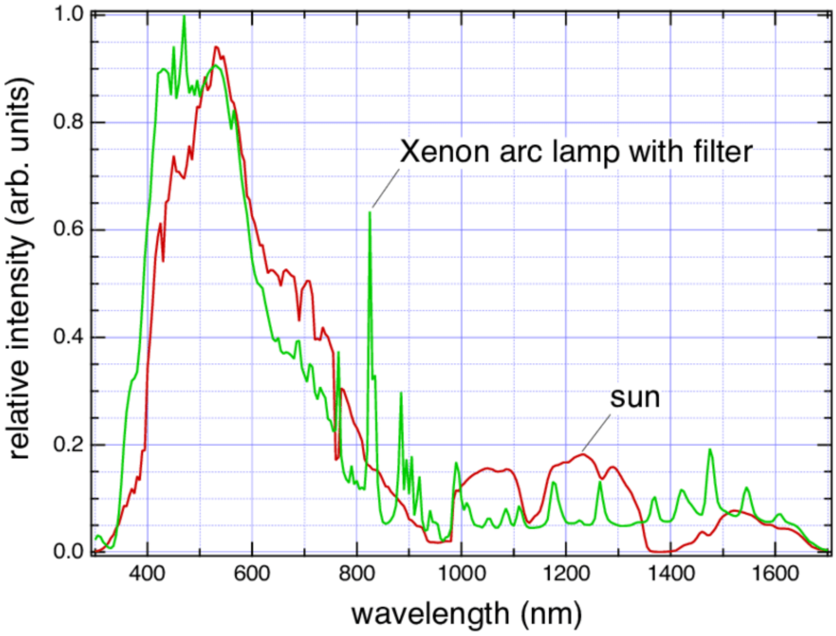

Figure 2.4. Xenon Lamp arc (with UV filter) and sunlight spectra.

The photocatalytic efficiency was evaluated by monitoring the absorbance variation of the main absorption peak (λ_{max}) of each pollutant in the UV-Vis spectrum (CLQ (λ_{max} = 342 nm), PAR (λ_{max} = 243 nm), DCF (λ_{max} = 276 nm) and CIP (λ_{max} = 277 nm)) in the samples taken out at different times during the degradation assays. After removing the photocatalysts in all the collected samples through centrifugation, 200 µL of the supernatant in each sample was taken out and analysed using a microplate reader Infinite 200 Pro in the range from 230 to 450 nm.

The photocatalytic degradation rate was fit to a pseudo-first-order reaction, which is based on the Langmuir–Hinshelwood model described by **Equation 2.5**:

$$\ln\left(\frac{C}{C_0}\right) = -kt \tag{2.5}$$

where C and C_0 represent the pollutant concentration at time t and at the beginning of the photocatalytic assessment, respectively, and *k* is the first-order rate constant of the reaction [7].

2.3. Results and discussion

2.3.1. Nanoparticles synthesis and characterisation

TEM (**Figure 2.5**) assessed the morphology of synthesised nanoparticles. Homogeneous size distribution is observed, with an average particle diameter of 11.55 ± 4.23 nm and 52.83 ± 8.27 nm, for TiO_2 and ZnO, respectively. Despite using the same synthesis method, ZnO presented a much bigger size, probably due to the difference in nucleation and growth kinetics in both syntheses [9].

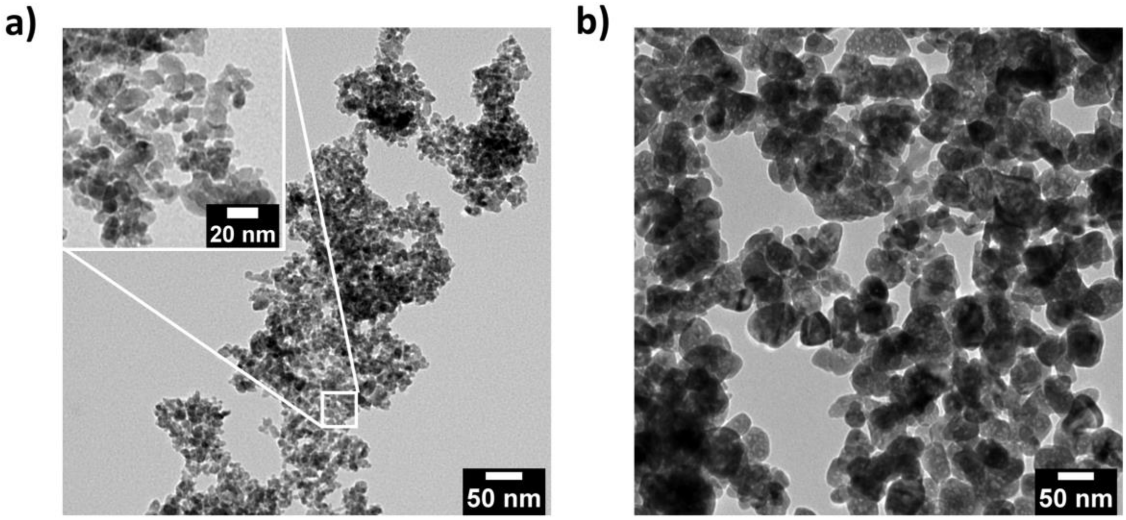

Figure 2.5. TEM images of pristine TiO_2 (a) with different magnification (inset) and ZnO (b) nanoparticles.

STEM-HAADF, offering higher contrast, was used to visualise the Au morphology and distribution on the surface of the semiconductors after sensitising the semiconductor nanoparticles (**Figure 2.6**). A homogenous dispersion of spherical Au NPs over the TiO_2 and ZnO surface was observed, with an average diameter of the Au component of 11.16 ± 1.57 nm on the TiO_2 surface and 20.61 ± 3.18 nm on the ZnO surface.

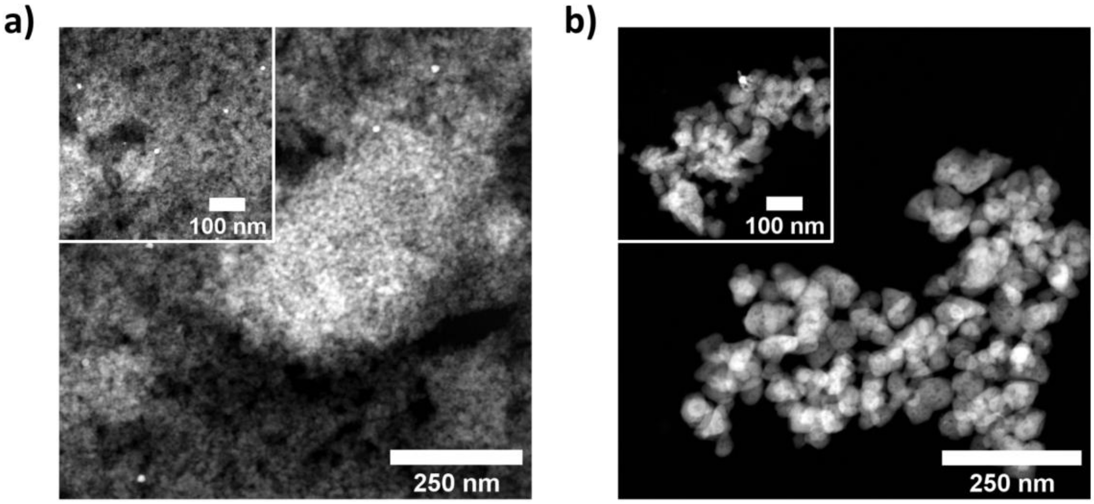

Figure 2.6. STEM-HAADF images of TiO_2:Au (a) and ZnO:Au (b) hybrid nanoparticles with different magnification.

XRD was performed to assess the crystal structure of the synthesised TiO_2 and ZnO nanoparticles and TiO_2:Au and ZnO:Au multicomponent nanoparticles (**Figure 2.7 a)** and **b)**). TiO_2 nanoparticles (**Figure 2.7 a)**) presented a crystalline structure composed mainly of anatase with a composition of 65%, being the rest of the components rutil 23% and brookite 12%, calculated by **Equations 2.1-2.3**. ZnO nanoparticles (**Figure 2.7 b)**) presented the positions of reflexes corresponding to the pure hexagonal wurtzite phase [24]. Additionally, after functionalising with Au, there was no significant difference in the crystal structure compared with the pristine semiconductors. On the other hand, no diffraction peaks of Au were detected neither in TiO_2:Au nor in ZnO:Au, which can be explained by the low amount of Au present in these samples (below the limit of detection).

DRS was used to evaluate the optical properties of the prepared samples to understand the differences in the photocatalytic performance of the semiconductor before and after functionalising with Au. For TiO_2 and TiO_2:Au (**Figure 2.7 c)**), both demonstrated similar behaviour in the UV range (200-400 nm). In the visible range (400-700 nm), the pristine TiO_2 nanoparticles reflected almost entirely (≈ 95%) of the radiation. The TiO_2:Au nanocomposite showed a reflectance below 75% with a minimum reflectance (≈ 63%) at 544 nm due to the LSPR of Au spherical nanoparticles, in good agreement with the literature [7,51]. Similar results are observed in the reflectance spectra of ZnO and ZnO:Au (**Figure 2.7 d)**). Both samples presented the same behaviour in the UV range, while the presence of Au on the surface of ZnO decreased the reflectance in the visible range from 88% to 69%.

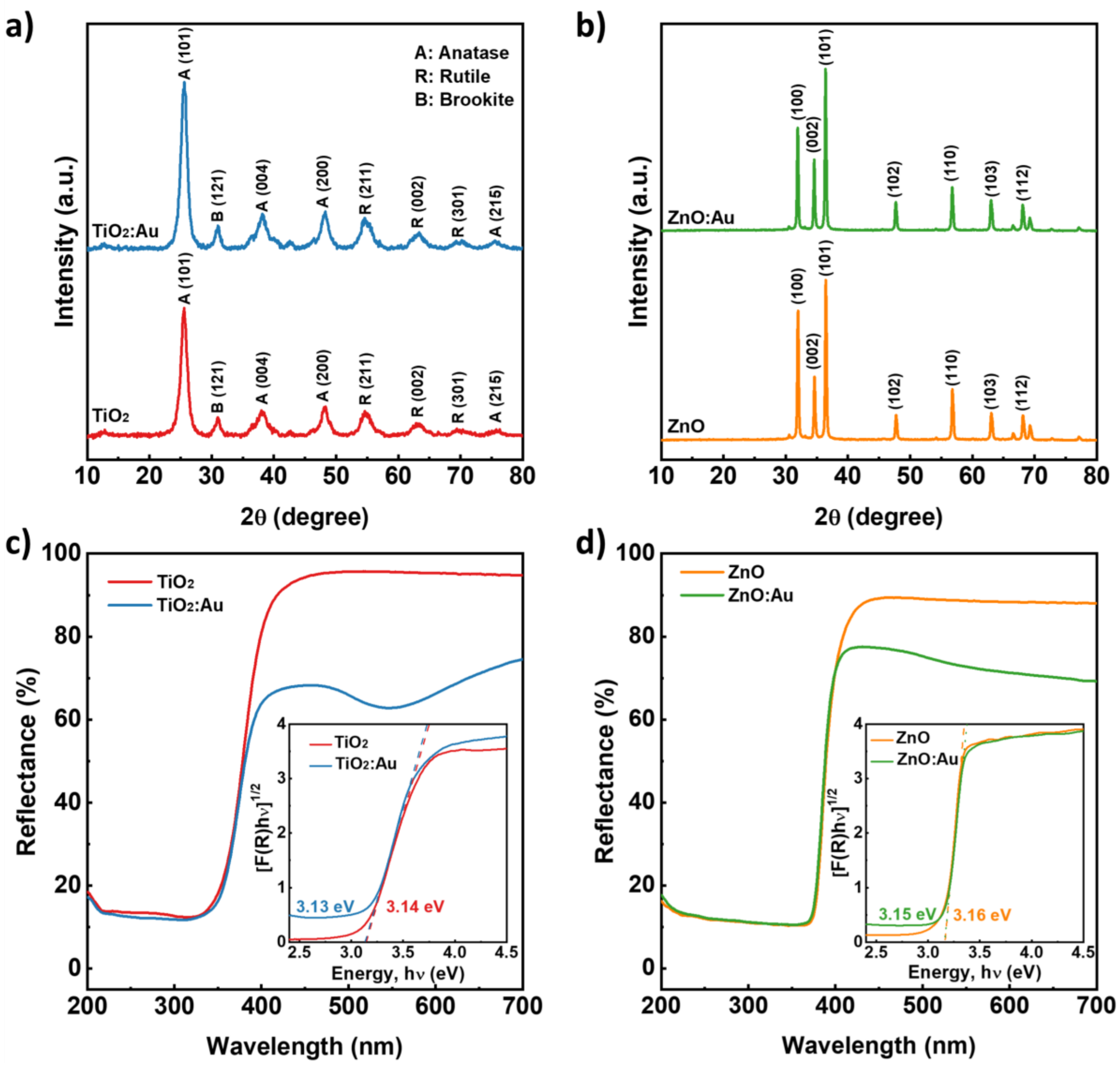

Figure 2.7. X-ray diffraction spectra (a, b) and UV-Vis reflectance spectra (c, d) with the estimation of the bandgap (inset) at $[F(R)h\upsilon]^{1/2} \rightarrow 0$ for pristine TiO_2 and TiO_2:Au nanoparticles (a, c) and ZnO and ZnO:Au nanoparticles (b, d).

The bandgap of all the samples was estimated from the DRS spectrum through Tauc plot method and after line fitting in the linear region 3.2-3.5 eV, shown in the inset graph of **Figures 2.7 c)** and **d)** and **Table 2.2**. The pristine TiO_2 nanoparticle presented a bandgap of 3.14 eV, typical for TiO_2 (3.0 to 3.2 eV) [52]. The TiO_2:Au showed a lower effective bandgap than pure TiO_2, 3.13 eV. Similar results are observed for ZnO:Au nanoparticle, which possessed a slightly lower effective bandgap (3.15 eV) than the pristine ZnO nanoparticle (3.16 eV). A decrease of the bandgap in semiconductors after functionalising with Au is related to the absorption of longer wavelengths, and the amount of Au can affect this reduction, as previously reported for other TiO_2:Au [7,53,54] and ZnO:Au [55,56] multicomponent nanoparticles. However, we did not observe a substantial change, and the slight difference could also be attributed to the measurement's precision or the low amount of Au in samples.

Table 2.2. Summary of the characteristics of TiO_2, TiO_2:Au, ZnO, and ZnO:Au nanoparticles.

	TiO_2	**TiO_2:Au**	**ZnO**	**ZnO:Au**
Particle size (nm)	11.55 ± 4.23	-	52.83 ± 8.27	-
Bandgap (eV)	3.14 ± 0.04	3.13 ± 0.04	3.16 ± 0.09	3.15 ± 0.17
Surface area (m^2/g)	152	144	8	8
Zeta-Potential at neutral media (mV)	-36 ± 0.41	-35 ± 0.47	38 ± 0.23	28 ± 1.22
Point of zero charge	6.1 ± 0.06	6.2 ± 0.03	8.2 ± 0.20	8.2 ± 0.30
Hydrodynamic size (nm)	251 ± 12.64	370 ± 35.35	517 ± 5.18	548 ± 10.46

The surface characteristics of all samples were assessed by N_2 adsorption-desorption isotherm measurements, as presented in **Figure 2.8 a)** and **b)**. **Table 2.2** shows the specific surface area of each sample calculated by Brunauer-Emmett-Teller (BET) method [46]. It is observed that the N_2 adsorption-desorption isotherms of TiO_2 (**Figure 2.8 a)**) and ZnO (**Figure 2.8 b)**) could be classified as type IV showing mesoporous characteristics [46,57] and type II, indicating non-porous or macroporous solid [46,57], respectively. Taking into account IUPAC classification, the hysteresis loops of TiO_2 and ZnO had different shapes and were considered type H1 [46] and H3 [46], respectively, indicating the formation of pores due to the agglomeration of particles [46,57]. TiO_2 presented a much higher specific surface area (152 m^2/g) than ZnO (8 m^2/g) due to its smaller particle size and mesopores formed by particles' agglomeration. Additional details of the BET analysis, as well as the pressure range used and the goodness of fit obtained, are shown in **Table 2.3**. This indicated that TiO_2 had an additional area than ZnO to contact with pollutants in the solution during the photocatalysis. Additionally, incorporating Au on the surface of TiO_2 and ZnO did not affect their surface characteristics in isotherms or specific surface areas.

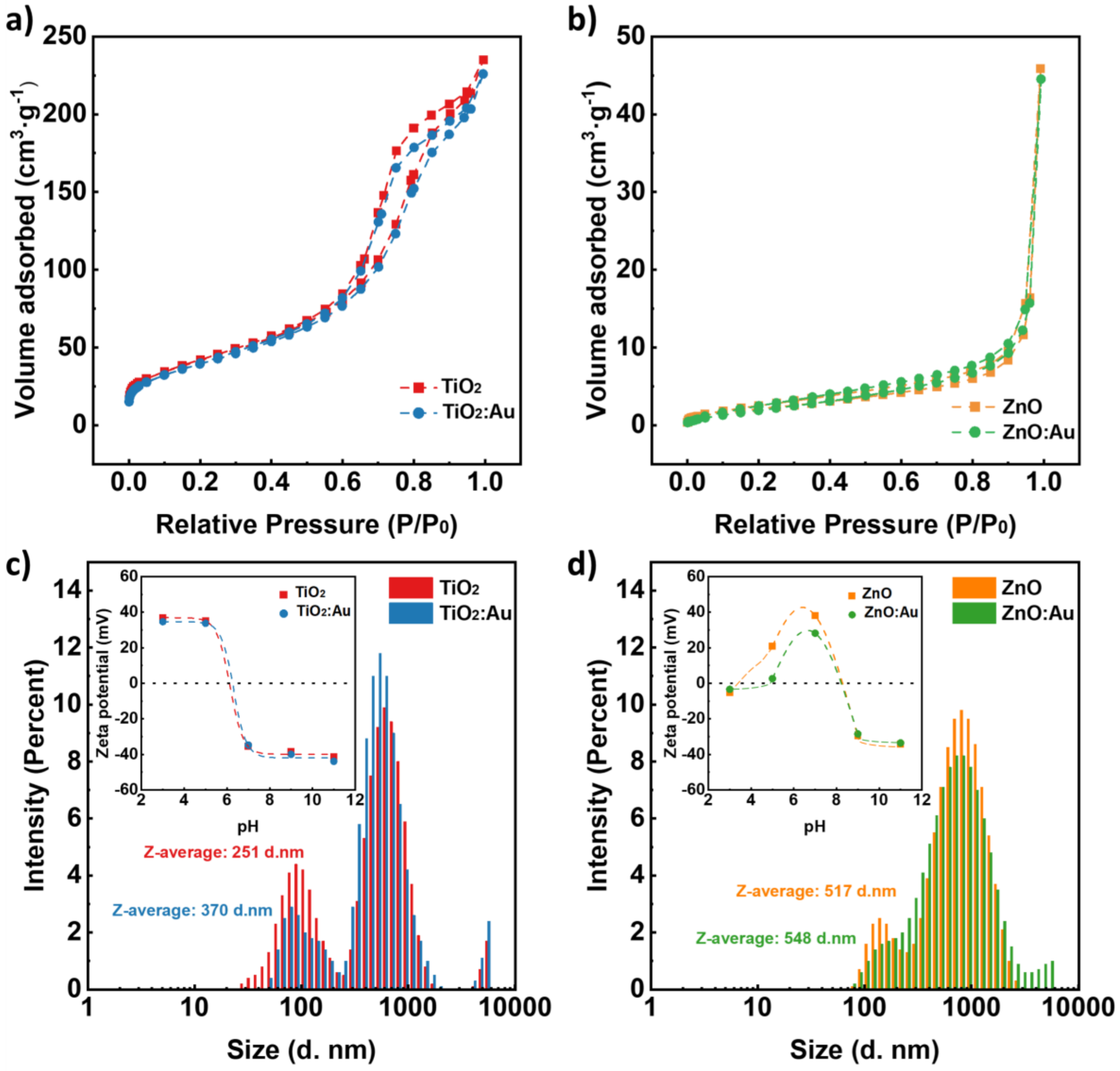

Figure 2.8. N_2 adsorption-desorption isotherms (a, b) and the intensity size distribution and respective Z-average hydrodynamic size (c, d) with zeta potential measurements (inset) performed at different pHs (3, 5, 7, 9, and 11) for pristine TiO_2 and TiO_2:Au nanoparticles (a, c) and ZnO and ZnO:Au nanoparticles (b, d).

Table 2.3. Surface area (S_{BET}), analysis pressure range ($\Delta P/P_0$), goodness of fit (R^2), microporous surface (S_{micro}), external surface (S_{ext}), microporous volume (V_{micro}) and total volume (V_T) for TiO_2, TiO_2:Au, ZnO, and ZnO:Au nanoparticles.

Sample	**S_{BET} (m^2/g)**	**$\Delta P/P_0$**	**R^2**	**S_{micro} (m^2/g)**	**S_{ext} (m^2/g)**	**V_{micro} (cm^3/g)**	**V_T (cm^3/g)**
TiO_2	152	0.029-0.299	0.999887	0	152	0	0.364
TiO_2:Au	144	0.028-0.299	0.999589	0	144	0	0.349
ZnO	8	0.049-0.3	0.998539	0	8	0	0.071
ZnO:Au	8	0.05-0.3	0.997843	0	8	0	0.068

The hydrodynamic size for all synthesised nanoparticles was studied by DLS, as shown in **Figures 2.8 c)** and **d)** and **Table 2.2**. The nanoparticles' size measured in DLS was larger than in TEM for all samples, attributed to the agglomeration of the nanoparticles in aqueous media [58]. On the other hand, ZnO possessed a bigger hydrodynamic size than TiO_2. Regarding TiO_2 and TiO_2:Au nanoparticles (**Figure 2.8 c)**), the hydrodynamic diameter was 251 ± 12.64 nm and 370 ± 35.35 nm (**Table 2.2**), respectively. The results of ZnO and ZnO:Au nanoparticles (**Figure 2.8 d)**) showed a diameter of 517 ± 5.18 nm and 548 ± 10.46 nm (**Table 2.2**), respectively. In both cases, the presence of Au on the semiconductors nanoparticle surface did not significantly change the size distribution when compared with the pristine semiconductors.

Zeta-potential of all the samples was carried out in a pH range of 3-11. TiO_2 and TiO_2:Au presented a very similar profile with an estimated point of zero charge (PZC) [59] around pH = 6 for both samples (**Figure 2.8 c)** and **Table 2.2**). The modulus of the Zeta-potential increased when separating from this pH, being positively charged at pH lower than the PZC and negatively charged at pH higher than the PZC. Moreover, it is observed that the modulus of the Zeta-potential for both samples showed values higher than 30 mV for pH below 5 or above 7 where the nanoparticles had superior electrostatic stability [60,61], improving the nanoparticles' repulsions and preventing their aggregation and precipitation [60,62].

Regarding the ZnO and ZnO:Au nanoparticles (**Figure 2.8 d)** and **Table 2.2**), at low pH values (pH < 5), the zeta potential exhibited negative values due to the effect of the nanoparticles dissolution [63]. Both samples showed a very similar profile when pH increased above 7, with an estimated PZC [59] around pH = 8. The modulus of the Zeta-potential of both samples was higher than 30 mV at pH above 9 and around 7 where the nanoparticles had superior electrostatic stability [60,61].

2.3.2. Photogenerated ROS ($^{\bullet}OH$ and $^1O_2$) measurements

As it has been previously reported, the photocatalytic efficiency is highly dependent on the photogenerated ROS at the photocatalysts surface [49,64–66]. Hence, detecting and quantifying the ROS during photocatalysis is essential, allowing an understanding of the photocatalytic performance of different semiconductors. Shortly, when a semiconductor absorbs a photon under illumination with energy (h_ν) higher than its bandgap (E_g), an electron (e_{CB}^-) promoted from its valence band (VB) to conduction band (CB) leaving a positively charged hole (h_{VB}^{+}) which initiate the reduction and oxidation reaction of O_2 and H_2O adsorbed on the semiconductor surface and generate ROS such as $^{\bullet}O_2^{-}$ and $^{\bullet}OH$. This process of ROS generation can be expressed by the following equations (**Equation 2.6-2.10**) [65,67]:

$$Semiconductor \xrightarrow{h_{\upsilon}} h_{VB}^{+} + e_{CB}^{-} \qquad \textbf{(2.6)}$$

$$H_2O + h_{VB}^{+} \rightarrow {}^{\bullet}OH + H^{+} \qquad \textbf{(2.7)}$$

$$O_2 + e_{CB}^{-} \rightarrow {}^{\bullet}O_2^{-} \qquad \textbf{(2.8)}$$

$${}^{\bullet}O_2^{-} + h_{VB}^{+} \rightarrow {}^{1}O_2 \qquad \textbf{(2.9)}$$

$${}^{\bullet}O_2^{-} + H^{+} \rightarrow {}^{\bullet}OOH \qquad \textbf{(2.10)}$$

Firstly, it is essential to determine the possibility of the generation of ROS in the synthesised nanoparticles, TiO_2 and ZnO. Thus, a theoretical approach can be used by comparing the energy levels of the valence band (VB) and conduction band (CB) of nanoparticles with the standard redox potential (E^0) of these ROS. The redox potential for the dissolved oxygen/superoxide couple ($O_2/^{\bullet}O_2^{-}$) is -0.16 eV (E^0 vs NHE), for the ($^{\bullet}O_2^{-}/^{1}O_2$) couple is 0.65 eV ($E^0$ vs NHE) and for the $H_2O/^{\bullet}OH$ couple is 2.32 eV (E^0 vs NHE). The conduction band (CB) and valence band (VB) edge positions of TiO_2 and ZnO nanoparticles were estimated according to the concept of electronegativity by **Equation 2.11-2.12** [64,68]:

$$E_{CB} = X - E_e + \frac{E_g}{2} \qquad \textbf{(2.11)}$$

$$E_{VB} = E_g - E_{CB} \qquad \textbf{(2.12)}$$

where E_{CB} and E_{VB} are the CB and VB edge potential, respectively, X is the electronegativity of the semiconductor (5.83 eV for TiO_2 and 5.57 eV for ZnO [69], respectively), which is the geometric mean of the electronegativity of the constituent atoms [64,68]. E_e is the energy of free electrons on the hydrogen scale (about 4.5 eV), and E_g is the band gap energy of the semiconductor [64,68].

The calculated CB and VB edge positions for TiO_2 nanoparticles were -0.24 eV and 2.9 eV, and for ZnO nanoparticles are -0.33 eV and 2.83 eV. Thus, the excited electrons in the conduction band and the holes in the valence band of the synthesised TiO_2 and ZnO can theoretically initiate the redox reactions and generate these ROS. Hence, experiments were conducted to detect and quantify the generated ROS. The $^{\bullet}OH$ radical was detected by the hydroxylation reaction of TA, while singlet oxygen ($^1O_2$) was determined by the histidine test as an indirect way to quantify the generated $^{\bullet}O_2^-$ radical [64].

The generation of hydroxyl radical ($^{\bullet}OH$) for TiO_2 and ZnO nanoparticles, as shown in **Figure 2.9 a)**, increased during the 60 min of UV irradiation. Additionally, the results demonstrated that ZnO nanoparticles generated six times more hydroxyl ($^{\bullet}OH$) radical than TiO_2 nanoparticles did under the same conditions, indicating the stronger oxidation ability of the ZnO nanoparticle. This higher quantity of $^{\bullet}OH$ could be attributed to the oxygen vacancies on the ZnO surface [9,10], which enhanced the water dissociation, improving the generation of $^{\bullet}OH$ [49].

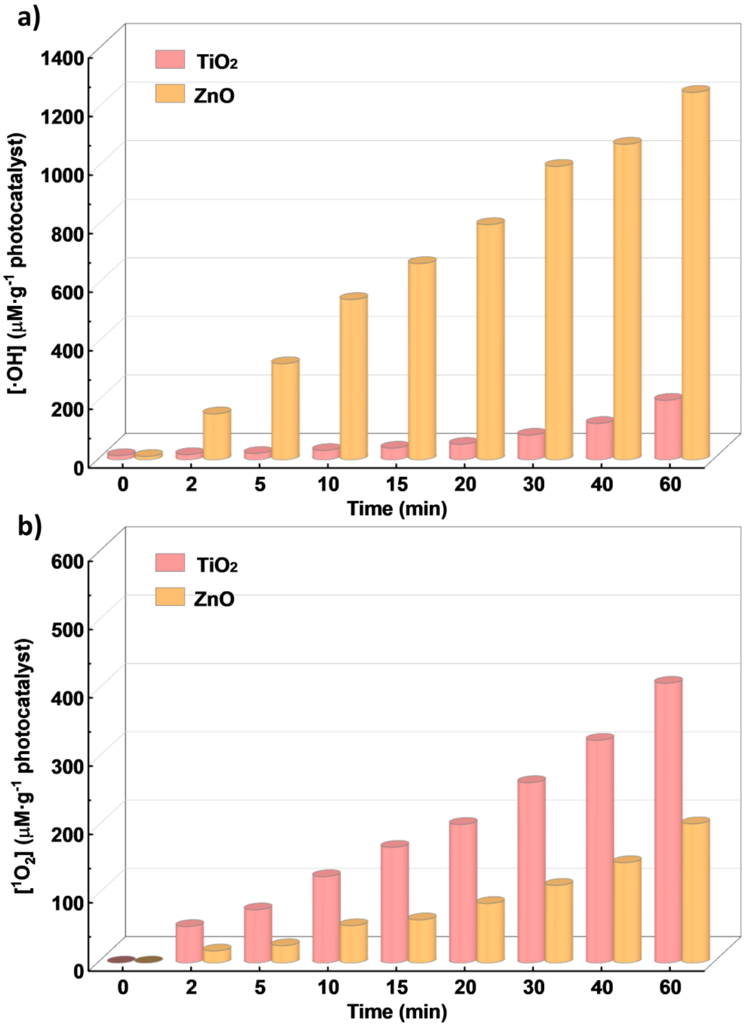

Figure 2.9. Quantification of photogenerated hydroxyl radical ($^{\bullet}OH$) (a) and singlet oxygen ($^1O_2$) (b) by TiO_2 and ZnO under 60 min of UV radiation.

The same tendency of the photogenerated singlet oxygen ($^1O_2$) for TiO_2 and ZnO was observed (**Figure 2.9 b)**). All the samples showed an increase in the production of $^1O_2$ over irradiation time. In contrast to the formation of $^{\bullet}OH$ radical, TiO_2 nanoparticles generated approximately two times more $^1O_2$ than ZnO under the same conditions. It should be noted that this measurement is an indirect way to quantify $^{\bullet}O_2^-$ and the capacity to form $^1O_2$, depending on the VB edge positions of the semiconductor. TiO_2 had VB edge positions at 2.9 eV vs 2.83 eV for ZnO, enhancing the oxidation of $^{\bullet}O_2^-$ to $^1O_2$ (**Equation 2.9**). On the other hand, a part of $^{\bullet}O_2^-$ formed by ZnO could react with H^+ (**Equation 2.10**) to form another type of ROS due to the high quantity of H^+ produced by ZnO (**Equation 2.7**), as mentioned before.

In general, ZnO nanoparticles generated more significant amount of ROS than TiO_2 nanoparticles, indicating that ZnO had more active centres than TiO_2 for photocatalysis despite its lower surface area. This may be partially attributed to the few anatase phase composition, only 65%, in the crystalline structure of TiO_2, which is the most photoactive phase in TiO_2 [4,5], and the oxygen vacancies on the ZnO surface [9,10].

2.3.3. Photocatalytic degradation under UV radiation

The photocatalytic activity of the produced nanoparticles under UV radiation was assessed for four different pollutants: CLQ, PAR, DCF, and CIP (**Figure 2.10** and **Table 2.4)**. **Table 2.4** shows the apparent reaction rate (*k*) calculated by **Equation 2.5** for the different nanoparticles. The photolysis of the target pollutants as controls was performed under UV radiation (**Figure 2.11**). In the absence of nanoparticles, there was minimal degradation of the four pollutants under UV radiation. A comparison of the photocatalytic activity of TiO_2 and ZnO under the same condition for pollutant removal (pH, photocatalysts and pollutant concentration, illumination condition, among others) is presented in **Figure 2.10 c)**. Although both TiO_2 and ZnO nanoparticles had similar bandgaps showing similar UV absorption during photocatalysis (**Figure 2.7 c)** and **d)**), very different behaviour was observed for the same pollutant under the same experimental conditions.

Since the pH of the solution can determine the surface charge and agglomeration of the photocatalysts, the generation of ROS and the structural form of pollutants molecule [4,70], all the solutions of the target pollutant used for this work were under the neutral condition. Considering the zeta-potential results, the surface charge was negative for TiO_2 and positive for ZnO (**Table 2.2**) at this pH, which correlates with the charge interaction with the pollutants and, therefore, the difference in adsorption. Under the experiment's fixed conditions, it is expected that the adsorption behaviour of pollutants on the surface of the photocatalyst – which is the first step for pollutant removal [4,70], together with the ROS formation, will be ultimately the main parameters that dictate the photocatalytic efficiency.

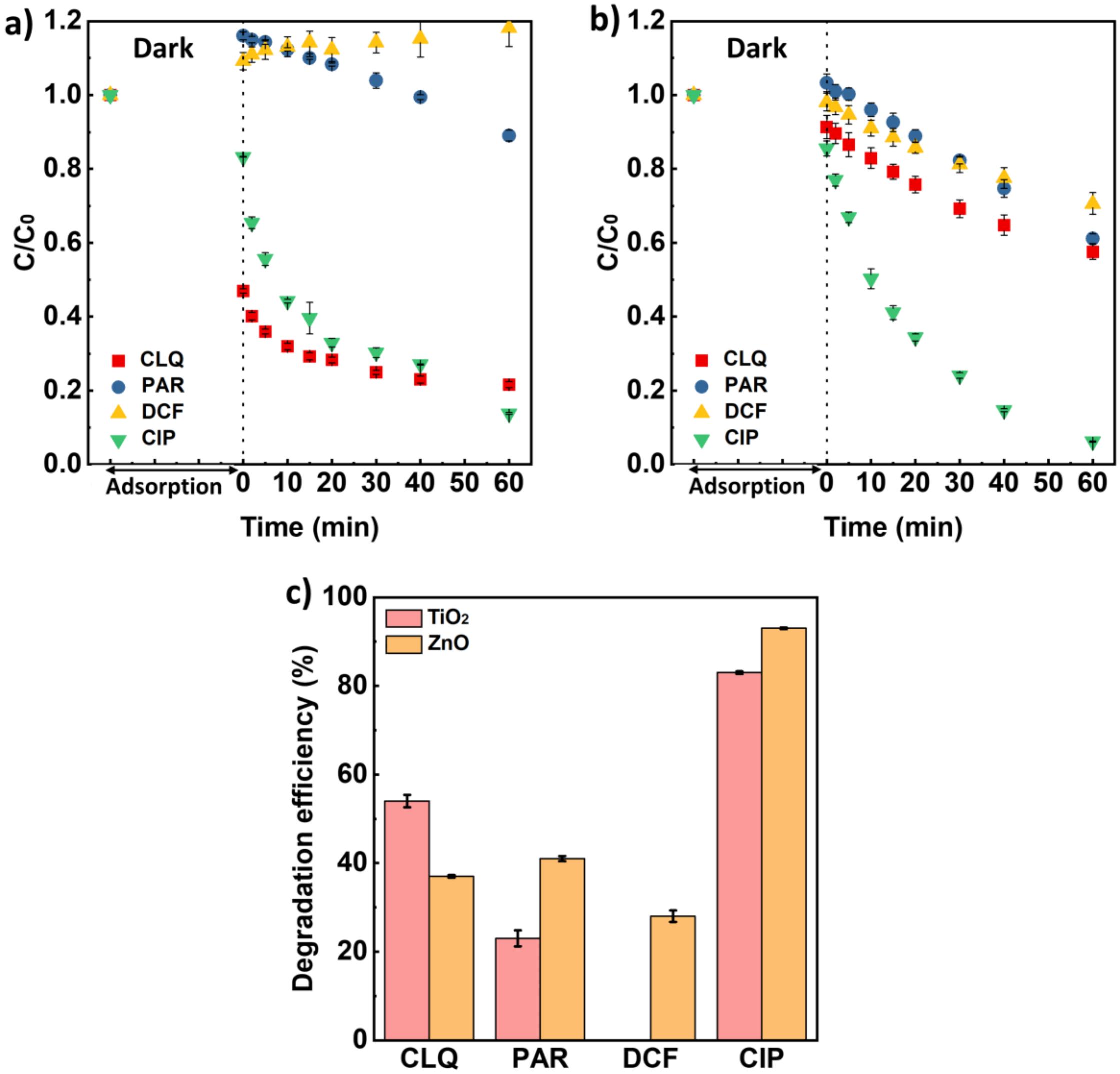

Figure 2.10. Photocatalytic degradation with TiO_2 (a) and ZnO (b) and comparison of degradation efficiency (%) between TiO_2 and ZnO (c) for CLQ (30 mg/L), PAR (15 mg/L), DCF (30 mg/L) and CIP (5 mg/L) removal under 60 min of UV radiation.

Table 2.4. CLQ, PAR, DCF, and CIP degradation efficiencies (DE) and corresponding apparent reaction rate constants (*k*) under 60 min of UV radiation for TiO_2 and ZnO.

Sample	Pollutant	$k \times 10^3$ (min^{-1})	DE (%)
TiO_2	CLQ	17.0 ± 0.7	54 ± 1.4
	PAR	4.1 ± 0.3	23 ± 1.8
	DCF	-	-
	CIP	32.4 ± 0.3	83 ± 0.3
ZnO	CLQ	8.3 ± 0.0	37 ± 0.3
	PAR	8.3 ± 0.3	41 ± 0.6
	DCF	5.9 ± 0.2	28 ± 1.3
	CIP	43.3 ± 0.6	94 ± 0.2

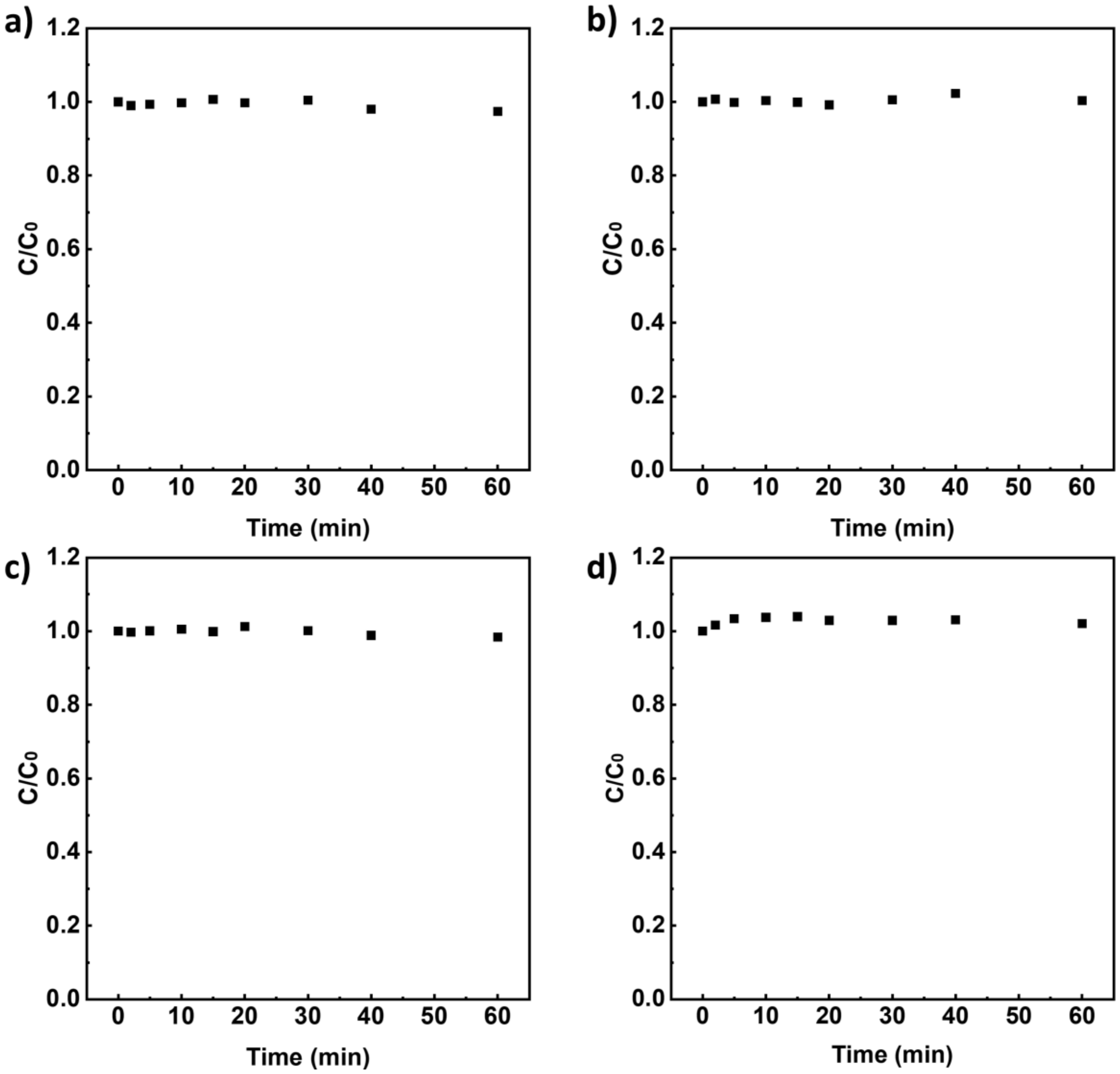

Figure 2.11. Photolysis assay of CLQ (30 mg/L) (a), PAR (15 mg/L) (b), DCF (30 mg/L) (c) and CIP (5 mg/L) (d) under 60 min of UV radiation.

Regarding chloroquine phosphate (CLQ) degradation, 53% of CLQ was adsorbed by TiO_2 in the dark and only 8.3% by ZnO. Despite generating higher ROS quantity, ZnO showed a degradation efficiency of 37% for CLQ removal with $k = 8.3\times10^{-3}$ min^{-1}, while TiO_2 degraded nearly 54% of CLQ with $k = 17\times10^{-3}$ min^{-1} under the same time. The high adsorption of CLQ on TiO_2 compared to ZnO is due to the electrostatic interaction (CLQ has pKa = 8.4 presenting cationic form [25]), which seemed to be the main reason for this difference in degradation efficiency. Furthermore, the much higher surface area of TiO_2 also played an important role in the electrostatic attraction during this adsorption process.

Regarding paracetamol (PAR) degradation, there was minimal PAR adsorbed on TiO_2 and ZnO surfaces under dark conditions. ZnO showed a degradation efficiency of 41% for PAR removal, higher than the 23% obtained with TiO_2 nanoparticles. ZnO also presented higher kinetic constant, $k = 8.3\times10^{-3}$ min^{-1}, than TiO_2 with $k = 4.1\times10^{-3}$ min^{-1}. PAR has a pKa = 9.3, being neutral with a different resonance structure at a pH lower than pKa [31]. Therefore, the electrostatic interaction between PAR and the photocatalysts can be discarded as the main factor affecting the photocatalytic results. The higher photocatalytic efficiency of ZnO can be attributed to the phenol group in PAR chemical structure having a large affinity to ZnO nanoparticles [71]. On the other hand, PAR acted as a Lewis base towards a positive ZnO surface during the experiments because the pH in the solution was lower than 9.3 [31]. Additionally, ZnO nanoparticles generated more ROS than TiO_2 under the same condition enhancing the photocatalytic performance.

For the diclofenac (DCF) degradation, no degradation nor adsorption of DCF were observed when using TiO_2 as a photocatalyst. On the contrary, ZnO degraded 28% of DCF with a degradation rate (k) 5.9×10^{-3} min^{-1} under the same condition. DCF has pKa = 4.1 being anionic form [37,39] during the experiments, which promoted an electrostatic repulsion between anionic DCF and negatively charged TiO_2 surface, opposite to ZnO nanoparticles, which inhibited the contact with formed ROS on the surface, reducing the photocatalytic efficiency.

Regarding ciprofloxacin (CIP) degradation, TiO_2 and ZnO presented similar adsorption of CIP under dark conditions, 17% and 16%, respectively. The degradation efficiency for TiO_2 and ZnO was 83% and 94%, respectively. The degradation rate (k) for TiO_2 and ZnO was 32.4×10^{-3} and 43.3×10^{-3} min^{-1}. During the experiments, CIP presented zwitterionic form [6,39] due to its pKa1= 6 and pKa2=8.7 [39]. This indicated that CIP molecules could be adsorbed on the surface of TiO_2 and ZnO due to the electrostatic interaction, improving photocatalytic activity. On the other hand, the higher photocatalytic degradation presented by ZnO is explained by, the higher amount of ROS produced, as previously demonstrated.

TiO_2:Au and ZnO:Au multicomponent nanoparticles were also tested under UV radiation, as shown in **Figure 2.12 a)** and **b)** and **Table 2.5**. There was no significant change in the photocatalytic degradation of the same pollutant between TiO_2 and TiO_2:Au (**Figure 2.12 a)**) nor between ZnO and ZnO:Au (**Figure 2.12 b)**).

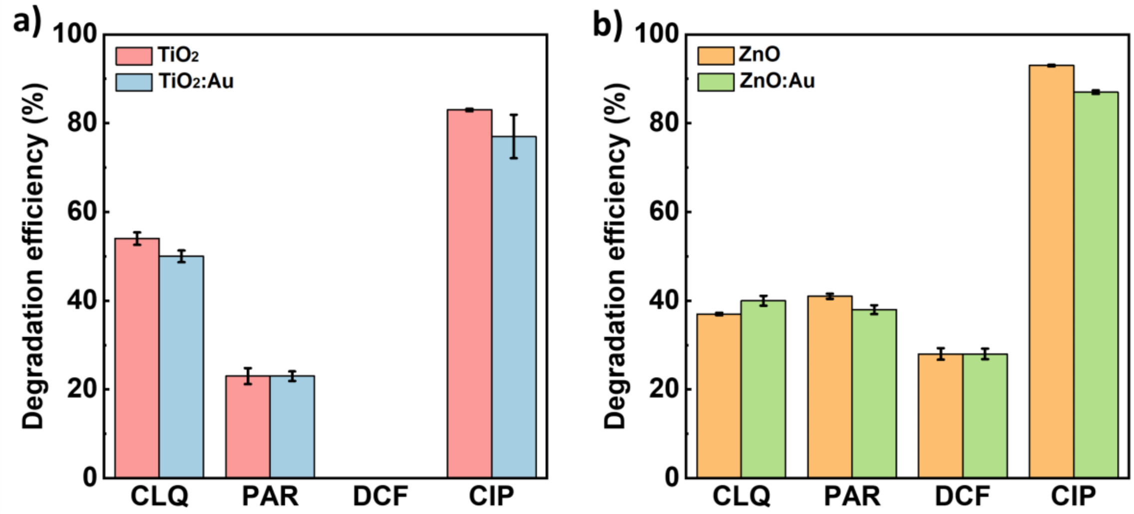

Figure 2.12. Comparison of degradation efficiency (%) between TiO_2 and TiO_2:Au (a), ZnO and ZnO:Au (b) for CLQ (30 mg/L), PAR (15 mg/L), DCF (30 mg/L) and CIP (5 mg/L) removal under 60 min of UV radiation.

Table 2.5. CLQ, PAR, DCF, and CIP degradation efficiencies (DE) and corresponding apparent reaction rate constants (*k*) under 60 min of UV radiation for TiO_2:Au, and ZnO:Au.

Sample	Pollutant	$k \times 10^3$ (min^{-1})	DE (%)
TiO_2:Au	CLQ	15.1 ± 0.5	50 ± 1.3
	PAR	4.3 ± 0.5	23 ± 1.1
	DCF	-	-
	CIP	24.6 ± 4.5	77 ± 4.9
ZnO:Au	CLQ	8.9 ± 0.4	40 ± 1.1
	PAR	7.7 ± 0.4	38 ± 1.0
	DCF	5.7 ± 0.3	28 ± 1.2
	CIP	33.7 ± 0.8	87 ± 0.4

When comparing the degradation efficiency between TiO_2:Au and ZnO:Au for the same pollutant (**Table 2.5**), similar behaviours were observed in the comparison between TiO_2 and ZnO (**Figure 2.10 c)**). These similar behaviours can be attributed to the fact that the surface characteristic of pristine semiconductors was maintained (**Figure 2.8** and **Table 2.2**), and the sensitisation of Au only enhanced the plasmonic absorption in the visible region, therefore not influencing the photocatalytic properties under UV radiation.

Although the conditions applied in the literature change from work to work, and there is not a single study that compares all the pollutants tested here; **Table 2.6** and **Table 2.7** summarise some of those results and the different conditions applied to the target pollutants. These comparisons are not straightforward, but the comparative study allows contextualising of the results. The results are in line with previous results for PAR, DCF, and CIP despite the much lower light power used in this work except for DCF-TiO_2, where we did not observe a significant degradation.

Table 2.6. Comparison of degradation efficiency (DE) between the present work and previous works that used TiO_2 on CLQ, PAR, DCF and CIP degradation.

Pollutant	[Pollutant] (mg/L)	[Photocatalyst] (mg/mL)	UV Radiation	DE (%)	Time (min)	Ref.
CLQ	30	1	3.3 W/m^2 (8W)	54	60	Present work
PAR	50	1.33	6.4 W	50	170	[72]
PAR	20	0.4	250 W/m^2	71	180	[73]
PAR	15	1	3.3 W/m^2 (8W)	23	60	Present work
DCF	5	0.05	150W	30	60	[74]
DCF	30	0.35	20W	54	180	[36]
DCF	30	1	3.3 W/m^2 (8W)	-	60	Present work
CIP	5	1	15−17 W/m^2	75	30	[7]
CIP	33	1.5	125 W	85	30	[75]
CIP	5	1	3.3 W/m^2 (8W)	83	60	Present work

As previously mentioned, the use of CLQ has been increasing due to COVID-19 [26–28]. Hence, only a few works [25,29,76–80] reported on its degradation using different materials and approaches like the ones in our work. The utmost similar studies for CLQ degradation were based on the advanced oxidation processes (AOPs) [25,29]. Yi et al. [25] used PDINH/MIL-88A(Fe) composites which was the combination of metal-organic frameworks, MIL-88A(Fe), and semiconductor, 34,910-pyre- netetracarboxydiimine (PDINH), to remove CLQ through the synergistic effects of peroxydisulfate (PDS) photocatalytic activation. Despite the remarkable degradation efficiency under 30 min of visible radiation, 95.7%, the used materials, PDINH/MIL-88A(Fe), and processes using persulfate solution were more costly than ours. Furthermore, Electro-Fenton oxidation was reported on CLQ degradation showing a degradation efficiency of 92% after 60 min of reaction [29]. However, the electro-Fenton oxidation process required the electrical consumption, which was more complex and costly than our work.

Table 2.7. Comparison of degradation efficiency (DE) between the present work and previous works that used ZnO on the degradation of CLQ, PAR, DCF and CIP.

Pollutant	[Pollutant] (mg/L)	[Photocatalyst] (mg/mL)	UV Radiation	DE (%)	Time (min)	Ref.
CLQ	30	1	3.3 W/m^2 (8W)	37	60	Present work
PAR	200	1	20 W	70	180	[81]
PAR	7.5	0.5	40 W/m^2	90	180	[71]
PAR	15	1	3.3 W/m^2 (8W)	41	60	Present work
DCF	30	0.35	20 W	80	180	[36]
DCF	25	0.1	37 W/m^2 (500 W)	50	350	[82]
DCF	30	1	3.3 W/m^2 (8W)	28	60	Present work
CIP	0.3	1	17 W/m^2	100	45	[83]
CIP	10	0.15	9 W	100	140	[84]
CIP	5	1	3.3 W/m^2 (8 W)	93	60	Present work

Concerning PAR, DCF and CIP, the results show comparable results to previous works, producing in general higher degradation efficiencies under UV radiation using TiO_2 (**Table 2.6**) or ZnO (**Table 2.7**). Compared to experimental conditions used in our work, these results are expected as all the previous works used a much higher intensity of UV radiation [7,36,84,71–75,81–83] (in some cases more than one order of magnitude and therefore being a less cost-effective process) like the work of Silva et al. using 17 W/m^2 UV radiation for ciprofloxacin removal [83] or longer reaction time [36,71–73,81,82,84], like the work of Lozano-Morales et al. maintaining 180 min for paracetamol degradation [73].

2.3.4. Photocatalytic degradation under visible radiation

After the systematic comparison of the photocatalytic activity of synthesised TiO_2 and ZnO nanoparticles and their Au-sensitised versions under UV radiation, photocatalytic assays were also carried out under visible radiation. **Table 2.8** and **Figure 2.13** show the results. As controls, photolysis of the target pollutants (CLQ, PAR, DCF, and CIP) was performed under visible radiation (**Figure 2.14**). In the absence of nanoparticles, there was negligible degradation of the pollutants under visible radiation except for DCF, which was degraded by nearly 20% only during the first 20 min.

Table 2.8. CLQ, PAR, DCF, and CIP degradation efficiencies (DE) and corresponding apparent reaction rate constants (*k*) under 240 min of visible radiation for TiO_2:Au and ZnO:Au.

Sample	Pollutant	$k \times 10^3$ (min^{-1})	DE (%)
TiO_2:Au	CLQ	3.3 ± 0.6	70 ± 2.9
	PAR	3.7 ± 0.1	61 ± 1.0
	DCF	3.0 ± 0.2	53 ± 0.9
	CIP	2.0 ± 0.0	55 ± 0.7
ZnO:Au	CLQ	3.0 ± 0.0	54 ± 0.4
	PAR	5.7 ± 0.1	76 ± 0.3
	DCF	4.0 ± 0.1	57 ± 1.1
	CIP	5.7 ± 0.6	81 ± 2.9

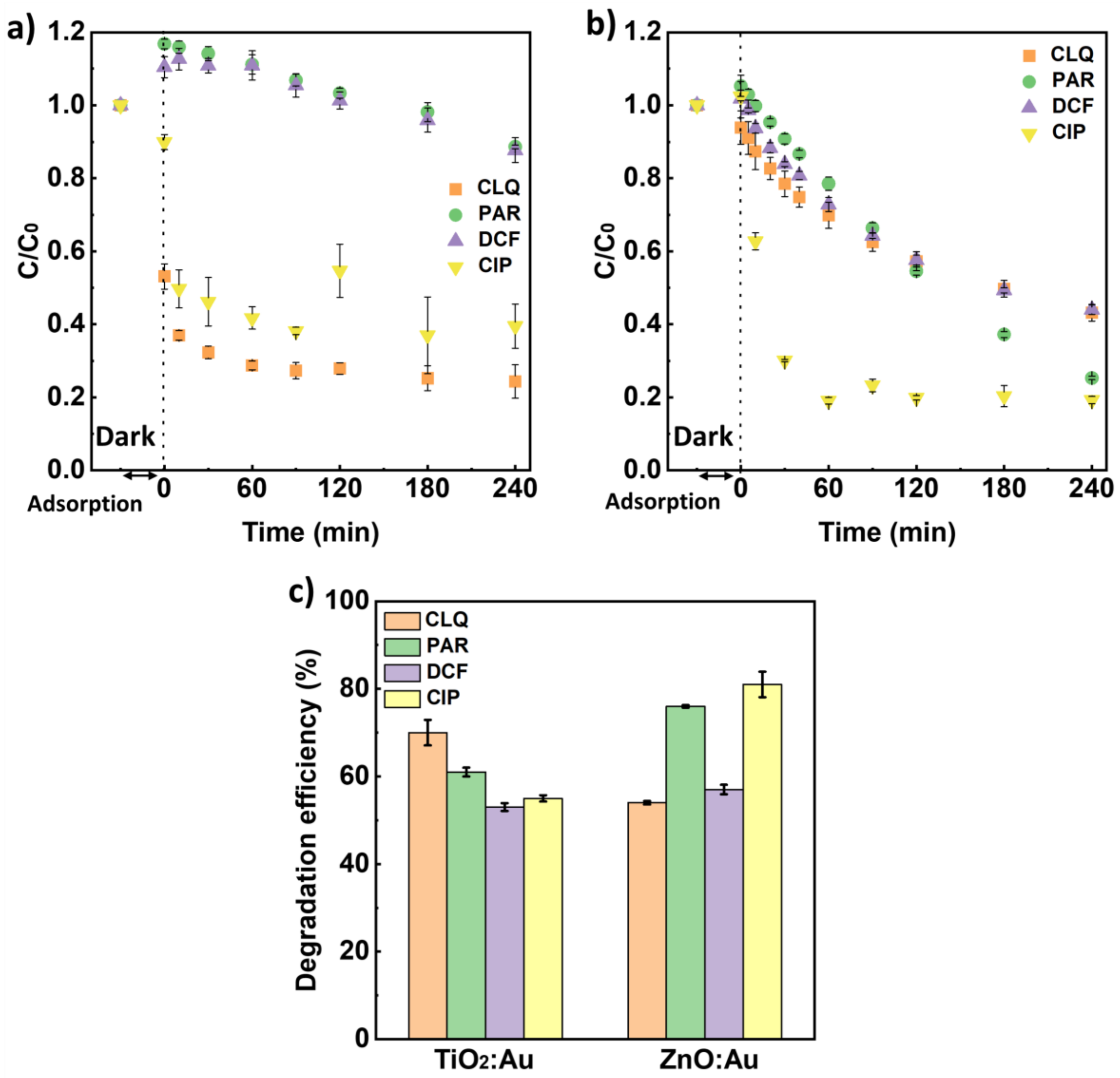

Figure 2.13. Photocatalytic degradation with TiO_2:Au (a) and ZnO:Au (b) and comparison of degradation efficiency (%) between TiO_2:Au and ZnO:Au (c) for CLQ (30 mg/L), PAR (15 mg/L), DCF (30 mg/L) and CIP (5 mg/L) removal under 240 min of visible radiation.

As presented in **Figure 2.13 a)** and **b)**, the incorporation of Au on the surface of TiO_2 and ZnO made them possible to produce the photocatalytic degradation of CLQ, PAR, DCF, and CIP under visible light due to the improvement of the absorption of longer solar wavelengths as well as the lower bandgap (**Figure 2.7 c)** and **d)**). Note that in the absence of Au, negligible degradation is produced, presenting only similar adsorption in the dark (for clarity, those results are therefore not included in the comparative).

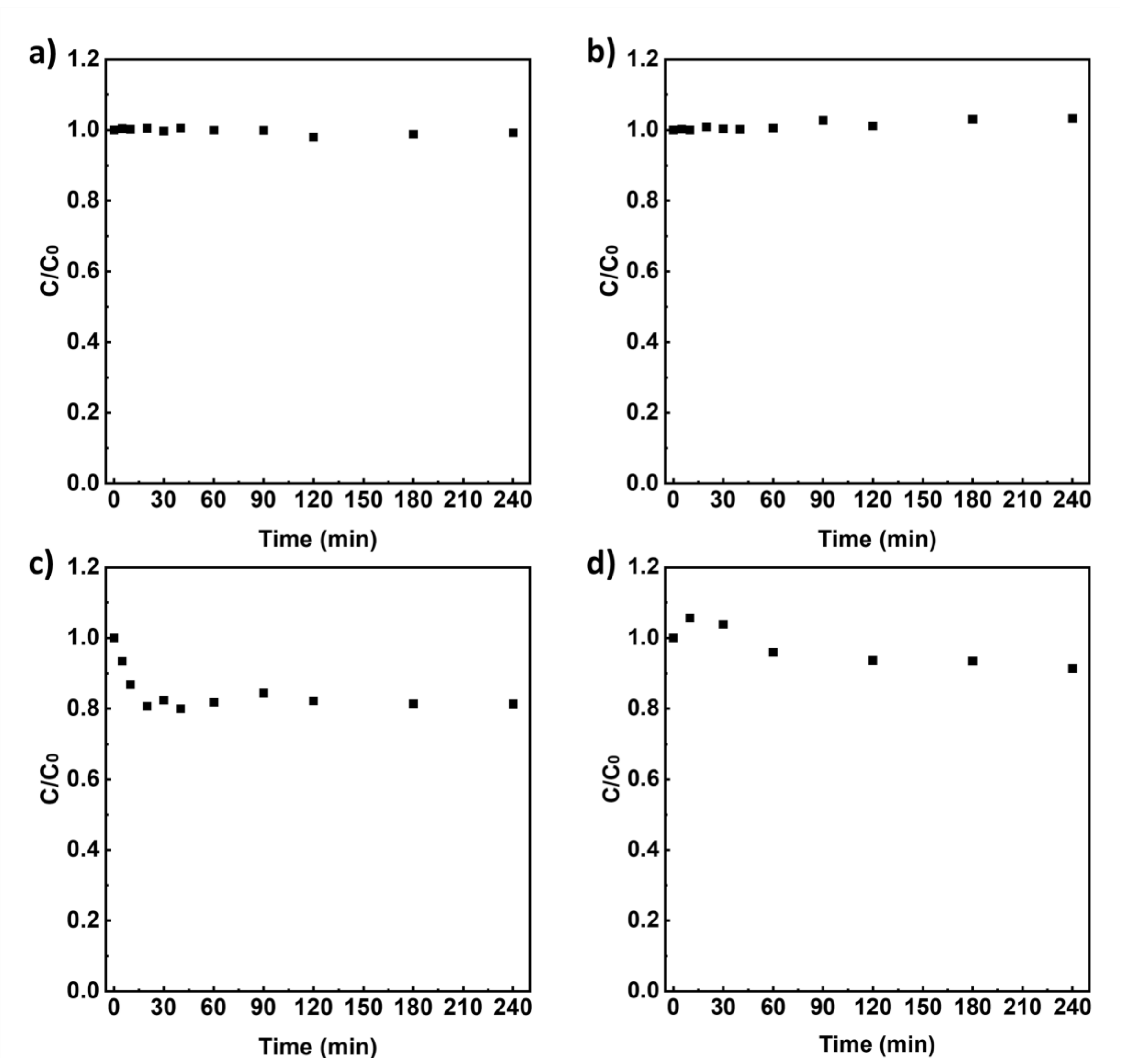

Figure 2.14. Photolysis assay of CLQ (30 mg/L) (a), PAR (15 mg/L) (b), DCF (30 mg/L) (c) and CIP (5 mg/L) (d) under 240 min of visible radiation.

Interestingly, when comparing the degradation efficiency between TiO_2:Au and ZnO:Au for the different pollutants under visible light (**Figure 2.13 c)**), a similar trend to the degradation under UV radiation shown above was observed (**Table 2.4**). This similar trend indicates that surface characteristics are maintained and play a substantial role in the photocatalytic processes. Regarding CLQ degradation, TiO_2:Au and ZnO:Au showed a degradation efficiency of 70 and 54%, with the kinetic constant (k) 3.3×10^{-3} and 3.0×10^{-3} min^{-1}. As exposed above, this is due to the high adsorption of cationic CLQ on the negatively charged TiO_2:Au surface, enhancing the photocatalytic efficiency. For PAR degradation, ZnO:Au showed a photocatalytic degradation of 76% with a $k = 5.7\times10^{-3}$ min^{-1}. TiO_2:Au presented lower degradation efficiency of PAR, 61%, with a $k = 3.7\times10^{-3}$ min^{-1}. As also mentioned, this difference could be due to the great affinity of the PAR molecule to ZnO:Au surface, improving photocatalytic performance. In terms of CIP degradation, ZnO:Au presented higher degradation efficiency and kinetic constant (81% and 5.7×10^{-3} min^{-1}) than TiO_2:Au (55% and 2.0×10^{-3} min^{-1}) due to the higher amount of generated ROS on the surface of ZnO:Au. Finally, for the DCF degradation, the ZnO:Au showed a degradation efficiency of 57%, slightly higher than the 53% obtained with TiO_2:Au. Surprisingly, DCF could be degraded by TiO_2:Au under visible radiation, which was not observed under UV radiation. The difference in illumination intensity between UV and xenon lamps applied in the assays could explain these results, indicating that under UV radiation some degradation also took place but was not detected due to the meagre power used in the assays.

2.4. Conclusions

TiO_2 and ZnO, TiO_2:Au and ZnO:Au were synthesised under the same conditions, using simple and low-cost synthesis methods, characterised, and the photocatalytic degradation of four different pharmaceuticals compared. The co-precipitation synthesis applied here yielded TiO_2 (11.55 ± 4.23 nm) and ZnO (52.83 ± 8.27 nm) nanoparticles with homogeneous size distribution, being TiO_2 with smaller particle size and, therefore, a higher specific surface area (152 m^2/g) than ZnO (8 m^2/g). These surface properties were maintained after Au functionalisation but reducing the band gap of the pristine semiconductors. Regarding the ROS generation over the surface of both nanoparticles, despite the difference in their surface area, ZnO(:Au) generated nearly 2.3 times more ROS than TiO_2(:Au).

Afterwards, four pharmaceuticals with different physicochemical properties were selected and tested for photocatalytic assays. A correlation was observed between the affinity of pollutants and nanoparticles' surface and the photocatalytic degradation efficiency and kinetics. This correlation was independent of the Au functionalisation of the nanoparticle and was highly related to the electrostatic attraction-repulsion. Under UV and at neutral pH, zwitterionic molecules such as CIP were highly degraded by all photocatalysts, a degradation efficiency of 83% and 94% for TiO_2 and ZnO. On the other hand, cationic molecules such as CLQ were superiorly degraded under TiO_2 showing a degradation efficiency of 54%. Moreover, anionic molecules such as DCF were more efficiently degraded by ZnO, with a degradation efficiency of 28%, but lowly or negligibly degraded by TiO_2. For the case of neutral molecules such as PAR, all nanocatalysts show degradation, although better for the

ZnO nanoparticles, attributed in this case to the higher amount of generated ROS. After Au functionalisation, TiO_2:Au and ZnO:Au presented similar photocatalytic behaviour of pharmaceuticals degradation as pristine semiconductors under UV radiation.

However, the sensitisation of semiconductors with Au made photocatalysis possible under visible light; the nanoparticles could absorb a higher amount of light (reflectance decreased from 94% to 74% for TiO_2:Au, and from 88% to 68% for ZnO:Au) and use it as an energy source to degrade the different pharmaceutical pollutants. The trend of efficiencies was very similar to the case observed under UV light, pointing out the significant influence on the pollutants' nanoparticle affinity and the higher ROS generation of the ZnO-based catalysts.

In short, this work indicates that the photocatalytic efficiency highly depends on the kind and capacity of ROS generation by the photocatalyst, the type of pollutants to degrade, and their interaction with the photocatalyst surface. This study makes a broad classification possible for selecting the best photocatalyst, or combinations of photocatalysts, for more efficient degradation of pharmaceuticals in polluted water bodies. Finally, photocatalytic degradation under visible light was remarkably enhanced using semiconductor:Au multicomponent nanoparticles that, with a small amount of added Au (0.05 wt. %), can use sunlight to generate similar pharmaceuticals degradation, making the process more cost-effective and sustainable.

2.5. References

1. Dey, S.; Bano, F.; Malik, A. Pharmaceuticals and Personal Care Product (PPCP) Contamination—a Global Discharge Inventory. In *Pharmaceuticals and Personal Care Products: Waste Management and Treatment Technology*; Elsevier Inc., 2019; pp. 1–26 ISBN 9780128161890, doi:10.1016/B978-0-12-816189-0.00001-9.

2. Cuerda-correa, E.M.; Alexandre-franco, M.F.; Fern, C. Antibiotics from Water. An Overview. *Water* **2020**, *12*, 102, doi:10.3390/w12010102.

3. Reyes, N.J.D.G.; Geronimo, F.K.F.; Yano, K.A. V.; Guerra, H.B.; Kim, L.-H. Pharmaceutical and Personal Care Products in Different Matrices: Occurrence, Pathways, and Treatment Processes. *Water* **2021**, *13*, 1159, doi:10.3390/ w13091159.

4. Koe, W.S.; Lee, J.W.; Chong, W.C.; Pang, Y.L.; Sim, L.C. An Overview of Photocatalytic Degradation: Photocatalysts, Mechanisms, and Development of Photocatalytic Membrane. *Environ. Sci. Pollut. Res.* **2020**, *27*, 2522–2565, doi:10.1007/s11356-019-07193-5.

5. Byrne, C.; Subramanian, G.; Pillai, S.C. Recent Advances in Photocatalysis for Environmental Applications. *J. Environ. Chem. Eng.* **2018**, *6*, 3531–3555, doi:10.1016/j.jece.2017.07.080.

6. Anastasiya Kutuzova, Tetiana Dontsova, W.K. Application of TiO_2-Based Photocatalysts to Antibiotics Degradation: Cases of Sulfamethoxazole, Trimethoprim and Ciprofloxacin. *Catalysts* **2021**, *11*, 728, doi:10.3390/catal11060728.

7. Martins, P.; Kappert, S.; Le, H.N.; Sebastian, V.; Kühn, K.; Alves, M.; Pereira, L.; Cuniberti, G.; Melle-franco, M.; Lanceros-Méndez, S. Enhanced Photocatalytic Activity of Au/TiO_2 Nanoparticles against Ciprofloxacin. *Catalysts* **2020**, *10*, 234, doi:10.3390/catal10020234.

8. Reguera, J.; Zheng, F.; Shalan, A.E.; Lizundia, E. Upcycling Discarded Cellulosic Surgical Masks into Catalytically Active Freestanding Materials. *Cellulose* **2022**, *29*, 2223–2240, doi:10.1007/s10570-022-04441-9.

9. Zhang, F.; Wang, X.; Liu, H.; Liu, C.; Wan, Y.; Long, Y.; Cai, Z. Recent Advances and Applications of Semiconductor Photocatalytic Technology. *Appl. Sci.* **2019**, *9*, 2489, doi:10.3390/app9122489.

10. Abdullah, F.H.; Bakar, N.H.H.A.; Bakar, M.A. Current Advancements on the Fabrication, Modification, and Industrial Application of Zinc Oxide as Photocatalyst in the Removal of Organic and Inorganic Contaminants in Aquatic Systems. *J. Hazard. Mater.* **2022**, *424*, 127416, doi:10.1016/j.jhazmat.2021.127416.
11. Udom, I.; Ram, M.K.; Stefanakos, E.K.; Hepp, A.F.; Goswami, D.Y. One Dimensional-ZnO Nanostructures: Synthesis, Properties and Environmental Applications. *Mater. Sci. Semicond. Process.* **2013**, *16*, 2070–2083, doi:10.1016/j.mssp.2013.06.017.
12. Vasilachi, I.C.; Asiminicesei, D.M.; Fertu, D.I.; Gavrilescu, M. Occurrence and Fate of Emerging Pollutants in Water Environment and Options for Their Removal. *Water* **2021**, *13*, 181, doi:10.3390/w13020181.
13. Zhang, X.; Chen, Y.L.; Liu, R.-S.; Tsai, D.P. Plasmonic Photocatalysis. *Reports Prog. Phys.* **2013**, *76*, 046401, doi:10.1088/0034-4885/76/4/046401.
14. Wang, C.; Astruc, D. Nanogold Plasmonic Photocatalysis for Organic Synthesis and Clean Energy Conversion. *Chem. Soc. Rev.* **2014**, *43*, 7188–7216, doi:10.1039/c4cs00145a.
15. Shi, Y.; Ma, J.; Chen, Y.; Qian, Y.; Xu, B.; Chu, W.; An, D. Recent Progress of Silver-Containing Photocatalysts for Water Disinfection under Visible Light Irradiation: A Review. *Sci. Total Environ.* **2022**, *804*, 150024, doi:10.1016/j.scitotenv.2021.150024.
16. Janczarek, M.; Kowalska, E. On the Origin of Enhanced Photocatalytic Activity of Copper-Modified Titania in the Oxidative Reaction Systems. *Catalysts* **2017**, *7*, 317, doi:10.3390/catal7110317.
17. Wang, M.; Ye, M.; Iocozzia, J.; Lin, C.; Lin, Z. Plasmon-Mediated Solar Energy Conversion via Photocatalysis in Noble Metal/Semiconductor Composites. *Adv. Sci.* **2016**, *3*, 1600024, doi:10.1002/advs.201600024.
18. Dodekatos, G.; Schünemann, S.; Tüysüz, H. Surface Plasmon-Assisted Solar Energy Conversion. *Top. Curr. Chem.* **2016**, *371*, 215–252, doi:10.1007/128_2015_642.
19. Gupta, B.; Melvin, A.A.; Matthews, T.; Dash, S.; Tyagi, A.K. TiO_2 Modification by Gold (Au) for Photocatalytic Hydrogen (H_2) Production. *Renew. Sustain. Energy Rev.* **2016**, *58*, 1366–1375, doi:10.1016/j.rser.2015.12.236.

20. Bortamuly, R.; Miah, A.T.; Saikia, P. Development of CeO_2- and TiO_2-Based Au Nanocatalysts for Catalytic Applications. In *Noble Metal-Metal Oxide Hybrid Nanoparticles*; Matthew Deans, 2019; pp. 517–533 ISBN 9780128141342, doi: 10.1016/B978-0-12-814134-2.00024-3.

21. Sankar, M.; He, Q.; Engel, R. V; Sainna, M.A.; Logsdail, A.J.; Roldan, A.; Willock, D.J.; Agarwal, N.; Kiely, C.J.; Hutchings, G.J. Role of the Support in Gold-Containing Nanoparticles as Heterogeneous Catalysts. *Chem. Rev.* **2020**, *12*, 3890–3938, doi:10.1021/acs.chemrev.9b00662.

22. Wang, C.; Astruc, D. Nanogold Plasmonic Photocatalysis for Organic Synthesis and Clean Energy Conversion. *Chem. Soc. Rev.* **2014**, *43*, 7188–7216, doi:10.1039/c4cs00145a.

23. Buraso, W.; Lachom, V.; Siriya, P.; Laokul, P. Synthesis of TiO_2 Nanoparticles via a Simple Precipitation Method and Photocatalytic Performance. *Mater. Res. Express* **2018**, *5*, 115003, doi:10.1088/2053-1591/aadbf0.

24. Vlazan, P.; Irina-Moisescu, C.; Miron, I.; Sfirloaga, P.; Grozescu, I. Structural Characterization of ZnO Nanoparticles Synthesized by Co-Precipitation and Sol-Gel Method. *Optoelectron. Adv. Mater. Rapid Commun.* **2015**, *9*, 1139–1142.

25. Yi, X.; Ji, H.; Wang, C.; Li, Y.; Li, Y.; Zhao, C.; Wang, A.; Fu, H.; Wang, P.; Zhao, X.; et al. Photocatalysis-Activated SR-AOP over PDINH/MIL-88A(Fe) Composites for Boosted Chloroquine Phosphate Degradation: Performance, Mechanism, Pathway and DFT Calculations. *Appl. Catal. B Environ.* **2021**, *293*, 120229, doi:10.1016/j.apcatb.2021.120229.

26. Zhang, X.; Li, Z.; Ye, J.; Lu, J.; Ye, L.L.; Zhang, C.; Liu, P.; Duan, D.D. Pharmacological and Cardiovascular Perspectives on the Treatment of COVID-19 with Chloroquine Derivatives. *Acta Pharmacol. Sin.* **2020**, *41*, 1377–1386, doi:10.1038/s41401-020-00519-x.

27. Salvi, R.; Patankar, P. Emerging Pharmacotherapies for COVID-19. *Biomed. Pharmacother.* **2020**, *128*, 110267, doi:10.1016/j.biopha.2020.110267.

28. Prayitno, L.; Mawuntu, J.R.; Herna; Angkasawati, T.J. Review the Use of Antivirus for COVID-19 Treatment. *J. Health Manag.* **2020**, *22*, 578–592, doi:10.1177/0972063420983113.

29. Midassi, S.; Bedoui, A.; Bensalah, N. Efficient Degradation of Chloroquine Drug by Electro-Fenton Oxidation: Effects of Operating Conditions and Degradation Mechanism. *Chemosphere* **2020**, *260*, 127558, doi:10.1016/j.chemosphere.2020.127558.

30. Wastesson, J.W.; Martikainen, J.E.; Zoëga, H.; Schmidt, M.; Karlstad, Ø.; Pottegard, A. Trends in Use of Paracetamol in the Nordic Countries. *Basic Clin. Pharmacol. Toxicol.* **2018**, *123*, 301–307, doi:10.1111/bcpt.13003.

31. Zyoud, A.H.; Zubi, A.; Hejjawi, S.; Zyoud, S.H.; Helal, M.H.; Zyoud, S.H.; Qamhieh, N.; Hajamohideen, A.; Hilal, H.S. Removal of Acetaminophen from Water by Simulated Solar Light Photodegradation with ZnO and TiO_2 Nanoparticles: Catalytic Efficiency Assessment for Future Prospects. *J. Environ. Chem. Eng.* **2020**, *8*, 104038, doi:10.1016/j.jece.2020.104038.

32. Jallouli, N.; Elghniji, K.; Trabelsi, H.; Ksibi, M. Photocatalytic Degradation of Paracetamol on TiO_2 Nanoparticles and TiO_2/Cellulosic Fiber under UV and Sunlight Irradiation. *Arab. J. Chem.* **2017**, *10*, S3640–S3645, doi:10.1016/j.arabjc.2014.03.014.

33. López Zavala, M.Á.; Lara Jaber, C.R. Degradation of Paracetamol and Its Oxidation Products in Surface Water by Electrochemical Oxidation. *Environ. Eng. Sci.* **2018**, *35*, 1248–1254, doi:10.1089/ees.2018.0023.

34. Leal, N.S.; Yu, Y.; Chen, Y.; Fedele, G.; Martins, L.M. Paracetamol Is Associated with a Lower Risk of COVID-19 Infection and Decreased ACE2 Protein Expression: A Retrospective Analysis. *COVID* **2021**, *1*, 218–229, doi:10.3390/covid1010018.

35. Imazio, M.; Brucato, A.; Lazaros, G.; Andreis, A.; Scarsi, M.; Klein, A.; Ferrari, G.M. De; Adler, Y. Anti-Inflammatory Therapies for Pericardial Diseases in the COVID-19 Pandemic: Safety and Potentiality. *J. Cardiovasc. Med.* **2020**, *21*, 625–629, doi:10.2459/JCM.0000000000001059.

36. Diaz-Angulo, J.; Porras, J.; Mueses, M.; Torres-Palma, R.A.; Hernandez-Ramirez, A.; Machuca-Martinez, F. Coupling of Heterogeneous Photocatalysis and Photosensitized Oxidation for Diclofenac Degradation: Role of the Oxidant Species. *J. Photochem. Photobiol. A Chem.* **2019**, *383*, 112015, doi:10.1016/j.jphotochem.2019.112015.

37. Lara-Pérez, C.; Leyva, E.; Zermeño, B.; Osorio, I.; Montalvo, C.; Moctezuma, E. Photocatalytic Degradation of Diclofenac Sodium Salt: Adsorption and Reaction Kinetic Studies. *Environ. Earth Sci.* **2020**, *79*, 277, doi:10.1007/s12665-020-09017-z.

38. Bagal, M. V; Gogate, P.R. Degradation of Diclofenac Sodium Using Combined Processes Based on Hydrodynamic Cavitation and Heterogeneous Photocatalysis. *Ultrason. Sonochem.* **2014**, *21*, 1035–1043, doi:10.1016/j.ultsonch.2013.10.020.

39. Dhiman, N.; Sharma, N. Removal of Pharmaceutical Drugs from Binary Mixtures by Use of ZnO Nanoparticles. *Environ. Technol. Innov.* **2019**, *15*, 100392, doi:10.1016/j.eti.2019.100392.

40. Daneshfar, A.; Vafafard, S. Solubility of Chloroquine Diphosphate and 4,7-Dichloroquinoline in Water, Ethanol, Tetrahydrofuran, Acetonitrile, and Acetone from (298.2 to 333.2) K. *J. Chem. Eng. Data* **2009**, *54*, 2170–2173, doi:10.1021/je8007099.

41. Granberg, R.A.; Rasmuson, A.C. Solubility of Paracetamol in Pure Solvents. *J. Chem. Eng. Data* **1999**, *44*, 1391–1395, doi:10.1021/je990124v.

42. Kincl, M.; Meleh, M.; Veber, M.; Vrečer, F. Study of Physicochemical Parameters Affecting the Release of Diclofenac Sodium from Lipophilic Matrix Tablets. *Acta Chim. Slov.* **2004**, *51*, 409–425.

43. Cano-Casanova, L.; Amorós-Pérez, A.; Ouzzine, M.; Lillo-Ródenas, M.A.; Román-Martínez, M.C. One Step Hydrothermal Synthesis of TiO_2 with Variable HCl Concentration: Detailed Characterization and Photocatalytic Activity in Propene Oxidation. *Appl. Catal. B Environ.* **2018**, *220*, 645–653, doi:10.1016/j.apcatb.2017.08.060.

44. Abdullahi, S.S.; Güner, S.; Koseoglu, Y.; Musa, I.M.; Adamu, B.I.; Abdulhamid, M.I. Simple Method for the Determination of Band Gap of a Nanopowdered Sample Using Kubelka Munk Theory. *J. Niger. Assoc. Math. Phys.* **2016**, *35*, 241–246.

45. Sakthivel, S.; Hidalgo, M.C.; Bahnemann, D.W.; Geissen, S.U.; Murugesan, V.; Vogelpohl, A. A Fine Route to Tune the Photocatalytic Activity of TiO_2. *Appl. Catal. B Environ.* **2006**, *63*, 31–40, doi:10.1016/j.apcatb.2005.08.011.

46. Leofanti, G.; Padovan, M.; Tozzola, G.; Venturelli, B. Surface Area and Pore Texture of Catalysts. *Catal. Today* **1998**, *41*, 207–219, doi:10.1016/S0920-5861(98)00050-9.

47. Kim, K.C.; Yoon, T.U.; Bae, Y.S. Applicability of Using CO_2 Adsorption Isotherms to Determine BET Surface Areas of Microporous Materials. *Microporous Mesoporous Mater.* **2016**, *224*, 294–301, doi:10.1016/j.micromeso.2016.01.003.

48. Karmakar, S. Particle Size Distribution and Zeta Potential Based on Dynamic Light Scattering: Techniques to Characterize Stability and Surface Charge Distribution of Charged Colloids. In *Recent Trends in Materials: Physics and Chemistry*; Studium Press, 2019; pp. 117–159.

49. Rosales, M.; Zoltan, T.; Yadarola, C.; Mosquera, E.; Gracia, F.; García, A. The Influence of the Morphology of 1D TiO_2 Nanostructures on Photogeneration of Reactive Oxygen Species and Enhanced Photocatalytic Activity. *J. Mol. Liq.* **2019**, *281*, 59–69, doi:10.1016/j.molliq.2019.02.070.

50. Qu, X.; Kirschenbaum, L.J.; Borish, E.T. Hydroxyterephthalate as a Fluorescent Probe for Hydroxyl Radicals: Application to Hair Melanin. *Photochem. Photobiol.* **2000**, *71*, 307–313, doi:10.1562/0031-8655(2000)071<0307:haafpf>2.0.co;2.

51. Chen, W.; Zhang, J.; Cai, W. Sonochemical Preparation of Au, Ag, Pd/SiO_2 Mesoporous Nanocomposites. *Scr. Mater.* **2003**, *48*, 1061–1066, doi:10.1016/S1359-6462(02)00635-8.

52. Fujishima, A.; Zhang, X.; Tryk, D.A. TiO_2 Photocatalysis and Related Surface Phenomena. *Surf. Sci. Rep.* **2008**, *63*, 515–582, doi:10.1016/j.surfrep.2008.10.001.

53. Fonseca-cervantes, O.R.; Alejandro, P.; Romero, H.; Sulbaran-rangel, B. Effects in Band Gap for Photocatalysis in TiO_2 Support by Adding Gold and Ruthenium. *Processes* **2020**, *8*, 1032, doi:10.3390/pr8091032.

54. Supriya K. Khore, Sunil. R. Kadam, Sonali D. Naik, Bharat B. Kale, R.S.S. Solar Light Active Plasmonic Au@TiO_2 Nanocomposite with Superior Photocatalytic Performance for H_2 Production and Pollutant Degradation. *New J. Chem.* **2018**, *42*, 10958–10968, doi:10.1039/C8NJ01410H.

55. Mehrani, A.; Dorranian, D.; Solati, E. Properties of Au/ZnO Nanocomposite Prepared by Laser Irradiation of the Mixture of Individual Colloids. *J. Clust. Sci.* **2015**, *26*, 1743–1754, doi:10.1007/s10876-015-0872-z.

56. Mishra, S.M.; Satpati, B. Morphology of ZnO Nanorods and Au–ZnO Heterostructures on Different Seed Layers and Their Influence on the Optical Behavior. *J. Lumin.* **2022**, *246*, 118813, doi:10.1016/j.jlumin.2022.118813.

57. Sing, K.S.W.; Everett, D.H.; Haul, R.A.W.; Moscou, L.; Pierotti, R.A.; Rouquérol, J.; Siemieniewska, T. Reporting Physisorption Data for Gas/Solid Systems - with Special Reference to the Determination of Surface Area and Porosity. *Pure Appl. Chem.* **1985**, *57*, 603–619, doi:10.1351/pac198557040603.

58. Martins, P.M.; Miranda, R.; Marques, J.; Tavares, C.J.; Botelhob, G.; Lanceros-Mendez, S. Comparative Efficiency of TiO_2 Nanoparticles in Suspension vs. Immobilization into P(VDF–TrFE) Porous Membranes. *RSC Adv.* **2016**, *6*, 12708–12716, doi:10.1039/c5ra25385c.

59. Chong, M.N.; Jin, B.; Chow, C.W.K.; Saint, C. Recent Developments in Photocatalytic Water Treatment Technology: A Review. *Water Res.* **2010**, *44*, 2997–3027, doi:10.1016/j.watres.2010.02.039.

60. Carole Sentein, Benoit Guizard, Sophie Giraud, C.Y. and F.T. Dispersion and Stability of TiO_2 Nanoparticles Synthesized by Laser Pyrolysis in Aqueous Suspensions. *J. Phys.* **2009**, *170*, 012013, doi:10.1088/1742-6596/170/1/012013.

61. Israelachvili, J.N. *Intermolecular and Surface Forces*; Third Edit.; Elsevier, 2011; ISBN 9780123751829, doi:10.1016/C2009-0-21560-1.

62. Martins, P.M.; Miranda, R.; Marques, J.; Tavares, C.J.; Botelho, G.; Lanceros-Mendez, S. Comparative Efficiency of TiO_2 Nanoparticles in Suspension vs. Immobilization into P(VDF–TrFE) Porous Membranes. *RSC Adv.* **2016**, *6*, 12708–12716, doi:10.1039/C5RA25385C.

63. Fatehah, M.O.; Aziz, H.A.; Stoll, S. Stability of ZnO Nanoparticles in Solution. Influence of PH, Dissolution, Aggregation and Disaggregation Effects. *J. Colloid Sci. Biotechnol.* **2014**, *3*, 75–84, doi:10.1166/jcsb.2014.1072.

64. García, A.; Rosales, M.; Thomas, M.; Golemme, G. Arsenic Photocatalytic Oxidation over TiO_2-Loaded SBA-15. *J. Environ. Chem. Eng.* **2021**, *9*, 106443, doi:10.1016/j.jece.2021.106443.

65. Rosales, M.; Orive, J.; Espinoza-González, R.; Fernández de Luis, R.; Gauvin, R.; Brodusch, N.; Rodríguez, B.; Gracia, F.; García, A. Evaluating the Bi-Functional

Capacity for Arsenic Photo-Oxidation and Adsorption on Anatase TiO_2 Nanostructures with Tunable Morphology. *Chem. Eng. J.* **2021**, *415*, 128906, doi:10.1016/j.cej.2021.128906.

66. Rosales, M.; Garcia, A.; Fuenzalida, V.M.; Espinoza-González, R.; Song, G.; Wang, B.; Yu, J.; Gracia, F.; Rosenkranz, A. Unprecedented Arsenic Photo-Oxidation Behavior of Few- and Multi-Layer $Ti_3C_2T_x$ Nano-Sheets. *Appl. Mater. Today* **2020**, *20*, 100769, doi:10.1016/j.apmt.2020.100769.

67. Verbruggen, S.W. TiO_2 Photocatalysis for the Degradation of Pollutants in Gas Phase: From Morphological Design to Plasmonic Enhancement. *J. Photochem. Photobiol. C Photochem. Rev.* **2015**, *24*, 64–82, doi:10.1016/j.jphotochemrev.2015.07.001.

68. Cao, J.; Luo, B.; Lin, H.; Xu, B.; Chen, S. Visible Light Photocatalytic Activity Enhancement and Mechanism of $AgBr/Ag_3PO_4$ Hybrids for Degradation of Methyl Orange. *J. Hazard. Mater.* **2012**, *217–218*, 107–115, doi:10.1016/j.jhazmat.2012.03.002.

69. Butler, M.A.; Ginley, D.S. Prediction of Flatband Potentials at Semiconductor-Electrolyte Interfaces from Atomic Electronegativities. *J. Electrochem. Soc.* **1978**, *125*, 228, doi:10.1149/1.2131419.

70. Akerdi, A.G.; Bahrami, S.H. Application of Heterogeneous Nano-Semiconductors for Photocatalytic Advanced Oxidation of Organic Compounds: A Review. *J. Environ. Chem. Eng.* **2019**, *7*, 103283, doi:10.1016/j.jece.2019.103283.

71. Cantarella, M.; Mauro, A. Di; Gulino, A.; Spitaleri, L.; Nicotra, G.; Privitera, V.; Impellizzeri, G. Selective Photodegradation of Paracetamol by Molecularly Imprinted ZnO Nanonuts. *Appl. Catal. B Environ.* **2018**, *238*, 509–517, doi:10.1016/j.apcatb.2018.07.055.

72. Trujillano, R.; Rives, V.; García, I. Photocatalytic Degradation of Paracetamol in Aqueous Medium Using TiO_2 Prepared by the Sol–Gel Method. *Molecules* **2022**, *27*, 2904, doi:10.3390/molecules27092904.

73. Lozano-Morales, S.A.; Morales, G.; Zavala, M.Á.L.; Arce-Sarria, A.; Machuca-Martínez, F. Photocatalytic Treatment of Paracetamol Using TiO_2 Nanotubes: Effect of PH. *Process* **2019**, *7*, 319, doi:10.3390/pr7060319.

74. Bohdziewicz, J.; Kudlek, E.; Dudziak, M. Influence of the Catalyst Type (TiO_2 and ZnO) on the Photocatalytic Oxidation of Pharmaceuticals in the Aquatic Environment. *Desalin. Water Treat.* **2016**, *57*, 1552–1563, doi:10.1080/19443994.2014.988411.

75. An, T.; Yang, H.; Li, G.; Song, W.; Cooper, W.J.; Nie, X. Kinetics and Mechanism of Advanced Oxidation Processes (AOPs) in Degradation of Ciprofloxacin in Water. *Appl. Catal. B Environ. J.* **2010**, *94*, 288–294, doi:10.1016/j.apcatb.2009.12.002.

76. Nord, K.; Karlsen, J.; Tønnesen, H.H. Photochemical Stability of Biologically Active Compounds. IV. Photochemical Degradation of Chloroquine. *Int. J. Pharm.* **1991**, *72*, 11–18, doi:10.1016/0378-5173(91)90375-X.

77. Karim, E.I.A.; Ibrahim, K.E.E.; Abdelrahman, A.N.; Fell, A.F. Photodegradation Studies on Chloroquine Phosphate by High-Performance Liquid Chromatography. *J. Pharmacruticrrl Biomed. Anal.* **1994**, *12*, 667–674, doi:10.1016/0731-7085(93)e0026-j.

78. Doddaga, S.; Peddakonda, R. Chloroquine-N-Oxide, a Major Oxidative Degradation Product of Chloroquine: Identification, Synthesis and Characterization. *J. Pharm. Biomed. Anal.* **2013**, *81–82*, 118–125, doi:10.1016/j.jpba.2013.04.004.

79. Ahmad, I.; Ahmed, S.; Anwar, Z.; Sheraz, M.A.; Sikorski, M. Photostability and Photostabilization of Drugs and Drug Products. *Int. J. Photoenergy* **2016**, *2016*, 1–19, doi:10.1155/2016/8135608.

80. Coelho, A.S.; Chagas, C.E.P.; Pádua, R.M. de; Pianetti, G.A.; Fernandes, C. A Comprehensive Stability-Indicating HPLC Method for Determination of Chloroquine in Active Pharmaceutical Ingredient and Tablets: Identification of Oxidation Impurities. *J. Pharm. Biomed. Anal.* **2017**, *145*, 248–254, doi:10.1016/j.jpba.2017.06.023.

81. Thi, V.H.; Lee, B. Effective Photocatalytic Degradation of Paracetamol Using La-Doped ZnO Photocatalyst under Visible Light Irradiation. *Mater. Res. Bull.* **2017**, *96*, 171–182, doi:10.1016/j.materresbull.2017.04.028.

82. Meroni, D.; Bianchi, C.L.; Boffito, D.C.; Cerrato, G.; Bruni, A.; Sartirana, M.; Falletta, E. Piezo-Enhanced Photocatalytic Diclofenac Mineralization over ZnO. *Ultrason. Sonochem.* **2021**, *75*, 105615, doi:10.1016/j.ultsonch.2021.105615.

83. Silva, A.R.; Martins, P.M.; Teixeira, S.; Carabineiro, S.A.C.; Kuehn, K.; Cuniberti, G.; Alves, M.M.; Lanceros-mendez, S.; Pereira, L. Ciprofloxacin Wastewater Treated by UVA Photocatalysis: Contribution of Irradiated TiO_2 and ZnO Nanoparticles on the Final Toxicity as Assessed by Vibrio Fischeri. *RSC Adv.* **2016**, *6*, 95494–95503, doi:10.1039/C6RA19202E.

84. Eskandari, M.; Goudarzi, N.; Moussavi, S.G. Application of Low-Voltage UVC Light and Synthetic ZnO Nanoparticles to Photocatalytic Degradation of Ciprofloxacin in Aqueous Sample Solutions. *Water Environ. J.* **2018**, *32*, 58–66, doi:10.1111/wej.12291.

Chapter 3

3. Size effect in hybrid TiO_2:Au nanostar for photocatalysis

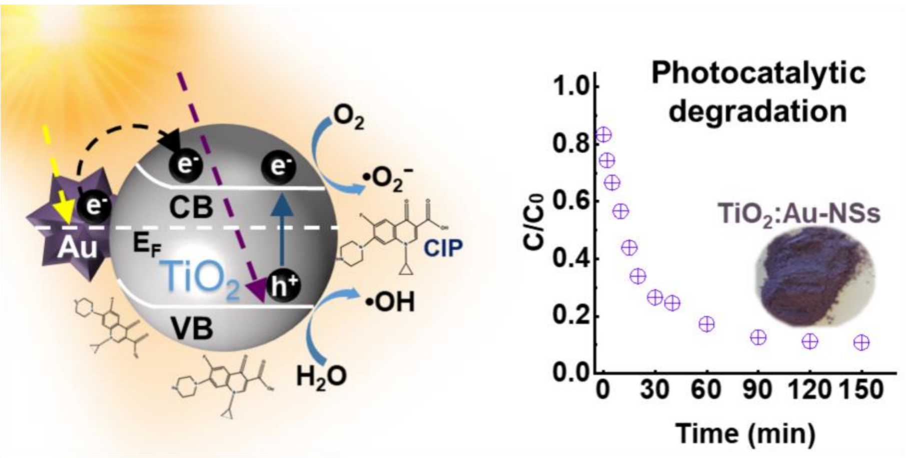

This work repots on the development of novel hybrid nanoparticles, TiO_2:Au-NSs, for photocatalytic application. Under different synthesis conditions, TiO_2 nanoparticles were functionalised with different size of Au nanostar nanoparticles. The produced TiO_2:Au-NSs nanoparticles were characterised and then assessed them in ciprofloxacin degradation. Finally, the most efficient TiO_2:Au-NSs nanoparticles were incorporated into PVDF-HFP based polymer matrix to validate its photocatalytic application

This chapter is based on the following publication: Zheng, F., et al., Size Effect in Hybrid TiO_2:Au Nanostars for Photocatalytic Water Remediation Applications. *Int. J. Mol. Sci.* **2022**, *23*, 13741, doi:10.3390/ijms232213741.

3.1. Introduction

As explained in the previous chapter, the photocatalytic performance of the semiconductors under sunlight not only depends on their affinity with pollutants and generation of ROS, but also on their absorption of light under sunlight. In this context, Au nanoparticles have been used to functionalise semiconductors to extend their light absorption improving the photocatalytic performance under sunlight [1–3].

Nevertheless, most works use spherical Au nanoparticles, limiting its sensitising use to a relatively narrow plasmonic band around 520 nm, leaving unused a large region of visible and infrared (IR) radiation of the sunlight spectrum [4]. Although the plasmonic resonance of Au highly depends on the size and shape of the nanoparticles [1,2,5], there are just a few studies [4,6–15] expanding this response to other wavelengths of the visible spectrum by using gold with different morphologies (mainly combined with TiO_2 macroscopic substrates) such as nanorods [4,6–10,12,14], nanostar [11,13,15], trigonal nanoprisms [9], and hexagonal nanoprisms [9]. Au nanostars (Au with branched morphology), which are particles with the morphology of multiple highly sharp branches protruding from a central core [15], are ideally suited platforms for the synthesis of nanostructured photocatalysts due to their multiple plasmonic electromagnetic hot-spots and high light absorption cross-section [13,15]. Furthermore, they allow localised surface plasmon resonance (LSPR) tunability by changing the size of the Au nanostars (NSs), concomitant with a change of the nanostar spikes aspect ratio, which can be used to enhance its light absorption from the visible to near infrared (NIR) region [13,16].

Among several wet chemistry-based synthesis methods for Au nanostar preparation, the seed-mediated-growth process is a common method for the synthesis of monodisperse nanostars [17]. Many of these synthesis methods use surfactants or polymers as shape-directing agents [13,16]. However, their presence can reduce the photocatalytic efficiency by blocking the active sites of the photocatalysts [18]. In this sense, surfactant-free methods, mainly based on the use of Ag as a shape-directing agent [19] to synthesise the Au nanostar are highly suited for catalytic applications with variable plasmon resonance from visible to NIR.

In this chapter, we have developed a multistep approach to produce new hybrid Au-sensitised TiO_2 nanoparticles that are surfactant-free and where the gold component has a size-tunable nanostar morphology. In this multistep approach, Au spherical nanoparticles were initially generated onto commercial TiO_2 nanoparticles (TiO_2-P25) through a deposition–precipitation method, and then further modified (growth) to induce a change in shape by a surfactant-free nanostars synthesis, generating a branched morphology. The TiO_2-P25 was chosen since it is one of the most studied TiO_2 sample presenting a proven excellent photocatalytic performance, as explained in the **Chapter 1**. By changing the synthesis conditions (seeds to growth Au ratio) different sizes of Au NSs were produced which support broadening the absorption band to the whole visible region and a part of the NIR region.

The different versions of these nanoparticles, with different nanostar sizes, were evaluated and compared for their photocatalytic activity under UV and visible light radiation to degrade the antibiotic ciprofloxacin (CIP). CIP was chosen as the target contaminant as it is one of the most detected antibiotics in different water matrixes [20–22] due to its inefficient removal by conventional wastewater treatment plants and, like all antibiotics, due to their risk to generating antimicrobial resistance bacteria in water reservoirs [22]. Moreover, the photocatalytic assay under different wavelengths from the visible to NIR region was also carried out to understand the correlation between the increase of size of Au branched nanoparticles and its capability to absorb light and transform it in the generation of hole-electron pairs.

Finally, it was studied the possibility of incorporating these novel nanoparticles into a porous polymer matrix of poly(vinylidene fluoride-co-hexafluoropropylene) (PVDF-HFP) for photocatalytic application, degrading pollutants in a cost-effective way and avoiding the possible secondary pollution coming from nanoparticles [23,24].

3.2. Experimental

3.2.1. Materials

Poly(vinylidene fluoride-co-hexafluoropropylene) (PVDF-HFP, SOLEF® 21216/1001) was purchased from Solvay. *N*, *N*-dimethylformamide (DMF, ≥99%) and sodium chloride (NaCl, analytical reagent grade) were supplied by Fisher-Scientific. Titanium dioxide (TiO_2) nanoparticles were provided by Evonik Industries AG. Hydrogen tetrachloroaurate (III) trihydrate ($HAuCl_4 \cdot 3H_2O$, 99.99%) was supplied by Alfa Aesar. Sodium hydroxide (NaOH, 98.0–100.5%) was obtained from Panreac. Hydrochloric Acid (HCl, 37%) was supplied by LABKEM. L-ascorbic acid (AA, ≥99%) and silver nitrate ($AgNO_3$, ≥99%) were purchased from Sigma-Aldrich. Milli-Q ultrapure water (resistivity 18.2 MΩ·cm) was used in all experiments. Ciprofloxacin (CIP, ≥98% (HPLG), $C_{17}H_{18}FN_3O_3$) with maximum light absorption at a wavelength of 277 nm was supplied by Sigma-Aldrich. Absolute ethanol (C_2H_5OH, ≥99.5%) were purchased from Sigma-Aldrich.

3.2.2. Sample preparation

3.2.2.1. TiO_2:Au-NSs nanoparticles synthesis

The synthesis of TiO_2:Au-NSs hybrid nanoparticles was divided into two steps. In the first step, Au nanoparticles (NPs) were grown into TiO_2 nanoparticles by a deposition–precipitation method (DP) as described by Martins et al. [3] to obtain TiO_2:Au nanoparticles, where the Au part formed small spherical particles (NSph) of around 5 nm. Briefly, 200 mg of TiO_2 nanoparticles were dispersed in 40 mL of ultrapure water in a sonication bath for 30 min. Afterwards, a specific volume of $HAuCl_4$ (1 mM) was added to achieve an Au loading of 0.05 wt.% and stirred at room temperature for 10 min to disperse the gold precursor homogeneously. Later, NaOH (0.1 M) was added dropwise to obtain a pH = 9 and then stirred for 10 min. Finally, the solution was centrifuged and washed twice with ultrapure water. In the last step, the nanoparticles were dried overnight in an oven at 80 °C and then grounded with a mortar to obtain a fine powder (TiO_2:Au-NSph).

In a second step, the Au morphology in the TiO_2:Au-NSph was modified by the seed-mediated-growth process, from spherical Au to star-shaped (NS) Au, using the modified surfactant-free method with the assistance of Ag as a shape-directing agent [25]. Then, 150 mg of TiO_2:Au-NSph nanoparticles were dispersed in 3.8 mL of ultrapure water in a sonication bath for 30 min as the seed solution. Afterwards, a growth solution was prepared by mixing 18.9 mL of ultrapure water, 19 µL of HCl (1 M), and 95 µL of $HAuCl_4$ (50 mM), considering a volume ratio between the gold solution ($HAuCl_4$, 50 mM) and seed solution of 0.025. Then, the prepared seed solution was added to this growth solution at room temperature and under moderate stirring. According to the used growth solution volume, 57 µL of $AgNO_3$ (10 mM) and 95 µL of AA (100 mM) solution were simultaneously and quickly added to the above mixture under vigorous stirring. The solution rapidly turned from light pink to purplish-grey, indicating the modification of Au morphology from Au sphere to star. This colour tended to be more bluish when the ratio of the gold solution to seed solution increased, indicative of the formation of bigger nanostars with higher aspect ratio branches. The obtained samples (TiO_2:Au-NSs) were centrifuged and washed twice with ultrapure water, resuspended in ultrapure water, and named Sample A for the final application.

In terms of NP size tuning, the final Au star size was controlled by modifying the volume ratio between the gold solution and seed solution in the seed-mediated-growth synthesis step. Samples B and C were obtained by maintaining the volume of the seed solution but modifying the volume of the gold solution ($HAuCl_4$, 50 mM), with a volume ratio between gold solution and seed solution of 0.1 and 0.25, for Samples B and C, respectively. The volume of the other reagents in the growth solution, $AgNO_3$ and AA solution, were prepared proportionally to the volume of gold solution ($HAuCl_4$, 50 mM).

3.2.2.2. Membranes production

The most photocatalytic efficient TiO_2:Au-NSs of the previously synthesized nanoparticles were used to prepare nanoparticle-loaded membranes through a salt leaching technique combined with a Non-solvent-Induced Phase Separation (NIPS) following the main guidelines previously described [26] but using different type of coagulation bath. 111 mg of TiO_2:Au-NSs nanoparticles were dispersed in 9 mL of DMF to obtain a TiO_2:Au-NSs/PVDF-HFP final mass ratio of 0 and 10 wt.% in an ultrasonication bath for 2 hours with control of temperature to achieve a good nanoparticles dispersion. Later, 1 g of PVDF-HFP polymer was added to the solution to obtain a PVDF-HFP/DMF concentration of 1:9 v/v. After dissolving the polymer completely, 5 g of NaCl particles with a diameter of 90 µm were added and stirred for 1 hour to achieve a homogeneous distribution of the NaCl particles. Then, the mixed solution was spread onto a glass substrate by a doctor blade with a defined gap of 950 µm. Afterwards, the glass substrate was immersed in an absolute ethanol coagulation bath at room temperature and detached the films. Then, the films were immersed in a distilled water bath at 45 °C to remove possible traces of solvent and dried at room temperature for 24 hours. Finally, the film was washed in deionized water for 1 week to remove NaCl particles and then dried at room temperature.

3.2.3. Sample characterisation

Transmission electron microscopy (TEM) images were acquired with a JEOL JEM 1400 Plus set up operating at 100 kV in bright field and a Talos (Thermo Scientific) system working at 200 kV for the HAADF-STEM and EDX-STEM measurements. To prepare the samples, the nanoparticle powder was dispersed in ultrapure water and sonicated for 1 min, and then 2 μL of the suspension was placed on a 400-mesh carbon-coated copper grid and left to dry at room temperature. The analysis of the images was performed using the ImageJ software package.

To perform diffuse reflectance spectroscopy (DRS), a UV-Visible-NIR Jasco V-770 spectrometer equipped with a 150 mm diameter integrating sphere coated with Spectralon with 1 nm spectral resolution was used. DRS was carried out in the 250–2200 nm wavelength range. A Spectralon reference was used to measure the 100% reflectance, and internal attenuators were used to determine zero reflectance to remove background and noise. The samples saved in ultrapure water were placed in the support and dried at room temperature and the powder samples were placed in a quartz cuvette, sealed, and mounted on a Teflon sample holder before the DRS measurement. The measured reflectance spectra were subsequently converted to Kubelka–Munk (K-M) absorption factors to evaluate the absorption spectra of the samples. This conversion was performed using the K-M equation (**Equation 3.1**) [27]:

$$F(R) = (1 - R_\infty)^2/(2R_\infty) \qquad \textbf{(3.1)}$$

where R_∞ ($R_{Sample}/R_{Spectralon}$) corresponds to the reflectance of the sample and F(R) is the absorbance.

The sample bandgap was estimated using the Tauc plot:

$$[F(R)h\upsilon]^{1/n} \; versus \; h\upsilon$$

where h is Planck's constant, υ the frequency, and n the nature of the electronic bandgap transition type, taken as n = 2 for indirect transition [28].

Dynamic light scattering (DLS) and Z-potential were measured with a Zetasizer NANO ZS-ZEN3600 (Malvern Instruments Limited, United Kingdom), equipped with a He–Ne laser (wavelength 633 nm) and backscatter configuration (173°). The nanoparticles were dispersed (1 mg/mL) in ultrapure water in an ultrasonication bath at room temperature for 1 h to avoid aggregation, and each sample was measured five times at pH = 3 to obtain the hydrodynamic diameter. The Z- potential was evaluated at different pH (3, 5, 7, 9, and 11), and each sample was measured five times. HCl (0.1 M) and NaOH (0.1 M) solutions were used to adjust the pH. The resulting particle size was determined using the Smoluchowski model [29]. The manufacturer software (Zetasizer 7.13) was used to estimate the hydrodynamic diameter of the nanoparticles (cumulant diameter), the polydispersity index (PDI), and zeta potential values.

The crystal structure of the nanoparticles was assessed by X-ray diffraction (XRD) using a Philips X'pert PRO automatic diffractometer operating at 40 kV and 40 mA, in theta-theta configuration, secondary monochromator with Cu-Kα radiation ($\lambda = 1.5418$ Å) and a PIXcel solid-state detector (active length in 2θ 3.347°). Data were collected from 5 to 80° 2θ, step size 0.026° and time per step of 60 s at room temperature, total measurement time 10 min. Then, 1° fixed soller slit and divergence slit which provided a constant volume of sample illumination, was used.

X-ray fluorescence (XRF) was used to quantify the ratio of Au:TiO_2 (wt.%). The measurements were obtained by using a MIDEX SD (Spectro) X-ray microfluorescence spectrometer, energy dispersion ED-XRF for elemental analysis. Automatic XYZ tray and collimator changer, X-ray with Mo tube with maximum power 40 W/voltage 48 kV and silicon drift detector (SDD) with 30 mm^2 area. The calibration and calculations were done by fundamental parameters FP Plus.

A field emission gun scanning electron microscope (FEG-SEM) Hitachi S-4800N operating at 10 kV voltage was used to image the membranes. The samples were coated with a thin layer of gold (≈15 nm) in an Emitech K550X ion-sputter before measurement.

Elemental analysis was carried out by Energy Dispersive X-ray spectroscopy (EDX) using a Carl Zeiss EVO 40 (Oberkochen, Germany) SEM equipped with an EDX Oxford Instrument X-Max detector (Abingdon, U.K.). The measurement were performed in a high vacuum condition, at a voltage of 20 kV, a current of 100–400 pA and a working distance of 9–10 mm.

3.2.4. Photogenerated ROS ($^{\bullet}OH$ and $^1O_2$) measurements

3.2.4.1. Detection of hydroxyl radicals ($^{\bullet}OH$)

The hydroxyl radicals ($^{\bullet}OH$) produced after illumination were detected and quantified as previously reported [30] by fluorescence spectroscopy through the hydroxylation reaction of terephthalic acid (TA) to 2-hydroxyterephthalic acid (2-HTA) in the heterogeneous phase, as shown **Figure 3.1.**

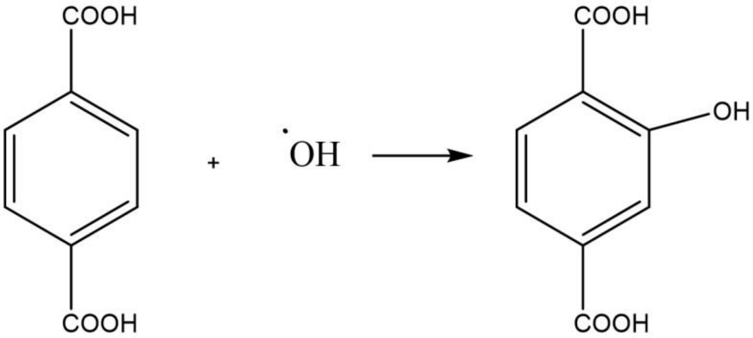

Figure 3.1. Scheme of hydroxylation reaction of terephthalic acid (TA).

Firstly, a TA solution (0.5 mM) was prepared by dissolving TA in a dilute NaOH solution (2 mM). Then, 50 mg nanoparticles as photocatalysts were dispersed in 50 mL of TA solution (0.5 mM) and stirred in the dark for 30 min. Afterwards, the suspension was stirred and irradiated for 30 min under UV illumination. An aliquot was taken out at different irradiation times and centrifuged to remove the nanoparticles. 200 µL of supernatant was collected and analysed using a microplate reader Infinite 200 Pro. This analysis was performed by evaluating the emission peak at 425 nm of the 2-HTA, which has an excitation wavelength of 315 nm [31] in the fluorescence spectrum. The 2-hydroxyterephthalic acid a standard calibration curve was constructed to quantify the relationship between the fluorescence signal and the produced hydroxyl radicals.

3.2.4.2. Detection of singlet oxygen ($^1O_2$)

Singlet oxygen ($^1O_2$) was determined as previously reported [30] by applying histidine test (**Figure 3.2)** in a heterogeneous phase as an indirect way to quantify the generated $^{\bullet}O_2^-$. 50 mg of nanoparticles were added to a mixed solution of 40 ml L-histidine solution (0.2 mM) and 10 mL of N,N-p-nitrosodimethylaniline solution (0.2 mM). Afterwards, the suspension was stirred in the dark for 30 min, and then irradiated for 30 min under UV illumination. At different irradiation times, aliquots were taken out, centrifuged, and then analysed using an Agilent Cary 60 UV-Vis Spectrophotometer. This analysis evaluated the characteristic band of N,N-p-nitrosodimethylaniline at 440 nm in the UV-Vis spectrum. The reaction between histidine and $^1O_2$ produces a trans-annular peroxide, as presented in **Figure 3.2**. The latter compound was detected by bleaching the p-nitrosodimethylaniline at 440 nm. Singlet oxygen alone cannot cause bleaching of the latter compound; no bleaching occurs in the mixture of histidine and p-nitrosodimethylaniline without singlet oxygen. The produced $^1O_2$ was quantified from the calibration curve between absorbance and N,N-pnitrosodimethylaniline solution concentration.

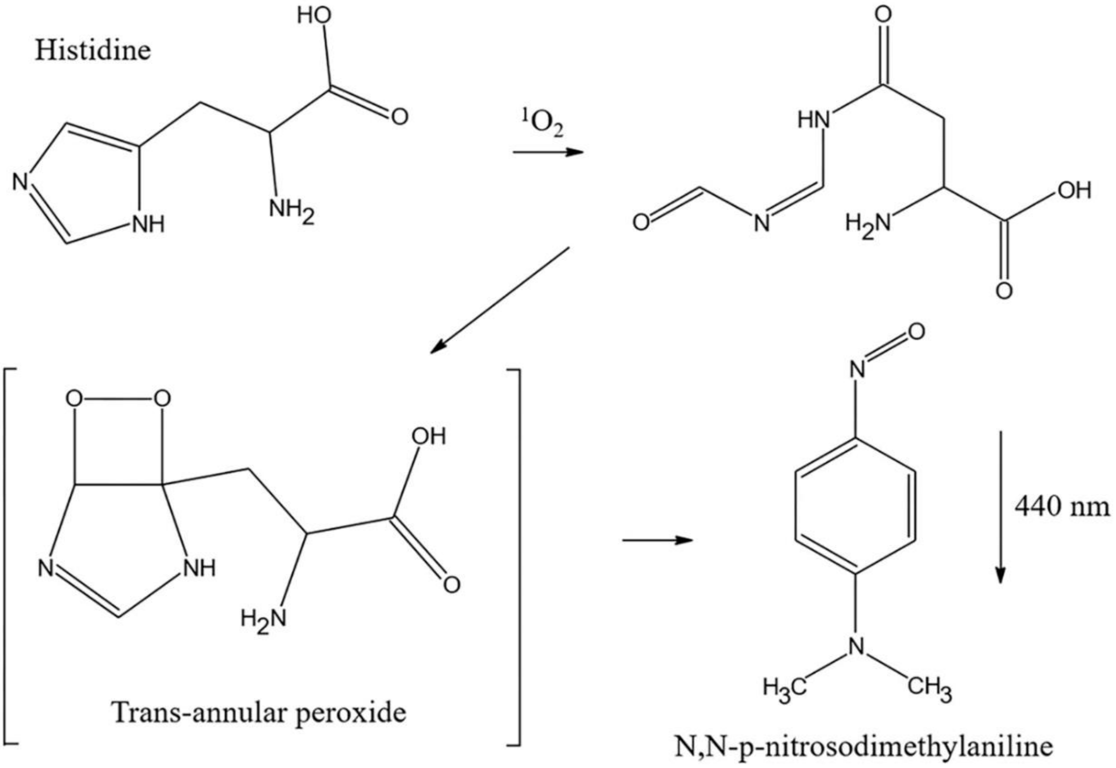

Figure 3.2. Mechanism of histidine test.

3.2.5. Photocatalytic degradation under UV and visible radiation

The photocatalytic activity of the produced TiO_2:Au-NSs nanoparticles, A, B, and C, were tested under both UV and visible light radiation. Firstly, the CIP solution of 5 mg/L was prepared and adjusted to pH = 3. Before the degradation assays, 50 mg of nanoparticles as photocatalysts were stirred in 50 mL of CIP solution in the dark for 30 min to achieve an adsorption-desorption equilibrium.

The photocatalytic activity of the produced membranes was tested under visible light radiation using the same CIP solution. Before the degradation assays, the membrane, with a sample area of 18 cm^2, was immersed and stirred in 50 mL of CIP solution in the dark for 30 min to achieve an adsorption–desorption equilibrium.

The UV degradation of CIP was performed in a photoreactor with eight UV lamps of 8 W, with an emission peak at 365 nm, over 30 min. The suspensions of photocatalysts and CIP were kept stirred in a 100 mL beaker under illumination from the top. The distance between the solution and the lamp was 13.5 cm, and the irradiance at the solution was 3.3 W/m^2.

For the visible light degradation, a filtered Xenon lamp (sun emulator) with an excitation peak at 550 nm and irradiance of 300 W/m^2 (spectra in **Figure 3.3**) was used, over 150 min for degradation in suspension and 600 min for degradation using membranes. The suspensions of photocatalysts and CIP were stirred in a 100 mL beaker under lateral illumination. The distance between the CIP solution and the lamp was 21 cm.

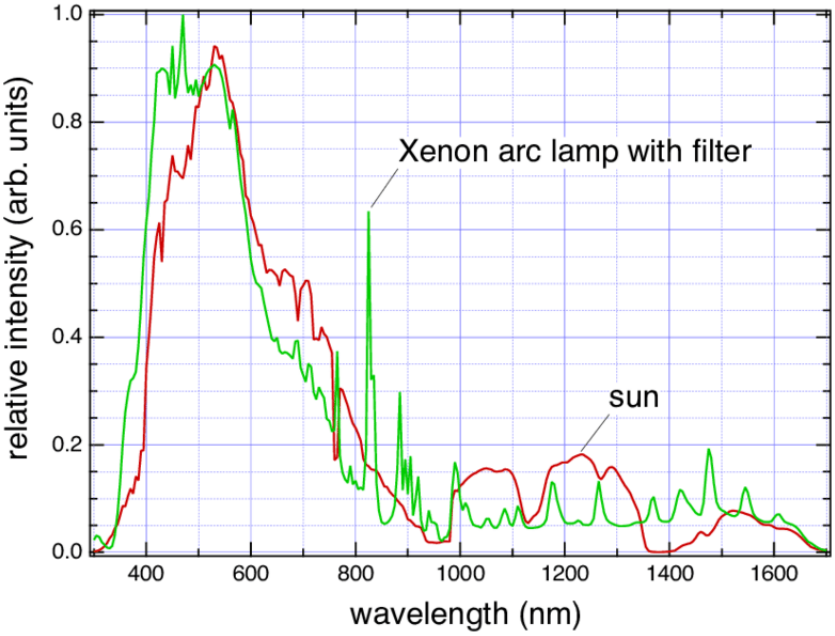

Figure 3.3. Xenon Lamp arc (with UV filter) and sunlight spectra.

Aliquots as samples were taken out at different periods during the degradation assays and centrifuged to remove the photocatalysts. Afterwards, the 200 µL of the supernatant in each sample after centrifugation was analysed by UV-Vis spectroscopy. The absorbance variation of the 277 nm peak of the CIP spectrum was monitored using a microplate reader Infinite 200 Pro in the range of 230 to 450 nm.

The photocatalytic degradation rate was fit to a pseudo-first-order reaction, which is based on the Langmuir–Hinshelwood model described by **Equation 3.2**:

$$\ln\left(\frac{C}{C_0}\right) = -kt \qquad \textbf{(3.2)}$$

where C and C_0 represent the pollutant concentration at time t and at the beginning of the photocatalytic assessment respectively, and *k* is the first-order rate constant of the reaction [3].

3.2.6. Photocatalytic degradation under different wavelengths

The photocatalytic activity of the produced TiO_2:Au-NSs nanoparticles, A, B, and C was also assessed under different wavelengths of light radiation: blue light (emission peak at 460 nm), green light (emission peak at 530 nm), red light (emission peak at 630 nm), NIR light (emission peak at 730 nm), for ciprofloxacin degradation.

Firstly, the CIP solution of 5 mg/L was prepared and adjusted to pH = 3. After achieving the adsorption–desorption equilibrium of the photocatalysts and CIP solution as described previously (**Section 3.2.5**), the degradation of CIP was carried out in a cuvette under different wavelengths of light radiation with an intensity of 0.5 W, over 180 min. The suspensions of photocatalysts and CIP were kept stirred under lateral illumination. The distance between the CIP solution and the lamp was 1 cm.

Aliquots were withdrawn at different times during the degradation assessment, and centrifuged and analysed using an Agilent Cary 60 UV-Vis Spectrophotometer.

3.3. Results and discussion

3.3.1. Nanoparticle synthesis and characterisation

Hybrid nanoparticles of Au and TiO_2 were synthesised following a multistep approach (**Section 3.2.2.1**). Starting with commercial TiO_2 nanoparticles, Au nanoparticles (NPs) were grown from those nanoparticles through a deposition–precipitation method. As previously described [3], this step generates the formation of small randomly distributed Au spherical nanoparticles attached to the TiO_2 nanoparticles (TiO_2:Au-NSph) (**Figure 3.4 a)** and **b)**). EDX mapping was used to confirm the homogeneous distribution of small Au NPs (red colour) on the surface of TiO_2 (blue colour) in TiO_2:Au-NSph (**Figure 3.4 c)**). In a second step, the Au component of the hybrid nanoparticles was further grown through a seed-mediated-growth process and using Ag, a shape-directing agent, to generate Au nanostars attached to the TiO_2 nanoparticles (TiO_2:Au-NSs). The added Au grows from the

Au component of the TiO_2:Au-NSph because it is a more energetically favourable process as has been shown in other hybrid nanoparticles [32–34]. This branched-induction mechanism has the advantage that it is produced through a surfactant-free method offering a non-coated nanoparticle surface, which is advantageous for the catalytic function of the nanoparticles. Based on this method, three different versions of nanoparticles, Sample A, B, and C, were generated with an increasing quantity of Au and, therefore, with the expanding size of the Au nanostar parts (bigger size and longer spikes).

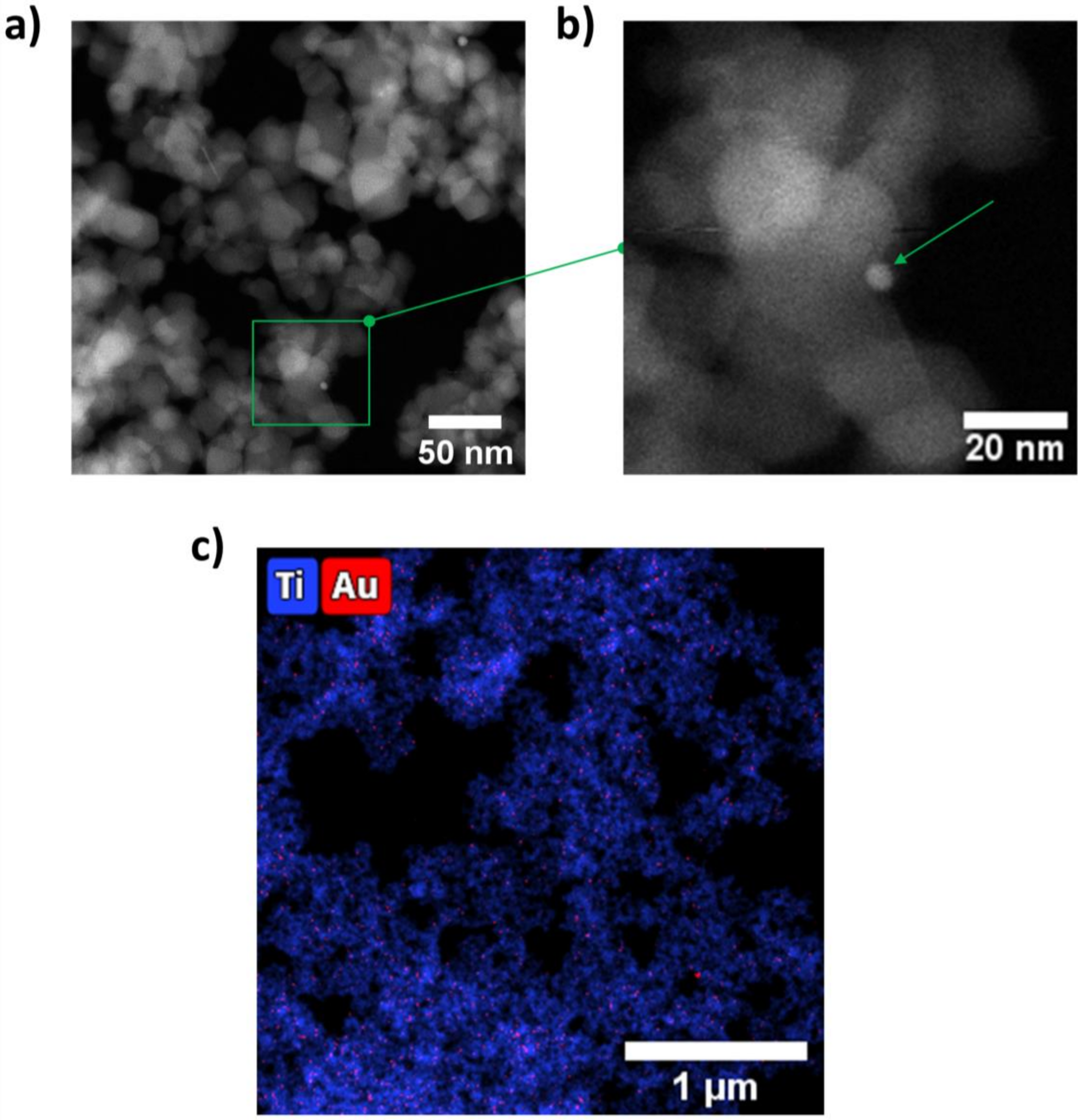

Figure 3.4. STEM-HAADF micrographs of TiO_2:Au-NSph with different magnifications (a, b). Au nanoparticles appear as whiter, smaller, and quite circular shapes, scattered through the sample. The zoom-in, with the green arrow, shows one of these Au nanoparticles bound to a TiO_2 nanoparticle surface. EDX mapping of TiO_2:Au-NSph: Au (red) and Ti (blue) (c).

STEM-HAADF was used to assess the morphology of the synthesised nanoparticles. As presented in **Figure 3.5 a), b), d), e), g)** and **h)**, non-spherical Au nanoparticles on the TiO_2 surface can be detected as high contrast areas in the STEM-HAADF. The shape of the Au part depends on the synthesis conditions. Increasing the volume ratio of the gold solution to the seed solution generated bigger Au NSs with more developed tips exhibiting higher aspect ratios (**Figure 3.5 b), e)** and **h)**). Moreover, EDX mapping was used to confirm the presence of Au (red colour) on the surface of TiO_2 (blue colour) in TiO_2:Au-NSs-A, B**,** and C (**Figure 3.5 c), f)** and **i)**).

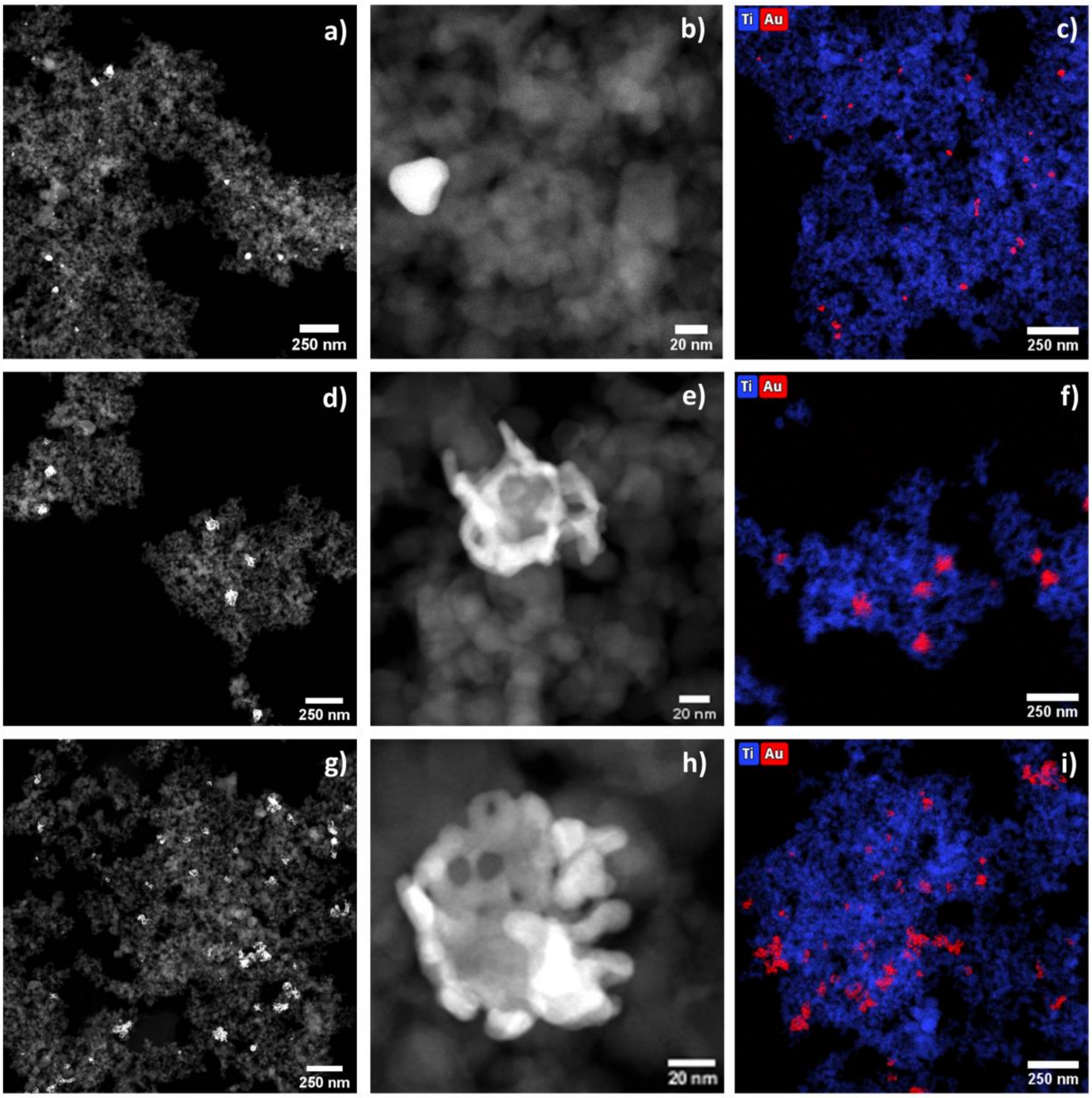

Figure 3.5. STEM-HAADF micrographs with the different magnifications (a, b, d, e, g, h) and EDX mapping (c, f, i) of TiO_2:Au-NSs, Sample A (a–c), Sample B (d–f), and Sample C (g–i).

Regarding the crystal structure, XRD (**Figure 3.6 a)**) showed the presence of anatase (peaks at 25.3, 37.8, and 48.0°) and rutile (peaks at 27.49°) in all the samples, in good agreement with the literature [3,35]. Moreover, there was no significant difference between the intensities or positions of the peaks from these samples, independent of the Au presence and size. On the other hand, no diffraction peaks of Au were detected in TiO_2:Au-NSph and TiO_2:Au-NSs-A, -B and -C, which can be explained by the low amount of Au present in these samples. In addition, XRF was used to detect the amount of Au in the synthesised hybrid nanoparticles (**Figure 3.6** and **Table 3.1**).

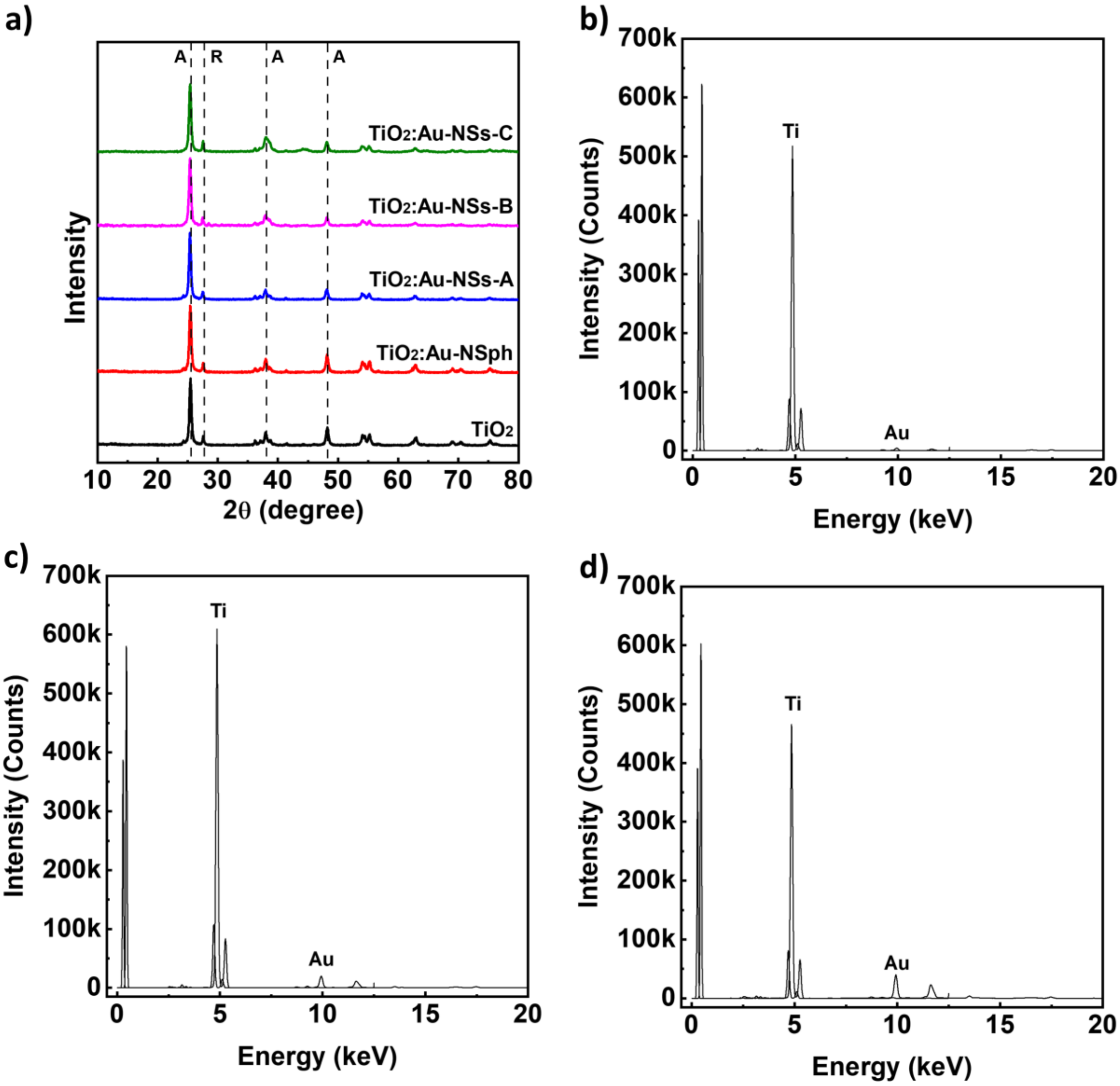

Figure 3.6. X-ray diffraction spectra of pristine TiO_2, TiO_2:Au-NSph, TiO_2:Au-NSs-A, B, and C nanocomposites and identification of the representative diffraction peaks for anatase (A) and rutile (R) phases (a). XRF spectrum of TiO_2:Au-NSs-A (b), TiO_2:Au-NSs-B (c), and TiO_2:Au-NSs-C (d).

Table 3.1. Amount of Au with respect to TiO_2 (wt. %) in the samples, theoretical value (considering the added reagents in the synthesis reaction) vs. XRF measurement.

Sample	Au:TiO_2 wt.% theoretical	Au:TiO_2 wt.% XRF
TiO_2:Au-NSph	0.05	*
TiO_2:Au-NSs-A	0.68	*
TiO_2:Au-NSs-B	2.55	2.38
TiO_2:Au-NSs-C	6.3	5.83

* No detected Au since the amount of Au is less than 1% wt. in sample

The amount of Au with respect to TiO_2 was 2.38 and 5.83 wt.% in TiO_2:Au-NSs-B, and -C, respectively, very similar to the theoretical values, considering the quantities of the reagents, indicating a high yield of the Au reduction. Due to the quantification limit of the technique, <1wt.%, the amount of Au could not be determined for TiO_2:Au-NSph and TiO_2:Au-NSs-A although similar results are expected.

The hydrodynamic size for Samples A, B, and C was studied by DLS, (**Figure 3.7 a)**). The results show diameters of 390 ± 13.4, 126 ± 2.9, and 122 ± 0.8 nm for A, B, and C, respectively. These diameters were much smaller than the one of the pristine TiO_2 nanoparticles previously reported [3] and decreased when increasing the Au-NS size. This is probably due to the different processing that takes place during the growth of Au on the hybrid nanoparticles, with respect to other methods, and the presence of Au nanoparticles over the TiO_2 surface, preventing the formation of big nanoparticles' aggregates [3].

Concerning Z-potential, the measurements were performed as a function of the pH and it is presented in **Figure 3.7 b)**. In general, they presented a zero potential around a pH range of 6–7 and a Z-potential modulus that rapidly increased when separating from that point to reach values higher than 30 mV for pH below 3 or above 9 where the nanoparticles show superior electrostatic stability [36,37]. When comparing the different nanoparticles, a slight increase of the pH at zero potential was observed when increasing the Au-NS size from Sample A to Samples B and C together with a more pronounced slope, probably due to the smaller aggregate size as indicated in the DLS measurements.

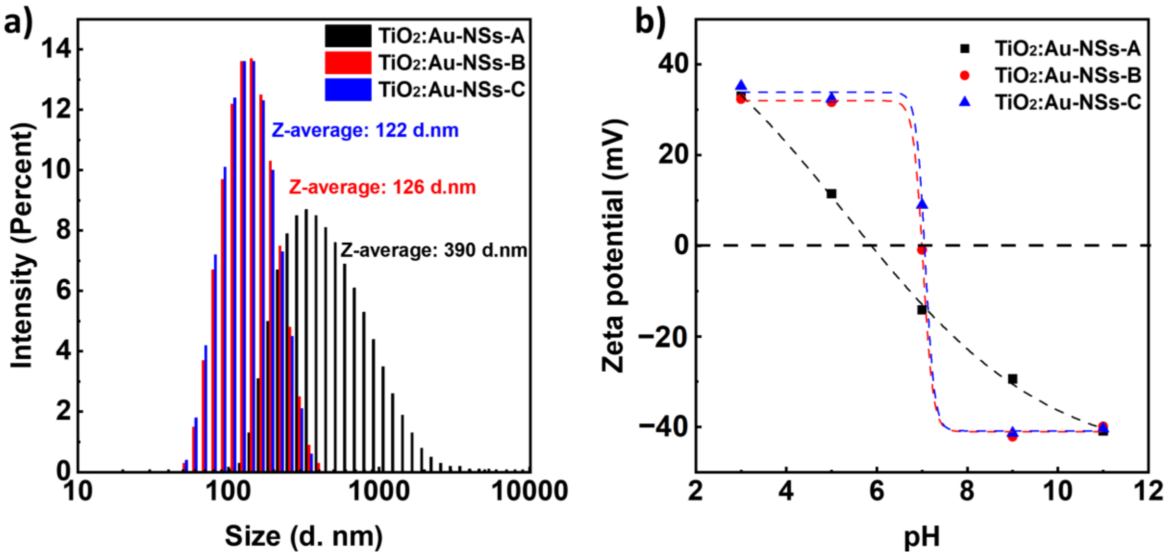

Figure 3.7. The intensity size distribution of the TiO_2:Au-NSs-A, B, and C nanocomposite and respective Z-average hydrodynamic size (a). Zeta potential measurements performed at different pHs (3, 5, 7, 9, and 11) for TiO_2:Au-NSs-A, B, and C nanocomposite (b).

This change in Au morphology affected the optical properties of the nanoparticles. DRS was used to evaluate the optical properties of pure TiO_2 nanoparticles, TiO_2:Au-NSph and TiO_2:Au-NSs (**Figure 3.8 a), c)** and **e)**), and TiO_2:Au-NSs at different Au-NSs sizes (**Figure 3.8 b), d)** and **f)**).

When observing the reflectance spectra of the three types of nanoparticles (**Figure 3.8 a)**), all the samples showed similar low reflectance in the UV range (200–400 nm) mainly due to the TiO_2 high cross-section at the UV. On the other hand, in the visible range (400–700 nm), the pure TiO_2 nanoparticles had a reflection of ≈87% of the radiation, while the nanohybrids TiO_2:Au-NSph presented a reflectance below 75% for the same range with a minimum reflectance (≈63%) at 544 nm due to the surface plasmon of Au spherical nanoparticles, which are in line with the literature [3,38]. In the same range, TiO_2:Au-NSs-A showed a reflectance below 51% due to the higher content of Au and its branched morphology. When comparing the TiO_2:Au-NSs at different Au-NSs sizes (**Figure 3.8 b)**), reflectance decreased further with the increasing amount and size of gold nanostars. TiO_2:Au-NSs-B and C, in the same range, presented a reflectance below 32% and 14%, respectively.

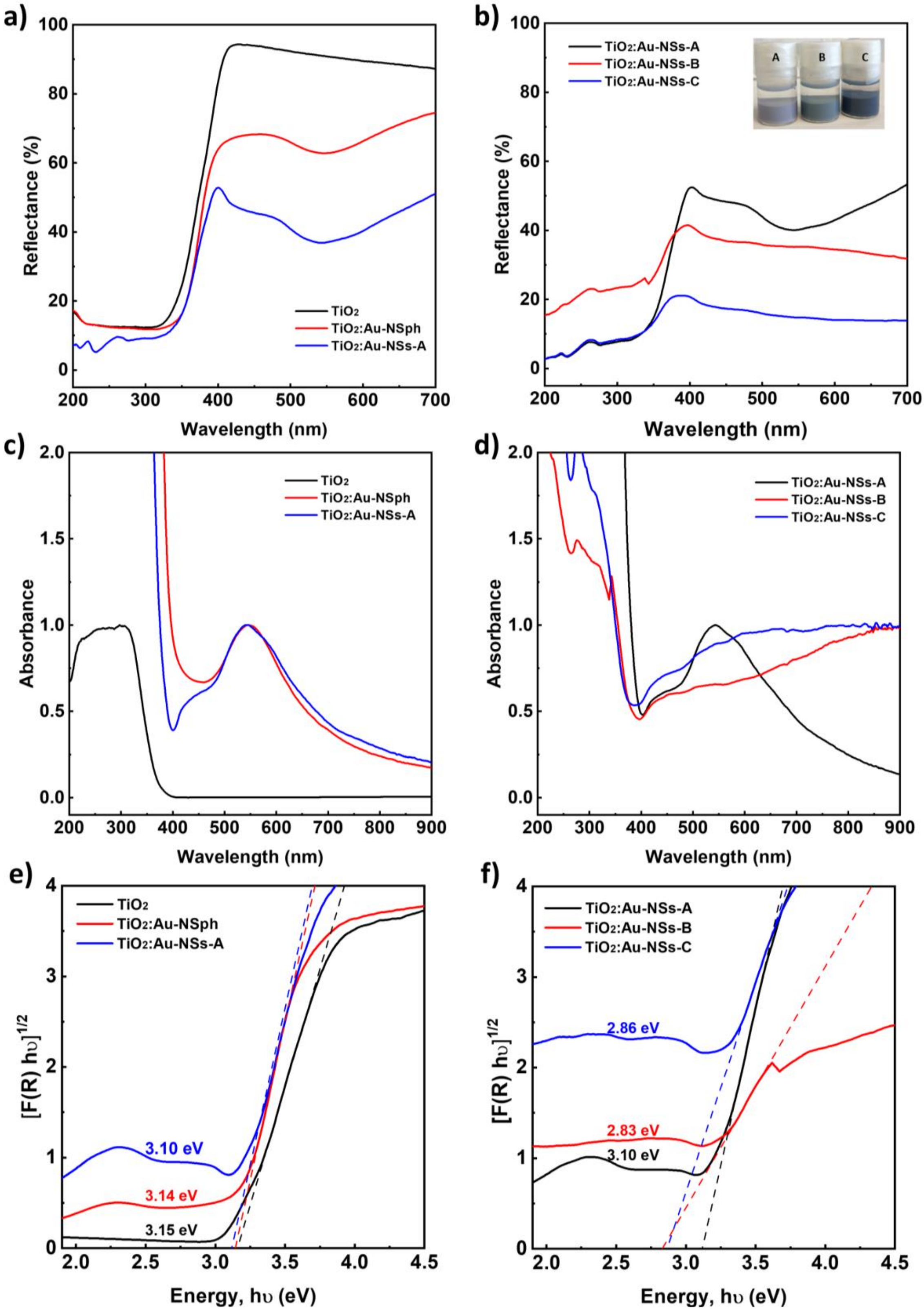

Figure 3.8. UV-Vis reflectance spectra (a, b) and UV-Vis absorption spectra (c, d) of the nanoparticles in the different synthesis steps (a, c) and nanoparticles with different Au NS sizes (b, d). Estimation of the bandgap for nanoparticles at different steps of the synthesis (e) and nanoparticles with different Au-NS sizes (f). (The bandgap is taken as the extrapolation of the linear part at $[F(R)h\upsilon]^{1/2} = 0$).

The complementary graph of absorbance shows that this one changed significantly when Au was included, with the appearance of a plasmonic peak in the visible region that extended to near IR (**Figure 3.8 c)**). This absorption increased with the concentration of Au and the size of Au-branched NPs, generating a broader peak that extended to much higher wavelengths (Samples B and C in **Figure 3.8 d)**). This redshift is in agreement with the literature for homocomponent nanostars [16,19], while the broadening can be due to the interaction with the excess of TiO_2 nanoparticles affecting its uniformity and morphology.

The bandgap of the samples was estimated from the DRS spectrum by applying Tauc plot method and after line fitting in the linear region 3.3–3.6 eV, as shown in **Figure 3.8 e)** and **f)**. The pure TiO_2 nanoparticle showed a bandgap of 3.15 eV, typical for TiO_2 (3.0 to 3.2 eV depending on the ratio of crystalline phases) [39]. The TiO_2:Au-NSph and TiO_2:Au-NSs-A showed a lower bandgap than pure TiO_2: 3.14 and 3.10 eV, respectively. This decrease in the bandgap is related to the absorption of longer wavelengths and has been previously reported for other hybrid systems [3,35,40]. The bandgap reduction was more evident when increasing the Au nanostar size due to their higher absorption in the visible region with values of 2.83 and 2.86 for TiO_2:Au-NSs-B and C, respectively (**Figure 3.8 f)**).

3.3.2. Photocatalytic degradation under UV and visible radiation

The photocatalytic activity of the synthesized TiO_2:Au-NSs-A, B, and C nanoparticles was evaluated and compared with TiO_2:Au-NSph under both UV and visible light radiation in the degradation of CIP under colloidal suspension conditions. **Table 3.2** shows the apparent reaction rate constant (*k*) calculated by **Equation 3.2** for the different synthesized nanoparticles.

Table 3.2. CIP degradation efficiencies (DE) and corresponding apparent reaction rate constants (*k*) under 30 min of UV radiation and 150 min of visible radiation for TiO_2:Au-NSs-A, B, and C nanoparticles.

Sample	**UV**		**Visible**	
	k (min^{-1})	**DE (%)**	**k (min^{-1})**	**DE (%)**
TiO_2:Au-NSs-A	0.053	83	0.014	89
TiO_2:Au-NSs-B	0.040	78	0.012	88
TiO_2:Au-NSs-C	0.023	64	0.009	86
TiO_2:Au-NSph	0.031	76	0.008	84

Figure 3.9 a) and **b)** show the results of photocatalytic experiments under UV and visible radiation, respectively. As a control procedure, it should be noted that under the same irradiation conditions of UV or visible light and in the absence of nanoparticles, there was very low photolysis of CIP (**Figures 3.10**).

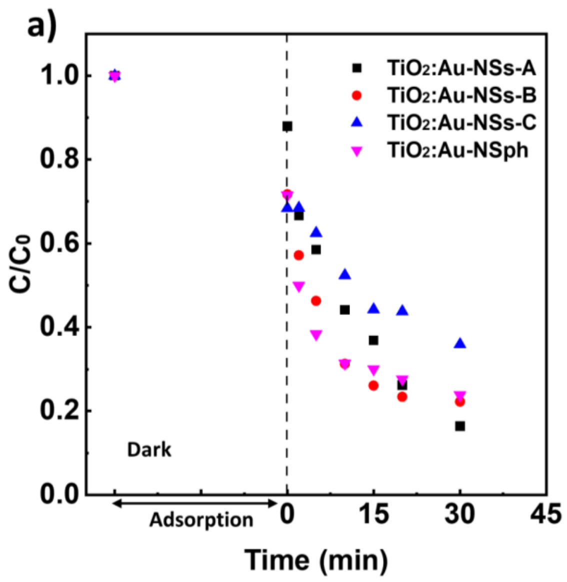

Figure 3.9. Photocatalytic degradation of CIP (5 mg/L) with TiO_2:Au-NSph, TiO_2:Au-NSs-A, B, and C nanoparticles under 30 min of UV radiation (a) and 150 min of visible radiation (b).

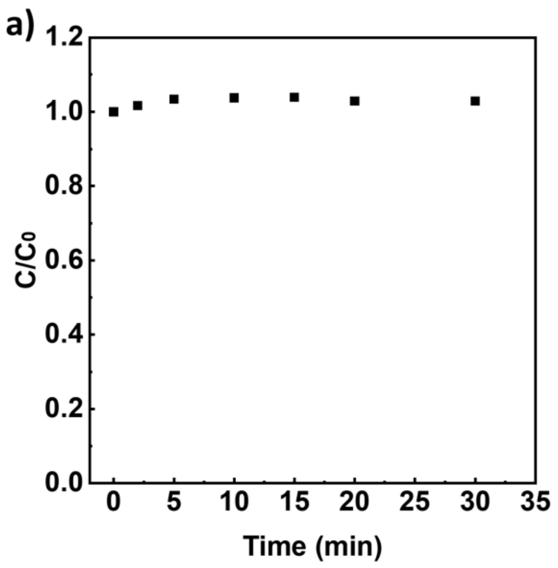

Figure 3.10. Photolysis assay of CIP (5 mg/L) under 30 min of UV radiation (a) and 150 min of visible radiation (b).

The photocatalytic assays under UV light had a degradation efficiency of 83, 78, and 64% for A, B, and C nanoparticles, respectively, under the same experimental conditions. The reaction rate constant showed a similar tendency, k = 0.053, 0.040, and 0.023 min^{-1} for A, B, and C nanoparticles, respectively. Nanoparticles A presented the best degradation efficiency under UV of the three samples. This result can be rationalized by the lower quantity of TiO_2 (total nanoparticle mass is kept constant) and the lower active area presented by the photocatalyst when adding the Au to its surface for an increasing quantity of Au. Among these samples, A showed better photocatalytic activity than TiO_2:Au-NSph, which presented a degradation efficiency of 76%, with k = 0.031 min^{-1}. The change of the Au spherical morphology to branched morphology reduced the bandgap of TiO_2 and improved the photocatalytic efficiency.

On the other hand, in the adsorption process in the dark (before irradiation), Samples A, B, and C adsorbed 12%, 28%, and 32% of CIP, respectively. The higher amount of Au on TiO_2 surface led to a higher CIP adsorption, which agrees with previously reported work [3].

Interestingly, the addition of Au onto the TiO_2 surface made it possible to produce the photocatalytic degradation of CIP by the nanoparticles under visible light (**Figure 3.9 b)**) due to the improvement of the absorption of longer solar wavelengths as well as the lower bandgap (**Figure 3.8 e)** and **f)**). Under this illumination, all the TiO_2:Au-NSs nanoparticles presented very similar degradation efficiency, 89%, 88%, and 86%, with k = 0.014, 0.013, and 0.009 min^{-1}, for A, B, and C, respectively. The nanoparticle TiO_2:Au-NSph showed slightly lower photocatalytic performance with a degradation efficiency of 84% with k = 0.008 min^{-1} compared with A, B, and C. Note here that although TiO_2:Au-NSs-A, B, and C showed a similar effect under visible radiation, Samples B and C showed a broader plasmonic band that extended deeper into the near IR and could be beneficial for the light-harvesting of higher wavelengths of the sunlight radiation. Finally, the TiO_2:Au-NSs-A, B, and C after the photocatalytic tests were recovered and assessed by XRD to confirm their stability after photocatalytic application. There was no difference observed in the crystal structure of nanoparticles before (**Figure 3.6 a)**) and after photocatalysis (**Figure 3.11 a)**).

Based on the photocatalytic activity results presented, Sample A—with the best photocatalytic performance—was selected as the best candidate to immobilise into a PVDF-HFP-based nanocomposite membrane. Additionally, further experiments were carried out for highly reactive oxygen species (ROS) detection, •OH and $^1O_2$, in Sample A. **Figure 3.11 b)** shows that the generation of hydroxyl radical (•OH) increased during the 30 min of UV radiation. The result also indicates that the concentration of $^1O_2$ achieved a maximum at an irradiation time of 15 min, after which the generation of $^1O_2$ became constant. Therefore, •OH played the dominant role during the photocatalytic degradation of CIP.

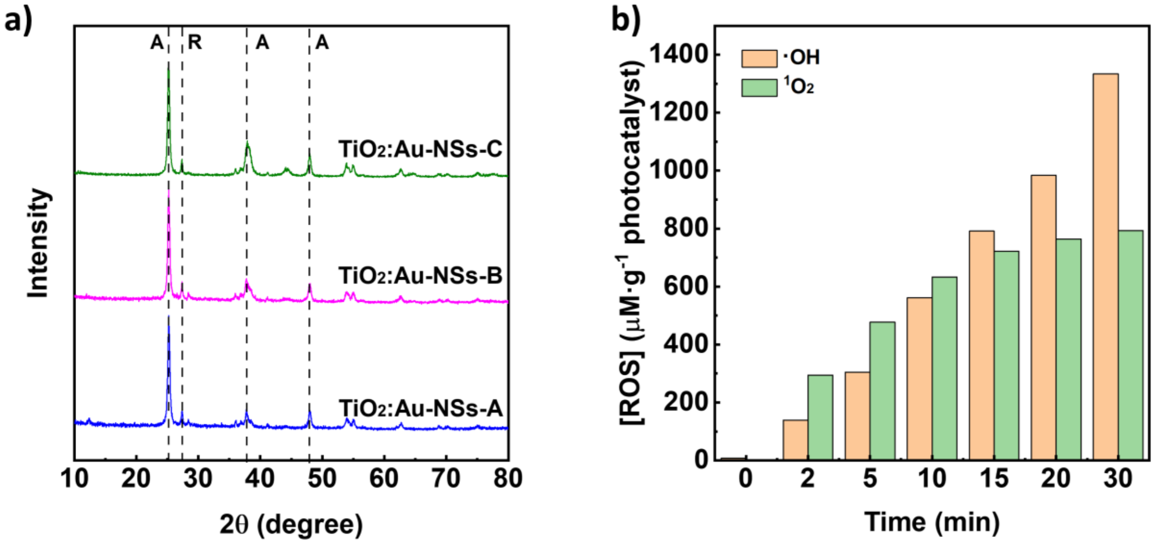

Figure 3.11. X-ray diffraction spectra of TiO_2:Au-NSs-A, B, and C nanocomposites after photocatalytic application (a). Quantification of photogenerated hydroxyl radical (•OH) and singlet oxygen ($^1O_2$) by TiO_2:Au-NSs-A under 30 min of UV radiation (b).

On the other hand, a comparison between TiO_2:Au-NSs-A and previous work using TiO_2-based plasmonic photocatalysts was performed (**Table 3.3**). Due to the different experimental conditions applied in each work, this comparison is not straightforward but allows contextualizing of our results. Although the previous works showed a slightly higher degradation of CIP than our results, they used a much higher amount of plasmonic nanoparticles and intensity of visible radiation (less cost-effective process) or longer degradation time than the one we used, which makes the comparison less straightforward.

Table 3.3. Comparison of degradation efficiency (DE) between the present work and previous work that used plasmonic nanoparticles to functionalise TiO_2 for ciprofloxacin (CIP) degradation under visible light.

[CIP] (mg/L)	Photocatalyst	Cu, Ag or Au amount (wt.%)	[Photocatalyst] (mg/mL)	Irradiation	DE (%)	Time (min)	Ref.
30	Cu/TiO_2	1.0	0.5	500 W/m^2	99	180	[41]
80	Cu/TiO_2	1.0	0.25	500 W/m^2	85	240	[42]
3.3	Ag/TiO_2	5.0	0.5	60 W	87	60	[43]
30	Ag/TiO_2	1.5	0.5	500 W/m^2	99	240	[41]
30	Au/TiO_2	1.5	0.5	500 W/m^2	99	180	[41]
5	Au/TiO_2	0.5	1.0	98 W/m^2	45	180	[3]
5	TiO_2:Au-NSs-A	0.68	1.0	300 W/m^2	89	150	Present work

3.3.3. Photocatalytic degradation under different wavelengths

To understand the photocatalytic behaviour of the nanoparticles after increasing the Au branched morphology, the synthesized TiO_2:Au-NSs-A, B and C nanoparticles were evaluated under different wavelengths of light radiation in the visible and NIR region for the degradation of CIP.

Table 3.4 shows the apparent reaction rate calculated by **Equation 3.2**. **Figures 3.12 a)-d)** show the results of photocatalytic experiments under blue (460 nm), green (530 nm), red (630 nm), and NIR (730 nm) light radiation, respectively. It should be noted that under the same irradiation conditions of these types of light and in the absence of nanoparticles, there was no photolysis of CIP (**Figure 3.13**).

Regarding the photocatalytic assays under blue light, all nanoparticles showed an excellent degradation activity. A degradation efficiency of 53, 53, and 37% was observed for A, B, and C nanoparticles, respectively, under the same experimental conditions. The rate constant presented a similar tendency, $k = 0.031$, 0.038 and 0.027 min^{-1} for A, B and C nanoparticles, respectively. This wavelength is lower than the plasmonic band of the Au NSs, however as observed in **Figure 3.8 d)**, the nanoparticles still showed a high absorbance. Interestingly, the nanoparticles showing the highest absorbance are the ones with the lowest degradation activity.

Table 3.4. CIP degradation efficiencies (DE, %) and corresponding apparent reaction rate constants (*k*) under 150 min of blue, green, red and NIR radiation for TiO_2:Au-NSs-A, B, and C nanoparticles.

Sample	**Blue**		**Green**		**Red**		**NIR**	
	***k* (min^{-1})**	**DE (%)**	***k* (min^{-1})**	**DE (%)**	***k* (min^{-1})**	**DE (%)**	***k* (min^{-1})**	**DE (%)**
TiO_2:Au-NSs-A	0.0031	53	0.0024	34	0.0025	39	-	-
TiO_2:Au-NSs-B	0.0038	53	-	-	-	-	-	-
TiO_2:Au-NSs-C	0.0027	37	-	-	-	-	-	-

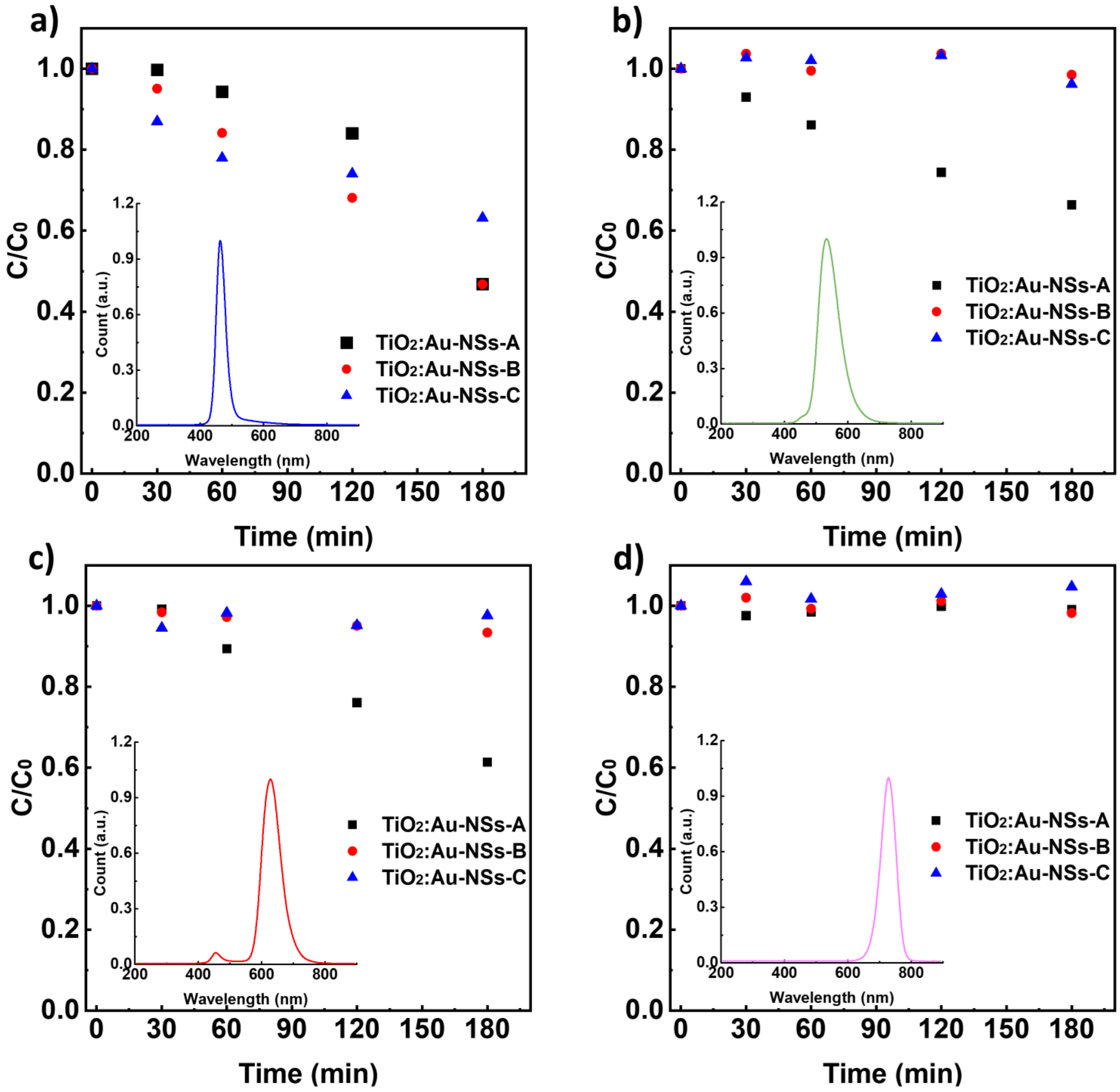

Figure 3.12. Photocatalytic degradation of CIP (5 mg/L) with TiO_2:Au-NSs-A, B and C nanoparticles under 180 min of different wavelengths of light (inset): blue (a), green (b), red (c) and NIR light (d) radiation.

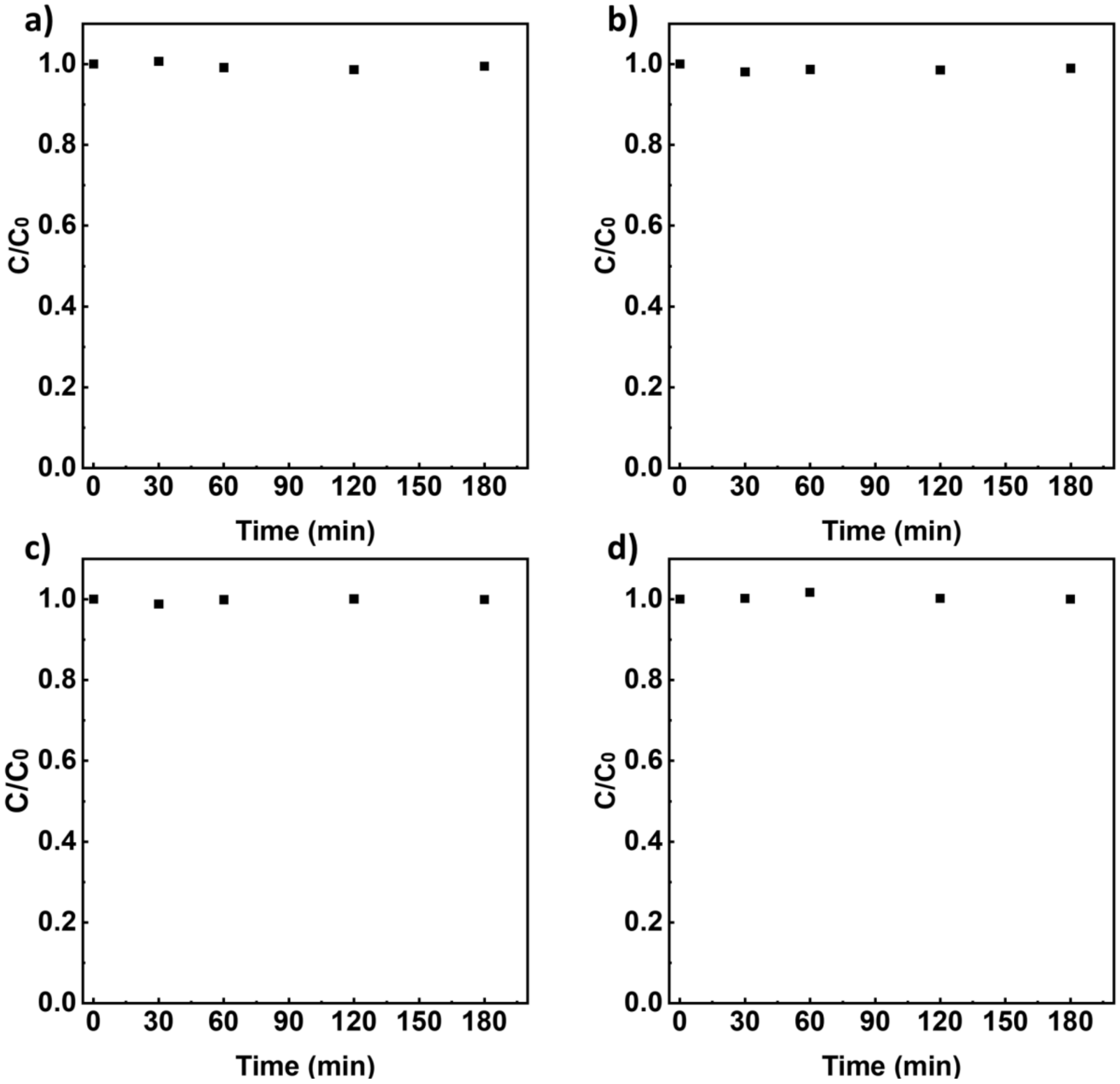

Figure 3.13. Photolysis assay of CIP (5 mg/L) under 180 minutes of blue (a), green (b), red (c) and NIR light (d) radiation.

This counterintuitive trend can be rationalized by the high absorbance of light by the nanoparticles that block the pass of light deeper in the cuvette and produce the catalytic effect only in the first part of the optical path. In fact, sample C, the one with the highest absorbance, completely blocked the light in a few millimeters. In addition, the highest content of gold, as shown above, produced higher absorption in the dark, and reduced the TiO_2 surface area (total mass of nanoparticles constant for all experiments) contributing to the lower performance. As the wavelength was increased to green and red light, only TiO_2:Au-NSs- Sample A was activated in the CIP degradation. A degradation efficiency of 34% and 39% of TiO_2:Au-NSs-A, with k = 0.0024 and 0.0025 min^{-1} for the green and red light radiation was found, respectively. According to the results of photocatalytic assays under NIR light, none of these three nanoparticles could be activated.

For the catalytic process to become activated, electrons from the Au part should gain enough energy from the incident absorbed photon to overpass the Shottky barrier, i.e., the difference between the work function of the Au and the electron affinity in the TiO_2 as determined by the Schottky–Mott equation ($\Phi_{SB} = \phi_M - \chi_{SM}$) [44]. Then a lower limit is expected in the absorbed photon energies, i.e., a higher limit in the wavelength. On the other hand, several studies have shown that Φ_{SB} is not only determined by ϕ_M and χ_{SM}, but also is significantly influenced by interfacial chemistry, giving rise to differences between different types of nanoparticles, in this case with a limit in the 635–735 nm region [45,46].

3.3.4. Membranes production and characterisation

Non-solvent-Induced Phase Separation, NIPS, combined with salt leaching was used to incorporate the synthesized TiO_2:Au-NSs nanoparticles into the PVDF-HFP polymer matrix and to obtain a porous microstructure. The successful incorporation of the nanoparticles in the polymer matrix extends their reuse, assuring the recovery of the catalyst and, therefore, allowing for a more sustainable and cost-effective application.

The porous morphology and the presence of nanoparticles were analysed by SEM-EDX (**Figures 3.14 a)** and **b)**). The thickness of the membranes was 271 µm and 217 µm for 0 and 10 wt.% TiO_2:Au-NSs/PVDF-HFP, respectively. After the incorporation of nanoparticles, the thickness of the membranes was slightly reduced.

High porosity and well-distributed and interconnected pores were observed in both membranes. Notably, the incorporated nanoparticles with 10 wt.% amount did not produce significant changes in the morphology of the pristine membranes. Both membranes presented two ranges of porous distribution due to the polydisperse NaCl grains [26] located mainly in the lower part of the membrane and the additional porous formation by the simultaneous NIPS mechanism [26]. The EDS spectrum (inset) also confirmed the successful incorporation of TiO_2:Au-NSs nanoparticles into PVDF-HFP membranes.

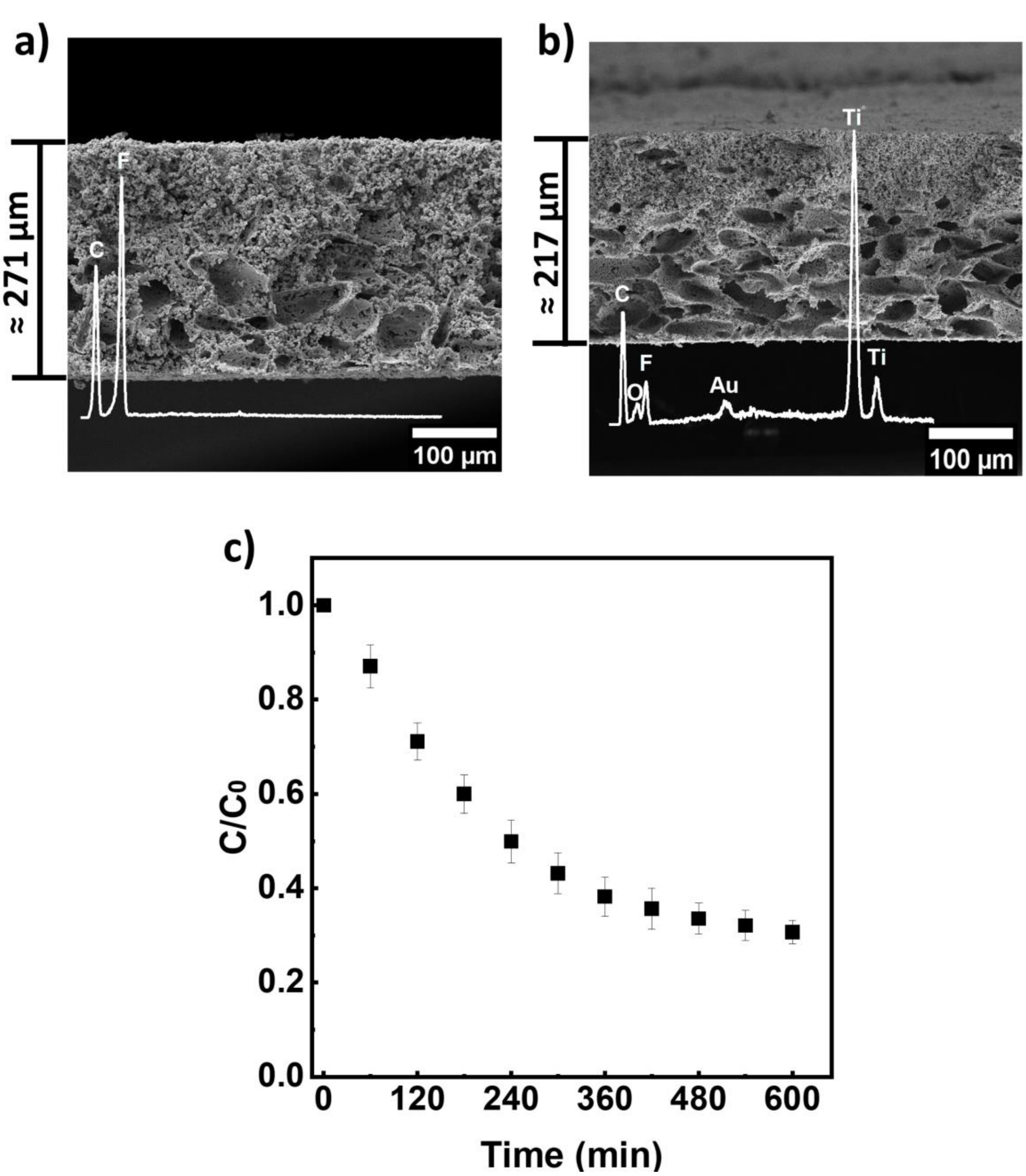

Figure 3.14. Cross-section SEM images of 0 wt.% (a) and 10 wt.% TiO_2:Au-NSs/PVDF-HFP membranes (b) with EDS spectrum (inset). Photocatalytic degradation of CIP (5 mg/L) with 10 wt.% TiO_2:Au-NSs/PVDF-HFP membrane under 600 min of visible radiation (c).

The prepared membrane with 10 wt.% TiO_2:Au-NSs nanoparticles was tested in the degradation of CIP under visible light (**Figure 3.14 c)**). The membrane did not show a release of nanoparticles to the solution and a CIP degradation efficiency of 69% at 600 min, with $k = 0.002$ min^{-1}.

The photocatalytic degradation process was lower when compared to the corresponding colloidal dispersion, mainly due to the blocking of part of the nanoparticle surface by the polymer; however, it was enough to obtain a good degradation of the antibiotic and its application facilitates the catalyst recovery and the reusability, and decreases the secondary pollution by nanoparticles to the medium, which makes it an excellent system for environmental application.

3.4. Conclusions

Novel hybrid nanoparticles, TiO_2:Au-NSs, with a Au branched morphology were synthesised successfully through the surfactant-free method and characterised and tested in photocatalytic assays for ciprofloxacin (CIP) degradation. The characterisation results of TEM and DRS show that different sizes of Au NPs with branched morphology were produced by modifying the synthesis conditions, which allowed the tuning of the optical properties of hybrid nanoparticles. When increasing the size of Au NPs with branched morphology, the reflectance of the hybrid nanoparticles decreased from 57% to 13% in the visible region. Additionally, the increase in the size of the Au branched nanoparticles extended the light absorption to the whole visible and part of the NIR region and reduced the bandgap from 3.10 eV to 2.86 eV, respectively.

The photocatalytic assays confirmed that all the synthesised nanoparticles degraded target compound CIP under both UV and visible radiation. It was also possible to understand the impact of the size of Au branched nanoparticles in the photocatalytic response. TiO_2:Au-NSs nanoparticles with smaller Au branched morphology and lowest amount of added Au among these hybrid nanoparticles showed a better photocatalytic performance degrading 83% and 89% ciprofloxacin under UV and visible radiation, respectively.

According to the results, under the different wavelengths of light in the visible and NIR region, the nanoparticles could be activated under blue, green, and red light radiation showing a CIP degradation efficiency of 57%, 34%, and 39%, respectively. However, there was no photocatalytic degradation of CIP under NIR radiation. The bigger size of Au branched nanoparticles limited the light-harvesting of $TiO_{2,}$ and reduced the photocatalytic activity, although they showed a broader light absorption in the whole visible and part of the NIR region of sunlight radiation.

The nanoparticles TiO_2:Au-NSs with lower branching and best performance were selected as the best candidates to incorporate into a PVDF-HFP polymer matrix through the NIPS technique. The produced membranes presented a porous structure and degraded successfully ciprofloxacin in water, opening the door to future application in a cost-effective way to degrade a high number of contaminants of emerging concern, among other possible applications. Moreover, the synthesis method of Au NSs explained here could also be applied to other semiconductors.

3.5. References

1. Wang, M.; Ye, M.; Iocozzia, J.; Lin, C.; Lin, Z. Plasmon-Mediated Solar Energy Conversion via Photocatalysis in Noble Metal/Semiconductor Composites. *Adv. Sci.* **2016**, *3*, 1600024, doi:10.1002/advs.201600024.
2. Zhang, X.; Chen, Y.L.; Liu, R.-S.; Tsai, D.P. Plasmonic Photocatalysis. *Reports Prog. Phys.* **2013**, *76*, 046401, doi:10.1088/0034-4885/76/4/046401.
3. Martins, P.; Kappert, S.; Le, H.N.; Sebastian, V.; Kühn, K.; Alves, M.; Pereira, L.; Cuniberti, G.; Melle-franco, M.; Lanceros-Méndez, S. Enhanced Photocatalytic Activity of Au/TiO_2 Nanoparticles against Ciprofloxacin. *Catalysts* **2020**, *10*, 234, doi:10.3390/catal10020234.
4. Liu, L.; Ouyang, S.; Ye, J. Gold-Nanorod-Photosensitized Titanium Dioxide with Wide-Range Visible-Light Harvesting Based on Localized Surface Plasmon Resonance. *Angew. Chemie Int. Ed.* **2013**, *52*, 6689–6693, doi:10.1002/anie.201300239.
5. Wang, C.; Astruc, D. Nanogold Plasmonic Photocatalysis for Organic Synthesis and Clean Energy Conversion. *Chem. Soc. Rev.* **2014**, *43*, 7188–7216, doi:10.1039/c4cs00145a.
6. Ying, L.; Shuo, C.; Xie, Q.; Hongtao, Y. Fabrication of a TiO_2/Au Nanorod Array for Enhanced Photocatalysis. *Chinese J. Catal.* **2011**, *32*, 1838–1843, doi:10.1016/S1872-2067(10)60288-4.
7. Xiao, Y.; Huang, Y.; Xue, S.; Zhao, J. Light Switching of Amine Oxidation Products from Oximes to Imines: Superior Activity of Plasmonic Gold Nanorods-Loaded TiO_2(B) Nanofibers under Visible-near IR Light. *Appl. Catal. B Environ.* **2020**, *265*, 118596, doi:10.1016/j.apcatb.2020.118596.
8. Sharma, V.; Kumar, S.; Krishnan, V. Clustered Au on TiO_2 Snowman-Like Nanoassemblies for Photocatalytic Applications. *ChemistrySelect* **2016**, *1*, 2963–2970, doi:10.1002/slct.201600671.
9. Sharma, V.; Kumar, S.; Krishnan, V. Shape Selective Au-TiO_2 Nanocomposites for Photocatalytic Applications. *Mater. Today Proc.* **2016**, *3*, 1939–1948, doi:10.1016/j.matpr.2016.04.095.

10. Hang Sun, Shan Zeng, Qinrong He, Ping She, Kongliang Xu, Z.L. Spiky TiO_2/Au Nanorod Plasmonic Photocatalysts with Enhanced Visible-Light Photocatalytic Activity. *Dalt. Trans.* **2017**, *46*, 3887–3894, doi:10.1039/C7DT00345E.

11. Wang, L.; Wang, Y.; Schmuki, P.; Kment, S.; Zboril, R. Nanostar Morphology of Plasmonic Particles Strongly Enhances Photoelectrochemical Water Splitting of TiO_2 Nanorods with Superior Incident Photon-to-Current Conversion Efficiency in Visible/near-Infrared Region. *Electrochim. Acta* **2018**, *260*, 212–220, doi:10.1016/j.electacta.2017.11.106.

12. Si, Y.; Cao, S.; Wu, Z.; Ji, Y.; Mi, Y.; Wu, X.; Liu, X.; Piao, L. What Is the Predominant Electron Transfer Process for Au NRs/TiO_2 Nanodumbbell Heterostructure under Sunlight Irradiation? *Appl. Catal. B Environ.* **2018**, *220*, 471–476, doi:10.1016/j.apcatb.2017.08.024.

13. Atta, S.; Pennington, A.M.; Celik, F.E.; Fabris, L. TiO_2 on Gold Nanostars Enhances Photocatalytic Water Reduction in the Near- Infrared Regime TiO_2 on Gold Nanostars Enhances Photocatalytic Water Reduction in the Near-Infrared Regime. *CHEM* **2018**, *4*, 2140–2153, doi:10.1016/j.chempr.2018.06.004.

14. Liu, Y.; Xiao, Z.; Cao, S.; Li, J.; Piao, L. Controllable Synthesis of Au-TiO_2 Nanodumbbell Photocatalysts with Spatial Redox Region. *Chinese J. Catal.* **2020**, *41*, 219–226, doi:10.1016/S1872-2067(19)63477-7.

15. Zhang, H.; Li, X.; Chooi, K.S.; Jaenicke, S.; Chuah, G. TiO_2 Encapsulated Au Nanostars as Catalysts for Aerobic Photo- Oxidation of Benzyl Alcohol under Visible Light. *Catal. Today* **2020**, *375*, 558–564, doi:10.1016/j.cattod.2020.03.028.

16. Khoury, C.G.; Vo-dinh, T. Gold Nanostars For Surface-Enhanced Raman Scattering: Synthesis, Characterization and Optimization. *J. Phys. Chem. C* **2008**, *112*, 18849–18859, doi:10.1021/jp8054747.

17. Guerrero-martínez, A.; Barbosa, S.; Pastoriza-santos, I.; Liz-marzán, L.M. Current Opinion in Colloid & Interface Science Nanostars Shine Bright for You Colloidal Synthesis , Properties and Applications of Branched Metallic Nanoparticles. *Curr. Opin. Colloid Interface Sci.* **2011**, *16*, 118–127, doi:10.1016/j.cocis.2010.12.007.

18. Koczkur, K.M.; Mourdikoudis, S.; Polavarapu, L.; Skrabalak, S.E. Polyvinylpyrrolidone (PVP) in Nanoparticle Synthesis. *Dalt. Trans.* **2015**, *44*, 17883–17905, doi:10.1039/c5dt02964c.

19. Ramsey, J.D.; Zhou, L.; Almlie, C.K.; Lange, J.D.; Burrows, S.M. Achieving Plasmon Reproducibility from Surfactant Free Gold Nanostar Synthesis. *New J. Chem.* **2015**, *39*, 9098–9108, doi:10.1039/C5NJ01590A.

20. Reyes, N.J.D.G.; Geronimo, F.K.F.; Yano, K.A. V.; Guerra, H.B.; Kim, L.-H. Pharmaceutical and Personal Care Products in Different Matrices: Occurrence, Pathways, and Treatment Processes. *Water* **2021**, *13*, 1159, doi:10.3390/ w13091159.

21. Shurbaji, S.; Huong, P.T.; Altahtamouni, T.M. Review on the Visible Light Photocatalysis for the Decomposition of Ciprofloxacin, Norfloxacin, Tetracyclines, and Sulfonamides Antibiotics in Wastewater. *Catalysts* **2021**, *11*, 437, doi:10.3390/catal11040437.

22. Anastasiya Kutuzova, Tetiana Dontsova, W.K. Application of TiO_2-Based Photocatalysts to Antibiotics Degradation: Cases of Sulfamethoxazole, Trimethoprim and Ciprofloxacin. *Catalysts* **2021**, *11*, 728, doi:10.3390/catal11060728.

23. Martins, P.M.; Ribeiro, J.M.; Teixeira, S.; Petrovykh, D.Y.; Cuniberti, G.; Pereira, L.; Lanceros-Méndez, S. Photocatalytic Microporous Membrane against the Increasing Problem of Water Emerging Pollutants. *Materials (Basel).* **2019**, *12*, 1649, doi:10.3390/ma12101649.

24. Salazar, H.; Martins, P.M.; Santos, B.; Fernandes, M.M.; Reizabal, A.; Sebastian, V.; Botelho, G.; Tavares, C.J.; Vilas-Viela, J.L.; Lanceros-Mendez, S. Photocatalytic and Antimicrobial Multifunctional Nanocomposite Membranes for Emerging Pollutants Water Treatment Applications. *Chemosphere* **2020**, *250*, 126299, doi:10.1016/j.chemosphere.2020.126299.

25. Serrano-montes, A.B.; Langer, J.; Henriksen-lacey, M.; Aberasturi, D.J. De; Solís, D.M.; Taboada, J.M.; Obelleiro, F.; Bals, S.; Bekdemir, A.; Stellacci, F.; et al. Gold Nanostar-Coated Polystyrene Beads as Multifunctional Nanoprobes for SERS Bioimaging. *J. Phys. Chem. C* **2016**, *120*, 20860–20868, doi:10.1021/acs.jpcc.6b02282.

26. Ribeiro, C.; Costa, C.M.; Correia, D.M.; Nunes-pereira, J.; Oliveira, J.; Martins, P.; Gonçalves, R.; Cardoso, V.F.; Lanceros-méndez, S. Electroactive Poly(Vinylidene Fluoride)-Based Structures for Advanced Applications. *Nat. Protoc.* **2018**, *13*, 681–704, doi:10.1038/nprot.2017.157.

27. Abdullahi, S.S.; Güner, S.; Koseoglu, Y.; Musa, I.M.; Adamu, B.I.; Abdulhamid, M.I. Simple Method for the Determination of Band Gap of a Nanopowdered Sample Using Kubelka Munk Theory. *J. Niger. Assoc. Math. Phys.* **2016**, *35*, 241–246.

28. Sakthivel, S.; Hidalgo, M.C.; Bahnemann, D.W.; Geissen, S.U.; Murugesan, V.; Vogelpohl, A. A Fine Route to Tune the Photocatalytic Activity of TiO_2. *Appl. Catal. B Environ.* **2006**, *63*, 31–40, doi:10.1016/j.apcatb.2005.08.011.

29. Karmakar, S. Particle Size Distribution and Zeta Potential Based on Dynamic Light Scattering: Techniques to Characterize Stability and Surface Charge Distribution of Charged Colloids. In *Recent Trends in Materials: Physics and Chemistry*; Studium Press, 2019; pp. 117–159.

30. Rosales, M.; Zoltan, T.; Yadarola, C.; Mosquera, E.; Gracia, F.; García, A. The Influence of the Morphology of 1D TiO_2 Nanostructures on Photogeneration of Reactive Oxygen Species and Enhanced Photocatalytic Activity. *J. Mol. Liq.* **2019**, *281*, 59–69, doi:10.1016/j.molliq.2019.02.070.

31. Qu, X.; Kirschenbaum, L.J.; Borish, E.T. Hydroxyterephthalate as a Fluorescent Probe for Hydroxyl Radicals: Application to Hair Melanin. *Photochem. Photobiol.* **2000**, *71*, 307–313, doi:10.1562/0031-8655(2000)071<0307:haafpf>2.0.co;2.

32. Reguera, J.; Jiménez De Aberasturi, D.; Henriksen-Lacey, M.; Langer, J.; Espinosa, A.; Szczupak, B.; Wilhelm, C.; Liz-Marzán, L.M. Janus Plasmonic-Magnetic Gold-Iron Oxide Nanoparticles as Contrast Agents for Multimodal Imaging. *Nanoscale* **2017**, *9*, 9467–9480, doi:10.1039/c7nr01406f.

33. Reguera, J.; Aberasturi, D.J. de; Winckelmans, N.; Langer, J.; Bals, S.; Liz-Marzán, L.M. Synthesis of Janus Plasmonic-Magnetic, Star-Sphere Nanoparticles, and Their Application in SERS Detection. *Faraday Discuss.* **2016**, *191*, 47–59, doi:10.1039/C6FD00012F.

34. Espinosa, A.; Reguera, J.; Curcio, A.; Muñoz-noval, Á.; Kuttner, C.; Walle, A. Van De; Liz-marzán, L.M.; Wilhelm, C. Janus Magnetic-Plasmonic Nanoparticles for

Magnetically Guided and Thermally Activated Cancer Therapy. *Small* **2020**, *16*, 1904960, doi:10.1002/smll.201904960.

35. Fonseca-cervantes, O.R.; Alejandro, P.; Romero, H.; Sulbaran-rangel, B. Effects in Band Gap for Photocatalysis in TiO_2 Support by Adding Gold and Ruthenium. *Processes* **2020**, *8*, 1032, doi:10.3390/pr8091032.

36. Carole Sentein, Benoit Guizard, Sophie Giraud, C.Y. and F.T. Dispersion and Stability of TiO_2 Nanoparticles Synthesized by Laser Pyrolysis in Aqueous Suspensions. *J. Phys.* **2009**, *170*, 012013, doi:10.1088/1742-6596/170/1/012013.

37. Israelachvili, J.N. *Intermolecular and Surface Forces*; Third Edit.; Elsevier, 2011; ISBN 9780123751829, doi:10.1016/C2009-0-21560-1.

38. Chen, W.; Zhang, J.; Cai, W. Sonochemical Preparation of Au, Ag, Pd/SiO_2 Mesoporous Nanocomposites. *Scr. Mater.* **2003**, *48*, 1061–1066, doi:10.1016/S1359-6462(02)00635-8.

39. Fujishima, A.; Zhang, X.; Tryk, D.A. TiO_2 Photocatalysis and Related Surface Phenomena. *Surf. Sci. Rep.* **2008**, *63*, 515–582, doi:10.1016/j.surfrep.2008.10.001.

40. Supriya K. Khore, Sunil. R. Kadam, Sonali D. Naik, Bharat B. Kale, R.S.S. Solar Light Active Plasmonic Au@TiO_2 Nanocomposite with Superior Photocatalytic Performance for H_2 Production and Pollutant Degradation. *New J. Chem.* **2018**, *42*, 10958–10968, doi:10.1039/C8NJ01410H.

41. Durán-Álvarez, J.C.; Avella, E.; Ramírez-Zamora, R.M.; Zanella, R. Photocatalytic Degradation of Ciprofloxacin Using Mono- (Au, Ag and Cu) and Bi- (Au–Ag and Au–Cu) Metallic Nanoparticles Supported on TiO_2 under UV-C and Simulated Sunlight. *Catal. Today* **2016**, *266*, 175–187, doi:10.1016/j.cattod.2015.07.033.

42. Gan, Y.; Zhang, M.; Xiong, J.; Zhu, J.; Li, W.; Zhang, C.; Cheng, G. Impact of Cu Particles on Adsorption and Photocatalytic Capability of Mesoporous Cu@ TiO_2 Hybrid towards Ciprofloxacin Antibiotic Removal. *J. Taiwan Inst. Chem. Eng.* **2019**, *96*, 229–242, doi:10.1016/j.jtice.2018.11.015.

43. Photocatalysts, A.T.; Mach, A.; Font, K.; Garc, D.; Sampayo, P.; Col, C.; Claudio-serrano, G.J.; Soto-v, L.; Resto, E.; Petrescu, F.I.; et al. Hydrogen Production and Degradation of Ciprofloxacin by Ag@TiO_2-MoS_2 Photocatalysts. *Catalysts* **2022**, *12*, 1–19, doi:10.3390/catal12030267.

44. Zhang, Y.; He, S.; Guo, W.; Hu, Y.; Huang, J.; Mulcahy, J.R.; Wei, W.D. Surface-Plasmon-Driven Hot Electron Photochemistry. *Chem. Rev.* **2018**, *118*, 2927–2954, doi:10.1021/acs.chemrev.7b00430.

45. Jiang, W.; Bai, S.; Wang, L.; Wang, X.; Yang, L.; Li, Y.; Liu, D.; Wang, X.; Li, Z.; Jiang, J.; et al. Integration of Multiple Plasmonic and Co-Catalyst Nanostructures on TiO_2 Nanosheets for Visible-Near-Infrared Photocatalytic Hydrogen Evolution. *Small* **2016**, *12*, 1640–1648, doi:10.1002/smll.201503552.

46. Nishijima, Y.; Ueno, K.; Yokota, Y.; Murakoshi, K.; Misawa, H. Plasmon-Assisted Photocurrent Generation from Visible to near-Infrared Wavelength Using a Au-Nanorods/TiO_2 Electrode. *J. Phys. Chem. Lett.* **2010**, *1*, 2031–2036, doi:10.1021/jz1006675.

Chapter 4

4. Hybrid TiO_2:Au nanostars based polymeric membranes for photocatalysis

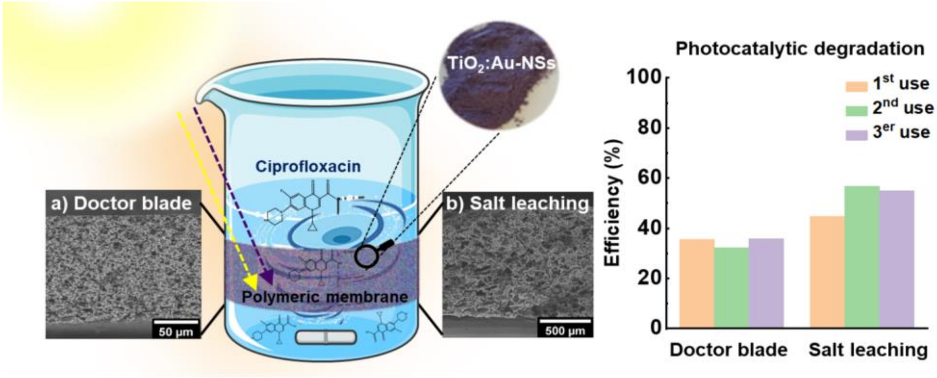

This research reports on the development of two porous membranes based on TiO_2:Au-NSs hybrid nanoparticles immobilised into PVDF-HFP membrane by doctor blade and salt leaching techniques. After a comparative study of their photocatalytic activity for ciprofloxacin degradation, the reusability assays of membranes were performed in different types of water matrix: ultrapure water and real treated effluent.

This chapter is based on the following publication: Zheng, F., et al., Hybrid TiO_2:Au Nanostars Based Polymeric Membranes for Photocatalytic Degradation of Ciprofloxacin in Water Samples. *Chemosphere* **2023**, *313*, 137630, doi:10.1016/j.chemosphere.2022.137630.

4.1. Introduction

As explained in the previous chapters**,** the cost-effective way to remove contaminants of emerging concern (CECs), such as pharmaceuticals, in water through photocatalysis not only depends on the improvement of efficiency of photocatalyst under sunlight, but also on the recovery/reuse of photocatalyst after use. Therefore, it is important to develop robust, durable and efficient substrates for photocatalysts immobilisation.

As mentioned in the **Chapter 1**, the PVDF-HFP polymers have been extensively used as membrane materials due to their excellent chemical, mechanical, thermal, and UV resistance characteristics, related to the stable C-F bonds of the polymer chain [1–4]. Furthermore, they can be produced in different morphologies such as thin films or porous membranes and fibre mats with controlled porosity and pore size, which can allow high photocatalytic efficiency of the nanoparticles after being supported on the membranes [1,3,5,6]. It has been also demonstrated that the photocatalytic efficiency highly depends on the different morphologies of the PVDF membranes [3]. Nonetheless, the immobilisation of photocatalysts remains a challenge, namely the mass transfer limitation, reduction of light-harvesting, loss of available active sites of photocatalyst, aggregation of photocatalysts in the support materials, or detachment of photocatalysts, leading to a lower efficiency [7].

On the other hand, most photocatalytic materials for CECs degradation are tested in ultrapure water, and little is known about its performance in natural water matrixes such as a river, treated effluent and wastewater [8–10]. Nevertheless, the composition in the real water matrixes, namely inorganic anions and organic matter, is more complex, which could have a significant effect on the photocatalytic efficiency [10–13], as stated in **Chapter 1**.

In this sense, once the PVDF-HFP polymer matrix was experimentally validated as support for novel TiO_2:Au-NSs nanoparticles incorporation, further studies should shift to the influence of the immobilisation processing techniques, the different morphologies of PVDF-HFP and the amount of incorporated nanoparticles, the type of water matrix on the final photocatalytic performance.

In this chapter, different amounts of synthesised TiO_2:Au-NSs hybrid nanoparticles have been incorporated into PVDF-HFP polymer matrix, through two different methods, doctor blade and salt leaching, in combination with Temperature-Induced Phase Separation (TIPS). TIPS method has chosen because it allows the production of membranes with higher mechanical strength, as explained in **Chapter 1**. Moreover, the influence of the membranes processing techniques on the membranes´ characteristics and photocatalytic performance has been studied through the degradation of ciprofloxacin (CIP) as a model antibiotic, under UV and visible radiation. Finally, the reuse of the membranes and their application in CIP degradation in a real treated effluent water matrix was assessed.

4.2. Experimental

4.2.1. Materials

Poly(vinylidene fluoride-co-hexafluoropropylene) (PVDF-HFP, SOLEF® 21216/1001) was purchased from Solvay. N, N-dimethylformamide (DMF, ≥99%) and sodium chloride (NaCl, analytical reagent grade) were supplied by Fisher-Scientific. Titanium dioxide (TiO_2) nanoparticles were provided by Evonik Industries AG. Hydrogen tetrachloroaurate (III) trihydrate ($HAuCl_4 \cdot 3H_2O$, 99.99%) was supplied by Alfa Aesar. Sodium hydroxide (NaOH, 98.0-100.5%) was obtained from Panreac. Hydrochloric Acid (HCl, 37%) was supplied by LABKEM. L-ascorbic acid (AA, ≥99%) and silver nitrate ($AgNO_3$, ≥99%) were purchased from Sigma-Aldrich. Milli-Q ultrapure water (resistivity 18.2 MΩ·cm) was used in all experiments. Ciprofloxacin (CIP, ≥98% (HPLG), $C_{17}H_{18}FN_3O_3$) with maximum light absorption at a wavelength of 277 nm was supplied by Sigma-Aldrich.

4.2.2. Sample preparation

4.2.2.1. TiO_2:Au-NSs nanoparticles synthesis

The synthesis of TiO_2:Au-NSs hybrid nanoparticles has been previously described [14]. In the first step, 200 mg of TiO_2 nanoparticles in 40 mL of ultrapure water were dispersed in a sonication bath for 30 min. Then, this solution was stirred at room temperature, and a specific volume of $HAuCl_4$ (1 mM) was added to achieve an Au loading of 0.05 wt.%. Later, the solution was stirred for 10 min to disperse the gold precursor homogeneously. Afterwards, NaOH (0.1 M) was added dropwise to obtain a pH = 9 and then mixed for 10 min. Finally, the solution was centrifuged and washed twice with ultrapure water. The nanoparticles were dried overnight in an oven at 80 ºC and subsequently grounded with a mortar to obtain a fine powder of TiO_2:Au nanospheres (TiO_2:Au-NSph). In the second step, 150 mg of TiO_2:Au-NSph nanoparticles were dispersed in 3.8 mL of ultrapure water in a sonication bath for 30 min as seed solution. Then, a growth solution was prepared by mixing 18.9 mL of ultrapure water, 19 µL of HCl (1 M), and 95 µL of $HAuCl_4$ (50 mM), considering a volume ratio between gold solution ($HAuCl_4$, 50 mM) and seed solution of 0.025. Afterwards, the prepared seed solution was added to this growth solution at room temperature and under moderate stirring. According to the used growth solution volume, 57 µL of $AgNO_3$ (10 mM) and 95 µL of AA (100 mM) solution were simultaneously added to the above mixture under vigorous stirring. The solution rapidly turned from light pink to purplish-grey, indicating the modification of Au morphology from Au sphere to star. The obtained samples (TiO_2:Au-NSs) were centrifuged, washed twice with ultrapure water, and resuspended in ultrapure water.

4.2.2.2. Doctor blade membranes production

The previously synthesised TiO_2:Au-NSs nanoparticles were used as fillers to prepare nanoparticle-loaded membranes through the Temperature-Induced Phase Separation (TIPS) technique, using a doctor blade casting and following the main guidelines described by Ribeiro et al. [15]. First, different amounts of TiO_2:Au-NSs were dispersed in 9 mL of DMF to obtain a TiO_2:Au-NSs/PVDF-HFP final mass ratio of 0%, 3%, 8%, and 10%, and placed in an ultrasonication bath for 2 hours at room temperature to achieve a good nanoparticles dispersion. Afterwards, 1 g of PVDF-HFP polymer was added to the solution to obtain a PVDF-HFP/DMF concentration of 1:9 v/v. The solution was stirred at 100 rpm until complete dissolution of the polymer is achieved. The nanoparticle/polymer solution was then placed in a glass substrate and spread by a doctor blade with a defined gap of 950 µm. The DMF was evaporated at room temperature for nearly 2 weeks leading to membranes with an average thickness of 120 µm. Based on the nanoparticle/polymer mass relation, the doctor blade membranes were identified as 0%, 3%, 8%, and 10% TiO_2:Au-NSs_PVDF-HFP.

4.2.2.3. Salt leaching membranes production

The nanoparticle/PVDF-HFP solution was prepared according to the process described above (**Section 4.2.2.2**), and then 1 g of NaCl particles with a diameter of 150 µm were added and mixed. After 1 hour of stirring, to achieve a homogeneous distribution of the NaCl particles, this mixture was placed in a glass Petri dish to evaporate DMF at room temperature. After drying, the membranes were washed in deionised water for 1 week to remove NaCl particles and then dried at room temperature, leading to membranes with an average thickness of 1100 µm. The nanoparticle/polymer mass relation identified the salt leaching membranes as 0%, 3%, 8%, and 10% TiO_2:Au-NSs_PVDF-HFP.

4.2.3. Sample characterisation

Transmission electron microscopy (TEM) images were acquired with a JEOL JEM 1400 Plus setup operating at 100 kV, and a Talos (Thermo Scientific) system working at 200 kV for the HAADF-STEM measurements. To prepare the samples, the nanoparticle powder was dispersed in ultrapure water and sonicated for 1 minute, and then 4 µL of the suspension was placed on a 400-mesh carbon-coated copper grid and left to dry at room temperature. The analysis of the images was performed using the ImageJ software package.

A field emission gun scanning electron microscope (FEG-SEM) Hitachi S-4800N operating at 10 kV voltage was used to image the membranes. Before measurement, the samples were coated with a thin layer of gold (≈15 nm) in an Emitech K550X ion-sputter. The average pore size of the membranes was averaged from the SEM images using the ImageJ software.

The porous structure of the membranes was determined by mercury intrusion porosimetry (MIP) in a Quantachrome Instruments Poremaster-60 GT, operating in the pressure range from vacuum (10^{-4} MPa) to 414 MPa. Samples were degassed in situ at 100 ºC for 12 hours prior to the measurements. A contact angle of 140º and surface tension of 480 $dyn{\cdot}cm^{-1}$ for mercury and a pressure equilibration time of 11 s were used. Before measuring MIP, the He densities for all the samples were measured in a Quantachrome Instruments automatic Micro Ultrapycnometer.

Elemental analysis of the membranes was carried out by Energy Dispersive X-ray spectroscopy (EDX) using a Carl Zeiss EVO 40 (Oberkochen, Germany) SEM equipped with an EDX Oxford Instrument X-Max detector (Abingdon, UK). The measurement conditions were in a high vacuum, at a voltage of 20 kV, a current of 100-400 pA, and a working distance of 9-10 mm.

Fourier-transform infrared spectroscopy (FTIR) measurements were carried out using a Jasco FT/IR-6100 spectrometer. Analyses were conducted from 600 to 4000 cm^{-1} after 32 scans with a resolution of 4 cm^{-1}.

Differential scanning calorimetric (DSC) analyses were carried out in a Mettler Toledo DSC 822e equipment from room temperature up to 200 °C at 10 °C/min, under a nitrogen atmosphere (flow rate, 20 mL/min). Approximately 4-6 mg of the samples was measured in aluminium pans with perforated lids to allow the release and removal of volatiles.

The hydrophobicity/hydrophilicity of the membranes was assessed by measuring the contact angle of CIP solution at room temperature using an Ossila Contact Angle Goniometer. Three drops of 5 µL of CIP solution (5 mg/L) were deposited at different places of each membrane. The contact angle was measured immediately after the drop deposition. The curve was fitted to the edge of the drop using the contact angle software, and the corresponding angle was calculated. The same measurements were repeated after the membranes were exposed to UV light for 30 min.

Ultrahigh-performance liquid chromatography (UHPLC), coupled with time-of-flight high-resolution mass spectrometry (TOF-HRMS, Synapt G2 from Waters Cromatografia S.A) by an electrospray ionisation source in positive mode (ESI+), was used to detect the products in liquid solution. The chromatographic separation was achieved using an Acquity UPLC BEH C18 column (1.7 µm, 2.1×50 mm i.d.) with an Acquity UPLC BEH C18 1.7 µm VanGuard pre-column (2.1×5 mm) (Waters Cromatografia S.A.) and a binary A/B gradient (solvent A: water with 0.1% formic acid and solvent B: methanol). The gradient program was established as follows: initial conditions were 5% B, raised to 99% B over 2.5 min, held at 99% B until 4 min, decreased to 5% B over the next 0.1 min, and held at 5% B until 5 min for re-equilibration of the system before the next injection. A flow rate of 0.25 mL/min was used, the column temperature was 30 ºC, the autosampler temperature 4 ºC, and the injection volume 5 µL.

4.2.4. Photocatalytic degradation under UV and visible radiation

The photocatalytic activity of the produced membranes was evaluated under both UV and visible light radiation. Firstly, a CIP solution of 5 mg/L was prepared and adjusted to pH=3. Before the degradation assays, a piece of the membrane was cut to obtain an area of 18 cm^2 guaranteeing the same radiation dose for all the membranes. On the other hand, due to the difference in processing and load of nanoparticles, its quantity can vary from 3.8 to 40 mg. The substrate was immersed and stirred in 50 mL of CIP solution in the dark for 30 min to achieve an adsorption-desorption equilibrium.

The UV degradation of CIP was carried out in a photoreactor with eight UV lamps of 8 W, with an emission peak at 365 nm, over 30 min. The membrane and CIP were kept stirred in a 100 mL beaker under illumination from the top. The distance between the solution and the lamp was 13.5 cm, and the irradiance at the sample was 3.3 W/m^2.

For the visible light degradation, a Xenon lamp was used with an excitation peak at 550 nm and irradiance of 300 W/m^2 (spectra in **Figure 4.1**), over 150 min. The membrane and CIP were kept stirred in a 100 mL beaker under lateral illumination. The distance between the solution and the lamp was 21 cm.

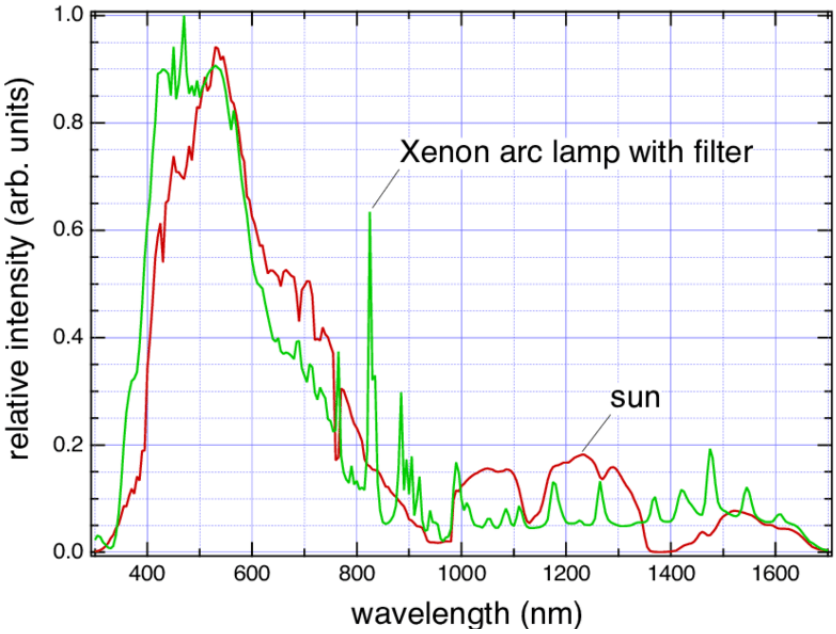

Figure 4.1. Xenon Lamp arc (with UV filter) and sunlight spectra.

Aliquots as samples were taken out at different times during the degradation assays to analyse the photocatalytic performance. This analysis was conducted by monitoring the absorbance variation of the absorption peak at 277 nm of the CIP in the UV-Vis spectrum, using a microplate reader Infinite 200 Pro in the range 230 to 450 nm.

The degradation rate of CIP fits a pseudo-first-order reaction, the Langmuir-Hinshelwood model [6], described by **Equation 4.1**:

$$\ln\left(\frac{C}{C_0}\right) = -kt \qquad \textbf{(4.1)}$$

where C and C_0 represent the CIP concentration at time t and t=0, taken at a given time and the beginning of the photocatalytic assessment, respectively. *k* is the first-order rate constant of the reaction [6].

4.3. Results and discussion

4.3.1. Nanoparticles and membranes characterisation

Hybrid nanoparticles of TiO_2:Au were synthesised following a multistep approach as previously described [14]. The final nanoparticles exhibited quasispherical TiO_2 nanoparticles with randomly distributed non-spherical Au nanoparticles (Au NSs) (grey and white parts of **Figure 4.2**, respectively).

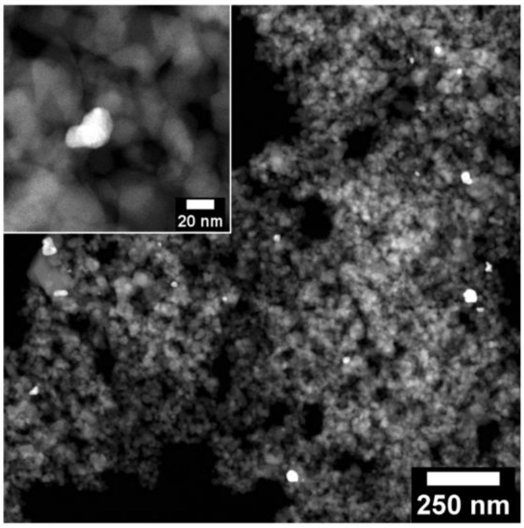

Figure 4.2. STEM-HAADF micrographs of TiO_2:Au-NSs.

Two different processing techniques were used to generate two porous matrices of PVDF-HFP incorporating the TiO_2:Au-NSs hybrid nanoparticles. One processing strategy relied on a Temperature-Induced Phase Separation (TIPS) process and doctor blade casting (hereafter called doctor blade membranes), and the second one is based on a salt leaching technique, where NaCl grains were used as porous generation agent (hereafter called salt leaching membranes).

The morphology of the produced membranes is shown in the representative SEM images in **Figures 4.3 a)-d)**. High porosity and well-distributed and interconnected pores are observed in both types of membranes. Notably, the incorporated nanoparticles at the working amounts did not introduce significant changes in the morphology of the membranes concerning the pristine polymer ones.

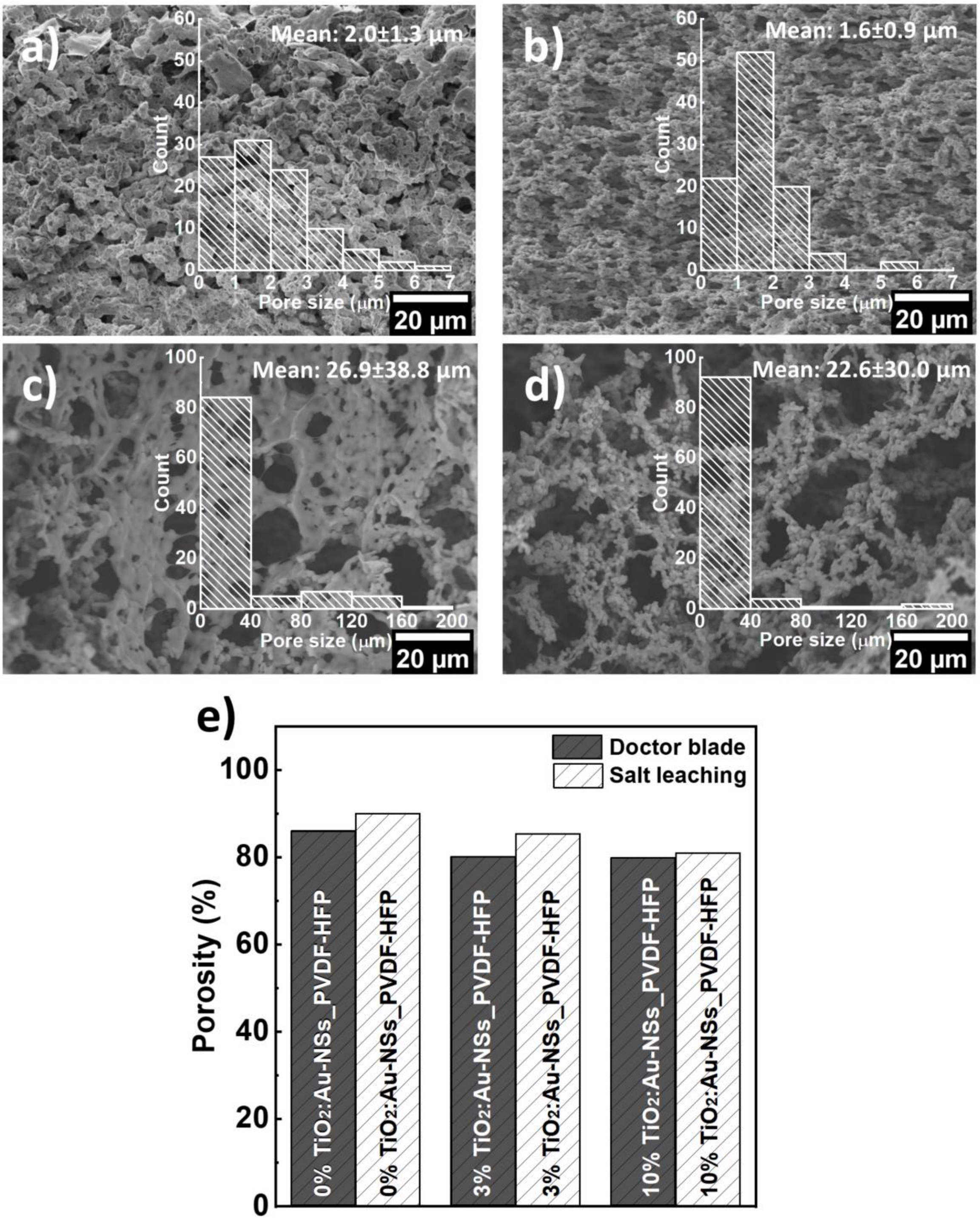

Figure 4.3. SEM micrographs with porous diameter histogram distribution (inset) of the doctor blade (a, b) and salt leaching membranes (c, d) with 0 wt.% (a, c) and 10 wt.% (b, d) incorporated TiO_2:Au-NSs nanoparticles. Porosity obtained by mercury intrusion porosimetry (MIP) for the doctor blade and salt leaching membranes (e).

Concerning the doctor blade membranes, the membranes presented a pore size between 0.5 and 7.0 µm, with prevalence in the range 1-2 µm (**Figures 4.3 a)-b)**). The incorporation of nanoparticles led to a slight decrease in pore size only for the high nanoparticle loading of

10 wt.%, with average porous sizes of 1.6 vs. the 2.0 µm observed in the non-loaded membrane. The obtained average pore sizes are in line with the ones observed in the literature for PVDF-based membranes obtained by TIPS [15,16]. Moreover, the porosity of the membranes was slightly reduced, from 86% to 80%, when increasing nanoparticle loading from 0 to 10 wt.% (**Figure 4.3 e)**). Salt leaching membranes, on the other hand, presented a broader pore size range due to the polydisperse NaCl grains [15] and the additional porous formation by the simultaneous TIPS mechanism. The larger pores were in the range of 120-200 µm, similar to the size of added NaCl particles (≈150 µm), while smaller pores, related to the simultaneous TIPS process, had a prevalence in the range of 5-40 µm (**Figure 4.3 c)-d)**). When nanoparticles were included, there was also a slight decrease in average pore size for the membranes with the highest loading of 10 wt.%, from 26.9 µm to 22.6 µm. Furthermore, at this nanoparticle concentration the porosity of the membranes decreased from 90 to 81% with increasing nanoparticle loading from 0 to 10 wt.% (**Figure 4.3 e)**).

EDX allowed to evaluate the elemental composition of the membranes and the nanoparticles distribution, as shown for the 10 wt.% nanoparticles-loaded membranes (**Figure 4.4**).

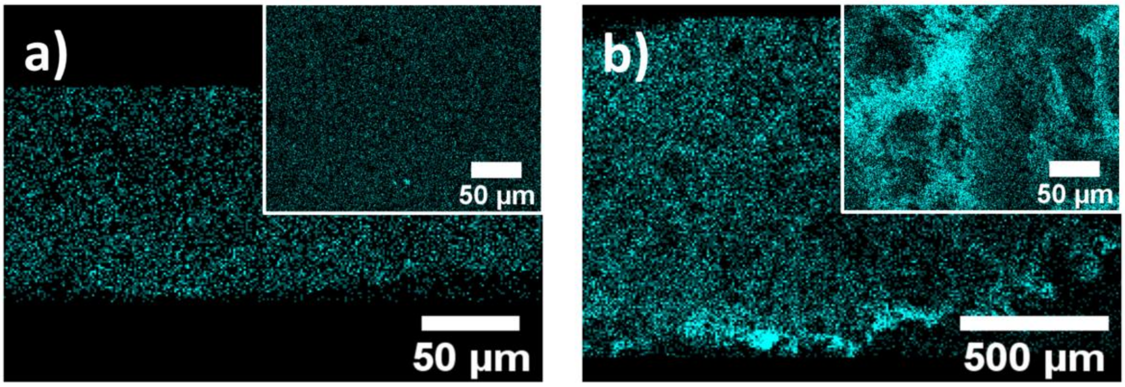

Figure 4.4. EDX chemical mapping of Ti along the membrane cross-section (a, b) and surface (inset) of the 10% TiO_2:Au-NSs_PVDF-HFP doctor blade (a) and salt leaching membrane (b).

EDX mapping, in both the top surface and the cross-section, confirms the homogeneous dispersion of nanoparticles within the polymer matrix, independently of the processing technique employed to produce the membranes, and discards the formation of large nanoparticles agglomerates. Nanoparticles inside the pores and on the membrane surface are also confirmed.

PVDF-HFP is a semicrystalline polymer that can crystallise in different phases depending on the processing conditions and/or the presence of fillers [15,17]. Hence, FTIR measurement was used to evaluate the polymer phase before and after incorporating the nanoparticles and to assess possible chemical interaction between the nanoparticles and the polymer matrix. **Figures 4.5 a)** and **b)** present the FTIR spectra for the doctor blade and salt leaching membranes, respectively. The results confirmed the presence of the polar β-phase of the polymer by the characteristic bands at 840 and 1400 cm^{-1}, as well as the non-polar α-phase, identified by the bands at 766 cm^{-1} [1,6,17,18] for all membranes.

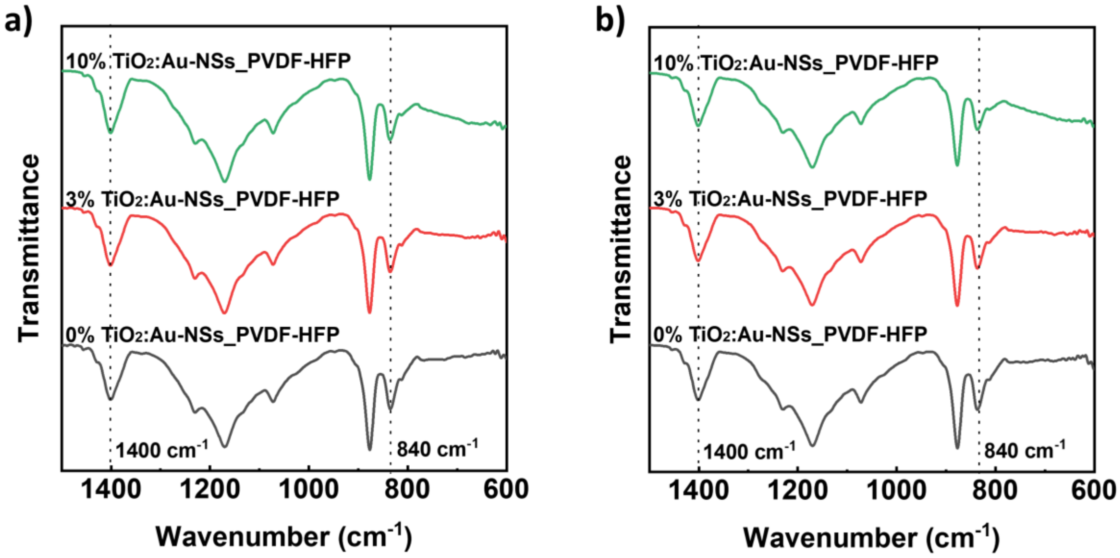

Figure 4.5. FTIR spectrum of doctor blade (a) and salt leaching membranes (b).

The relative fraction of the β-phase, F(β), of the polymer for each membrane was calculated by the **Equation 4.2** [17]:

$$F(\beta) = \frac{A_\beta}{(\frac{K_\beta}{K_\alpha})A_\alpha + A_\beta} \qquad \textbf{(4.2)}$$

where A_α and A_β are the absorbances at 766 and 840 cm^{-1}, respectively, and K_α (6.1×10^4 cm^2/mol) and K_β (7.7×10^4 cm^2/mol) are the corresponding absorption coefficients [17].

The calculated β-phase content in each membrane is presented in **Table 4.1**, showing that it is very similar and dominant in pristine membranes regardless of the processing technique, as it has been demonstrated that solvent evaporation at room temperature leads to the crystallization of the polymer mainly in the electroactive β-phase [15–17]. On the other hand, increasing nanoparticle loading decreased the β-phase content in both types of membranes due to the polymer-filler interactions during polymer crystallization, which is also in line with the literature [3].

Table 4.1. β phase content (%) of doctor blade and salt leaching membranes.

Sample	β phase content (%)	
	Doctor blade	**Salt leaching**
0% TiO_2:Au-NSs_PVDF-HFP	73.2	73.5
3% TiO_2:Au-NSs_PVDF-HFP	64.5	67.2
10% TiO_2:Au-NSs_PVDF-HFP	57.0	56.7

DSC allowed assessing the melting temperature and the degree of crystallinity of the membranes. **Figures 4.6 a)** and **b)** present the DSC thermograms of the doctor blade and salt leaching membranes, respectively. All the samples showed similar behaviour regardless of membranes preparation techniques and the amount of incorporated nanoparticles since the processing conditions, room temperature solvent evaporation, dominates the crystallization process of the samples. In all cases, a single endothermic peak around 141ºC is observed, which identifies the melting temperature of the sample [3,16].

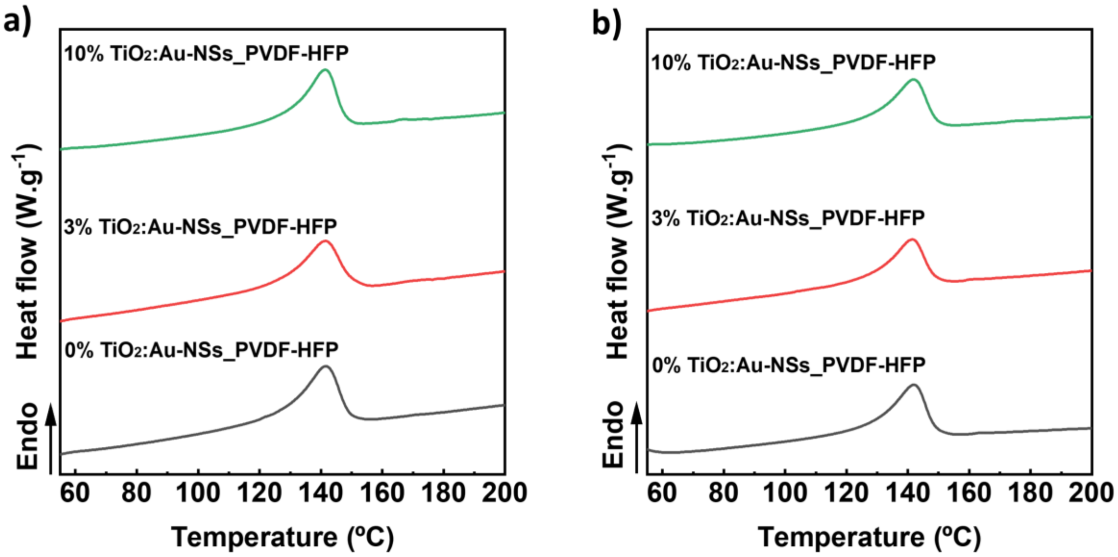

Figure 4.6. DSC thermograms of doctor blade (a) and salt leaching membranes (b).

The degree of crystallinity of the samples was calculated by **Equation 4.3** [16,18]:

$$\chi_c = \frac{\Delta H_f}{x\Delta H_\alpha + y\Delta H_\beta} \tag{4.3}$$

where ΔH_f is the melting enthalpy of the polymer obtained from the DSC, x and y are the α and β-phase contents, respectively, calculated from the FTIR spectrum. ΔH_α and ΔH_β are the melting enthalpies of pure crystalline α-PVDF (93.04 J/g) and β-PVDF (103.40 J/g), respectively [16,18].

Table 4.2 presents the degree of crystallinity of the membranes. All samples showed a high degree of crystallinity >30%, however, the degree of crystallinity in the membranes prepared by doctor blade was slightly higher than in salt leaching membranes, and the degree of crystallinity increased with increasing nanoparticles loading in both types of membranes, which can be attributed to the nucleation effect of nanofillers during polymer crystallization [19].

Table 4.2. Degree of crystallinity (%) of doctor blade and salt leaching membranes.

Sample	**Crystallinity (%)**	
	Doctor blade	**Salt leaching**
0% TiO_2:Au-NSs_PVDF-HFP	36.2	33.0
3% TiO_2:Au-NSs_PVDF-HFP	36.1	31.6
10% TiO_2:Au-NSs_PVDF-HFP	37.4	36.7

Finally, the wettability of the membranes was assessed by contact angle measurements before and after exposition to UV light using CIP solution (5 mg/L) to mimic the conditions of the photocatalytic experiments (**Figure 4.7**).

The pristine doctor blade and salt leaching membranes showed a hydrophobic character [20] with a contact angle of 99 ± 5 and 97 ± 5 degrees, respectively. After exposure to UV radiation, there was no significant change in the contact angle, which corroborates the well-known UV-resistant nature of PVDF polymers [1–3]. In contrast to the pristine membranes, the incorporation of nanoparticles decreased the contact angle due to their more hydrophilic nature. This decrease was more marked in salt leaching (82 ± 5°) than for doctor blade membranes (94 ± 1°) with 10% nanoparticles loading. Furthermore, the contact angle of these membranes was reduced even further after the UV radiation (84 ± 10, and 73 ± 6 degrees for doctor blade and salt leaching membranes), showing hydrophilic characteristics [20]. This result is in line with previously reported works for TiO_2 nanoparticles [1] and the more hydrophilic properties of TiO_2 immediately after UV irradiation [21]. The marked difference in the contact angle values between the two types of membranes is in agreement with their different porous microstructure, as shown in SEM images (**Figures 4.3 a)-d)**), where the larger pores contribute to a higher exposure of the nanoparticle surfaces to water and UV radiation.

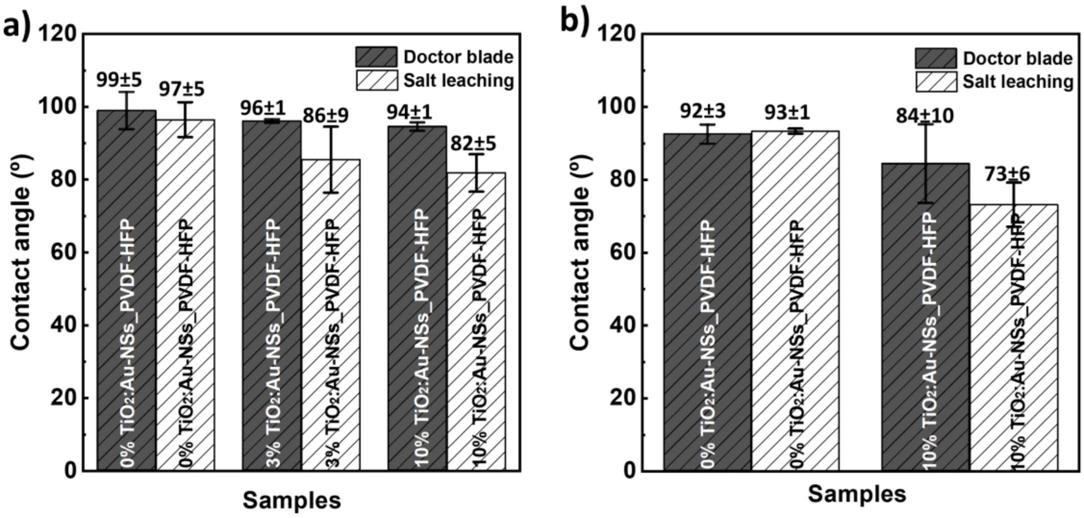

Figure 4.7. Average water contact angle of three measurements at room temperature of doctor blade and salt leaching membranes before (a) and after (b) UV radiation 30 min.

4.3.2. Photocatalytic degradation under UV and visible radiation

The photocatalytic activity of the produced membranes under both UV and visible radiation was assessed for CIP degradation (**Figure 4.8**). As controls, the photocatalytic activity of the pristine membranes, the photolysis of the CIP, and the adsorption of CIP solution in the dark were carried out (**Figure 4.8** and **Figure 4.9**). As expected, in the absence of nanoparticles, there was minimal degradation of CIP by photolysis under both UV and visible light in the pristine membranes (**Figure 4.8**) or in absence of membranes (**Figures 4.9 a)-b)**). Moreover, the pristine membranes showed null adsorption of CIP without illumination, regardless of the processing method and their corresponding membrane characteristics (**Figures 4.9 c)-d)**).

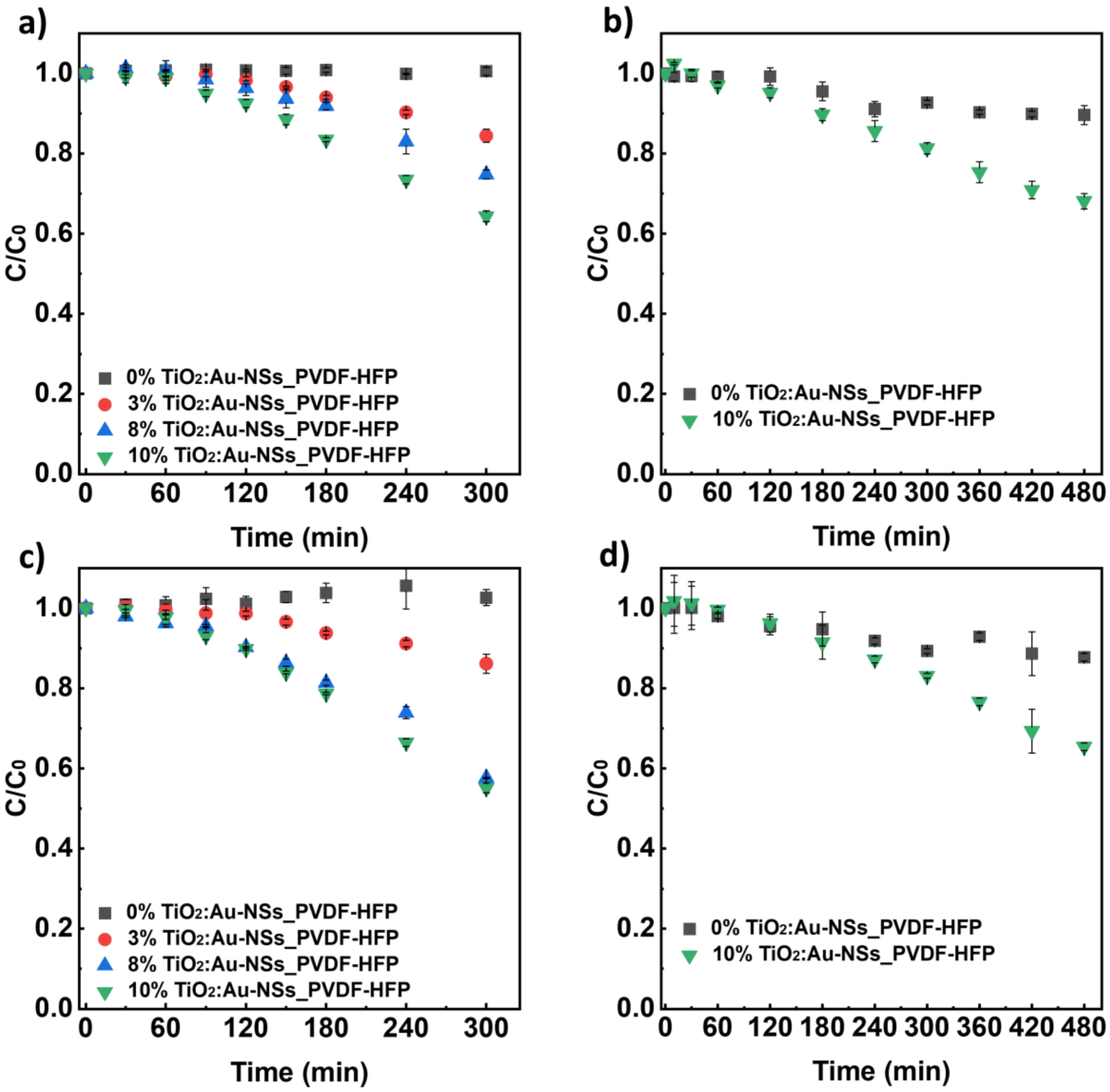

Figure 4.8. Photocatalytic degradation of CIP (5 mg/L) with doctor blade (a, b) and salt leaching membranes (c, d) under 300 min of UV radiation (a, c) and 480 min of visible radiation (b, d).

Under UV radiation, the degradation efficiency (DE) of CIP increased with increasing nanoparticles' load in both types of membranes due to the higher available area of photocatalyst [22]. An increase from 3 to 10 wt.% of nanoparticles loading raised CIP degradation efficiency from $DE_{db,uv}$ = 16 to 36% for doctor blade membranes and from $DE_{sl,uv}$ = 14 to 45% for salt leaching membranes. Thus, it is shown that at high enough nanoparticle loading, the salt leaching membranes possessed higher photocatalytic efficiency than doctor blade membranes under the same conditions. This is in good agreement with the larger pores and better wettability of salt leaching membranes, as indicated by the SEM (**Figures 4.3 a)-d)**) and contact angle results (**Figure 4.7**), respectively. The larger pores imply a higher exposure of the nanocatalyst and a higher available catalytic surface, while a better wettability leads to a better mass transfer of CIP throughout the membrane microporous structure, favouring the photocatalytic reaction.

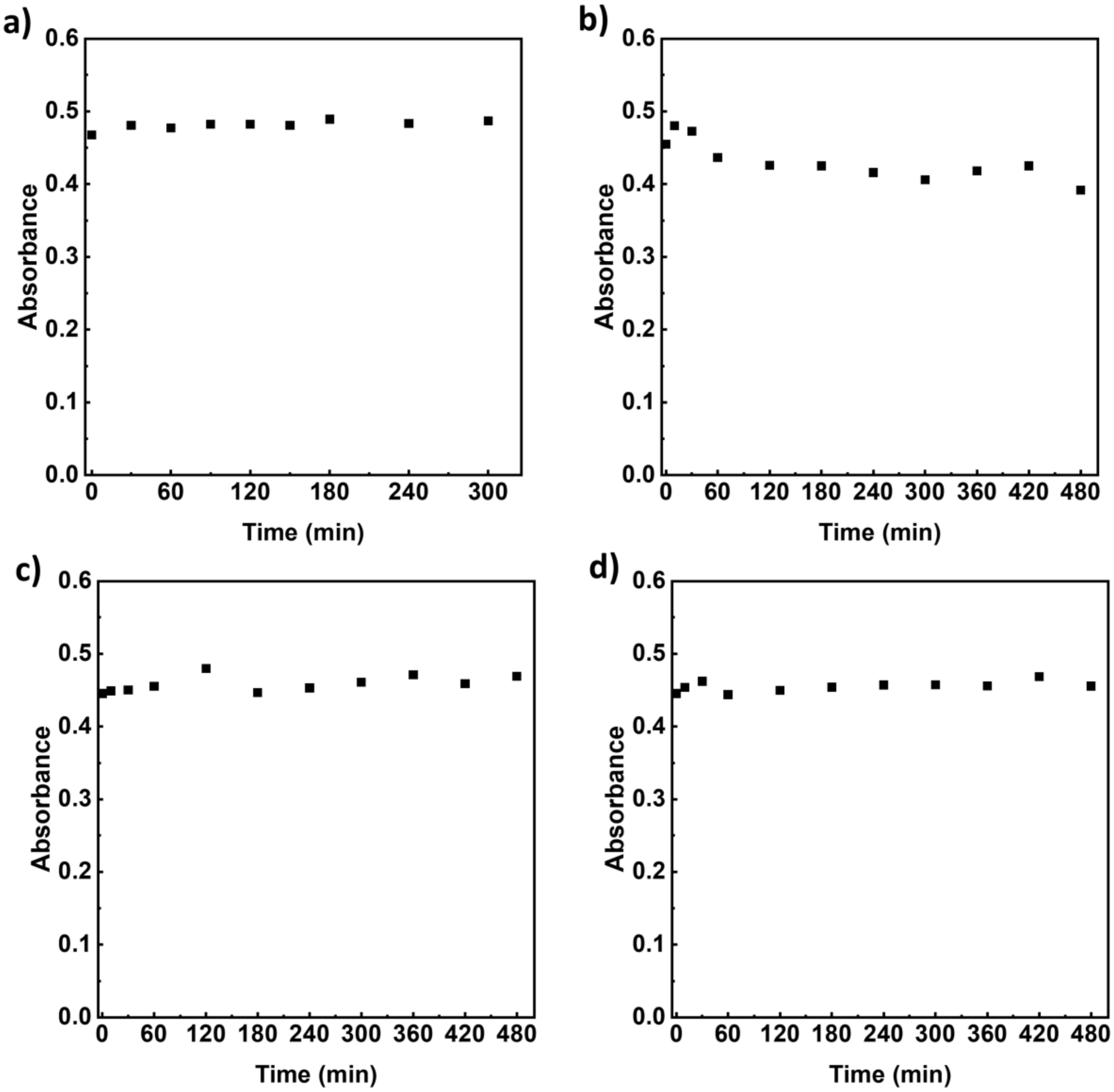

Figure 4.9. Photolysis assay of CIP (5 mg/L) under 300 min of UV radiation (a) and 480 min of visible radiation (b). Adsorption of CIP (5 mg/L) in the dark, using pristine PVDF-HFP doctor blade (c) and salt leaching membrane (d).

Table 4.3 shows the apparent reaction rate (*k*) calculated by **Equation 4.1** for the different membranes. As expected, a higher load of photocatalysts led to a higher apparent reaction rate and degradation efficiency. On the other hand, when the two types of membranes are compared, the highest degradation rate constant values obtained for doctor blade membranes and salt leaching membranes were $k_{db,uv} = 1.2\times10^{-3}$ and $k_{sl,uv} = 1.6\times10^{-3}$ min^{-1}, respectively, again showing the highest photocatalytic capabilities of the salt leaching membranes.

Table 4.3. CIP degradation efficiencies (DE) and corresponding apparent reaction rate constants (*k*) under 300 min of UV radiation and 480 min of visible radiation for doctor blade and salt leaching membranes.

Sample	UV		Visible	
	$k_{uv}\times10^4$ (min^{-1})	DE_{uv} (%)	$k_{vis}\times10^4$ (min^{-1})	DE_{vis} (%)
Doctor blade membranes				
0% TiO_2:Au-NSs_PVDF-HFP	-	-	3.0±0.6	10±1.3
3% TiO_2:Au-NSs_PVDF-HFP	4.0±0.6	16±0.6	-	-
8% TiO_2:Au-NSs_PVDF-HFP	7.0±1.0	25±1.6	-	-
10% TiO_2:Au-NSs_PVDF-HFP	12.0±0.0	36±1.0	8.0±0.0	32±1.3
Salt leaching membranes				
0% TiO_2:Au-NSs_PVDF-HFP	-	-	3.0±0.6	12±2.5
3% TiO_2:Au-NSs_PVDF-HFP	4.0±0.6	14±1.3	-	-
8% TiO_2:Au-NSs_PVDF-HFP	14.0±0.0	42±0.6	-	-
10% TiO_2:Au-NSs_PVDF-HFP	16.0±0.0	45±0.8	8.0±1.1	35±2.7

Under visible light radiation, the membranes with 10 wt.% nanoparticles load were also evaluated. The salt leaching membranes presented higher photocatalytic degradation, $DE_{sl,vis}$ = 35%, than the doctor blade membranes, $DE_{db,vis}$ = 32%, under the same conditions and similar $k_{db,vis} = k_{sl,vis} = 8\times10^{-4}$ min^{-1}. Similarly to the results under UV radiation, the difference in microstructure and hydrophilic characteristics between salt leaching and doctor blade membranes explains the better performance of the first one.

Finally, a photocatalytic process can form intermediate compounds (byproducts) [13,23]. Thus, to determine the possible degradation products of CIP during photocatalysis, the aqueous solutions under UV radiation were analysed by UHPLC-TOF-HRMS. The chromatographic analysis (**Figure 4.10**) shows a minimum difference in the mass signal intensity between the -30 min and 0 min (dark conditions) due to an almost null adsorption of CIP molecules onto the membrane surface. On the other hand, a significant decrease between 0 min and 300 min of irradiation indicated the degradation of CIP.

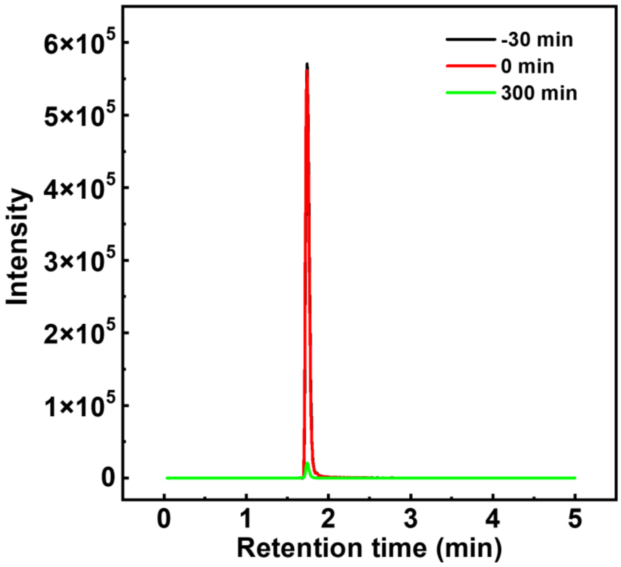

Figure 4.10. Chromatograms of CIP degradation using 10% TiO_2:Au-NSs_PVDF-HFP salt leaching membrane under 300 min of UV radiation.

Furthermore, **Table 4.4** presents the detected products, which indicated that at least under these conditions, the degradation led to the formation of a high number of intermediate subproducts and emphasised the effective photocatalytic degradation of CIP in the presence of the prepared membranes.

Table 4.4. Detected degradation products of CIP.

Detected molecule	*Detected m/z	Theoretical m/z	Mass error (mDa)	Mass error (ppm)
$C_{17}H_{19}N_3O_3F$	332.1412	332.141	0.2	0.5
$C_{17}H_{20}N_3O_4$	330.1451	330.1454	-0.3	-0.9
$C_{16}H_{17}N_3O_4F$	334.1202	334.1203	-0.1	-0.3
$C_{15}H_{17}N_3O_3F$	306.1253	306.1254	-0.1	-0.3
$C_{17}H_{17}N_3O_3F$	330.1257	330.1254	0.3	0.9
$C_{13}H_{12}N_2O_3F$	263.0831	263.0832	-0.1	-0.4
$C_{17}H_{18}N_3O_5$	344.1241	344.1246	-0.5	-1.6
$C_{17}H_{19}N_3O_4F$	348.135	348.136	-1	-2.8
$C_{15}H_{18}N_3O_4$	304.1293	304.1297	-0.4	-1.4
$C_{17}H_{17}N_3O_5F$	362.1146	362.1152	-0.6	-1.7
$C_{17}H_{19}N_3O_5F$	364.1308	364.1309	-0.1	-0.2
$C_{17}H_{17}N_3O_4F$	346.1194	346.1203	-0.9	-2.6

*The masses found correspond to protonated molecule [M+H]+

4.3.3. Reusability of the membranes

The immobilisation of photocatalyst addresses the costly post-separation process of nanoparticles and their possible secondary pollution after the photocatalytic process in suspension [1,7]. However, the immobilised systems present lower efficiency than suspended systems due to mass transfer limitations [7], and detachment of weak attached nanoparticles after use [3]. Hence, evaluating and studying the efficiency loss of the prepared membranes after reusing is essential, allowing the understanding of the potential reusability of the developed membranes for a cost-effective pollutants degradation.

Membranes containing 10 wt.% of TiO_2:Au-NSs nanoparticles were evaluated for reusability. The same experimental conditions for the photocatalytic test of membranes under UV and visible radiation were applied in three consecutive uses. The membranes were washed using ultrapure water three times and dried at room temperature between each use. Afterwards, the membranes were immersed into a new CIP solution (5 mg/L), and the new assay was performed under the same experimental conditions. The results are presented in **Figure 4.11**. The degradation efficiency (DE) and the estimated apparent reaction rate (k) for each use cycle (**Equation 4.1**) are presented in **Table 4.5**.

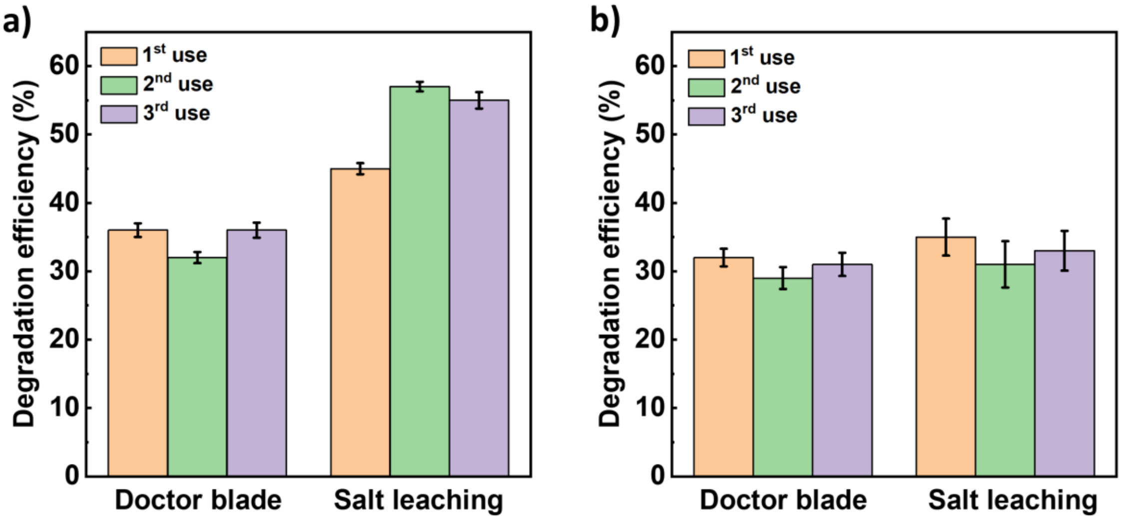

Figure 4.11. Degradation efficiency for CIP (5 mg/L) removal in three consecutive uses in ultrapure water with 10% TiO_2:Au-NSs_PVDF-HFP doctor blade and salt leaching membranes under 300 min of UV radiation (a) and 480 min of visible radiation (b).

Regarding the doctor blade membranes, there was no significant variation of degradation efficiency under UV radiation after three uses ($DE_{db,uv}$ = 36, 32, and 36%), nor a difference in the kinetic constant ($k_{db,uv} = 1.2\times10^{-3}$, 1.1×10^{-3}, and 1.2×10^{-3} min^{-1}). The same behaviour was presented under visible light radiation among the three cycles, with no significant loss of photocatalytic efficiency ($DE_{db,vis}$ = 32, 29, and 31%) and similar kinetic constants ($k_{db,vis}$= 8.0×10^{-4}, 7.0×10^{-4}, and 8.0×10^{-4} min^{-1}). These results indicate that the nanoparticle immobilisation was accomplished and that no degradation occurred in the membranes, as no significant amount of nanoparticles detached from the polymeric matrix, promoting a remarkable reusability of the doctor blade membranes.

Table 4.5. CIP degradation efficiencies (DE) and corresponding apparent reaction rate constants (*k*) in three consecutive uses with 10% TiO_2:Au-NSs_PVDF-HFP doctor blade and salt leaching membranes in ultrapure water under 300 min of UV radiation and 480 min of visible radiation.

Sample	UV		Visible	
	$k_{uv}\times10^4$ (min^{-1})	DE_{uv} (%)	$k_{vis}\times10^4$ (min^{-1})	DE_{vis} (%)
Doctor blade membranes				
1st	12.0±0.0	36±1.0	8.0±0.6	32±1.3
2nd	11.0±0.6	32±0.8	7.0±0.7	29±1.6
3rd	12.0±0.6	36±1.1	8.0±0.6	31±1.7
Salt leaching membranes				
1st	16.0±0.0	45±0.8	8.0±1.1	35±2.7
2nd	25.0±0.0	57±0.7	6.0±1.4	31±3.4
3rd	23.0±0.6	55±1.2	8.0±1.2	33±2.9

Different results were obtained for the salt leaching membranes. Under UV light, an increasing efficiency ($DE_{sl,uv}$ = 45, 57, and 55%) and increasing kinetic constant ($k_{sl,uv}$ = 1.6×10^{-3}, 2.5×10^{-3}, and 2.3×10^{-3} min^{-1}) were observed after three cycles, which is ascribed to the better contact between the pollutant and photocatalysts [1]. In contrast to the results obtained under UV, there was no significant change in photocatalytic efficiency after three use cycles under visible light radiation. The degradation efficiencies were $DE_{sl,vis}$ = 35, 31 and 33%, and the rate constants were $k_{sl,vis}$ = 8.0×10^{-4}, 6.0×10^{-4} and 8.0×10^{-4} min^{-1} for the first, second, and third uses, respectively.

Thus, the consecutive uses of the membrane for CIP degradation support their robustness in the scope of reusability. Besides the reusability assays, the membrane's physical-chemical properties were also assessed after the reusability assays under UV radiation by SEM, SEM-EDX, FTIR, and DSC techniques to further support it. These results are presented in **Figures 4.12-4.14** and **Table 4.6**.

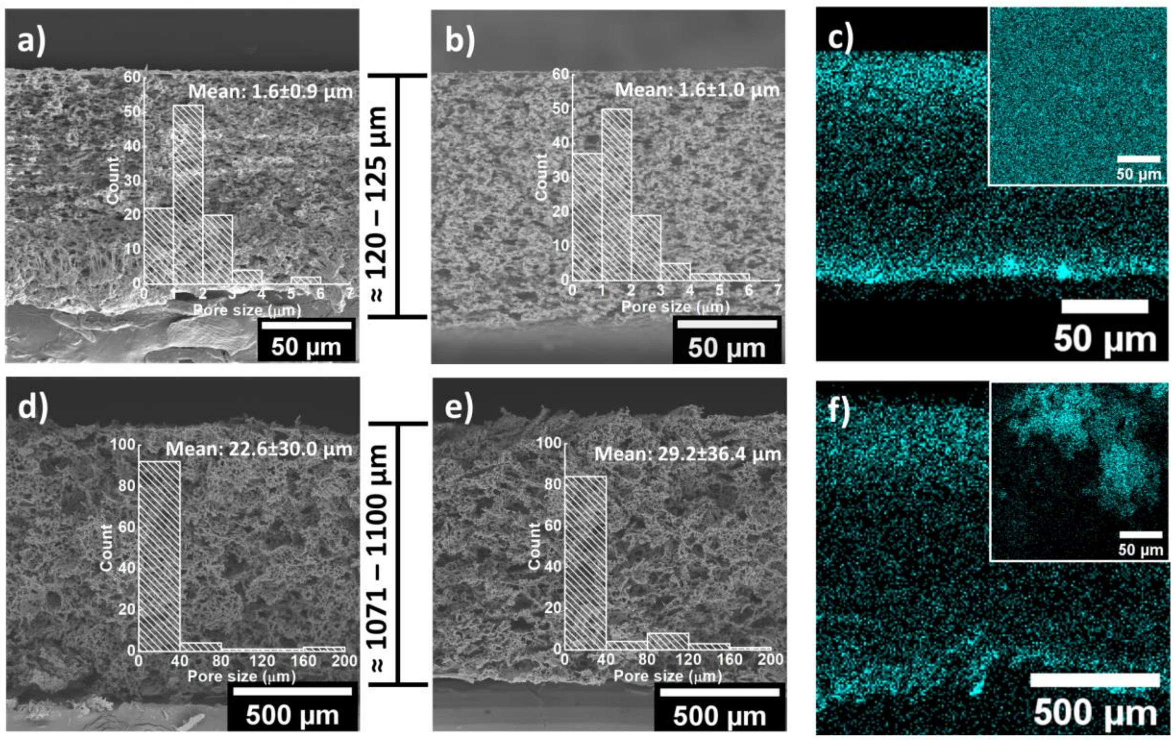

Figure 4.12. Cross-section SEM images of 10% TiO_2:Au-NSs_PVDF-HFP doctor blade (a, b) and salt leaching membranes (d, e) before (a, d) and after (b, e) the reusability assays with the corresponding pore diameter histograms distribution (inset). EDX mapping of the cross-section (c, f) and surface (inset) of 10% TiO_2:Au-NSs_PVDF-HFP doctor blade (c) and salt leaching membranes (f) after the reusability assays.

By analysing the SEM images of the 10% TiO_2:Au-NSs_PVDF-HFP doctor blade membranes (**Figures 4.12 a)** and **b)**), it is observed that the thickness of the membrane remained constant after reuse (≈ 120-125 µm). Furthermore, the average pore size was also maintained before and after three photocatalytic use cycles, as well as the pore size distribution. Additionally, the EDX results (**Figure 4.12 c)** and **Figures 4.13 a)** and **c)**) confirmed the efficient attachment of photocatalyst to the surface pores, maintaining the number of photocatalytic sites in the membranes after repeated cycles, even after cleaning and drying processes. Additionally, based on the FTIR and DSC measurement (**Figures 4.14 a)-b)** and **Table 4.6**), the photocatalytic reuses did not affect the polymer phases chemical structure, melting temperature, and crystallinity of the membrane, which agrees with previous work showing that PVDF and copolymers are stable under UV radiation and photocatalytic processes [1–3].

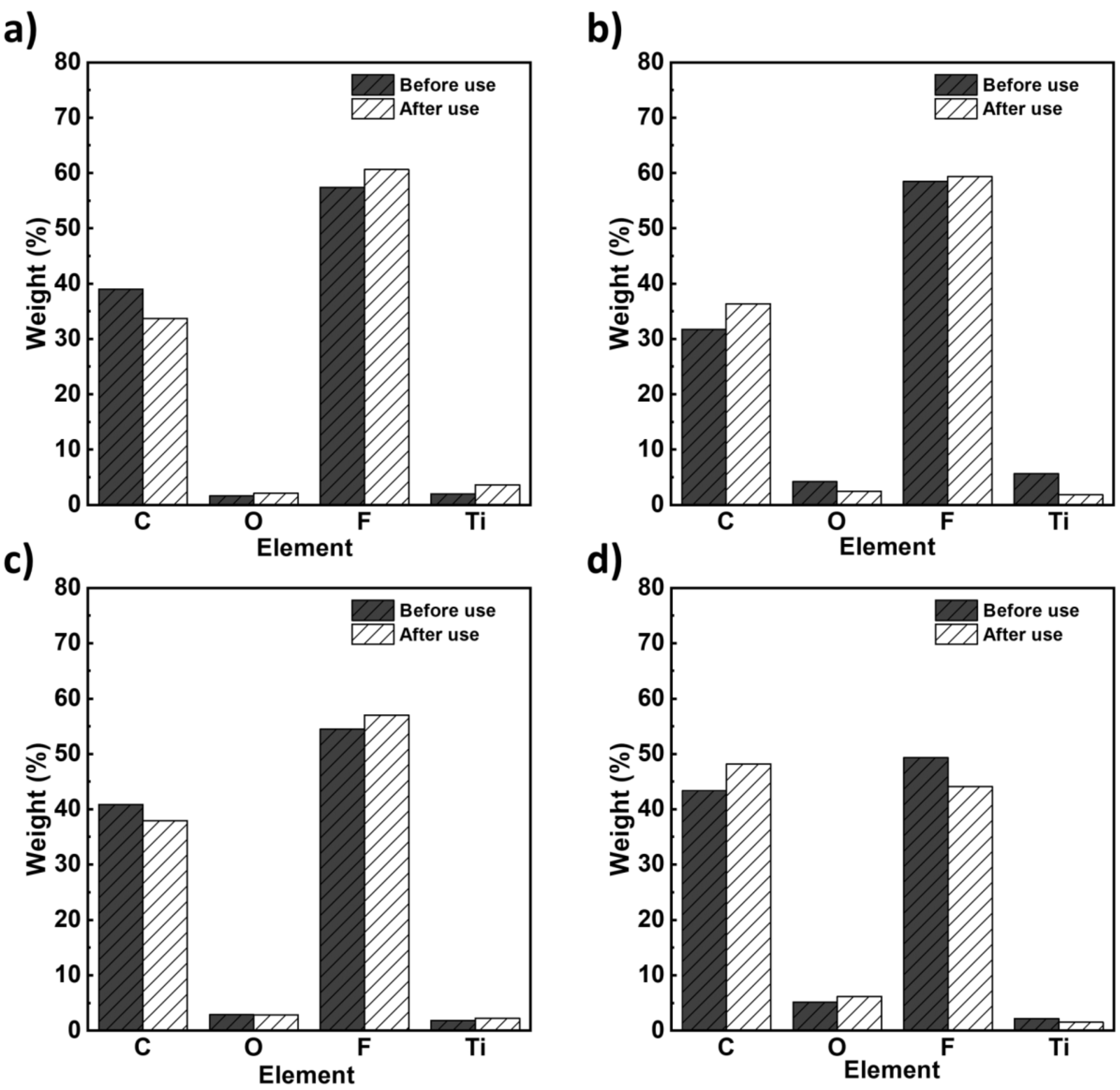

Figure 4.13. Elemental percentage of C, O, F, Ti in surface (a, b) and cross-section (c, d) of 10% TiO_2:Au-NSs_PVDF-HFP doctor blade (a, c) and salt leaching membranes (b, d) before and after the reusability assays.

Similarly, for 10% TiO_2:Au-NSs_PVDF-HFP salt leaching membranes before and after the reusability assays (**Figures 4.12 d)** and **e)**), it is observed that the photocatalytic application did not change the microstructure/morphology nor membranes thickness (≈ 1071-1100 µm). Furthermore, the average pore size slightly increased after the photocatalytic application, improving water percolation and thus promoting the superior contact between the CIP and the photocatalyst. Oppositely to this effect, there was a loss of photocatalysts in the outer surfaces after the reusability assays (EDX **Figure 4.12 f)** and **Figure 4.13 b)**). At the same time, a homogeneous distribution, with similar quantities of nanoparticles in the membrane interior, was maintained (**Figure 4.12 f)** and **Figure 4.13 d)**). This change is attributed to the loss of the inefficiently attached photocatalysts at the outer surface during the first use cycle and the washing step, while the efficiently attached photocatalysts for the subsequent uses remain constant. Thus, the photocatalytic efficiency during the second and third use was very similar. Finally, according to the FTIR and DSC measurements (**Figures 4.14 c)-d)** and **Table 4.6**), there was no significant variation in polymer phase, chemical structure, melting temperature, or crystallinity of salt leaching membranes along the photocatalytic use.

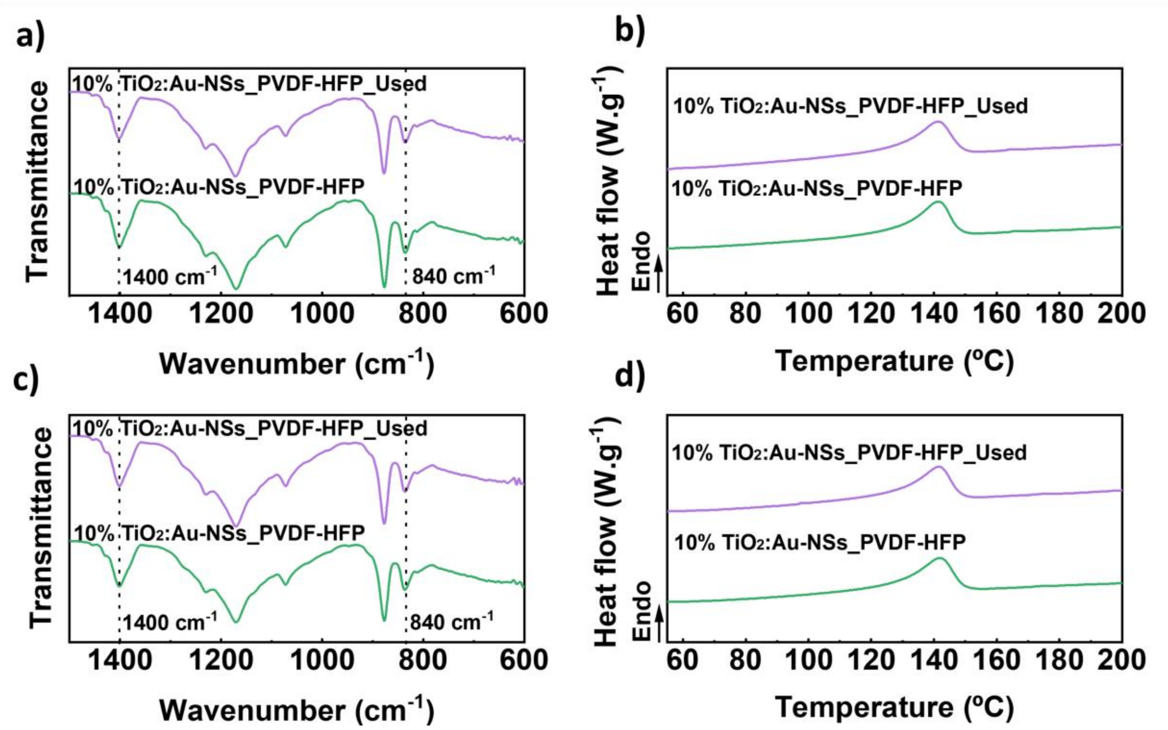

Figure 4.14. FTIR spectrum (a, c) and DSC thermograms (b, d) of 10% TiO_2:Au-NSs_PVDF-HFP doctor blade (a, b) and salt leaching membranes (c, d) before and after the reusability assays.

Table 4.6. β phase content (%) and degree of crystallinity (%) of 10% TiO_2:Au-NSs_PVDF-HFP doctor blade and salt leaching membranes before and after the reusability assays.

Sample	**β phase content (%)**		**Crystallinity (%)**	
	Doctor blade	**Salt leaching**	**Doctor blade**	**Salt leaching**
10% TiO_2:Au-NSs_PVDF-HFP	57.0	56.7	37.4	36.7
10% TiO_2:Au-NSs_PVDF-HFP_Used	53.1	55.6	37.7	36.2

Comparative evaluation with previous works related to the reusability of immobilised photocatalysts for pollutant degradation is shown in **Table 4.7**. Due to the different experimental conditions and materials in each work, the comparison is focused on the degradation efficiency loss after the reusability assay. Although this comparison is not straightforward, the comparative study allows contextualising our results.

In general, previously reported works showed an efficiency loss higher than the one in the present work. Regarding membrane systems, TiO_2/PVDF presented a 16% efficiency loss after three uses of Methylene Blue (MB) degradation [22], and TiO_2 in poly(ethylene terephthalate) support (TiO_2/PET) showed a 21% efficiency loss after being used five times for antibiotic mixture degradation [12]. Ag-TiO_2/PVDF-HFP presented an 8-16% efficiency loss after three uses of Norfloxacin (NOR) degradation [3]. These reports indicate that the detachment of the inefficiently attached nanoparticles to the polymer matrix after use [3,22] and the adsorption of the pollutants on the photocatalyst surface [12] are the main reasons for the photocatalytic efficiency loss.

Table 4.7. Comparison of the efficiency losses after reusability assays in the present work with previous studies using immobilised photocatalysts for pollutants degradation.

Materials	Pollutant	Number of use cycles	Efficiency loss (%)	Ref.
TiO_2/MMT	Ciprofloxacin (CIP)	5	6.6	[11]
TiO_2/PVDF	Methylene Blue (MB)	3	16	[22]
TiO_2/PET	Antibiotic mixture	5	21	[12]
Ag-TiO_2/PVDF-HFP	Norfloxacin (NOR)	3	8-16	[3]
TiO_2:Au-NSs_PVDF-HFP	Ciprofloxacin (CIP)	3	1-2	Present work

4.3.4. Photocatalytic degradation in a real treated effluent

The degradation of CIP presented until now was performed in an ultrapure water matrix. However, the composition in a real treated effluent is more complex, affecting the photocatalytic efficiency [10–12]. Thus, evaluating the photocatalytic efficiency and reusability of the prepared membranes in real treated effluents is essential, allowing us to understand the suitability of the developed membranes for solving real societal problems.

Salt leaching membranes containing 10 wt.% of TiO_2:Au-NSs nanoparticles (the most efficient in ultrapure water conditions) were evaluated in terms of photocatalytic performance and reusability for degradation of CIP in real treated effluents. Águas de Portugal (https://www.adp.pt/pt/) provided a sample of real treated effluents (see main features in **Table 4.8**) with the same CIP concentration (5 mg/L) and the process and experimental conditions for the evaluation of photocatalytic performance and reusability study in ultrapure water were applied to real treated effluent as a water matrix. The results are presented in **Figure 4.15** and **Table 4.9**.

Table 4.8. Chemical and physical properties of the real treated effluents.

Parameter	**Value**
pH	7.7
Temperature	21 ºC
Turbidity	0 NTU
Conductivity	123 µS/cm
Aluminium	8.39 µg/L
Calcium	12.9 mg/L
Chloride	0.83 mg/L
Magnesium	0.89 mg/L
Nitrate	6.34 mg/L
Nitrite	0.16 mg/L
Sulphate	23.7 mg/L
Ammonia nitrogen	0 mg/L
Total hardness	35.9 mg/L
Hardness (Calcium)	12.9 mg/L
Hardness (Magnesium)	0.89 mg/L
E. coli	0 N/100 mL
Coliform bacteria	0 N/100 mL
Clostridium perfringens	0 N/100 mL
Enterococos	0 N/100 mL

When comparing these results with the ones in the reusability study using ultrapure water (**Table 4.5**), the differences were negligible under UV radiation. On the other hand, a clear performance improvement was observed for visible light degradation of the real treated effluent. This may be ascribed to the pH difference between the real treated effluent and ultrapure water [11].

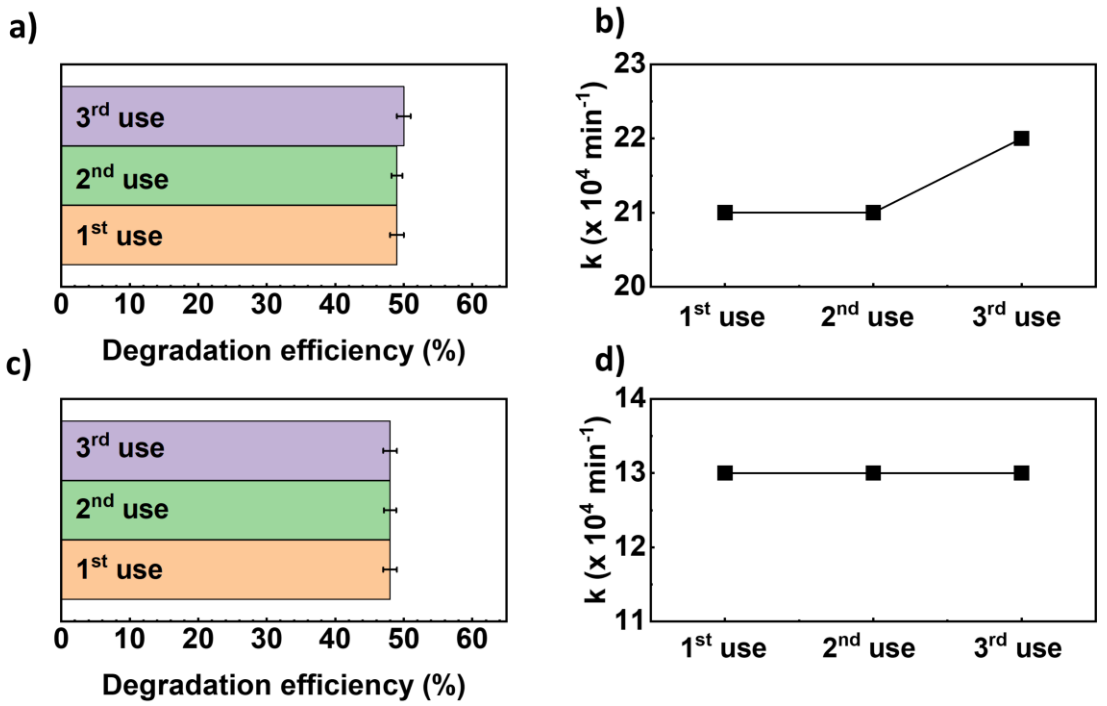

Figure 4.15. Degradation efficiency (a, c) and rate constant (b, d) for CIP (5 mg/L) removal in three consecutive uses in real treated effluent with 10% TiO_2:Au-NSs_PVDF-HFP salt leaching membranes under 300 min of UV radiation (a, b) and 480 min of visible radiation (c, d).

Table 4.9. CIP degradation efficiencies (DE) and corresponding apparent reaction rate constants (*k*) in three consecutive uses with 10% TiO_2:Au-NSs_PVDF-HFP salt leaching membranes in real treated effluent under 300 min of UV radiation and 480 min of visible radiation.

Sample	**UV**		**Visible**	
	$k_{uv} \times 10^4$ (min^{-1})	DE_{uv} (%)	$k_{vis} \times 10^4$ (min^{-1})	DE_{vis} (%)
1st	21.0±0.0	49±1.0	13.0±0.0	48±1.0
2nd	21.0±0.0	49±0.8	13.0±0.0	48±0.9
3rd	22.0±0.0	50±1.0	13.0±0.0	48±1.0

There was no significant change in degradation efficiency of CIP under UV radiation after three use cycles ($DE_{sl,uv}$ = 49, 49, and 50%), nor a difference in the kinetic constant ($k_{sl,uv}$ = 2.1×10^{-3}, 2.1×10^{-3} and 2.2×10^{-3} min^{-1}). The same behaviour was shown under visible light radiation among the three uses, without significant loss of photocatalytic efficiency ($DE_{sl,vis}$ = 48, 48, and 48%) and maintained kinetic constants, $k_{sl,vis} = 1.3\times10^{-3}$ min^{-1}, for each use. The membrane's reusability performance was maintained in the real effluent water matrix.

Comparative studies with previous works related to photocatalytic efficiency of pollutants degradation in real treated effluent are shown in **Table 4.10**. Due to the different experimental conditions and features of the used water matrix in each work, the comparisons are just focused on the degradation efficiency loss after using real treated effluent instead of an ultrapure water matrix. The reported works [10–12] generally showed higher efficiency loss than the present work in assays using real treated effluent, indicative of the adsorption of inorganic and organic constituents on the surface of the photocatalyst, reducing the available active site, as the main reason for the photocatalytic efficiency loss. Note that this comparison, although informative, could be affected by the different operational parameters of photocatalysis and the used water matrix, and a more precise absolute comparison would require testing all catalysts under the same experimental conditions.

Table 4.10. Comparison of efficiency losses between using real treated effluent water matrix and ultrapure water for pollutants degradation in the present work with previous works. In our case, we presented the maximum efficiency loss after 3 cycles (worst case).

Materials	Pollutant	Number of use cycles	Efficiency loss (%)	Ref.
TiO_2	Moxifloxacin (MOX)	1	50	[10]
TiO_2/MMT	Ciprofloxacin (CIP)	1	15	[11]
TiO_2/PET	Antibiotic mixture	1	40	[12]
TiO_2:Au-NSs_PVDF-HFP	Ciprofloxacin (CIP)	3	5	Present work

4.4. Conclusions

PVDF-HFP-based membranes containing different amounts of homogeneously distributed TiO_2:Au-NSs nanoparticles (0, 3, 8 and 10 wt.%) were successfully produced by two processing techniques, doctor blade and salt leaching, giving rise to photocatalytic membranes with different porous microstructures. It has been shown that, despite both types of membranes presenting well-distributed and interconnected pores regardless of the nanoparticle content, they showed marked differences. Doctor blade membranes showed a narrower pore (0.5-7 µm) and a constant contact angle, of more than 90° regardless of UV radiation and nanoparticles load. On the contrary, salt leaching membranes presented a broader pore size distribution with a larger pore size (5-200 µm) and a contact angle dependent on nanoparticle content (from 96 to 80°) and UV radiation (down to 71°).

The photocatalytic activity results showed that an increase in nanoparticle load improved photocatalytic efficiency regardless of the processing technique of membranes. Under the same conditions, the salt leaching membranes presented higher photocatalytic activity attributed to the higher porosity and access of the contaminant to the nanoparticle surface. They showed a degradation efficiency of 45% with a rate constant of 16×10^{-3} min^{-1} under UV radiation, and 35% with a rate constant of 8.0×10^{-3} min^{-1} under visible radiation. At the same time, doctor blade membranes presented a more limited degradation efficiency of 36% with a rate constant of 12×10^{-3} min^{-1} under UV radiation and 32% with a rate constant of 8.0×10^{-4} min^{-1} under visible radiation. Most importantly, the reusability assays of both membranes demonstrated the membrane robustness, with an average efficiency loss of only around 2% for the worst case, and even improved efficiencies for salt leaching membranes. Moreover, it has been demonstrated that the membranes were fully functional in a real treated effluents water matrix for ciprofloxacin degradation. In this case, membranes reached degradation efficiency of 50 and 48% under UV and visible radiation, respectively, after three consecutive photocatalytic uses.

In short, these results indicate the suitability of the processing methods to obtain membranes for water remediation applications in the degradation of contaminants of emerging concerns such as ciprofloxacin. This work opens the door to degrade a high number of contaminants of emerging concern cost-effectively, using sunlight energy as the power source, with good reusability and avoiding harmful secondary pollution in the aquatic organisms caused by free nanoparticles.

4.5. References

1. Martins, P.M.; Ribeiro, J.M.; Teixeira, S.; Petrovykh, D.Y.; Cuniberti, G.; Pereira, L.; Lanceros-Méndez, S. Photocatalytic Microporous Membrane against the Increasing Problem of Water Emerging Pollutants. *Materials (Basel).* **2019**, *12*, 1649, doi:10.3390/ma12101649.

2. Liu, F.; Hashim, N.A.; Liu, Y.; Abed, M.R.M.; Li, K. Progress in the Production and Modification of PVDF Membranes. *J. Memb. Sci.* **2011**, *375*, 1–27, doi:10.1016/j.memsci.2011.03.014.

3. Salazar, H.; Martins, P.M.; Santos, B.; Fernandes, M.M.; Reizabal, A.; Sebastian, V.; Botelho, G.; Tavares, C.J.; Vilas-Viela, J.L.; Lanceros-Mendez, S. Photocatalytic and Antimicrobial Multifunctional Nanocomposite Membranes for Emerging Pollutants Water Treatment Applications. *Chemosphere* **2020**, *250*, 126299, doi:10.1016/j.chemosphere.2020.126299.

4. Martins, P.M.; Santos, B.; Salazar, H.; Carabineiro, S.A.C.; Botelho, G.; Tavares, C.J.; Lanceros-Mendez, S. Multifunctional Hybrid Membranes for Photocatalytic and Adsorptive Removal of Water Contaminants of Emerging Concern. *Chemosphere* **2022**, *293*, 133548, doi:10.1016/J.CHEMOSPHERE.2022.133548.

5. Martins, P.M.; Gomez, V.; Lopes, A.C.; Tavares, C.J.; Botelho, G.; Irusta, S.; Lanceros-Mendez, S. Improving Photocatalytic Performance and Recyclability by Development of Er-Doped and Er/Pr-Codoped TiO2/Poly (Vinylidene Difluoride)−Trifluoroethylene Composite Membranes. *J. Phys. Chem. C* **2014**, *118*, 27944–27953, doi:10.1021/jp509294v.

6. Martins, P.M.; Miranda, R.; Marques, J.; Tavares, C.J.; Botelho, G.; Lanceros-Mendez, S. Comparative Efficiency of TiO_2 Nanoparticles in Suspension vs. Immobilization into P(VDF–TrFE) Porous Membranes. *RSC Adv.* **2016**, *6*, 12708–12716, doi:10.1039/C5RA25385C.

7. Singh, S.; Mahalingam, H.; Singh, P.K. Polymer-Supported Titanium Dioxide Photocatalysts for Environmental Remediation: A Review. *Appl. Catal. A Gen.* **2013**, *462–463*, 178–195, doi:10.1016/j.apcata.2013.04.039.

8. Barros, M.A.; Sampaio, M.J.; Ribeiro, A.R.; Silva, C.G.; Silva, A.M.T.; Faria, J.L. Interactions of Pharmaceutical Compounds in Water Matrices under Visible-Driven

Photocatalysis. *J. Environ. Chem. Eng.* **2021**, *9*, 104747, doi:10.1016/j.jece.2020.104747.

9. Rioja, N.; Zorita, S.; J., P.F. Effect of Water Matrix on Photocatalytic Degradation and General Kinetic Modeling. *Appl. Catal. B Environ.* **2016**, *180*, 330–335, doi:10.1016/j.apcatb.2015.06.038.

10. Doorslaer, X. Van; Dewulf, J.; Maerschalk, J. De; Langenhove, H. Van; Demeestere, K. Heterogeneous Photocatalysis of Moxifloxacin in Hospital Effluent: Effect of Selected Matrix Constituents. *Chem. Eng. J.* **2015**, *261*, 9–16, doi:10.1016/j.cej.2014.06.079.

11. Hassani, A.; Khataee, A.; Karaca, S. Photocatalytic Degradation of Ciprofloxacin by Synthesized TiO_2 Nanoparticles on Montmorillonite: Effect of Operation Parameters and Artificial Neural Network Modeling. *J. Mol. Catal. A Chem.* **2015**, *409*, 149–161, doi:10.1016/j.molcata.2015.08.020.

12. Malesic-Eleftheriadou, N.; Evgenidou, E.N.; Kyzas, G.Z.; Bikiaris, D.N.; Lambropoulou, D.A. Removal of Antibiotics in Aqueous Media by Using New Synthesized Bio-Based Poly(Ethylene Terephthalate)-TiO_2 Photocatalysts. *Chemosphere* **2019**, *234*, 746–755, doi:10.1016/j.chemosphere.2019.05.239.

13. Anastasiya Kutuzova, Tetiana Dontsova, W.K. Application of TiO_2-Based Photocatalysts to Antibiotics Degradation: Cases of Sulfamethoxazole, Trimethoprim and Ciprofloxacin. *Catalysts* **2021**, *11*, 728, doi:10.3390/catal11060728.

14. Zheng, F.; Martins, P.M.; Queirós, J.M.; Tavares, C.J.; Vilas-Vilela, J.L.; Lanceros-Méndez, S.; Reguera, J. Size Effect in Hybrid TiO2:Au Nanostars for Photocatalytic Water Remediation Applications. *Int. J. Mol. Sci.* **2022**, *23*, 13741, doi:10.3390/ijms232213741.

15. Ribeiro, C.; Costa, C.M.; Correia, D.M.; Nunes-pereira, J.; Oliveira, J.; Martins, P.; Gonçalves, R.; Cardoso, V.F.; Lanceros-méndez, S. Electroactive Poly(Vinylidene Fluoride)-Based Structures for Advanced Applications. *Nat. Protoc.* **2018**, *13*, 681–704, doi:10.1038/nprot.2017.157.

16. Sousa, R.E.; Nunes-pereira, J.; Ferreira, J.C.C.; Costa, C.M.; Machado, A. V; Silva, M.M.; Lanceros-mendez, S. Microstructural Variations of Poly (Vinylidene Fluoride Co-Hexafluoropropylene) and Their Influence on the Thermal, Dielectric and

Piezoelectric Properties. *Polym. Test.* **2014**, *40*, 245–255, doi:10.1016/j.polymertesting.2014.09.012.

17. Martins, P.; Lopes, A.C.; Lanceros-Mendez, S. Electroactive Phases of Poly(Vinylidene Fluoride): Determination, Processing and Applications. *Prog. Polym. Sci.* 2014, *39*, 683–706, doi:10.1016/j.progpolymsci.2013.07.006.

18. Correia, D.M.; Ribeiro, C.; Sencadas, V.; Vikingsson, L.; Gasch, M.O.; Ribelles, J.L.G.; Botelho, G.; Lanceros-méndez, S. Strategies for the Development of Three Dimensional Scaffolds from Piezoelectric Poly (Vinylidene Fluoride). *Mater. Des.* **2016**, *92*, 674–681, doi:10.1016/j.matdes.2015.12.043.

19. Martins, P.; Caparros, C.; Gonçalves, R.; Martins, P.M.; Benelmekki, M.; Botelho, G.; Lanceros-Mendez, S. Role of Nanoparticle Surface Charge on the Nucleation of the Electroactive β-Poly(Vinylidene Fluoride) Nanocomposites for Sensor and Actuator Applications. *J. Phys. Chem. C* **2012**, *116*, 15790–15794, doi:10.1021/jp3038768.

20. Law, K.-Y. Definitions for Hydrophilicity, Hydrophobicity, and Superhydrophobicity: Getting the Basics Right. *J. Phys. Chem. Lett.* **2014**, *5*, 686–688, doi:10.1021/JZ402762H.

21. Wang, B.R.; Hashimoto, K.; Fujishima, A.; Chikuni, M.; Kojima, E.; Kitamura, A. Photogeneration of Highly Amphiphilic TiO_2 Surfaces. *Adv. Mater.* **1998**, *10*, 135–138, doi:10.1002/(SICI)1521-4095(199801)10:2<135::AID-ADMA135>3.0.CO;2-M.

22. Teixeira, S.; Martins, P.M.; Kühn, K.; Cuniberti, G. Reusability of Photocatalytic TiO_2 and ZnO Nanoparticles Immobilized in Poly(Vinylidene Difluoride)-Co-Trifluoroethylene. *Appl. Surf. Sci.* **2016**, *384*, 497–504, doi:10.1016/j.apsusc.2016.05.073.

23. Silva, A.R.; Martins, P.M.; Teixeira, S.; Carabineiro, S.A.C.; Kuehn, K.; Cuniberti, G.; Alves, M.M.; Lanceros-mendez, S.; Pereira, L. Ciprofloxacin Wastewater Treated by UVA Photocatalysis: Contribution of Irradiated TiO_2 and ZnO Nanoparticles on the Final Toxicity as Assessed by Vibrio Fischeri. *RSC Adv.* **2016**, *6*, 95494–95503, doi:10.1039/C6RA19202E.

Chapter 5

5. Conclusions and Future Work

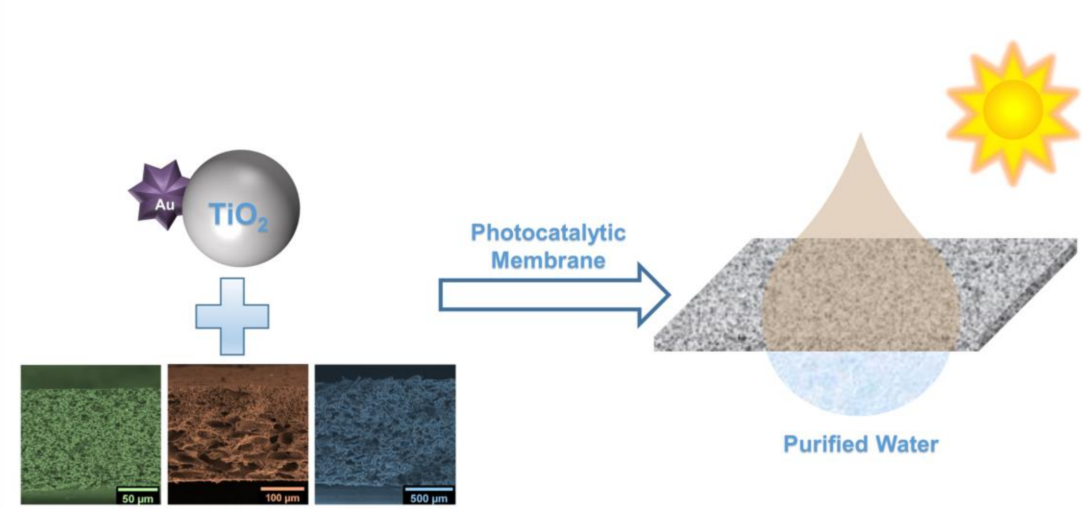

This chapter presents the main conclusions of the present work, which was mainly devoted to the development of new materials and immobilisation strategies to overcome the typical limitations of photocatalysis application in water remediation. Moreover, a few suggestions for future works are also provided.

5.1. Conclusions

The work herein presented, demonstrates a set of different approaches applied to surpass the main obstacles mentioned previously for photocatalysis application in water remediation: poor efficiency of photocatalysts under sunlight and time-consuming and expensive processes for photocatalyst recovery/reuse. In general, the main objective of this thesis have been satisfactorily fulfilled, opening the door to cost-effectively degrade a high variety of contaminants of emerging concern under sunlight for water remediation.

The main conclusions derived from this thesis are collected in this chapter. More detailed conclusions can be found at the end of each chapter.

Firstly, the two common photocatalysts, TiO_2 and ZnO, showed different photocatalytic performance in different pharmaceuticals degradation. The physicochemical properties of photocatalysts and pharmaceuticals play a decisive role in the adsorption behaviour of pollutants on the surface of the photocatalyst and the generation of ROS, which have a crucial influence on photocatalytic performance. The photocatalysts with a higher generation of ROS and higher affinity with pollutants presented higher photocatalytic performance. On the other hand, the production, characterisation and photocatalytic tests of TiO_2:Au and ZnO:Au showed that the functionalisation of semiconductors with spherical Au nanoparticles can reduce the bandgap of the pristine semiconductors and enhance the photocatalytic performance under visible light.

Afterwards, novel hybrid nanoparticles TiO_2:Au-NSs were synthesised successfully by a surfactant-free method, in order to further improve the efficiency of TiO_2:Au based photocatalysts and overcome the limitation of narrow plasmonic band (520nm) given by spherical Au nanoparticles. The characterisation results showed that the change of the shape of Au nanoparticles on the TiO_2 surface, from spherical morphology to branched morphology (nanostar), can enhance the visible light absorption. Furthermore, the increase of Au nanostar size can expand the absorption wavelength under sunlight, from the whole visible to part of NIR region and reduce significantly the bandgap of photocatalyst. The photocatalytic assays under UV, visible and different wavelengths of light showed that the TiO_2:Au-NSs nanoparticles with smaller Au nanostar degrade ciprofloxacin more efficiently than others since the bigger size of Au nanostar can limit the light-harvesting of TiO_2 reducing the photocatalytic activity. In the end, the most efficient TiO_2:Au-NSs nanoparticles, previously tested in suspension, were incorporated successfully into PVDF-HFP-based polymer matrix through NIPS technique for photocatalytic application.

Once the matrix to immobilise photocatalyst was experimentally validated, the focus of the research shifted to the exploration of new morphologies with PVDF-HFP. The previous TiO_2:Au-NSs hybrid nanoparticles were immobilised into two types of membranes with different morphologies/microstructures through doctor blade and salt leaching techniques, both in combination with TIPS. The characterisation results have shown that the presented two techniques allow obtaining membranes with well-distributed and interconnected pores and homogeneous distribution of TiO_2:Au-NSs nanoparticles. Considering the results of photocatalytic tests in the immobilised systems, the increased nanoparticles´ load enhanced the photocatalytic activity since the higher amount of nanoparticles, the more available active site. Furthermore, salt leaching membranes with higher porosity presented higher photocatalytic efficiency compared to doctor blade membranes because the higher porosity improves the interaction between incorporated photocatalysts and pollutants in water enhancing the photocatalytic performance. The membranes with the highest nanoparticles´ load, 10 wt.%, maintained efficiency even after three consecutive uses under both UV and visible light and were fully functional in real treated effluents water matrix for ciprofloxacin degradation. These results indicated the suitability of prepared membranes to degrade contaminants of emerging concern in a cost-effective way, avoiding harmful secondary pollution in the aquatic environment caused by the release of nanoparticles.

5.2. Future work

The work herein presented was mainly focused on the development of advanced materials that allow overcoming photocatalysis most significant limitations in water remediation. Firstly, the importance of the interaction between pollutants and photocatalysts and the generation of ROS for photocatalytic performance was considered. Secondly, new and more efficient photocatalysts were developed and tested for photocatalytic application. Additionally, photocatalysts were immobilised into polymer matrix through different techniques and tested for photocatalytic application. In this context, it would be interesting to advance in different aspects:

- Development of new photocatalytic screening methods for the easy and rapid match between photocatalysts and pollutants for an efficient pharmaceutical degradation

- Development of membranes incorporating two or more photocatalysts to increase photocatalytic activity for simultaneously degrading different pharmaceuticals
- Assays of the developed materials in a solar photoreactor under real sunlight radiation for pharmaceuticals degradation
- Assays of the developed materials for degrading other types of contaminants of emerging concern (CECs) as well as the study of the ecotoxicity of the intermediate products during the photocatalytic degradation
- Development of new multifunctional materials not only for water remediation degrading contaminants of emerging concern (CECs) but also for water disinfection degrading bacteria and viruses

Curriculum Vitae
& Contributions

FANGYUAN ZHENG

BCMaterials – Basque Center for Materials, Applications and Nanostructures

Edificio Martina Casiano, Planta 3, Parque Científico UPV/EHU, Barrio Sarriena, s/n, 48940 Leioa, Bizkaia

email: fangyuan.zheng@bcmaterials.net

ORCID: https://orcid.org/0000-0003-4486-4583

Language skills: Chinese, English, Spanish

RESEARCH TOPICS

Photocatalysis, water remediation, pharmaceuticals degradation

Polymer composite, nanomaterials, membranes, DSC, FTIR, TEM, DLS

EDUCATION

PhD:	University of the Basque Country – UPV/EHU (2019–2023)
Thesis Title:	Hybrid photocatalytic materials for contaminants of emerging concern degradation
Advisors:	Prof. José Luis Vilas Vilela (UPV/EHU)
	Dr. Javier Reguera Gómez (BCMaterials)
MSc in Chemical Engineering	University of the Basque Country – UPV/EHU (2016)
BSc in Chemical Engineering	University of the Basque Country – UPV/EHU (2014)

WORK EXPERIENCE

- **BCMaterials (September 2019-Present)**
  Pre-Doctoral Researcher
- **IDOM Consulting, Engineering, Architecture S.A. (December 2017 – August 2019)**
  Project engineer for test benches of wind turbine
- **SENER Ingeniería y Sistemas S.A (September 2015 – August 2017)**
  Technical responsible of the mechanical equipment for concentrated solar power plants

GRANTS

1. European Commission: Travel grant to attend the first EU TalentON activity (Leiden, Netherlands), 14–18/09/2022
2. BCMaterials and University of Basque Country Predoctoral Fellowship (PIFI20/08), 2020
3. Basque Government MSc. Scholarships, 2014 to 2016
4. Basque Government BSc. Scholarships, 2010 to 2014

AWARDS, MENTIONS AND DISTINCTIONS

Third Prize in EU TalentON 2022, announced by European Commission (18/09/2022)

Our group FORESEA won the 3rd prize in Mission Arenas "Restore our Ocean and Waters" related to the five EU Missions, due to project related to detecting and monitoring microplastics in surface waters.

LARGE FACILITIES PROPOSALS AND MEASUREMENTS

Synchrotron SOLEIL (France), from 01/06/2022 to 06/06/2022, SAMBA Beamline in the framework of proposal n°20211140 (XANES study of photo-induced electronic transformations on Au:TiO_2 Janus nanostars as NIR-activated plasmonic photocatalyst agents).

Researchers to participate:

- Ana Espinosa (Post-doctoral researcher at INDEAM Nanociencia research center)
- Alvaro Muñoz Noval (Professor from Universidad Complutense Madrid)
- Javier Reguera (Post-doctoral researcher at BCMaterials)
- **Fangyuan Zheng** (Pre-doctoral researcher at BCMaterials)

RESEARCH STAYS ABROAD

Universidade do Minho, Braga, Portugal (11 weeks; 7th May-23rd July 2021)

Advisor: Dr. Pedro Manuel Abreu Martins

Universidade do Minho, Braga, Portugal (9 weeks; 1st March-30th April 2022)

Advisor: Dr. Pedro Manuel Abreu Martins

SCIENTIFIC PUBLICATIONS

Part of the thesis:

1. **Zheng, F.**; Queirós, J.M.; Martins, P.M.; Fernández de Luis, R.; Fidalgo-Marijuan, A.; Vilas-Vilela, J.L.; Lanceros-Méndez, S.; Reguera, J. Au-Sensitised TiO_2 and ZnO Nanoparticles for Broadband Pharmaceuticals Photocatalytic Degradation in Water Remediation. *Submitted*.

2. **Zheng, F.**; Martins, P.M.; Queirós, J.M.; Vilas-Vilela, J.L.; Lanceros-Méndez, S.; Reguera, J. Hybrid TiO_2:Au Nanostars Based Polymeric Membranes for Photocatalytic Degradation of Ciprofloxacin in Water Samples. *Chemosphere* **2023**, *313*, 137630, doi:10.1016/j.chemosphere.2022.137630.

3. **Zheng, F.**; Martins, P.M.; Queirós, J.M.; Tavares, C.J.; Vilas-Vilela, J.L.; Lanceros-Méndez, S.; Reguera, J. Size Effect in Hybrid TiO2:Au Nanostars for Photocatalytic Water Remediation Applications. *Int. J. Mol. Sci.* **2022**, *23*, 13741, doi:10.3390/ijms232213741.

Other articles:

4. Reguera, J.; **Zheng, F.**; Shalan, A.E.; Lizundia, E. Upcycling Discarded Cellulosic Surgical Masks into Catalytically Active Freestanding Materials. *Cellulose* **2022**, *29*, 2223–2240, doi:10.1007/s10570-022-04441-9.

5. Jimenez, G.I.T.; Valverde, A.; Mendes-Felipe, C.; Wuttke, S.; Fidalgo-Marijuan, A.; Larrea, E.S.; Lezama, L.; **Zheng, F.**; Reguera, J.; Lanceros-Méndez, S.; et al. Chitin/Metal-Organic Framework Composites as Wide-Range Adsorbent. *ChemSusChem* **2021**, *14*, 2892–2901, doi:10.1002/cssc.202100675.

CONTRIBUTIONS TO MEETINGS

1. **Fangyuan Zheng**, Pedro M. Martins, Senentxu Lanceros-Méndez, Javier Reguera. *Photocatalytic PVDF/TiO_2:Au nanostars membranes for ciprofloxacin degradation in water remediation* "ImagineNano2021 International Event-Composites2021 Conference", 23/11/2021-25/11/2021. (Oral contribution)

2. Nerea Jiménez, **Fangyuan Zheng**, Javier Reguera. *Development of new material coatings based on hybrid Au@Ag nanostars and PVDF for biocid applications.* "New Materials for a Better Life: Advanced Materials for next-generation Biomedicine, Biotechnology and Bioelectronics", BCMaterials-Basque Center for Materials, Applications & Nanostructures (Leioa, Spain), 08/10/2021. (Poster contribution)

3. **Fangyuan Zheng**, Pedro M. Martins, Senentxu Lanceros-Méndez, Javier Reguera. *Synthesis of novel hybrid Au-TiO_2 nanoparticles for water remediation.* "B&B 2021: BCMaterials – University of Bordeaux symposium on bilateral cooperation in advanced materials and applications", Online Conference, 22/06/2021. (Poster contribution)

4. **Fangyuan Zheng**, Pedro M. Martins, Senentxu Lanceros-Méndez, Javier Reguera. *Synthesis of novel hybrid Au-TiO_2 nanoparticles for water remediation.* “New Materials for a Better Life: Advanced multifunctional materials and devices”, BCMaterials-Basque Center for Materials, Applications & Nanostructures (Leioa, Spain), 08/10/2020. (Poster contribution)

5. **Fangyuan Zheng**, Pedro M. Martins, Senentxu Lanceros-Méndez, Javier Reguera. Synthesis of novel hybrid Au-TiO_2 nanoparticles for plasmonic photocatalysis in water remediation “Imaginenano (IM2020)”, Online Conference, 29/09/2020-01/10/2020. (Poster contribution)

6. **Fangyuan Zheng**, Pedro M. Martins, Senentxu Lanceros-Méndez, Javier Reguera. *Synthesis of novel hybrid Au-TiO_2 nanoparticles for water remediation.* “The 3rd Biennial Young Researchers Workshop on Biomaterials and Applications (bioMAPP19)”, BCMaterials-Basque Center for Materials, Applications & Nanostructures (Leioa, Spain), 04-05/12/2019. (Poster contribution)

7. **Fangyuan Zheng**, Pedro M. Martins, Senentxu Lanceros-Méndez, Javier Reguera. *Synthesis of novel hybrid Au-TiO_2 nanoparticles for water remediation.* “New Materials for a Better Life! Advanced devices and Materials as Key Enabling Technologies for Sustainable Environment (NM4BL-2019)”, BCMaterials-Basque Center for Materials, Applications & Nanostructures (Leioa, Spain), 27/11/2019. (Poster contribution)

SCIENTIFIC DISSEMINATION

1. **EU TalentON 2022.** European Commission-Leiden 2022. (Leiden, Netherlands), 14–18/09/2022.

2. **School visit “Colegio San Adrián”** BCMaterials-Basque Center for Materials, Applications & Nanostructures (Leioa, Spain), 16/12/2021.

3. **European Researchers' Night.** University of the Basque Country – UPV/EHU (Bilbao, Spain), 24/09/2021.

4. **BCMaterials calendar.** Images selected to appear in the 2021 and 2022 editions of the company calendar.

5. **Fortnightly seminar** “Synthesis of novel hybrid nanoparticles. Removal of pollutants through plasmonic photocatalysis”, BCMaterials-Basque Center for Materials, Applications & Nanostructures (Leioa, Spain). 04/11/2020

6. **International day of women and girls in science events.** 11 February Initiative (2020-2023)

7. **Science week (Zientzia Astea)**. University of the Basque Country – UPV/EHU (09–13/ 11/2019)

TRAINING COURSE

1. **How to prepare a proposal for a review article.** Matt Pavlovich, Andrea Stephens, Online training. (30/11/2020, 1 hour)
2. **Introduction of Web of Science.** Cristina González Copeiro, online training. (14–18/09/2020, 9 hours)
3. **PhDing by Design: Designing and Preparing a Research Publication.** Tim Smithers. University of the Basque Country – UPV/EHU, online training. (30/04/2020–18/06/2020, 24 hours).
4. **Buenas prácticas en el laboratorio (II): gestión de residuos peligrosos.** University of the Basque Country – UPV/EHU, online training. (13/02/2020–24/03/2020, 25 hours).
5. **Gestión de residuos peligrosos de laboratorio.** University of the Basque Country – UPV/EHU. (20/11/2019, 2 hours).
6. **5th Fullprof training BEGINNERS.** Marine Reynaud, Maria Jauregui, Montse Galcerán and Montse Casas-Cabanas. CIC energiGUNE. (29–30/10/2019, 12 hours).

Copyright and Licencing information

Except where noted, all artwork and photographs are the work of the author.

Chapter 2. Au-sensitised TiO_2 and ZnO photocatalysts for broadband pharmaceuticals degradation

Cover image:

Water adapted from licensed work by upklyak / Freepik.